Gold-free Growth of InAs Nanowires: Growth, Structural & Electrical Properties

THÈSE N^{O} 7939 (2017)

PRÉSENTÉE LE 24 NOVEMBRE 2017
À LA FACULTÉ DES SCIENCES ET TECHNIQUES DE L'INGÉNIEUR
LABORATOIRE DES MATÉRIAUX SEMICONDUCTEURS
PROGRAMME DOCTORAL EN SCIENCE ET GÉNIE DES MATÉRIAUX

ÉCOLE POLYTECHNIQUE FÉDÉRALE DE LAUSANNE

POUR L'OBTENTION DU GRADE DE DOCTEUR ÈS SCIENCES

PAR

Heidi Andrea POTTS

acceptée sur proposition du jury:

Prof. C. Hébert, présidente du jury
Prof. A. Fontcuberta i Morral, directrice de thèse
Prof. P. C. McIntyre, rapporteur
Prof. K. Dick Thelander, rapporteuse
Prof. N. Grandjean, rapporteur

ÉCOLE POLYTECHNIQUE
FÉDÉRALE DE LAUSANNE

Suisse
2017

To my family.

Acknowledgements

I would like to express my gratitude to everyone who supported and helped me during my PhD, and also to everyone who made it a fun experience. In particular I would like to thank:

Anna Fontcuberta i Morral for giving me the opportunity to join your group and the great supervision throughout the four years. Thank you not only for your help with my professional development but also your invaluable coaching and personal support. You really know how to motivate people to work hard without putting pressure or forgetting the importance of family, friends, and fun.

Paul McIntyre, **Kimberly Dick Thelander**, **Nicolas Grandjean** and **Cécile Hébert** for taking the time to evaluate my thesis and giving some very helpful feedback.

The MBE team for the nice four years in the lab. I would like to thank **Gözde Tütünüoglu** and **Federico Matteini** for teaching me how to use and maintain our MBE. I will never forget the nice moments sweating in a tydex. I would also like to thank **Daniel Rüffer** for lots of technical advice when planning the installation of the antimony cell. Later on **Jean-Baptiste Leran** took over a big part of the responsibility and I am very grateful for your contribution. Finally, also **Martin Friedl** joined the MBE team and made lots of improvements, for example by installing a camera to monitor the icicle. I also want to acknowledge **Fauzia Jabeen** for showing me how to do RHEED.

The NCCR QSIT. QSIT did not only provide the funding for my PhD, but also a great network to discuss science and seek advice. In particular I am grateful for the opportunity to do a mini-sabbatical in the Wegscheider group to learn about the growth of antimonides. Thanks to **Werner Wegscheider**, **Christian Lehner** and **Thomas Tschirky**. I would also like to thank the Ensslin group for sharing their expertise about electrical measurements. Thanks to **Klaus Ensslin** and **Susanne Müller**. I was happy about the opportunity to organize the QSIT junior meeting, and would like to thank **Ilona Blatter** for your guidance and **Luca Francaviglia** for organizing the meeting with me. And of course I would like to thank QSIT for the nice general meeting in Arosa – including the legendary ski race.

All LMSC group members for interesting discussions and lots of social activities. First of all I would like to thank **Gözde Tütüncüoglu** for your great help and guidance. From my first growth results until my final project, you were always available for a scientific discussion (and some gossip). I would like to thank **Martin Friedl** for the great work during your Master thesis and later for your invaluable understanding of equipment and software. You always found time to discuss some problems with the electrical setup and you always had good ideas how to optimize a process. I would like to thank **Jelena Vukajlovic Plestina** for your great knowledge about any possible cleanroom fabrication process, and for your big heart. LMSC would not be the same without your cakes and your impressive skills to find the right birthday presents. And I would like to acknowledge **Francesca Amaduzzi** and **Esther Alacron-Llado** for providing additional insights by Raman spectroscopy. I would also like to thank the semester students and visiting students, who were working with me on small projects during my PhD, in particular **Nicholas Morgan** and **Youri van Hees**. Finally, I would like to thank all other group members of LMSC for the nice evenings in Satellite, hiking in the Alpes (**Alberto Casadei**), the short holiday in Split (thanks to **Jelena, Roko and Ruger**), sailing (**Luca Francaviglia**), correcting my French (**Elias Stutz**), loading samples (**Mahdi Zamani**), ice cream breaks (**Andreana Daniil**)...

Our collaborators for their help, additional results, and discussions. In particular I am grateful to **Kechao Tang** and **Paul McIntyre** (from Stanford University) for allowing us to study the effects of surface passivation, and also for the opportunity to visit Stanford. I would like to thank **Jessica Boland** and **Michael Johnston** (from Oxford) for doing Terahertz spectroscopy, as well as **Marta Rossell** (from EMPA) for the opportunity to do annealing experiments in a TEM. Furthermore I would like to thank **Philippe Caroff** (now at Cardiff University) for lots of fruitful discussions and for sharing your extensive knowledge of the literature.

The team of CIME - my PhD thesis would not have been possible without electron microscopy. I would like to express my gratitude to **Amelie Bazzoni** who first trained me on the TEM, **Marco Cantoni**, **Duncan Alexander** and **Thomas LaGrange** for your continuous TEM support, **Fabienne Bobard** for SEM support and keeping everything in order, and **Danièle Laub** and **Colette Vallotton** for teaching me how to make cross sections with the ultramicrotome.

The team of CMi for maintaining a professional cleanroom, giving training to users and offering lots of help with specific problems. In particular I would like to thank **Zdenek Benes** for your ebeam expertise and always a good joke, **Cyrille Hibert** and **Joffrey Pernollet** for etching advice, **Kaspar Suter** for photolithography, **Philippe Langlet** and **Guy Clerc** for ellipsometry, evaporation and sputtering, and **Patrick Madliger** for always being in a good mood – and for constantly reminding me to wear my safety goggles.

The team of the physics workshop and physics cleanroom for your great help and support with technical problems. **Gilles Grandjean** and **Nicolas Leiser** saved us many times when we encountered problems with our MBE, providing custom-made screws during a cryopump replacement just to give an example. I am also very grateful for the antimony cell holder designed by **Michel Longchamp**, without which the installation of our antimony cell would have been a nightmare.

Monika Salas-Tesar for organizing everything super fast without ever making any mistakes, and also for giving me the opportunity to practice my French. You were very patient with my explanations, even though you speak English and German perfectly.

My family and friends for your love and support. In particular I would like to thank my boyfriend **Patrick**, my parents **Dorle** and **Kevin**, my sister **Marike**, my brothers **Florian** and **Ryan**, and my grandma **Muhme**.

Lausanne, 28 July 2017 H. P.

Abstract

Semiconductor nanowires are interesting building blocks for a variety of electronic and optoelectronic applications, and they provide an excellent platform to probe fundamental physical effects. For the realization of nanowire based devices, a deep understanding of the growth mechanism and the nanowire properties is required. In this thesis we investigate gold-free growth of InAs(Sb) nanowires and their properties. Nanowires are grown by molecular beam epitaxy on GaAs(111)B substrates.

In the first part of this thesis we demonstrate the growth of InAs and $\mathrm{InAs}_{1-x}\mathrm{Sb}_x$ nanowires and show that polytypism can be suppressed by the incorporation of antimony. The electric properties of InAs(Sb) nanowires are studied by electrical measurements and by Raman spectroscopy, and a higher electron mobility is found for defect-free $\mathrm{InAs}_{0.65}\mathrm{Sb}_{0.35}$ nanowires compared to InAs nanowires. We also investigate surface passivation using aluminium oxide. The oxide layer not only serves as passivation layer but it can also be used as gate-dielectric for top-gated field-effect devices.

The second part of this thesis is dedicated to the nanowire growth direction and orientation with respect to the substrate. We analyze the existence of tilted nanowires on (111)B substrates, and demonstrate that in most cases they are a result of 3D twinning at the early stages of growth. In addition, also a few unconventional crystalline directions are observed. The ratio of tilted nanowires can be tuned by the growth conditions and substrate preparation. This allows to achieve either all vertical nanowires or a high density of tilted nanowires, whichever is desired for a certain application. Our results also shed light upon the growth mechanism of InAs nanowires, since 3D twinning is associated with the presence of a droplet.

Being able to control the formation of tilted nanowires is important, but for certain applications it is also desired to modify the growth direction during growth. For example topological qubits based on Majorana Fermions require junctions and networks. In the third part of this thesis we show a new approach to change growth direction. For this, InAs nanowires are annealed in vacuum in order to create indium droplets. The droplets first form on the top facet of the nanowires and then slide down onto the nanowire side facets. These droplets can act as catalyst-particle, and re-initiation of growth results in L-shaped nanostructures. Merging of these nanostructures constitutes a new approach for the formation of nanowire networks.

Key words: III-V semiconductors, nanowires, molecular beam epitaxy, crystal structure, polytypism, twinning, growth direction, surface passivation, atomic layer deposition, electrical properties

Zusammenfassung

Halbleiter Nanodrähte sind interessant als elektronische und optoelektronische Bauteile und sie bieten eine ausgezeichnete Platform, um grundlegende physikalische Effekte zu messen. Für die Realisierung von Bauteilen ist ein tiefes Verständnis für das Wachstum und die Eigenschaften der Nanodrähte notwendig. Diese Dissertation behandelt das Wachstum und die Eigenschaften von InAs(Sb) Nanodrähten, welche mittels Molekularstrahlepitaxie ohne Hilfe von Gold epitaktisch auf GaAs(111)B Substraten gewachsen werden.

Der erste Teil dieser Dissertation behandelt das Wachstum von InAs und $InAs_{1-x}Sb_x$ Nanodrähten. Wir zeigen, dass Polytypismus durch das Hinzufügen von Antimon unterdrückt werden kann und die elektrischen Eigenschaften der InAs(Sb) Nanodrähte werden mit elektrischen Messungen und mit Ramanspektroskopie untersucht. Fehlerfreie $InAs_{0.65}Sb_{0.35}$ Nanodrähte zeigen eine höhere Elektronenmobilität als InAs Nanodrähte. Weiterhin untersuchen wir die Möglichkeit der Oberflächenpassivierung mittels Aluminiumoxid. Das Oxid kann neben der Passivierung auch als Gate-Dielektrikum verwendet werden.

Im zweiten Teil steht die Wachstumsrichtung und Orientierung der Nanodrähte im Fokus. Wir zeigen, dass schiefe Nanodrähte auf (111)B Substraten hauptsächlich auf dreidimensionale Zwillingsbildung im Anfangsstadium des Wachstums zurückzuführen sind. Zusätzlich finden wir auch Drähte in unkonventionellen Kristallrichtungen. Das Vorkommen von schiefen Nanodrähten kann durch die Wachstumsbedingungen und Substratpreparation beeinflusst werden. Je nach Anwendung kann somit eine Probe mit komplett geraden Drähten, oder mit einer hohen Dichte an schiefen Drähten gewachsen werden. Zusätzlich beleuchten unsere Ergebnisse den Wachstumsmechanismus von InAs Nanodrähten, da die dreidimensionale Zwillingsbildung mit der Existenz eines Indium Tröpfchens in Verbindung steht.

Für bestimmte Anwendungen ist es erwünscht die Richtung während des Wachstums zu ändern. Topologische Quantenbits basierend auf Majorana Fermionen benötigen zum Beispiel verzweigte Nanodrähte. Im dritten Teil zeigen wir ein Vorgehen, um die Wachstumsrichtung zu ändern. Hierfür werden InAs Nanodrähte unter Vakuum aufgeheizt bis sich Indium Tröpfchen bilden. Die Tröpfchen beginnen an der Spitze der Nanodrähte und rutschen dann auf die Seitenflächen. Wird das Wachstum nun fortgesetzt, bilden sich L-förmige Nanostrukturen, welche durch Zusammenwachsen die Bildung eines Netzwerkes ermöglichen.

Stichwörter: III-V Halbleiter, Nanodrähte, Molekularstrahlepitaxie, Kristallstruktur, Polytypismus, Kristallzwilling, Wachstumsrichtung, Oberflächenpassivierung, Atomlagenabscheidung, elektrische Eigenschaften

Résumé

Les nanofils semi-conducteurs sont intéressants pour des applications électroniques et opto-électroniques, et servent de plateforme pour étudier des effets physiques fondamentaux. A cette fin, les mécanismes de croissance et les propriétés des nanofils doivent être compris et maitrisés. Dans cette thèse nous examinons la croissance de nanofils d'InAs(Sb) et leurs propriétés. La croissance est réalisée par épitaxie par jets moléculaires sur des substrats en GaAs(111)B sans utilisation d'un catalyseur étranger.

Dans la première partie nous montrons la croissance de nanofils en $\mathrm{InAs}_{1-x}\mathrm{Sb}_x$. Nous trouvons que le polytypisme peut être supprimé par l'incorporation d'antimoine. Les propriétés électriques sont analysées par des mesures électriques et par spectroscopie Raman. Nous trouvons que la mobilité des électrons des nanofils d'$\mathrm{InAs}_{0.65}\mathrm{Sb}_{0.35}$ est supérieure à celle des nanofils en InAs. De plus, nous étudions la passivation de surface en utilisant de l'oxyde d'aluminium. L'oxyde peut aussi servir comme couche diélectrique de grille pour des transistors.

La seconde partie concerne la direction de croissance cristalline des nanofils d'InAs et leur orientation par rapport au substrat. Nous montrons que les nanofils inclinés sur des substrats (111)B peuvent être expliqués par la formations de macles en 3D pendant les étapes initiales de la croissance. Nous trouvons aussi des directions cristallines non-conventionnelles. La formation des nanofils inclinés peut être contrôlée par les conditions de croissance et la préparation du substrat. Ainsi, il est possible d'obtenir des échantillons avec seulement des nanofils verticaux, ou avec une haute densité des nanofils inclinés, en fonction des besoins d'une application. Nos résultats aident aussi à éclairer le mécanisme de croissance des nanofils d'InAs, puisque la formation de macles en 3D indique la présence d'une gouttelette.

Pour certaines applications, il peut aussi être désirable de changer la direction des nanofils pendant la croissance. Par exemple, des jonctions ou des réseaux de nanofils sont nécessaires pour la réalisation de qubits topologiques basés sur les particules de Majorana. Dans la troisième partie nous démontrons une nouvelle approche pour la formation de réseaux. Dans ce but, les nanofils d'InAs sont chauffés sous vide jusqu'à la formation de gouttelettes d'indium. Les gouttelettes commencent à croître à la pointe des nanofils avant de glisser sur les facettes. Continuer la croissance aves ces gouttelettes donne lieu à des nanostructures en forme de 'L'. Un réseau de nanofils peut être réalisé en fusionnant plusieurs de ces structures.

Mots clefs : III-V semi-conducteurs, nanofils, épitaxie par jets moléculaires, structure cristalline, polytypisme, macles, directions cristalline, passivation de surface, atomic layer déposition, propriétés électriques

Contents

Curriculum Vitae

List of publications

Most of the work presented in this thesis has been published in peer-reviewed scientific journals. The publications are reproduced in chapter 4 with permission of the corresponding publishers. For the papers presented here, I planned the experiments, did the majority of the experimental work and data analysis, and wrote the largest part of the manuscripts.

A-I **H. Potts**, M. Friedl, F. Amaduzzi, K. Tang, G. Tutuncuoglu, F. Matteini, P. C. McIntyre, and A. Fontcuberta i Morral. From Twinning to Pure Zincblende Catalyst-Free InAs(Sb) Nanowires. *Nano Letters* **16**, 637 (2016)

A-II **H. Potts**, Y. van Hees, G. Tutuncuoglu, M. Friedl, J.-B. Leran, A. Fontcuberta i Morral. Tilting catalyst-free InAs nanowires by 3D- twinning and unusual growth directions. *Crystal Growth & Design* **17**, 3596 (2017)

A-III **H. Potts**, N. P. Morgan, G. Tutuncuoglu, M. Friedl, and A. Fontcuberta i Morral. Tuning growth direction of catalyst-free InAs(Sb) nanowires with indium droplets. *Nanotechnology* **28**, 054001 (2017)

During my thesis I also contributed to a variety of other projects by providing samples for experiments, performing transmission electron microscopy, and doing the maintenance and calibration of our molecular beam epitaxy system. As a result, I am co-author of the following papers:

B-I E. Russo-Averchi, J. Vukajlovic Plestina, G. Tutuncuoglu, F. Matteini, A. Dalmau-Malloqui, M. de la Mata, D. Rüffer, **H. Potts**, J. Arbiol, S. Conesa-Boj, and A. Fontcuberta i Morral. High yield of GaAs Nanowire Arrays on Si Mediated by the Pinning and Contact Angle of Ga. *Nano Letters* **15**, 2869 (2015)

B-II F. Matteini, G. Tutuncuoglu, **H. Potts**, F. Jabeen, and A. Fontcuberta i Morral. Wetting of Ga on SiOx and its Impact on GaAs Nanowire Growth. *Crystal Growth & Design* **15**, 3105 (2015)

B-III G. Tutuncuoglu, M. de la Mata, D. Deiana, **H. Potts**, F. Matteini, J. Arbiol, and A. Fontcuberta i Morral. Towards defect-free 1-D GaAs/AlGaAs Heterostructures based on GaAs nanomembranes. *Nanoscale* **7**, 19454 (2015)

B-IV A. D. Alvarez, T. Xu, G. Tutuncuoglu, T. Demonchaux, J. P. Nys, M. Berthe, F. Matteini, **H. Potts**, D. Troadec, G. Patriarche, J.-F. Lampin, C. Coinon, A. Fontcuberta i Morral, R.E.

Dunin-Borkowski, Ph. Ebert, and B. Grandidier. Nonstoichiometric Low-Temperature Grown GaAs Nanowires. *Nano Letters* **15**, 6440 (2015)

B-V M. Glaser, A. Kitzler, A. Johannes, S. Prucnal, **H. Potts**, S. Conesa-Boj, L. Filipovic, H. Kosina, W. Skorupa, E. Bertagnolli, C. Ronning, A. Fontcuberta i Morral, and A. Lugstein. Synthesis, Morphological, and Electro-optical Characterizations of Metal/Semiconductor Nanowire Heterostructures. *Nano Letters* **16**, 3507 (2016)

B-VI J. Vukajlovic-Plestina, V. Dubrovskii, G. Tutuncuoglu, **H. Potts**, R. Ricca, F. Meyer, F. Matteini, J.-B. Leran, and A. Fontcuberta i Morral. Molecular beam epitaxy of InAs nanowires in SiO2 nanotube templates: challenges and prospects for integration of III-Vs on Si. *Nanotechnology* **27**, 455601 (2016)

B-VII F. Matteini, G. Tutuncuoglu, D. Mikulik, J. Vukajlovic-Plestina, **H. Potts**, J.-B. Leran, W. Carter, and A. Fontcuberta i Morral. Impact of the Ga droplet wetting, morphology, and pinholes on the orientation of GaAs nanowires. *Crystal Growth & Design* **16**, 5781 (2016)

B-VIII J. Vukajlovic-Plestina, V. Derek, L. Francaviglia, F. Amaduzzi, **H. Potts**, M. Ivanda, and A. Fontcuberta i Morral. Nanoporous silicon tubes: the role of geometry in nanostructure formation and application to light emitting diodes. *Journal of Physics D: Applied Physics* **50**, 265101 (2017)

B-IX J. Vukajlovic-Plestina, W. Kim, V. G. Dubrovski, G. Tutuncuoglu, M. Lagier, **H. Potts**, M. Friedl, and A. Fontcuberta i Morral. Engineering the size distributions of ordered GaAs nanowires on silicon. *Nano Letters* **17**, 4101 (2017)

B-X W. Kim, V. Dubrovski, J. Vukajlovic-Plestina, G. Tutuncuoglu, L. Francaviglia, L. Guniat, **H. Potts**, M. Friedl, J.-B. Leran, A. Fontcuberta i Morral. Bi-stability of contact angle and its role in achieving quantum-thin self-assisted GaAs nanowires (submitted)

List of Figures

Acronyms

AFM atomic force microscopy.

ALD atomic layer deposition.

APT atom probe tomography.

BF bright field.

EDX energy dispersive x-ray.

FFT fast Fourier transform.

HAADF high angular annular dark field.

LO longitudinal optical.

MBE molecular beam epitaxy.

MOCVD metal-organic chemical vapour deposition.

OPTP optical pump terahertz probe.

PDMS Polydimethylsiloxane.

SAED selected area diffraction.

SEM scanning electron microscope.

STEM scanning transmission electron microscope.

TDS time-domain spectroscopy.

TEM transmission electron microscope.

TFET tunnel field effect transistor.

THz terahertz.

TMA trymethylaluminium.

TO transverse optical.

UHV ultra-high vacuum.

VLS vapour-liquid-solid.

VS vapour-solid.

WZ Wurtzite.

ZB zinc-blende.

1 Introduction & Motivation

Nowadays it is hard to imagine life without digital technology. Economics, transportation, social media, health care, daily communication - everything is based on digital electronics. It all started in 1947 with the invention of the first solid-state transistor at Bell Labs. Since then, research has enabled to rapidly decrease the size of electronic elements, going from several centimeters in size to the 14 nanometer node by Intel in 2014. For the last 50 years, the trend roughly followed the prediction by Gordon Moore, saying that the transistor density on a chip would double every 18 months. The scaling allowed to increase performance and decrease power consumption. To date, transistors in integrated circuits are fabricated by a top-down approach, meaning that they are defined by a lithography process and etching. When reaching the few nanometer dimension, this becomes increasingly difficult, since extremely precise control of dimensions, impurities and doping is required. At those length scales, bottom-up approaches based on self-assembly of atoms, become more interesting. Bottom-up growth facilitates the fabrication of three-dimensional electronic devices, and allows for the use of non-traditional materials. One very promising class of materials are III-V semiconducting nanostructures. III-V semiconductors offer both optical as well as electronic properties which are superior to silicon. GaAs for example has a direct band gap with an energy of 1.42 eV at room temperature, thereby making it attractive for a variety of optoelectronic applications. InAs and InSb on the other hand show extremely high electron mobilities up to 40000 $\mathrm{cm}^2/\mathrm{Vs}$ and 77000 $\mathrm{cm}^2/\mathrm{Vs}$ at room temperature [Ioffe17], making them ideal candidates for high-speed electronic devices.

High-quality III-V semiconductors can be grown in a bottom-up approach by molecular beam epitaxy (MBE). Since MBE growth is performed under ultra-high vacuum (UHV) conditions, it enables the control of impurity incorporation on a very precise level. Molecular beam epitaxy allows to grow two-dimensional layers, low-dimensional nanostructures (e.g. nanowires and nanomembranes), and zero-dimensional quantum dots. Nanostructures give access to novel properties due to their small dimensions and large surface-to-volume ratio. First of all, nanowires can be very efficient light absorbers. In combination with the direct band-gap of GaAs, solar cells with the potential to exceed the Shockley-Queisser limit have been demonstrated [Krogstrup13a]. Nanowire arrays not only allow to achieve higher efficiencies, but bottom-up growth would also allow to dramatically reduce the material use of solar cells. Nanowires also act as natural cavities, making them interesting for lasing applications [Saxena13, Mayer13, Burgess16, Bermudez-Urena17]. In terms of electrical applications, III-V nanowires are very interesting due to the high electron mobilities, and they can act as natural channels without the need for localized doping. Free-standing nanowires therefore allow the fabrication of gate-all-around transistors, which show superior performance [Goldberger06, Bryllert06, Tomioka12]. Furthermore, nanostructures facilitate the fabrication of heterostructures, combining different materials into one structure. While for two-dimensional heterostructures the lattice mismatch presents a big challenge, in nanowires the strain can be relaxed radially, allowing to combine materials with relatively large mismatch dislocation-free [Glas14]. The radial strain relaxation also allows to grow on different substrates (heteroepitaxy), thereby reducing the need for exotic substrate materials, and facilitating the integration of III-Vs with current silicon technologies. The fabrication of heterostructures is an active field of research, for example for the fabrication of single-photon sources [Heiss13]. Recently the integration of a III-V quantum emitter in a silicon based photonic circuit has been demonstrated [Zadeh16]. III-V heterostructures are also interesting for the realization of tunnel field effect transistor (TFET) [Ionescu11]. TFETs are a promising avenue to achieve further downscaling of transistors, since they are expected to show high performance at low power consumption due to an increased sub-threshold slope and minimized current at the off-state. It has been suggested that heterostructures showing a broken band-alignment (e.g. InAs/GaSb) are ideal candidates of tunnel injection, and at the same time one can benefit from the high carrier mobilities of III-V semiconductors [Ionescu11].

Current electronic technology does not only reach its limitations in terms of size, but there are also problems which are extremely hard to solve using conventional classical logic: any problem which requires the calculation of many different possibilities is extremely slow. This includes for example factoring of big numbers, searching through large datasets, exploring the properties of new materials, or simulating biological systems. While the difficulty of factoring big numbers is an advantage for cryptography used in daily life, it would certainly be advantageous to speed up the search for new catalyst materials or high temperature superconductors, and it would be nice to be able to model complex quantum mechanical systems in order to understand basic processes in living organisms. With these goals in mind, the quantum computer shows great promise. A quantum computer is based on qubits which can be in a superposition state of 0 and 1. This superposition allows a quantum computer to perform several calculations in parallel, leading to a dramatic speed up for calculations which require the testing of many different paths. Nowadays extensive research is dedicated to the realization of a quantum computer. Different types of qubits are being explored, including cold-atoms, superconducting circuits (Google, IBM), silicon quantum dots (Intel), and topological qubits (Microsoft, Bell Labs) [Popkin17]. In 2016 IBM presented the realization of five qubits based on superconducting circuits, and in May 2017 they already presented 16 qubit processor. With *Quantum Experience* IBM also offers a platform through which the public can simulate basic calculations and run them on their quantum processor [IBM17]. Even though 16 qubits are not nearly enough for useful computations, those recent advances show great promise for the technology, and quantum computers have been mentioned as one of the ten break-through technologies in 2017 [MIT17]. While the realization of IBM's quantum processors is a great step forward, scaling the technology is still a big challenge, and each of the qubit architectures has advantages and disadvantages. In particular for superconducting qubits, problems arise due to the short lifetime and relatively high error probability. Using topological qubits such as Majorana zero-modes in nanostructures is expected to offer significant improvement, since the excitation occurs at two ends of the nanostructure. This spatial separation makes it much harder to disturb the system and create errors [Beenakker13]. Majorana zero-modes can be realized by combining a semiconducting material with a large g-factor and high spin-orbit coupling (e.g. InAs and InSb) with a superconductor. While signatures of Majorana zero-modes have already been demonstrated for the first time five years ago [Mourik12], the implementation of several such excitations in the same nanostructure, as required for quantum operations, remains a challenge. Here networks of semiconducting nanostructures show great promise and are intensively being studied by many groups worldwide.

In order to advance materials which can be used both for the design of novel transistors and for quantum computation, as well as out of scientific curiosity, bottom-up growth of III-V semiconducting nanostructures by molecular beam epitaxy is studied in this thesis. The focus here lies on the optimization of the crystalline quality, as well as control of the growth direction, both of which are important requirements for the use of nanostructures for electronic applications. The crystalline quality is important since stacking defects locally change the band structure, thereby decreasing the mean-free path of carriers and leading to additional recombination pathways. In this thesis we demonstrate the growth of pure zinc-blende $\mathrm{InAs}_{1-x}\mathrm{Sb}_x$ nanowires which are practically defect-free. A precise control of the growth direction is important both for applications where nanowires are contacted in parallel (e.g. photo detectors and transistor applications) as well as for the growth of nanowire networks. In the first case it is desired that all nanowires grow in the same direction in order to avoid leakage pathways. We therefore intensively study the origin of tilted nanowires, discuss the underlying mechanism, and show how the occurrence of tilted nanowires can be suppressed. For the formation of nanowire networks it is necessary to have nanowires growing in different directions. One way to achieve nanowire networks is by changing direction during growth. In this thesis we show a new approach to change growth direction of nanowires grown without a foreign catalyst.

This thesis is divided into five chapters:

Chapter I: Introduction & Motivation

In the first chapter the topic of this thesis is introduced. The project is placed in a wider scientific context, and the motivation for this field of research is discussed.

Chapter II: Growth and properties of III-V Nanostructures

In the second chapter the growth mechanism and properties of III-V nanostructures are reviewed. We start with a brief overview of epitaxial growth by molecular beam epitaxy, and then explain the growth of nanowires in more detail. The rest of the chapter reviews the properties of InAs nanowires which are relevant for this thesis. In particular we discuss the crystal structure of self-catalyzed nanowires, the growth direction, and their electrical properties. We also discuss several techniques to investigate the electrical properties of nanowires.

Chapter III: Experimental Methods

In this chapter the experimental methods which are relevant for this thesis are presented. We start by explaining the substrate preparation and growth conditions that were used. Then we discuss about sample analysis using transmission electron microscopy. In particular we describe a process to make nanowire cross-sections, and how to measure the composition using energy dispersive x-ray spectroscopy. In the end we explain the fabrication of electrical devices based on nanowires, and describe the measurements which were done in this work.

Chapter IV: Results & Discussion

The main results of this thesis are presented in this chapter. Our results include suppression of polytypism by adding antimony, surface passivation using alumina, understanding the formation of tilted nanowires, and tuning to growth direction to achieve L-shaped nanostructures. For every topic we first discuss its motivation and relevance and then present the article which has been published in peer-reviewed scientific journals.

Chapter V: Conclusion & Outlook

In the last chapter we conclude the topic and present an outlook for further research.

2 Growth and properties of III-V Nanostructures

In this chapter, I will first give a general introduction to the growth of III-V materials using molecular beam epitaxy (MBE), and then describe the growth of nanostructures. I will discuss the properties of III-V nanowires, in particular focusing on InAs nanowires. This chapter is by far not exhaustive, it rather focuses on the topics which are relevant for this thesis and motivates the results which are presented in the publications in chapter 4.

2.1 Epitaxial growth using MBE

Epitaxy comes from the Greek words $\epsilon\pi\iota$ (above) and $\tau\alpha\xi\iota\zeta$ (in an ordered manner). It is used to describe the growth of a crystalline material on a crystalline substrate, when there is a relationship between the two crystals. Several techniques can be used for epitaxial growth. The most common ones are metal-organic chemical vapour deposition (MOCVD) and MBE. For MOCVD, the growth is based on metal-organic precursors which decompose on the surface. The advantage of this technique is that it is more easily scalable than other epitaxy techniques, and therefore interesting for industrial applications. The drawback is the possibility of unintentional doping of the materials due to incorporation of parts of the organic precursors. MBE on the other hand is based on the evaporation of pure materials and therefore ensures high purity. Figure 2.1(a)-(b) shows a schematic representation and a picture of our MBE chamber. It consists of an ultra-high vacuum chamber, which is kept at a base pressure of $1 \cdot 10^{-10}$ Torr by cryopumps and cryopanels (liquid nitrogen circulating in the reactor walls). Ultra-high vacuum is an important requirement for MBE growth, not only to avoid unintentional incorporation of atoms, but also to ensure that atoms which are emitted from a cell can travel almost ballistically to the substrate. The sample is mounted on a manipulator, which can be heated and rotated. At the bottom of the chamber ten ports for cells are available. In our MBE system we have gallium, indium and aluminum effusion cells, arsenic and antimony valved cracker cells, and silicon and carbon current cells for doping. The antimony cell is relatively new to our system, and was installed and calibrated as part of my PhD project during the first two years. Our growth chamber is part of a cluster tool, which is shown schematically in Figure 2.1(c). The cluster tool consists of two growth chambers, one central distribution chamber

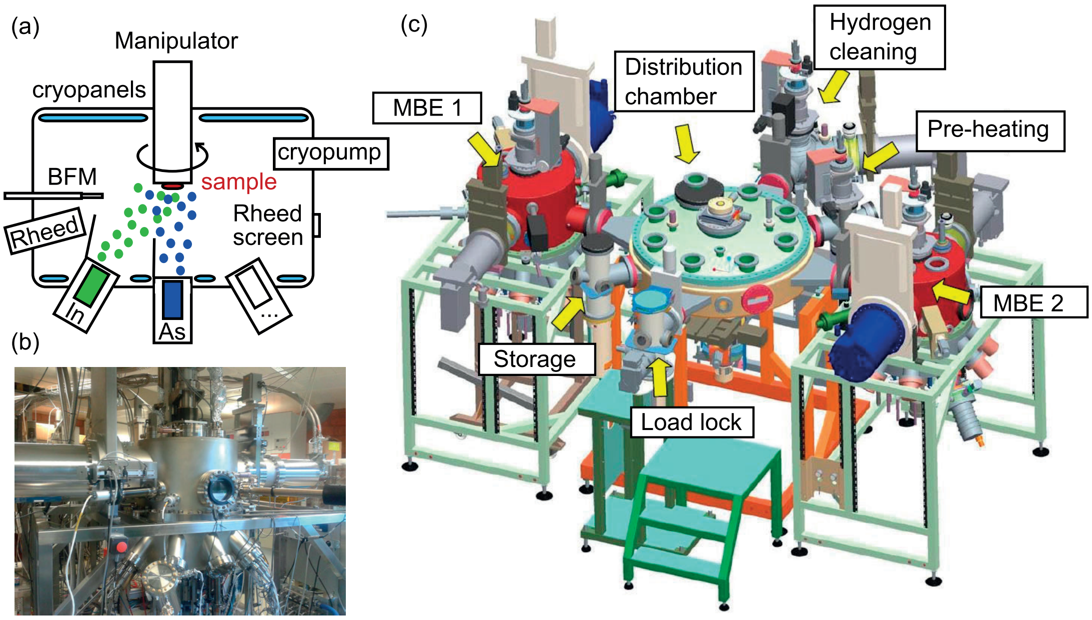

Figure 2.1 – MBE system. (a) Schematic representation of an MBE chamber. (b) Photo of our growth chamber. (c) Schematic representation of our DCA P600 MBE cluster tool (courtesy of DCA).

with a robot arm for automatic sample manipulation, one load lock, a storage chamber, a degassing chamber and a chamber for hydrogen cleaning.

Epitaxial growth differs from other deposition techniques by the epitaxial relationship between the substrate and the new layer. This is achieved by very slow growth rates, in combination with heating of the substrate. Exact control of the conditions and substrate morphology allows diffusion of the incoming atoms on the substrate until they find a lattice site, allowing to minimize the energy of the material. If the adatoms are not given enough time or energy to reach their lowest energy position before they are buried by the next layer of material, then random clusters are formed rather than an epitaxial crystal [Tsao93].

When growing a crystalline layer on top of a crystalline substrate, the lattice constant of the two materials is an important parameter. The lattice mismatch is defined as $(a_{subst} - a_{layer})/a_{subst}$, where a_{subst} and a_{layer} are the lattice constant of the substrate and the epitaxial layer. A lattice mismatch will lead to elastic strain in the growing layer. The strain can be relaxed, for example by forming dislocation having Burgers vectors with a component in the plane of the interface, by coherent roughening, or by dilatation in the case of nanowires where one end is fixed to the substrate). For epitaxial growth, the choice of substrate material is therefore critical. Figure 2.2 shows a graph with the band gap energies and lattice parameters for III-V semiconductor materials. It can be seen that III-Vs offer a variety of band gap energies, but there is also a significant difference in lattice parameter, which makes it difficult to grow the materials epitaxially. Nanostructures offer an important advantage for the growth of different III-V materials, since the interface between the substrate and the nanostructure is very small,

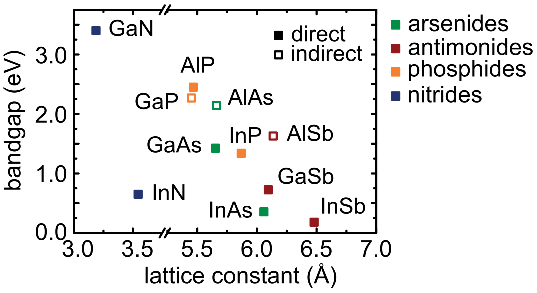

Figure 2.2 – Bandgap energy and lattice constant of III-V materials.

allowing to relax the strain via the surfaces of the free-standing nanostructure [Glas14].

Another critical parameter during the growth of III-V materials is the substrate morphology and polarity. III-V materials are binary compounds. The smallest indivisible unit is a pair of one group III atom and one group V atom, also called dumbbell. Therefore certain crystalline directions of the material are polar, i.e. they can be either group-III terminated or group-V terminated. When choosing a non-polar substrate material, the nucleation of the seed crystal can either start with a layer of group III atoms or a layer of group V atoms. A schematic of two seed crystal with different polarity on a (111) substrate is shown in Figure 2.3(a). In case of poly-nucleation on the substrate, the merging of seed crystals with different polarity will lead to the formation of antiphase boundaries, where atoms of the same type are connected as shown in Figure 2.3(b). For arsenides, antiphase boundaries are electrically active and lead to a high recombination velocity [Holt96]. On (100) substrates, also the existence of terraces can lead to the formation of antiphase boundaries, even when the nuclei have the same polarity [Kunert08].

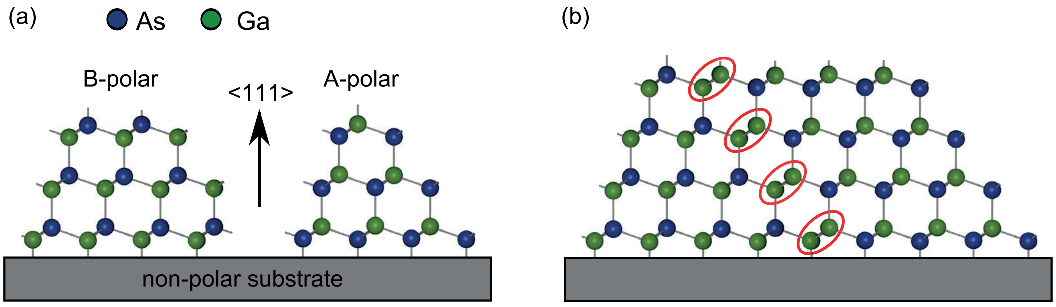

Figure 2.3 – Growth on non-polar substrates. (a) Schematic representation of polynucleation where one seed crystal is A-polar and the other one B-polar. (b) Merging of two seed crystals with different polarity leads to an antiphase boundary.

2.2 Growth of nanostructures

Growth of nanostructures usually requires substrate preparation in order to promote growth in certain positions and directions and preventing growth otherwise. The first observation of nanowire growth was based on using gold as a catalyst particle [Wagner64]. Today, this is still the most common approach. Metal particles are deposited onto the substrate either by lithography or by depositing a thin film and then annealing to form separate droplets. The metal droplets then act as collector and catalyst particles. When they reach supersaturation, crystalline material precipitates below the droplet. This growth process is called vapour-liquid-solid (VLS) mechanism and is schematically illustrated in Figure 2.4(a).

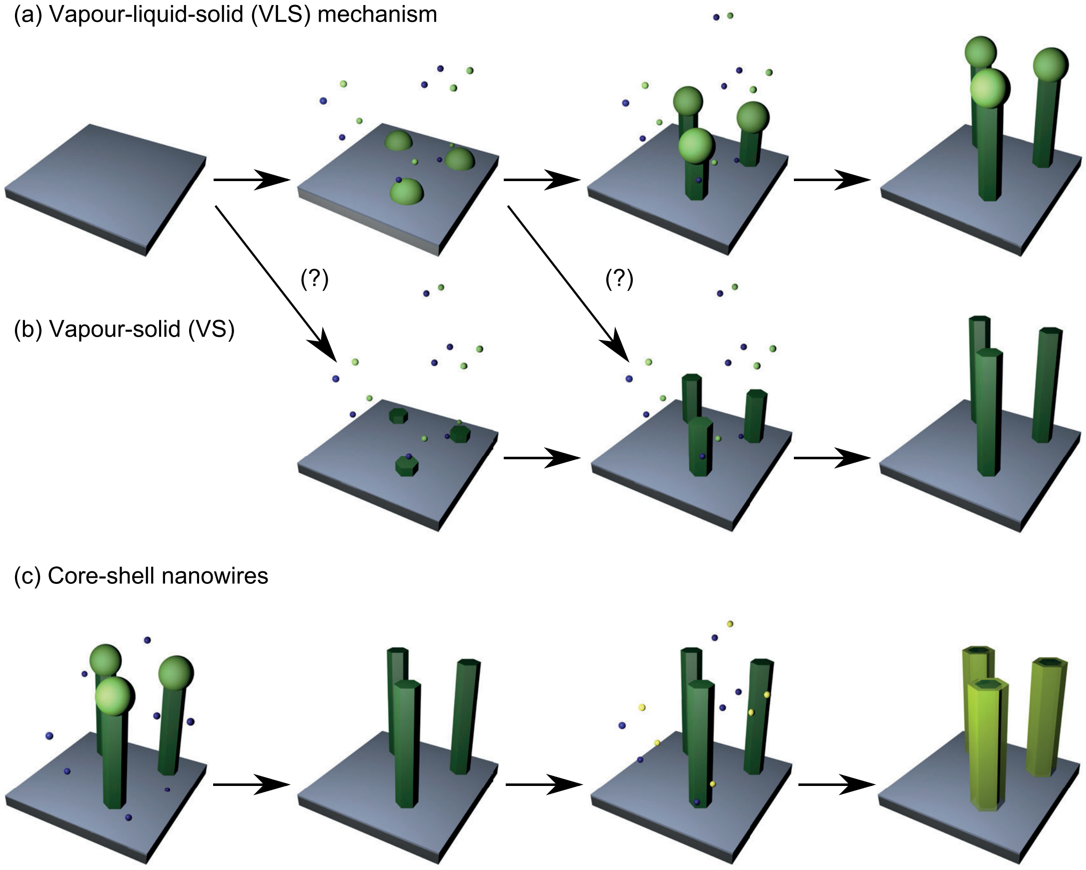

Figure 2.4 – Nanowire growth mechanism. (a)-(b) Schematic representation of vapour-liquid-solid growth and vapour-solid growth. (c) Growth of core-shell nanowires.

While the use of a foreign metal as catalyst allows to grow nanostructures of many different materials [Wagner64, Yazawa92, Björk02, Thelander03, Krishnamachari04, Borgström07], unfortunately, it cannot be excluded that small amounts of the catalyst material get incorporated into the growing nanostructure. Although the effect of using gold in III-V nanowires is still controversial, small gold inclusions have been found in silicon and GaAs nanostructures [Allen08, Bar-Sadan12]. These impurities can have dramatic effects on the optical and electrical properties of the material [Brotherton80, Tambe10]. An alternative approach for the growth of III-V nanowires is to use a droplet of the group III element as a catalyst particle. In this case the growth proceeds also via the VLS mechanism shown in Figure 2.4(a), but this time the droplet consists mostly of the group III element, which then becomes supersaturated with the group V element. The growth of self-catalyzed GaAs nanowires has been demonstrated already almost one decade ago [Colombo08], and the resulting nanowires show a very nice morphology with a gallium droplet on top, as well as excellent properties.

While the VLS growth mechanism is by far the most common, growth can also proceed with a solid catalyst particle, then called vapour-solid-solid (VSS), or without any catalytic droplet via the vapour-solid (VS) mode. Figure 2.4(b) shows a schematic of the VS mechanism. Here the atoms are incorporated directly from the vapour phase or after diffusion along the nanowire surface, and the growth direction is determined by surface energies. In the case of InAs nanowires grown without a foreign catalyst, the underlying growth mechanism is debated extensively, and both evidence for VS [Dimakis11] and for VLS [Grap13] has been reported. It is also possible that the growth starts with a droplet and then switches to the VS mechanism. In a recent study by Biermanns *et al*, the presence of a liquid indium droplet at the early stages of growth has been associated with the possibility to grow a defect-free wurtzite section [Biermanns14]. While our results presented in this thesis do not give a complete answer to these questions, we provide additional insights in publication 2 and 3.

In order to initiate growth of nanowires without a foreign catalyst, the surface properties are extremely important. In particular the surface energies have to favour the formation of droplets rather than homogeneous wetting of the surface. This can be achieved for example by coating the substrate with a thin dielectric layer (e.g. 5 nm of SiO_2 on GaAs) [Grap13, Matteini14], or by using a silicon substrate with a 1 nm thick layer of native oxide [Matteini15, Matteini16]. In order to have a crystalline relation with the substrate, these approaches rely on the opening of pinholes in the oxide. The nanowires are then randomly distributed across the substrate. Control of the nanowire position can be achieved by patterning a thicker dielectric layer for example by ebeam lithography and etching. This allows to open holes with well-defined size and distribution across the sample [Vukajlovic-Plestina17]. By choosing the substrate preparation and the growth conditions carefully, it is possible to achieve growth in all the pre-defined openings and not elsewhere on the sample. This method has a major advantage for applications where the distance between nanowires is critical, for example for photovoltaic applications where the absorption depends on the pitch [Heiss14]. Recently it was also demonstrated that elongated openings can be used as template to grow nano-membranes [Tutuncuoglu15], opening a whole new field of research.

Nanostructures are particularly interesting for the investigation of heterostructures. As discussed above, lattice mismatch is less critical in nanostructures due to the possibility to relax strain via dilatation permitted by the presence of free surfaces at a distance from the interface [Glas14]. Both axial and radial nanowire heterostructures can be grown. A schematic of core-shell growth is shown in Figure 2.4(c). First the nanowire core is grown using the VLS or VS approach, and then the conditions are switched to favour growth on the side facets. In the case of MBE growth, changing from axial to radial growth usually involves an increase in group V flux and a decrease in growth temperature. The incoming group III atoms thereby have less ability to diffuse on the nanowire surface, and get incorporated on the side facets, rather than being able to diffuse to the droplet at the tip.

2.3 Crystal structure

A big part of my thesis is dedicated to the analysis of the crystal structure of grown nanowires, which has a significant impact on their properties. Due to their particular growth mechanism and their large surface-to-volume ratio, nanowires can exhibit crystal phases that do not exist in bulk crystals of the same material. For example, the bulk crystal phase of III-arsenides is cubic zinc-blende (ZB), while in nanostructures also hexagonal Wurtzite (WZ) stacking can be observed. Figure 2.5(a)-(b) shows a schematic representation of zinc-blende and wurtzite stacking seen from a <110> zone axis. The two polytypes can be distinguished by their stacking sequence in the <111> direction, which is A-B-C-A-B-C for ZB and A-B-A-B for WZ. Nanowires often show a mixture of zinc-blende and wurtzite (called polytypism) and other stacking defects. A very common defect in zinc-blende crystals is the formation of a rotational twin, which corresponds to a rotation of 180° around a <111> direction. This results in a stacking sequence of A-B-C-B-A, as shown in Figure 2.5(c). The crystal structure of a nanostructure can be analyzed by transmission electron microscopy when the crystal is aligned in a <110> zone axis. High resolution transmission electron microscope (TEM) images allow to visualize the stacking sequence. Also fast Fourier transform (FFT) images of the high resolution TEM micrograph and selected area diffraction (SAED) images are useful to see the difference between zinc-blende, wurtzite und polytypic crystals. Figure 2.5(d)-(f) show low-resolution TEM micrographs, SAED images, and high-resolution TEM micrographs of nanowires with zinc-blende crystal structure, wurtzite crystal structure, and zinc-blende with a rotational twin.

The origin of the formation of WZ in nanowires has been studied by many groups. In particular the diameter of the nanowire, the supersaturation of the droplet, the contact angle of the droplet, and the nucleation site (whether or not nucleation occurs at the triple phase line) have an effect on the crystal structure [Glas07, Krogstrup13b, Jacobsson16]. The ionicity of the bond and size of the atoms is also expected to play a role. III-V materials have partially ionic or mixed bonds, and therefore favour WZ stacking, where the third-nearest neighbour spacing is shorter. On the other hand steric hindrance favours ZB stacking. During growth, the crystal will adopt the phase which has the lower formation energy, and the contributions from both effects have to be considered. Comparing the ionicity of different III-V materials, it can be observed that III-nitrides have the highest ionocity, and III-antimonides the lowest. These considerations can explain why III-nitrides crystallize in the WZ form, while anitmonides show ZB stacking [Dick10a]. For arsenides, the formation energy of ZB and WZ seems to be very similar, therefore leading to the co-existence of ZB and WZ under certain conditions.

As a result of a different band structure, the two polytypes zinc-blende and wurtzite show different optical and electrical properties, e.g. they have a different band gap, electron affinity, and effective mass. The possibility to grow both ZB and WZ III-arsenide nanowires of the

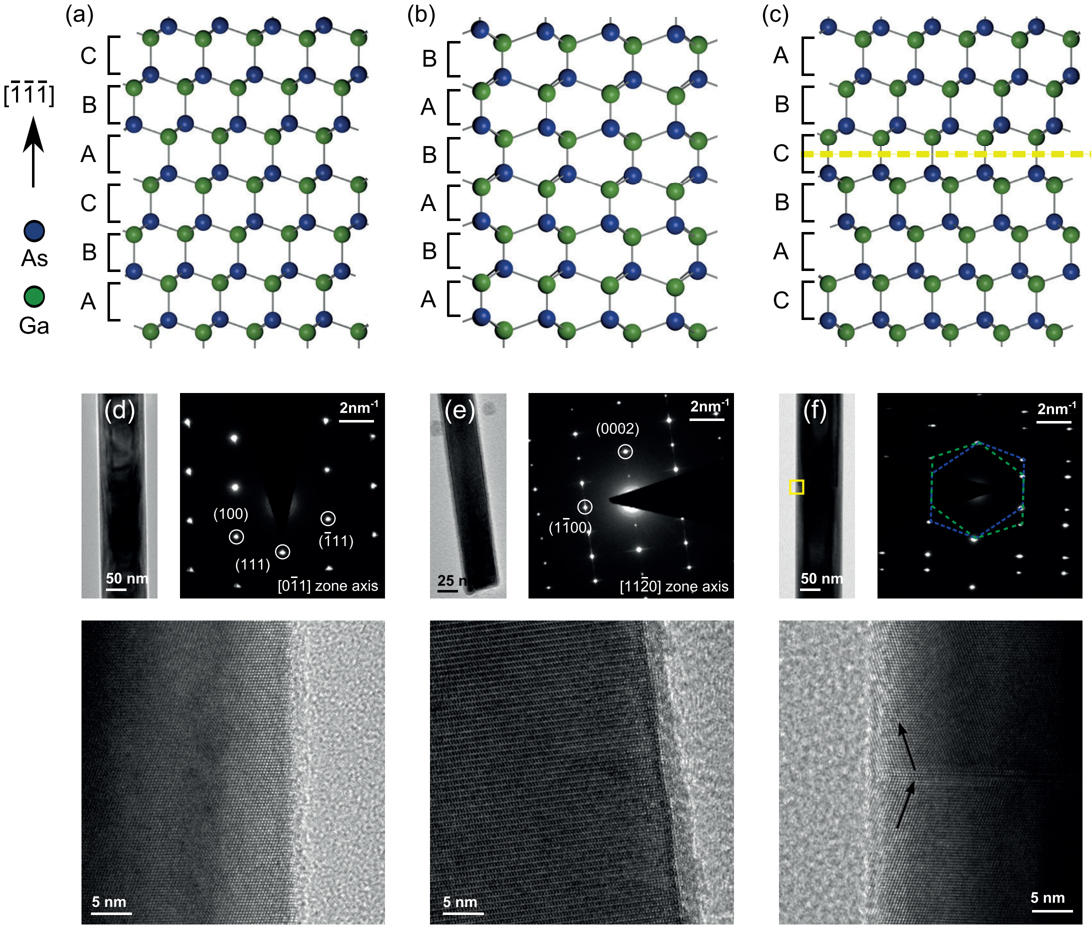

Figure 2.5 – Crystal structure of III-V materials. (a)-(c) Schematic representation of a zinc-blende crystal, a wurtzite crystal and a zinc-blende crystal with a rotational twin (from a <110> zone axis). (d)-(f) Low magnification TEM micrograph, SAED image, and high-resolution TEM micrograph of a ZB nanowire, a WZ nanowire, and a ZB nanowire with a rotational twin.

same material allowed to study and compare the electrical and optical properties the two polytypes for the first time [Hörmann11, Ketterer11]. For nanowires which show a polytypic crystal structure, the band alignment between the two materials is important. In the case of GaAs and InAs, a type-II staggered band alignment is expected, with the electron affinity of WZ being lower than for ZB. In terms of optical properties the existence of different polytypes leads to additional recombination pathways, i.e. from the conduction band of a zinc-blende section to the valence band of a wurtzite section, as observed for GaAs nanowires [Heiss11]. In a controlled way, ZB/WZ sections can also be used to design crystal phase quantum dots [Akopian10]. In terms of electrical properties, WZ sections can be used as tunneling barriers, allowing the fabrication of electrical crystal-phase quantum dots [Nilsson16]. These examples show that the existence of different polytypes in nanowires creates many opportunities, but it also causes undesired effects if it does not occur in a controlled way.

In the case of gold-catalyzed InAs nanowires, impressive results have been obtained in terms of controlling the crystal structure of nanowires [Dick10b, Joyce10, Nilsson16]. For self-catalyzed nanowires it is more challenging to control the formation of zinc-blende or wurtzite selectively. Pure ZB GaAs nanowire have been demonstrated [Krogstrup10], but self-catalyzed InAs nanowires always show polytypism [Grap13, Dimakis11]. In publication 1 we discuss the growth of ternary $InAs_{1-x}Sb_x$ nanowires, and show that incorporation of antimony allows to suppress polytypism.

2.4 Nanowire growth direction and orientation on the substrate

For many applications it is important to achieve full control of the nanowire growth direction and orientation. If several nanowires are contacted in parallel (e.g. for energy harvesting), it is desired to have all vertical nanowires, in order to avoid short circuits within the sample. For other applications, a change of crystalline direction can be advantageous. For example for quantum computation based on braiding of Majorana Fermions, nanowire junctions and nanowire networks are a requirement [Alicea11]. Furthermore, certain properties like the g-factor depend on the crystalline orientation, thereby giving another motivation to achieve a change of growth direction. Conventionally, III-arsenide and III-antimonide nanowires grow in <111>B direction and exhibit a hexagonal cross section terminated by $\{1\bar{1}0\}$ facets. The preferential growth direction and morphology of the nanowires can be understood considering that 3D crystals adopt the most energetically favourable configuration (equilibrium crystal shape). For III-arsenide materials {110} surfaces have the lowest surface energy, thereby favouring the formation of {110} facets in 3D crystals. One should note, that during growth, the systems is out of thermodynamic equilibrium and also kinetic factors can play a role. Therefore also other facets can be formed under certain conditions and have been observed for example in the case of nanomembranes [Tutuncuoglu15].

Considering the preferential growth direction of nanowires, one would expect to observe all vertical nanowires on a (111)B substrate. However, depending on the growth conditions, also a significant amount of tilted nanowires can be observed. This finding has been studied extensively in the case of self-catalyzed GaAs nanowires, and it has been found that the existence of tilted nanowires can be explained by a 3-dimensional twinning process [Uccelli11]. As described in section 2.3, rotational twins are commonly observed in III-arsenide nanostructures. Typically they are found perpendicular to the growth direction, since the structure is growing layer by layer. However, especially at the early stages of the growth the formation of other {111} facets which are non perpendicular to the growth direction is possible.

Figure 2.6(a) shows a schematic representation of a seed crystal on a (111)B substrate. All {111}B planes are highlighted in red. Rotational twins can in principle occurs around all <111> directions. Figure 2.6(b) shows a secondary seed crystal which presents the orientation of the crystalline planes after a 180° rotation around the $[\bar{1}11]$ direction. The indices of the planes of the secondary seed crystal are not changed in order to demonstrate the 180° rotation. However the planes are now oriented completely differently with respect to the primary seed crystal

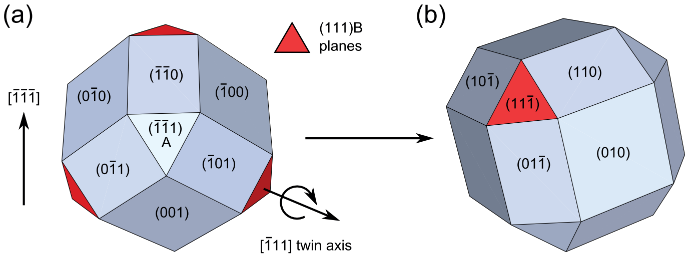

Figure 2.6 – Schematic of 3D twinning. (a) Cubic representation of a seed crystal on a (111)B substrate. (b) Secondary seed crystal after a twin around the $[\bar{1}11]$ direction. The cubic model was adapted from [Tsan17] (courtesy of Youri van Hees).

(and therefore to the substrate). For nanowire growth we are particularly interested in the orientation of the new {111}B planes, which can be the growth directions of tilted nanowires. Their direction can be calculated by basic linear algebra, as shown in publication 2. One should note that on a (111)B substrate, there is one <111>B direction which is perpendicular to the surface, and there are three <111>A directions pointing out of the substrate at an angle. All the other <111>B directions are pointing into the substrate. 3D twinning therefore requires either a twin in a <111>A direction, or it requires a very big seed crystal which allows the formation of facets oriented towards the substrate. Both options are unfavourable, giving another reason why typically mostly vertical nanowires are observed.

In the case of InAs nanowires, the existence of tilted nanowires has, to the best of our knowledge, not been studied before. In this thesis we study the existence and orientation of tilted InAs quantitatively and present that multiple order twinning can explain most of the nanowire orientations. In addition, a few unconventional growth directions are observed. The calculations of 3D twinning orientations and our experimental results are presented in publication 2. Understanding the formation of tilted InAs nanowires does not only help to achieve more homogeneous samples, it also provides additional insights about the initial stages of growth, since the 3D twinning phenomenon can be associated with the existence of a droplet.

2.5 Electrical properties & surface passivation

InAs and InSb nanowires are particularly interesting for electronic applications due to their high electron mobilities and low effective mass. The first experimental signatures of Majorana Fermions in 2012 were based on InAs and InSb nanowires [Mourik12, Das12], and several other experiments have been reported since then. The results are impressive and give a good reason to continue optimizing the growth of InAs nanowires. Nevertheless, there are still some open questions about the basic electronic properties of InAs nanowires. Here we discuss the topics which are relevant for this thesis.

The electrical properties of a nanowire differ significantly from the bulk material. In particular InAs nanowires typically do not show electron mobilities above 10000 $\mathrm{cm}^2/\mathrm{Vs}$ [Dayeh10, Gupta13] and the exact value depends on the nanowire diameter [Ford09], while the bulk mobility of InAs is reported to be up 40000 cm^2/Vs at room temperature [Ioffe17]. This relatively low mobility in InAs nanowires is attributed to crystal phase mixing and to scattering at the surface. Recently, it has been shown that the mobility is three times larger for InAs nanowires with pure crystal phase, compared to polytypic nanowires [Thelander11]. In the case of $InAs_{1-x}Sb_x$ nanowires an increase of mobility has been reported and explained by the reduction of stacking defects upon incorporation of antimony [Sourribes14]. Apart from the crystal structure, also surface scattering plays an important role. This not only causes a lower mobility, but can also explain the large variation of conductivity values and the dependence on the diameter that can be observed for nanowires of the same material [Scheffler09]. Adsorbates on the nanowire surface or substrate have been reported to dramatically change the electrical properties of InAs nanowires [Gül15], and hydrogen cleaning has been studied as a tool to reduce scattering at the surface [Webb15]. The strong dependence of the electrical properties on the nanowire surface create a need for measurements in vacuum or for passivation of the nanowire surface, since vacuum measurements are not a long-term solution when going towards applications.

2.5.1 Fermi level pinning

It is generally assumed that InAs nanowires show n-type behaviour, even without intentional doping, and it is easy to make ohmic contacts to the material using a variety of metals. This behaviour can be related to non-intentional doping due to incorporated carbon, but it is more commonly attributed to the existence of surface states which act as donors and lead to Fermi level pinning. Figure 2.7 shows a schematic representation of Fermi level pinning due to the existence of surface states in the conduction band. The theoretical location of the surface states with respect to the band gap of intrinsic InAs is shown in Figure 2.7(a). In reality the carriers will move to minimize their energy, leading to band bending at the surface, as shown in Figure 2.7(b). The Fermi level of the nominally undoped InAs now lies above the conduction band at the surface, which can explain the n-type behaviour of the nanowires. It also allows for the fabrication of ohmic contacts, which would otherwise require the electron affinity of the semiconductor to be larger than the work function of the contact metal.

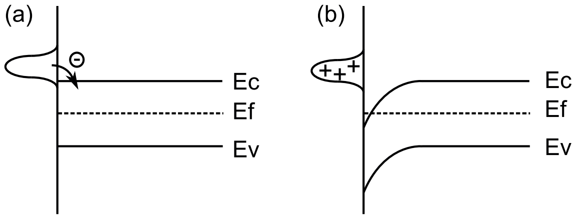

Figure 2.7 – Fermi level pinning in InAs. (a) Donor states at the surface are located in the conduction band. (b) Electrons are transferred from the donor states into the bulk, leading to an electron accumulation layer at the surface.

Fermi level pinning has been demonstrated for clean (100) and (111) InAs surfaces without a native oxide [Mead63, Olsson96, Lowe03]. The donor states are related to dangling bonds at the surface, and their properties depend on the surface orientation and reconstruction. Therefore it is not clear whether Fermi level pinning also exists in nanowires which typically have (110) surfaces. For oxide-free (110) surfaces, a dependence on surface defects has been observed. Defect-free (110) surfaces show no Fermi level pinning [Olsson96, Wildöer97, Hjort14], while the presence of defects results in the formation of an accumulation layer [Castleton13]. In the case of nanowire devices, the nanowires are usually covered with a thin layer of native oxide. With a native oxide, InAs (110) surfaces have been found to show Fermi level pinning [Halpern12], and has also been predicted theoretically [Weber10]. The position of the Fermi level is very sensitive to the composition of the oxide at the semiconductor-oxide interface [Timm11, Webb15]. Considering the strong dependence on the surface preparation and reconstruction, it is expected that the Fermi level pinning also depends on the material composition. This has been shown for ternary $\mathrm{InAs}_{1-x}\mathrm{Sb}_x$ nanowires [Thelander12].

2.5.2 Conductivity & Mobility

For a semiconductor, the conductivity and carrier mobility are important characteristics. The conductivity $\sigma = n \cdot e \cdot \mu_e + p \cdot e \cdot \mu_h$ depends on the carrier density of electrons n and holes p, and on the mobility of the electrons μ_e and holes μ_h. Temperature dependent measurements provide interesting information about the material. The carrier density depends on the temperature $n \propto \mathrm{e}^{-E_a/k_B T}$, where k_B is the Boltzmann constant, T is the temperature and E_a is the activation energy. The activation energy is related to the bandgap energy in the case of thermally excited carriers ($E_a = E_c - E_F = 0.5 \cdot E_g$ for undoped semiconductors), but it can also be smaller than the bandgap energy in the case of dopants, impurities, or trap states. The exponential relationship shows that a decrease in carrier density is expected for a decrease in temperature. Figure 2.8(a) shows a schematic representation of the carrier concentration n of a doped semiconductor (with doping concentration N_D) in dependence of the inverse temperature $1/T$ (Arrhenius plot). Three regimes can be observed: At high temperature, the carrier concentration changes due to excitation across the bandgap (intrinsic carriers). At medium temperature the carrier density is constant because the dopants are fully ionized and the energy is not enough to excite intrinsic carriers. And at low temperature freeze-out of the dopants can be observed.

The mobility depends on the temperature in a more complex way, due to different scattering mechanisms. The total mobility can be estimated by Matthiessen's rule

$$\frac{1}{\mu_{total}} = \sum_i \frac{1}{\mu_i} = \frac{1}{\mu_{phonon}} + \frac{1}{\mu_{impurities}} + \frac{1}{\mu_{surface}} \ldots \tag{2.1}$$

Figure 2.8(b) shows a schematic representation of the mobility of GaAs [Grundmann16]. The contributions from different scattering mechanisms are shown. We observe that at high temperature, the mobility is limited by phonon scattering. Since the phonon density decreases

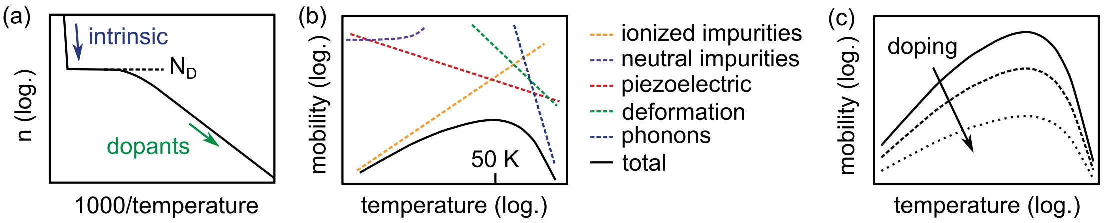

Figure 2.8 – Temperature dependence of electrical properties (a) Carrier concentration for a doped semiconductor. (b) Carrier mobility and the contribution from different scattering mechanisms. (c) Mobility dependence on the doping concentration. The schematics are adapted from [Grundmann16].

with decreasing temperature, we observe an increase in mobility. At around 50 K scattering due to ionized impurities becomes more pronounced than scattering due to phonons, leading to a decrease in mobility. The temperature dependence of the mobility also depends on the doping of the material, and typically a stronger temperature dependence is observed for lower doping, as shown in Figure 2.8(c). From the mobility dependence we can also gain some information about the scattering mechanism and the carrier location: if the carriers are at the surface, a higher scattering contribution is expected due to surface effects.

Different techniques can be used to measure the carrier density and mobility of a material. For nanowires, both electrical measurements and optical measurements are of interest. In the following sections we provide a brief description of the techniques of electrical measurements, Raman spectroscopy and Terahertz spectroscopy. A comparison and discussion of the techniques is presented at the end of the section.

Electrical measurements

The basic electrical properties of a semiconductor nanowire can be studied by current/voltage (I/V) measurements and field-effect measurements. From I/V curves the nanowire conductivity can be calculated using the dimensions (the cross sectional area A of the nanowire and length of the device L) measured in SEM images. For the calculation we assume that the current is uniform throughout the nanowire and the conductivity σ is therefore given by

$$\sigma = \frac{I}{V}\frac{L}{A} \tag{2.2}$$

This assumption may not be correct, considering that the carriers may be predominantly on the nanowire surface due to the Fermi level pinning. However without exact knowledge about the location of the carriers, this formula still constitutes the most appropriate way to compare different nanowires.

One way to extract the carrier concentration and mobility is to study the field-effect behaviour of nanowire devices. A gate voltage is applied either through a highly doped silicon substrate (back-gate measurements) or via a top-gate or side-gate. Figure 2.9(a) shows a schematic of a field-effect measurement with linear current axis for an n-type device. The field-effect mobility can be calculated by

$$\mu = g_m \frac{L^2}{C} \frac{1}{V_{ds}} \tag{2.3}$$

where $g_m = (dI_{ds})/(dV_g)$ is the transconductance in the linear operating region, L is the length of the device, C is the nanowire-gate capacitance, and V_{ds} is the source-drain voltage [Dayeh07]. The nanowire-gate capacitance needs to be modeled. Bottom-gated devices with an oxide thickness much larger than the nanowire diameter are typically approximated by a metallic cylinder on an infinite metallic plate [Dayeh07]. For this design, the capacitance is given by

$$C = \frac{2\pi\epsilon_0\epsilon_r L}{\mathrm{acosh}[(r+t_{ox})/r)]} \tag{2.4}$$

where r is the radius of the nanowire, and t_{ox} is the thickness of the dielectric layer. For bottom-gated devices a relative dielectric constant ϵ_r of 2.25 is used to account for the fact that the nanowire is not completely surrounded by the gate [Wunnicke06]. It is therefore possible to compare the mobility of different nanowire devices based on field-effect measurements. However a quantitative comparison is challenging since measurements typically show strong hysteresis between the forward and backward sweep of the gate voltage. This is usually attributed to trapped charges in the gate oxide or changes of the nanowire surface. In views of this, it is not clear whether the measured mobility describes the bulk of the nanowire or is rather limited by scattering at the surface (depending on the location of the carriers).

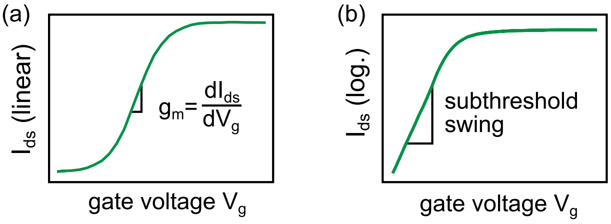

Figure 2.9 – Schematics of field-effect measurements. (a) A linear plot allows to extract the transconductance g_m. (b) A logarithmic y-axis allows to extract the sub-threshold swing.

Another important characteristic of a field-effect measurement is the sub-threshold swing, which should be as low as possible for an ideal transistor device. Figure 2.9(b) shows a schematic of a field-effect measurement, where the source-drain current I_{ds} is plotted logarithmically on the y-axis and the gate voltage V_g on the x-axis. The sub-threshold swing is defined as the gate voltage which is needed to change the current below the threshold by one order of magnitude, and is usually given as mV/dec. For a conduction process limited by the rate of thermal excitation over an energy barrier, the ideal value is 60 mV/dec.

Optical measurement techniques

Apart from electrical measurements, the carrier concentration and mobility can also be calculated from Raman measurements and terahertz (THz) spectroscopy. These techniques are interesting because they allow for contact-free measurements, and the analysis does not depend on the estimation of a gate capacitance. For the nanowires presented in this thesis, Francesca Amaduzzi (from LMSC) performed Raman measurements, and THz spectroscopy was done by Jessica Boland (from the Johnston group in Oxford). The complete theory behind the optical characterization is beyond the scope of this thesis, but the principal ideas are briefly described here.

1) Raman spectroscopy

For Raman spectroscopy, nanowires are transfered to a silicon substrate wafer. The sample is illuminated with a laser in the visible range and the inelastically scattered light is measured. Both light at higher energy (anti-Stokes shift) and at lower energy (Stokes shift) is observed. The energy shift is related to the vibrational modes in the material and provides information about the crystal structure, composition and orientation. Furthermore, also information about the electronic properties, for example the dopant concentration and carrier mobility can be extracted from Raman measurements [Ketterer12]. Depending on the orientation of the sample with respect to the laser, only certain modes are allowed. These selection rules can require special measurement geometries, e.g. measuring the nanowires in transmission geometry rather than backscattering geometry. This can also be achieved by positioning the nanowires on trenches [Amaduzzi16].

The basic Raman modes can be understood by looking at the crystal structure of the material and counting the number of atoms N in the unit cell. The primitive unit cell of a zinc-blende material contains two atoms. Each unit cell has $3N$ degrees of freedom, resulting in a total of six for a zinc-blende material. In a solid there are three modes corresponding to translations, which are referred to as acoustic phonons. The other $3N$-3 modes are related to vibrations and are referred to as optical phonons. Optical phonon modes can be excited by illumination with light. Even though the Indian physicist C. V. Raman claimed that he observed the Raman effect using sunlight [Raman17], typically a laser is used in Raman spectroscopy. The high power of a laser allows to get sufficient counts to plot a full spectrum in a reasonable amount of time. The momentum of light is small compared to the Brillouin zone and therefore we probe the modes at the Γ point. The optical phonons consist of one longitudinal optical (LO) mode and two degenerate transverse optical (TO) modes. For nanostructures an additional surface optical mode can be detected [Spirkoska08]. For wurtzite crystals, there are more phonon modes and their dispersion relation is different, which allows to distinguish the two polytypes. However, here we limit our description to ZB materials, since for our InAs(Sb) nanowires only ZB modes were observed. For our work on InAs(Sb) nanowires the Raman modes for ternary alloys are of interest. Ternary alloys typically show a two-mode behaviour. In the case of $\mathrm{InAs}_{1-x}\mathrm{Sb}_x$ we therefore expect to see both InAs-like and InSb-like LO and TO modes [Cherng88]. The intensity of those modes depends on the the bond fraction in the material, and the energy of the InAs-like and InSb-like modes is slightly shifted with respect to the energy of the respective binary compounds. In the case where a heavier Sb atom replaces a lighter As atom, the energy of the mode decreases. This behaviour allows to extract the composition of a ternary alloy [Alarcon-Llado13].

We are furthermore interested in extracting information about the carrier concentration and mobility in our nanowires. For this, the phonon-plasmon interaction can be studied. In a polar semiconductors like InAs(Sb) the Raman spectra may show additional features due to the interaction of light with the free carriers. The energy and width of those additional modes depend on the carrier density. Example Raman spectra are shown in Figure 2.10(a). At low carrier concentration only the LO and TO peaks are observed. When the carrier density increases, the LO peak broadens and shifts to higher energy. For even higher carrier density another peak appears at lower energy, and approaches the LO energy for increasing carrier density. This observation can be explained by phonon-plasmon interaction. Longitudinal phonons interact with the free charge carriers in the material and two coupled phonon-plasmon modes with frequencies ω_+ and ω_- appear. The energy of the coupled mode depends on the plasma frequency ω_p of the carriers in the semiconductor. Figure 2.10(b) shows a schematic of the energy shift of the two coupled modes in dependence of the plasma frequency. By fitting the position of the ω_+ and ω_- Raman peaks in the spectrum, we can therefore calculate the plasma frequency. The carrier density n is related to the plasma frequency by

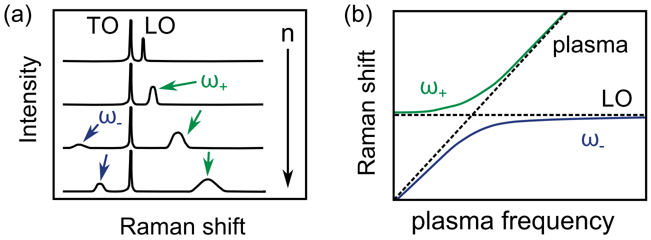

Figure 2.10 – Raman measurements.(a) Schematic of the Raman spectra in dependence of the carrier density (adapted from [Mooradian66]). (b) Schematic of the Raman shift of the two coupled modes in dependence on the plasma frequency (adapted from [Tell68]).

$$\omega_p^2 = \frac{ne^2}{\epsilon_0 \epsilon_\infty m_e^*} \tag{2.5}$$

where e is the charge of the electron, ϵ_0 is the vacuum dielectric constant, ϵ_∞ is the high frequency dielectric constant, and m_e^* is the effective mass of the electron. The observation of the coupled modes therefore allows to extract the carrier density. The mobility is related to the width of the coupled mode peaks and can therefore also be calculated from the same measurements. More information about the original model developed for GaAs can be found in [Mooradian66]. The calculations in the case of InAs(Sb) nanowires are described in detail in the supporting information of publication 1 and in the PhD thesis of Francesca Amaduzzi.

2) Terahertz spectroscopy

For THz spectroscopy, nanowires are transfered to quartz disks and illuminated with light in the THz range in transmission geometry. The THz range refers to frequencies between 0.1-10 THz, which corresponds to photon energies of 0.4-40 meV. In a semiconductor the THz energy corresponds to the excitation energy of phonons, and can induce motion of free charge carriers. An extensive review about THz spectroscopy can be found in the review by H. Joyce *et al* [Joyce16].

The conductivity of a sample in equilibrium can be measured by THz-time-domain spectroscopy (TDS). For this, the sample is exposed to a short THz pulse and the transmitted electric field is plotted over time. Figure 2.11(a) shows an example of a pulse. It is broadband and typically contains frequencies between 0.1 and a few THz. Upon interaction with the nanowires, the pulse is absorbed and delayed with respect to the original pulse measured on a reference sample. The transmission function $T(\omega)$ is defined as

$$T(\omega) = \frac{E_{nw}(\omega)}{E_{ref}(\omega)} \tag{2.6}$$

where $E_{nw}(\omega)$ and $E_{ref}(\omega)$ are the Fourier transforms of the electric fields of the pulses going through the nanowire sample and a reference sample (a quartz disk without any nanowires), respectively. The transmission function is directly related to the conductivity $\sigma(\omega)$ of the semiconductor. In the THz regime, the conductivity is a complex quantity, where the real part is related to the resistance and the imaginary part to the capacitance or inductance. To extract the conductivity, an ensemble of nanowires is measured, and an effective medium consisting of the nanowires surrounded by air is considered for fitting the data. The conductivity of the nanowires can then be obtained by effective medium theory, as explained in Ref. [Joyce16]. A schematic of the conductivity measured for GaAs nanowires is shown in Figure 2.11(b).

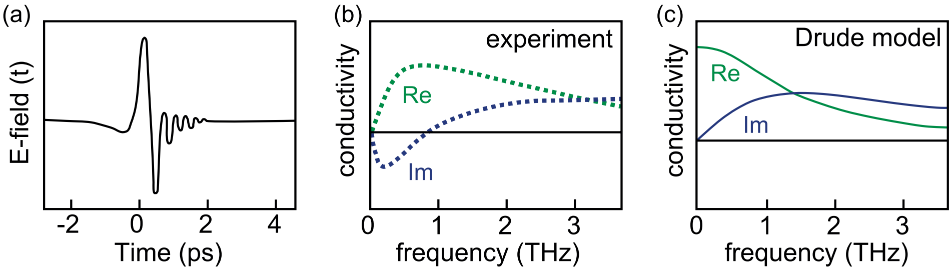

Figure 2.11 – Terahertz measurements. (a) Schematic of a terahertz pulse. (b) Schematic of the experimental conductivity in dependence on the frequency for GaAs nanowires. Schematic of the frequency dependence of the conductivity as expected from the Drude model. Figures (a)-(c) are adapted from [Joyce16].

In order to obtain the carrier density n and mobility μ of the sample, the complex conductivity needs to be modeled. The easiest model is the Drude model. Here the conductivity is given by

$$\sigma(\omega) = \frac{ne^2}{m^*}\frac{i}{\omega + i\gamma} \tag{2.7}$$

where e is the electric charge of the electron, m^* is the effective mass, and $\gamma = \tau^{-1}$ is the inverse of the average time between scattering events. The dc mobility is then given by $\mu = e\tau/m^*$. Figure 2.11(c) shows the conductivity $\sigma(\omega)$ according to the Drude model. Comparing with the experimental data, one can observe that the Drude model is not sufficient to explain the measurement. This is due to the finite size of the nanowires, which changes the transport properties for example by surface scattering and charge accumulation/depletion at the surface. In order to fit the experimental curves, more sophisticated models are needed. An in depth explanation can be found in Ref. [Joyce16].

THz spectroscopy not only allows to measure the conductivity in equilibrium, but it also allows to study the photo-excited conductivity and the carrier lifetime. This is possible by optical pump terahertz probe (OPTP) spectroscopy measurements. For OPTP spectroscopy, an optical pump pulse with an energy above the bandgap of the semiconductor is used to photo-excite carriers, and then the conductivity is measured by a THz pulse, similar to THz-TDS. The excitation of charge carriers increases the conductivity and thereby reduces the transmission of the pulse. The change in transmission $\Delta T = T^{ON}(\omega) - T^{OFF}(\omega)$ is given by substracting the signal of a reference measurement without photo-excitation. The photo-induced change in conductivity $\Delta\sigma(\omega)$ can be calculated from fractional change in transmission $\Delta T/T$. Varying the time between the photo-excitation pulse and the THz probe pulse allows to measure the decay of the photo-conductivity with time. A detailed discussion of OPTP spectroscopy can be found in Ref. [Joyce16].

It is interesting to note that in principle one THz-TDS measurement is sufficient to extract the equilibrium carrier density. However, in practice pump-probe measurements with different delay times are used to extrapolate the carrier density in equilibrium. Compared to a single THz-TDS experiment, this approach allows to reduce the measurement error significantly. In addition, the carrier lifetime can be calculated from the same dataset.

Comparison of electrical and optical techniques

In the previous sections we have presented how to extract the carrier mobility from field-effect measurements, Raman spectroscopy, and THz spectroscopy. It is interesting to note that electrical measurements and optical measurements are not necessarily expected to give the same results. In the case of electrical measurements we measure the field-effect mobility in the conductive channel of the device. Since the conductive channel is typically located near the surface, the field-effect mobility is very sensitive to defects and traps at the semiconductor surface and the interface with the gate-dielectric. In addition, the carrier density in the conductive channel of the device is typically very high, which further decreases their mobility. Raman and THz spectroscopy on the other hand are bulk techniques. The signal therefore includes a contribution both from the surface and from the core of a nanostructure. Comparing the mobility extracted from electrical and optical measurements we would therefore expect to obtain a higher value from optical techniques. This is in agreement with our results presented in publication 1. Using semiconductor nanostructures for electrical devices, we are limited by the field-effect mobility, and surface treatment and passivation schemes are desired in order to approach the bulk mobility.

2.5.3 Surface passivation

As discussed before, the electrical properties of nanowires depend significantly on the surface, and surface scattering offers one possible explanation for the low mobility observed in nanowires. It is therefore interesting to investigate surface passivation of nanowires.

III-V surfaces form a 2-5 nm thin layer of native oxide when exposed to air. The semiconductor-oxide interface is typically of poor quality and shows a high density of interface states across the bandgap. Valence band edge states are typically associated with filled dangling bonds on arsenic atoms, while empty dangling bonds on group III atoms lead to conduction band edge states. Furthermore, surface reconstruction can cause strained bond angles, and arsenic atoms in non-tetrahedral sites can result in both valence band and conduction band edge states (cf. [Ahn13] and references therein). The McIntyre group has shown that high-quality dielectrics can be deposited onto III-V materials by atomic layer deposition (ALD) and they have extensively studied InGaAs/Al_2O_3 stacks by capacitance-voltage (C/V) measurements. In order to achieve a high passivation quality, the InGaAs surfaces are capped with a layer of arsenic after growth. This capping layer prevents oxidation during transfer to the ALD chamber. The arsenic layer is then evaporated in the ALD chamber, resulting in a clean surface. In the case of a (100) surface it should ideally be terminated by arsenic-dimers. Alumina is then grown using trymethylaluminium (TMA) and water as precursors. Starting with TMA allows to create As-Al-As bonds and thereby restore the tetrahedral geometry of the arsenic atoms. The aluminium atoms are consecutively oxidized by water, and the alumina growth is continued by alternating TMA and water exposure until the desired thickness is reached. Exact control of the decapping temperature and a TMA pre-dosing step have been found to be important in order to achieve a low interface trap density [Ahn13]. Apart from interface traps, also border traps are a problem for InGaAs/Al_2O_3 stacks. Border traps are related to defects in the oxide layer, and can trap charges that tunnel into the oxide. They can be distinguished from interface traps by measuring the frequency dispersion of the capacitance in accumulation where interface traps are not active. Tang *et al* have shown that the border trap density can significantly be reduced by lowering the temperature during the ALD growth [Tang15]. Furthermore, it is possible to passivate both interface and border traps by annealing in a forming gas atmosphere. These impressive results on high-quality InGaAs/Al_2O_3 stacks motivated us to investigate passivation of InAs nanowires using ALD grown alumina.

To study the possibility of surface passivation, we sent arsenic capped InAs nanowire forests to the McIntyre group, where the alumina layer was grown by ALD. Electrical devices were fabricated in order to extract the conductivity of passivated nanowires from I/V curves, and top-gated field-effect devices were fabricated using the alumina as gate dielectric. In addition, the electron density and mobility were extracted form Raman spectroscopy. The results are presented in publication 1. Future work includes Terahertz spectroscopy and C/V measurements, as discussed in the outlook.

3 Experimental Methods

In this chapter we present relevant information about substrate preparation and growth parameters, TEM sample preparation (in particular the fabrication of cross-sections), the fabrication of electrical devices and electrical measurement procedures employed in this thesis.

3.1 Nanowire growth

In order to study the growth and properties of InAs(Sb) nanowires we used GaAs(111)B substrates covered with 4-5 nm of silicon oxide. The substrates were first cleaned with buffered oxide etch (7:1) for 20 s and then a solution of 2 % hydrogen-silsesquioxane (HSQ) and Methyl-isobutyl-ketone (MIBK). The ratio was 1:10 and the spin-coating speed 6000 rpm for a 4-5 nm SiO_2 thickness. The substrates were annealed at 300 °C for 10 min under nitrogen atmosphere in order to evaporate the solvent. After loading into our DCA P600 MBE systems, the substrates were first heated to 160 °C for 2 h in the load-lock and then degassed at approximately 300 °C in a dedicated degassing chamber. This procedure ensures that the main growth chamber of our MBE systems remains clean. A typical InAs nanowire growth is then started by heating the substrate (30 °C/min) to the growth temperature of 530 °C under arsenic flux of $1.9{\cdot}10^{-6}$ Torr. Simultaneously the indium cell is ramped up to the temperature resulting in a flux of $1.4{\cdot}10^{-7}$ Torr, which corresponds to a layer growth rate of 0.14 Å/s. After one hour of ramping/annealing, the growth is started by opening the indium shutter. After the growth time, the indium shutter is closed and the sample is rapidly cooled down (100 °C/min) under arsenic flux. Finally the arsenic shutter and valve are closed and the sample is unloaded. The procedure above describes the growth of standard InAs nanowires. For specific samples, the conditions were changed, e.g. the V/III ratio was varied, or an annealing step for droplet formation was included. The exact conditions are described along with the results in the corresponding publications.

3.2 Surface passivation

In order to passivate nanowires, we first capped them with thick layer of metallic arsenic immediately after growth. For this, the sample was cooled down to approximately room temperature (zero heating of the manipulator) and then arsenic was deposited for 30 min at a flux of approximately $1{\cdot}10^{-5}$ Torr. The resulting arsenic capping layer is amorphous and prevents the surface from oxidation. Figure 3.1 shows the nanowires at different steps during the passivation process. Figure 3.1(a) shows a top view SEM micrograph (15° tilt) of a standard nanowire without arsenic capping, as a reference. The typical hexagonal shape can be observed. Figure 3.1(b)-(c) show a tilted top view and a cross-sectional SEM micrograph of a nanowire sample after arsenic capping. The nanowires now have a round morphology due the amorphous capping layer. A STEM-HAADF image and an EDX map of an arsenic capped nanowire are shown in Figure 3.1(d)-(e), confirming the existence of a thick layer of arsenic around the InAs nanowire. Figure 3.1(f)-(g) show a TEM micrograph and a STEM-HAADF image of a nanowire after evaporation of the arsenic capping layer and ALD growth of alumina. It can be observed that the crystalline nanowire is coated with a thin layer. Figure 3.1(h)-(i) show elemental maps of InAs and aluminium, confirming that the shell contains aluminium. A high resolution TEM micrograph of a passivated nanowire is shown in Figure 3.1(j). One can observe the polytypic InAs nanowire and a 11 nm thick amorphous alumina layer around it. In collaboration with Marta Rossell at EMPA, we also visualized the decapping process by annealing of arsenic capped nanowires in a TEM. The results are presented in the appendix.

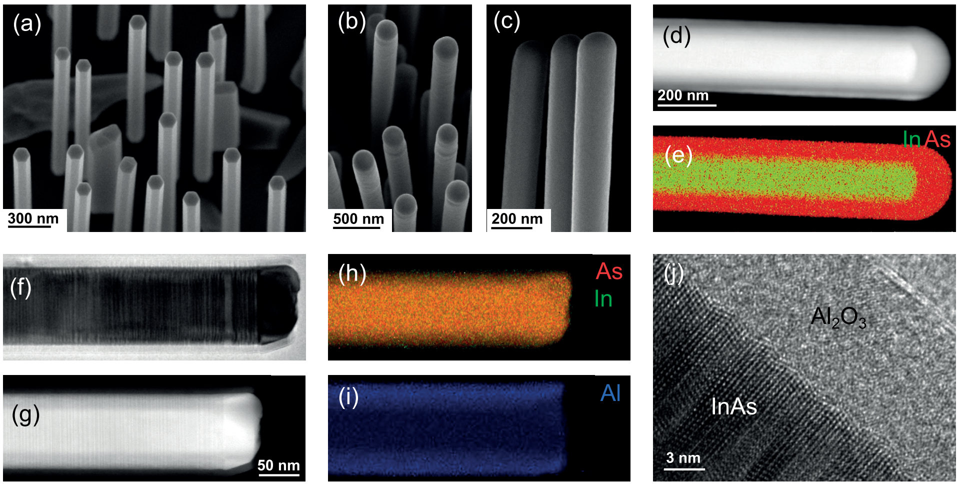

Figure 3.1 – Alumina passivation of InAs nanowires (a) Top view SEM micrograph (15° tilt) of a standard nanowire sample. (b)-(c) Top view and cross sectional SEM micrographs of a nanowire sample after arsenic capping. (d)-(e) STEM-HAADF image and EDX map of an arsenic capped InAs nanowire. (f)-(i) BF-TEM image, STEM-HAADF image, EDX maps of an alumina passivated InAs nanowire. (j) High resolution TEM micrograph of the passivated nanowire.

3.3 TEM sample analysis

The crystal structure and composition are important characteristics that determine the physical properties of our nanowires. During this thesis the crystal structure of single nanowires was analyzed using high resolution TEM and selected area electron diffraction. Free-standing nanowires can easily be transferred to TEM grids, by placing the grid onto a nanowire forest, and then slightly pressing down and scratching the surface with a Q-tip. The nanowires break off of the substrate and then lie flat on the carbon film, often with the $\{1\bar{1}0\}$ side facets perpendicular to the electron beam. Orienting a nanowire in a $<1\bar{1}0>$ zone axis is therefore typically very easy and only requires tilting of a few degrees to compensate for bending of the grid. This configuration allows to study defects perpendicular to the growth direction, for example rotational twins and polytypism. It also allows to study how the crystal structure and elemental composition may change along the nanowire. However, in particular for the case of radial heterostructures, in this configuration it is difficult to study the exact dimensions of core and shell, and it does not allow to get any information about the interface between the different materials. For this case, it is very useful to study nanowire cross-sections, where the nanowires are cut into thin slices perpendicular to the growth direction. During my thesis, I optimized a procedure to produce nanowire cross-sections and a short explanation of the process is presented here. We also used scanning TEM and energy dispersive x-ray spectroscopy to study the composition of our nanowires. Since this analysis was key for our understanding of $InAs_{1-x}Sb_x$ nanowires we present a short overview of the technique in this chapter.

3.3.1 Fabrication of cross-sections

Conventionally, nanowire cross-sections can be prepared by mechanical grinding or by focused ion beam. In the first case the nanowires are transfered to a substrate, aligned to be parallel to each other using micro manipulators, coated with an oxide film, and then cross-sections can be prepared using typical processing techniques for thin-films. For focused ion beam processing, the whole nanowire forest can be embedded, and then a TEM lamella is cut in the region of interest. These processes, however, are very time consuming and expensive, and result in only a few cross-sections per sample. A faster method for making many cross-sections is to use ultra microtomy. This technique is often used for biological samples, but it can also be adapted to make nanowire cross-sections [Guo13]. The process consists of two steps, first the nanowires are embedded in an epoxy and then the epoxy is cut with the microtome. A schematic of the embedding process is shown in Figure 3.2. First, a sample piece is sticked with silver paste or liquid indium onto a dummy wafer, as shown in Figure 3.2(a). A few dummy wafer pieces are attached next to it, allowing to use relatively small sample pieces. Then a Polydimethylsiloxane (PDMS) mould is prepared by punching a hole (diameter approximately 6 mm) into a cube of PDMS. This mould is then placed onto the nanowire sample and filled with epoxy as shown in Figure 3.2(b). We found that Epoxy Embedding Medium kit (available from Sigma-Aldrich) gives good results when mixing the ingredient with the provided standard recipe [Epon17]. The epoxy is then cured in an oven at 60 °C for 12 h.

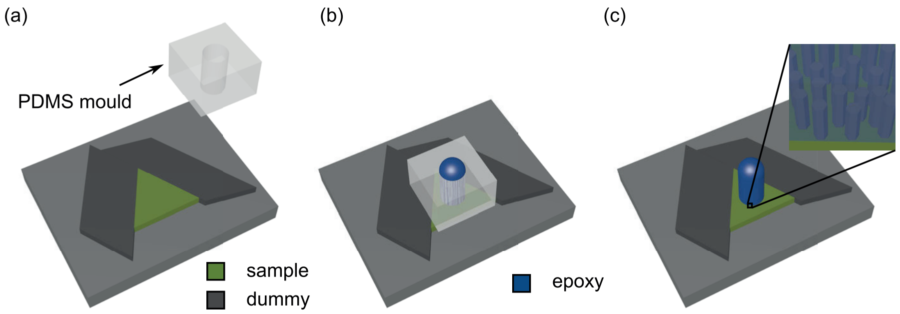

Figure 3.2 – Fabrication of cross-sections. (a) The sample (green) is sticked to a dummy wafer. (b) A PDMS mould is placed on the nanowire forest and filled with epoxy. (c) After curing, the PDMS mould is removed, resulting in an epoxy cylinder with embedded nanowires.

At 60 °C the epoxy first becomes very liquid and can spill out. We therefore established that leaving the sample for a few days at room temperature before the curing step helps to avoid the spilling. After the hardening, the PDMS mould is cut and peeled off, leaving a cylinder with embedded nanowires behind as shown in Figure 3.2(c). This cylinder can can be detached from the substrate by carefully cutting the edges with a very sharp and thin razor blade. This step can be quite challenging, especially since a bit of the resist has likely spilled out. Carefully detaching the sample is crucial in order not to break the substrate. From this point on, the standard microtomy procedure is used. First a truncated pyramid (1x1 mm^2) is prepared using a razor blade. Then the sample with the pyramid is mounted in the ultra microtome and thin slices (thickness below 60 nm) are cut with a diamond knife. The slices then swim in a water bath behind the diamond knife and can be fished with a loop tool and placed onto a TEM grid. This procedure allows to fabricate several slices with thousands of cross-sections at once. In principle also series through the nanowire length can be acquired, however keeping the slices ordered once they are in the water bath is is quite challenging.

3.3.2 Composition analysis

In order to study segregation effects, atom probe tomography (APT) is the ideal tool. However APT requires intensive sample preparation and the tool is not widely available yet. A much faster an easier approach is to use scanning transmission electron microscope (STEM). In STEM, the electrons are focused into a small spot which is then used to raster the sample. Several detectors can be used to acquire signal for each pixel of the image. For this thesis, the bright field (BF) detector, the high angular annular dark field (HAADF) detector, and the EDX detector are the most useful. The bright field image gives you an image of the sample based on coherent elastically scattered electrons (diffraction and phase contrast). The HAADF detector is a ring detector with a large collection angle, thereby collecting incoherently scattered electrons. The intensity I is given by $I = tZ^x$, where t is the sample thickness, Z is the atomic number of the atom, and x typically is a number between 1.6 and 2. For a sample with uniform thickness, it is thereby possible to get material contrast, which can be very useful for heterostructures. In our case, however, the heterostructure of interest is InAs/GaSb, and the mass of the binary compounds ($m_{In} + m_{As}$ = 114.8 u+74.9 u = 189.7 u and $m_{Ga} + m_{Sb}$ = 69.7 u+121.8 u = 191.5 u) give very similar intensity. Therefore it is very useful to acquire EDX spectra in order to distinguish the two materials. An EDX spectrum consists of the Bremsstrahlung signal convoluted with the characteristic x-ray lines of the elements. The characteristic x-ray spectra can be understood considering the Bohr model as shown in Figure 3.3. Electrons are considered to be in orbits around a positively charged core. Figure 3(a) shows a schematic representation of the orbitals. An electron from the inner orbit is ejected due to the interaction with the focused electron beam. The vacant site can then be filled with electrons from outer shells, and a photon is emitted with the energy corresponding to the energy difference between the outer shell and the inner shell. Every element therefore has a characteristic set of x-ray energies. X-ray lines are labeled as K, L and M lines, depending on the quantum number n of the inner shell. The K-lines correspond to electrons which emit energy while filling the K-shell (n=1), and equivalently there are also L (n=2) and M (n=3) lines for heavier elements. For a transition with $\Delta n = 1$ (e.g. a transition from the L shell to the K shell), one denotes the x-ray line as an α transition. Correspondingly a transition with $\Delta n = 2$ is denoted as β line. The K, L and M lines consist of different energies, depending on the energy of the electron and the hole. Figure 3.3(b) shows a schematic representation of the energy of the different shells. Within one shell, the energetic levels differ in energy due to the different angular momentum and spin. The selection rules for a transition are $\Delta l = \pm 1$ and $\Delta j = 0, \pm 1$, where l is the angular quantum number and j is the total angular momentum quantum number.

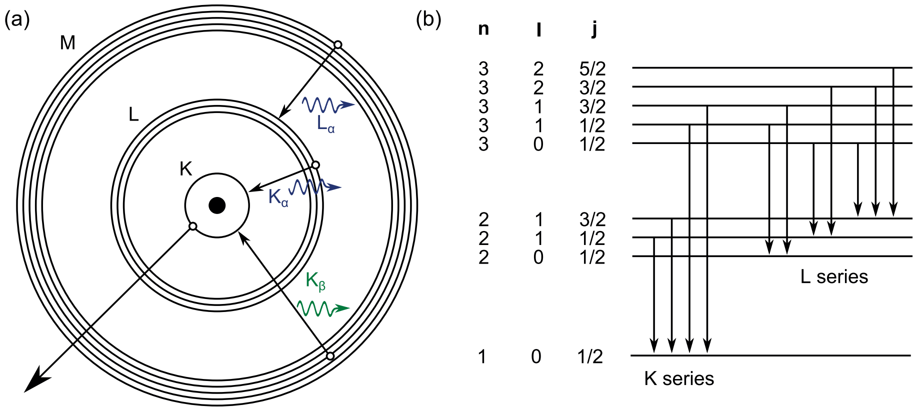

Figure 3.3 – Schematic of x-ray emission. (a) Bohr model showing the ejection of an electron from the K-shell and two possibilities to fill the vacancy with electrons from higher shells. (b) X-ray lines taking into account the selection rules.

When acquiring EDX spectra, it is important to note that the beam energy of course needs to be high enough to excite an electron. In STEM, where the beam energy is typically above 100 keV, this is not a problem and all characteristic x-ray lines can be observed. Indium, arsenic, gallium and antimony are relatively heavy elements, we observe both K and L lines. X-ray lines at higher energy offer the advantage of often being well-separated from other x-ray lines, while at low energy x-ray lines from many elements overlap. Sophisticated software tools (e.g. Esprit) allow to extract the elemental composition by deconvolution of the x-ray spectra and fitting them with a model (in our case we used the Cliff-Lorimer method). With STEM-EDX it is possible to create elemental maps, where the resolution depends on the STEM resolution as well as on the x-ray intensity, and the sample drift since typically maps need to be acquired over several minutes in order to get high enough x-ray counts for a meaningful deconvolution. In this thesis, EDX maps are extensively used to characterize the ternary material compounds (e.g. $InAs_{1-x}Sb_x$) and heterostructures (e.g. InAs/GaSb).

3.4 Electrical devices & measurements

Electrical devices were fabricated following the procedure and software initially established by Daniel Rüffer and Martin Heiss at LMSC [Blanc13]. Highly doped 4 inch silicon wafers with 200 nm of thermal oxide are used as substrates. If the process includes a wet etching step (e.g. to etch the oxide shell of InAs/Al_2O_3 nanowires) an additional 10 nm thick HfO_2 etch-stop layer is deposited on the substrate by atomic layer deposition. Then a pattern of alignment markers is defined on the substrate by photo lithography, evaporation of Ti/Au (10 nm/100 nm) and then lift-off. This results in a wafer with 128x128 cells which can be distinguished by a binary code, and the nanowires can be deposited on the substrate. To this end, a piece of nanowire sample is put into isopropanol and the nanowires are broken off the substrate in an ultrasonic bath. The nanowire solution can then be dropcast onto the substrate, and the nanowires adhere to the surface by van der Waals forces. After washing the substrate with acetone and isopropanol to remove any stains, the nanowires can now be located using optical images for contact fabrication. The images need to include one full cell and at least one nanowire to be contacted. An example image is shown in Figure 3.4(a). The optical images can then be loaded into the GUIContact software, which automatically adjusts the rotation of the image based on the four outer dots, and the binary code of the cell is recognized as shown in Figure 3.4(b). In the software one can then choose the contact design, either using an existent one or making a new one in the python pattern file (which was for example necessary for our L-shaped devices). Also the ebeam parameters (e.g. dose and resolution) can directly be set in the software. Then the file can be exported and used as an ebeam layout. After exposure, developing, metalization and lift-off, the final devices are ready (Fig. 3.4(c)-(e)). On one wafer there are 128x128 different cells, therefore in principle it is possible to make a large number of devices. However in order to avoid overlapping devices and to be able to cleave the wafer into smaller chips usually only up to 600 devices are fabricated (also, the software crashes if the file gets too large). Figure 3.4(f) shows an image of a full waver with alignment markers and many devices.

Nanowire devices were measured using several setups in our lab. Measurements at room temperature and atmospheric pressure are done using a table-top probe station. Low temperature measurements and magnetic field sweeps (up to 9 T) can be done using a Cryogenic

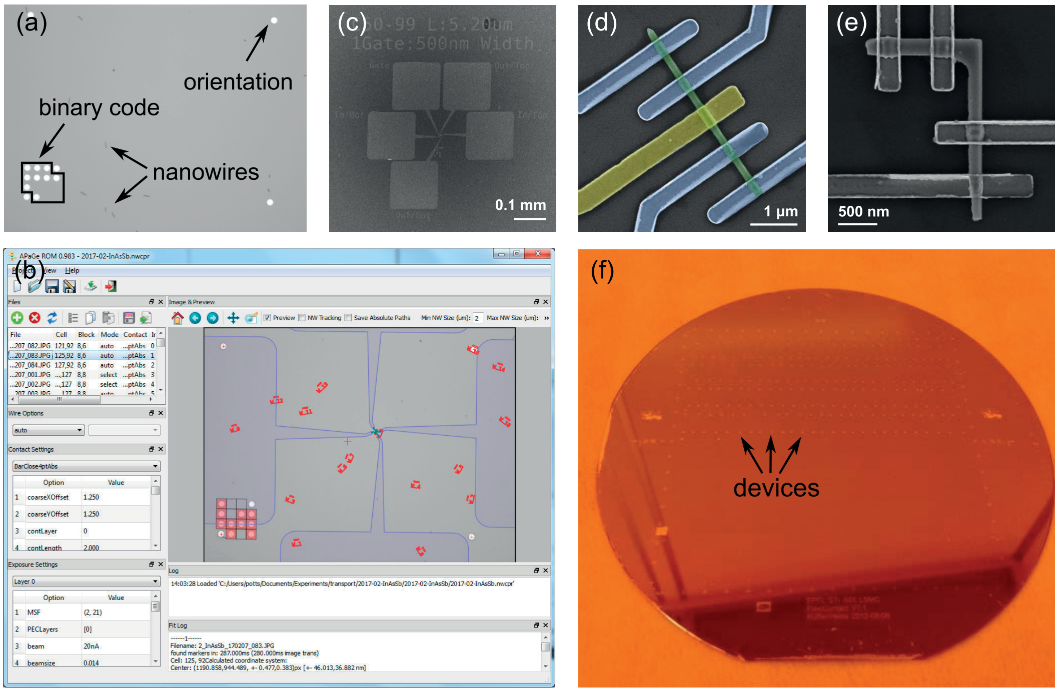

File	Cell	Block	Mode	Contact	Ir
...207_082.JPG	121,92	8,6	auto	...ptAbs	0
...207_083.JPG	125,92	8,6	auto	...ptAbs	1
...207_084.JPG	127,92	8,6	auto	...ptAbs	2
...207_001.JPG	...,127	8,8	select	...ptAbs	3
...207_002.JPG	...,127	8,8	select	...ptAbs	4

☑ Preview ☐ NW Tracking ☐ Save Absolute Paths Min NW Size (um): 2 Max NW Size (um):

Wire Options: auto

Contact Settings: BarClose4ptAbs

	Option	Value
1	coarseXOffset	1.250
2	coarseYOffset	1.250
3	contLayer	0
4	contLength	2.000

Exposure Settings: Layer 0

	Option	Value
1	MSF	(2, 21)
2	PECLayers	[0]
3	beam	20nA
4	beamsize	0.014

```
14:03:28 Loaded 'C:/Users/potts/Documents/Experiments/transport/2017-02-InAsSb/2017-02-InAsSb/2017-02-InAsSb.nwcpr'
```

```
------1------
Filename: 2_InAsSb_170207_083.JPG
found markers in: 287.000ms (280.000ms image trans)
Cell: 125, 92Calculated coordinate system:
Center: (1190.858,944.489, +-0.477,0.383)px [+-46.013,36.882 nm]
```

Figure 3.4 – Fabrication of electrical devices. (a) Optical micrograph showing one cell with alignment markers. (b) GUIContact software to make the ebeam layout. (c)-(e) SEM micrographs of devices: overview of the contact pads, top-gated devices, L-shaped device. (f) Overview image of a 4 inch substrate with alignment markers and many nanowire devices.

cryostat with variable temperature insert and superconducting magnet. Since recently, low temperature measurements can also be performed in vacuum by using the dipstick developed in collaboration with the Zumbühl group in Basel. The new dipstick does not only allow to measure in vacuum, but it also significantly facilitates to measure temperature dependence, since it can directly be inserted into a liquid helium dewar, and no pre-cooling with liquid nitrogen or transfer of helium is necessary.

We typically performed 2-point and 4-point measurements to calculate the nanowire resistance. Figure 3.5(a) shows a schematic of the measurements. In a 2-point measurement (blue) the voltage is applied to two contacts and the current is measured between the same two contacts. The disadvantage of this method is that the measured resistance also includes the contact resistance $R_{2pt} = R_{NW} + 2 \cdot R_{contact}$. For InAs nanowires, the contact resistance is very low and usually negligible. However to be on the safe side, 4-point measurements (green) can be performed. Here the nanowire resistance is calculated from the current between the outer contacts and the measured voltage drop-off between the inner contacts $R_{4pt} = V_{in}/I_{out}$. We usually used a Keithley 6487 voltage source and picoampermeter to apply a voltage and measure the current, and a Keithley 6517A nanovoltmeter to measure the voltage in 4-point measurements. This approach is ideal for voltage sweeps in order to check if the behaviour of the device is linear. For temperature dependent measurements we used a Stanford Research

Systems SR830 lock-in in order to reduce the noise. A schematic of a constant-current lock-in setup is shown in Figure 3.5(b). A shunt resistor with a high resistance allows to apply an almost constant current to the device. The nanowire resistance can then be extracted by measuring the voltage drop across the nanowire. Both 2-point and 4-point measurements are possible with this setup. It should be pointed out than one should be careful when performing a 4-point measurement, because the phase will change when the resistance changes. Therefore both the x and y component of the voltage across the inner contacts need to be measured, and the total voltage can be calculated by $V_{total} = \sqrt{V_X^2 + V_Y^2}$. In addition, when measuring nanowire devices it is extremely important to pay attention to avoiding electrostatic charging and to implement a good grounding scheme. A ground bar was installed at both measurement setups in order to allow to use the same ground potential for all measurement tools. Furthermore it is important to avoid ground loops, by checking how the shields of the co-axial cables are grounded. Typically on the measurement tools one can choose between grounding the shields or leaving them floating, in case the shields are already grounded on the other side of the cable (e.g. over the switchbox).

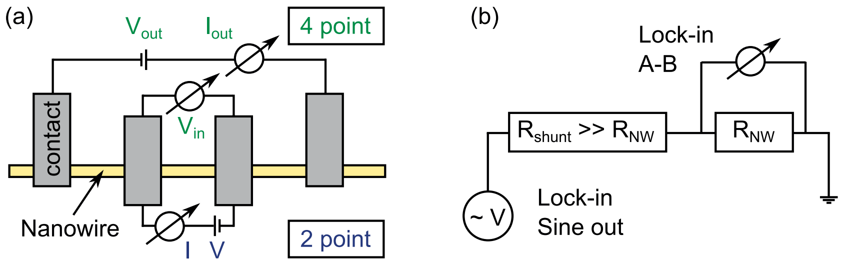

Figure 3.5 – Electrical measurements. (a) Schematic of 2-point (blue) and 4-point (green) measurements. (b) Schematic of a constant current setup using a lock-in.

4 Results & Discussion

In this chapter we present the main results of this thesis. The results were published in scientific journals. Here we first give an introduction to the topic of each publication and then include the article (with authorization of the corresponding publisher).

4.1 Defect-free nanowires & surface passivation

In this work we studied the possibility to suppress the defect formation in self-catalyzed InAs nanowire by the incorporation of antimony. Self-catalyzed InAs and GaAs nanowires usually show a high density of stacking faults perpendicular to the growth direction. In particular for self-catalyzed InAs nanowires is has not been possible to grow defect-free crystals by changing the growth conditions [Grap13, Dimakis11]. As discussed in section 2.3, the tendency to form wurtzite can be seen in relation to the ionicity of the bond between group III and group V atoms. One possible avenue to suppress defect formation is therefore the incorporation of antimony atoms, thereby reducing the ionic character of the bonds in the material. For $\mathrm{GaAs}_{1-x}\mathrm{Sb}_x$ it has already been demonstrated that nanowires can be grown without any twins or other stacking defects [Conesa-Boj14]. For $\mathrm{InAs}_{1-x}\mathrm{Sb}_x$ nanowires a decrease of stacking defects has been reported [Sourribes14, Farrell15], however so far the maximum antimony content was 15% and at this composition the nanowires still showed a considerable density of rotational twins. In this thesis we report $\mathrm{InAs}_{1-x}\mathrm{Sb}_x$ with an antimony content of up to 35% and show that the crystal structure can be considered defect-free (i.e. less than one defect per micrometer) at antimony contents above 25%.

The growth of ternary materials offers interesting perspectives in terms of material properties, for example by allowing to change the band gap, lattice constant, and crystal structure. Ternary alloys are also interesting when growing heterostructures, because the two binary materials typically have a different electron affinity, and the position of the conduction and valence band of a ternary material therefore change with the composition. The energies can be estimated by Vegard's law, or more accurately by considering the bowing of the bands. A calculation of $\mathrm{InAs}_{1-x}\mathrm{Sb}_x$ can be found in Ref. [Wei95]. The possibility to tune the electron affinity can allow to choose between a type-II staggered or a type-III broken band-alignment when combining $InAs_{1-x}Sb_x$ with certain materials. On the other hand, new challenges are encountered with ternary materials, including alloy scattering and the difficulty to achieve a homogeneous chemical composition. Segregation effects can be undesired for certain applications, but they can also bring additional functionality to the material system, for example allowing for the formation of quantum dots in core-shell nanowires [Heiss13]. Segregation can occur both along the nanowire axis as well as in radial direction. Typically nanowires show some radial overgrowth on the side facets. Due to the difference in surface energy, the local growth conditions on the side facets differ significantly from the conditions of the axial growth, which may affect the composition of a ternary material. To investigate this effect we fabricated nanowire cross sections and analyzed them using scanning transmission electron microscope (STEM)-energy dispersive x-ray (EDX) spectroscopy.

Polytypism affects the optical and electrical properties of nanowires, as discussed in section 2.3. Therefore it is interesting to compare the properties of polytypic InAs nanowires and defect-free $InAs_{1-x}Sb_x$ nanowires. The conductivity of $InAs_{1-x}Sb_x$ nanowires with different antimony content was compared using electrical measurements. We found an increase in conductivity upon incorporation of antimony. However we also observed a large variation between measurements even for nanowires of the same material. This can be attributed to surface effects, as discussed in section 2.5. The carrier density and mobility was investigated both by field-effect measurements and by Raman spectroscopy (the Raman spectroscopy was performed by Francesca Amaduzzi from EPFL). We found that nanowires with 35% antimony have a higher electron density and higher electron mobility compared to InAs nanowires. The mobility obtained from Raman measurements was higher compared to the values from electrical measurements. This is expected considering that the field-effect mobility is related to the mobility of the carriers in the conductive channel at the nanowire surface while Raman spectroscopy is a bulk technique probing both the core and the surface of the nanowires (cf. section 2.5.2).

The variations in conductivity and the lower mobility extracted from electrical measurements motivated us to study surface passivation with ALD-grown alumina. To this end, the nanowire surface was coated with a thick layer of metallic arsenic in the MBE chamber in order to avoid the formation of a native oxide. The samples were then shipped to the McIntyre group, where the arsenic capping layer was removed at 300°C, and then the alumina shell was grown by ALD. For more information about the decapping procedure, an in-situ STEM study during annealing is presented in the appendix. The effect of the passivation was studied by electrical measurements (including top-gated field-effect measurements) and by Raman spectroscopy.

Reprinted with permission from H. Potts *et al.* From Twinning to Pure Zincblende Catalyst-Free InAs(Sb) Nanowires. *Nano Letters* **16**, 637 (2016). © 2017 American Chemical Society.

NANO LETTERS
Letter
pubs.acs.org/NanoLett

From Twinning to Pure Zincblende Catalyst-Free InAs(Sb) Nanowires

Heidi Potts,[†] Martin Friedl,[†] Francesca Amaduzzi,[†] Kechao Tang,[‡] Gözde Tütüncüoglu,[†]
Federico Matteini,[†] Esther Alarcon Lladó,[†] Paul C. McIntyre,[‡] and Anna Fontcuberta i Morral[*,†]

[†]Laboratoire des Matériaux Semiconducteurs, École Polytechnique Fédérale de Lausanne, 1015 Lausanne, Switzerland
[‡]Department of Materials Science and Engineering, Stanford University, Stanford, California 94305, United States

Supporting Information

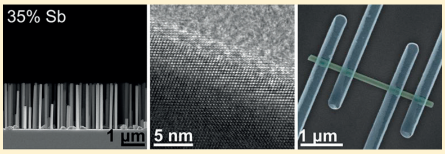

ABSTRACT: III−V nanowires are candidate building blocks for next generation electronic and optoelectronic platforms. Low bandgap semiconductors such as InAs and InSb are interesting because of their high electron mobility. Fine control of the structure, morphology, and composition are key to the control of their physical properties. In this work, we present how to grow catalyst-free $InAs_{1-x}Sb_x$ nanowires, which are stacking fault and twin defect-free over several hundreds of nanometers. We evaluate the impact of their crystal phase purity by probing their electrical properties in a transistor-like configuration and by measuring the phonon−plasmon interaction by Raman spectroscopy. We also highlight the importance of high-quality dielectric coating for the reduction of hysteresis in the electrical characteristics of the nanowire transistors. High channel carrier mobilities and reduced hysteresis open the path for high-frequency devices fabricated using $InAs_{1-x}Sb_x$ nanowires.

KEYWORDS: *InAs nanowires, InAsSb, catalyst-free, self-catalyzed, molecular beam epitaxy, crystal structure, electronic properties, surface passivation, atomic layer deposition, mobility, phonon−plasmon interaction*

III−V semiconductor nanowires are considered next generation building blocks in electronics, optoelectronics, and energy harvesting applications.[1−4] At the same time, they have proved to be an ideal platform to probe novel physical properties resulting from the small size or lower dimensionality.[5−7] Indium-based III−V nanowires are of particular interest due to their high electron mobility, high spin−orbit coupling, and large g-factor.[8,9] III−V nanowires typically show polytypism, that is, a mixture phases of zincblende (ZB) and wurtzite (WZ) stacking, as well as stacking faults and rotational twins. The coexistence of different polytypes can dramatically modify the optical and transport properties. In particular, it has been found that the photoluminescence energy changes due to the presence of mixed crystal phases,[10] the resistivity of polytypic nanowires is up to 2 orders of magnitude higher[11] and even a single twin plane acts as an optically active nanodot.[12] Using gold as a catalyst particle, it has been possible to achieve control of the nanowire crystal structure.[13,14] Although this is still highly controversial, gold could be incorporated as an impurity in the nanowires, thereby harming the functional properties.[15−18] In order to avoid the risk of metal incorporation, a self-catalyzed or catalyst-free growth process is favored, though reducing the stacking fault density in InAs nanowires grown without a foreign catalyst has been found to be a difficult task.[19−21] One pathway toward pure phase nanowires is the incorporation of Sb, resulting in the growth of ternary antimonide nanowires. For antimonide crystals, zincblende stacking is favored due to the small ionicity of the bond.[22] In the case of GaAs, it has been shown that the incorporation of antimony allows for the growth of defect-free ZB $GaAs_{1-x}Sb_x$ nanowires both for gold-catalyzed nanowires using metal organic vapor phase epitaxy[23] and for self-catalyzed nanowires using molecular beam epitaxy (MBE).[24] In the case of $InAs_{1-x}Sb_x$ nanowires, defect-free wires have been reported using gold as a catalyst,[25] whereas without a foreign catalyst, even the least defective nanowires still show a considerable density of rotational twins.[26−28]

In this work, we demonstrate the growth of $InAs_{1-x}Sb_x$ using MBE and report for the first time that the stacking defect density in $InAs_{1-x}Sb_x$ nanowires grown without a foreign catalyst can be reduced to a few twins per micrometer by increasing the antimony content. The change in crystal structure as a function of the antimony content is studied quantitatively while showing that increasing the antimony content results in a strong reduction of the defect density in $InAs_{1-x}Sb_x$ nanowires and the hexagonal wurtzite phase can be completely suppressed. Pure ZB nanowires with only a few rotational twins per micrometer are obtained for an antimony content greater than 25%. The defect density is therefore more than 1 order of magnitude lower than the best results reported in literature.[26] We further investigate the material composition of $InAs_{1-x}Sb_x$ nanowires with energy dispersive X-ray (EDX) spectroscopy maps that show that the antimony content along the nanowire growth axis is homogeneous. Using nanowire cross sections, we also observe a homogeneous antimony content in the nanowire core and a slightly lower antimony content in the radial overgrowth, with antisegregation at the nanowire corners. Field-effect transistor measurements and

Received: October 28, 2015
Revised: November 26, 2015
Published: December 19, 2015

DOI: 10.1021/acs.nanolett.5b04367
Nano Lett. 2016, 16, 637−643

Raman spectroscopy show that incorporation of antimony also has a significant effect on the electrical and optical properties of InAs$_{1-x}$Sb$_x$ nanowires. Finally, we demonstrate that a high-quality ALD-grown aluminum oxide deposited around the nanowires enables the fabrication of top-gated devices with increased on−off ratios, steeper subthreshold slope and reduced hysteresis during transconductance measurements. Our results constitute an important step toward high electron mobility InAs(Sb) nanowire-based devices.

We start by comparing the growth rate and morphology of our InAs$_{1-x}$Sb$_x$ nanowires as a function of their antimony content. Our nanowires grow vertically on GaAs(111)B substrates and the optimum growth temperature was found to be 520 °C (more details available in Supporting Information). We refer to our growth process as catalyst-free because no external metal is used to initiate and drive the one-dimensional growth. We note the exact growth mechanism for InAs nanowires without a foreign catalyst (self-catalyzed or not) is still highly controversial and both vapor−liquid−solid[19] and vapor−solid[20] growth has been reported. In order to study the effect of antimony incorporation on the nanowire morphology and crystal structure, samples were grown at different antimony fluxes, while keeping the rest of the growth parameters constant. SEM micrographs of representative samples are shown in Figure 1a−b. All nanowires exhibit a hexagonal cross section with facets parallel to the {110} orientation of the substrate. Nanowire lengths and diameters were quantified as shown in Figure 1c. The incorporation of antimony leads to a slightly increased nanowire diameter and a decreased length. This observation stands in contrast to the growth of pure InAs nanowires, where it is well established that an increase of the group V flux results in longer and thinner nanowires (more details available in Supporting Information).

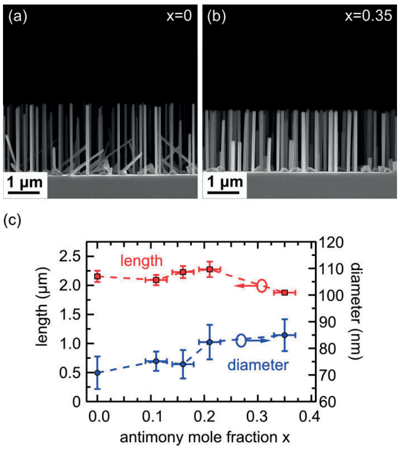

Figure 1. (a) and (b) Cross-sectional SEM micrographs of an InAs sample and an InAs$_{0.75}$Sb$_{0.35}$ sample grown for 1 h. (c) Quantification of the nanowire length and diameter as a function of the antimony content.

We turn now to the analysis of the crystal structure of the nanowires as a function of the Sb content. In order to show a figure of merit that integrates both polytypism and stacking-fault formation, we count the number of interfaces, that is, the sum of ZB/WZ transitions, stacking faults and rotational twins. Pure InAs nanowires show polytypism and a high density of interfaces. Interestingly, wurtzite stacking predominantly occurs at the nanowire stem, and pure WZ segments of several tens of nanometers in length can be observed as shown in Figure 2a. The existence of a WZ stem seems to be favored for thin diameters, which occur at the early stages of growth and at higher V/III ratios. A more detailed study is required to confirm this assumption. In the rest of the wire, the defect density is approximately 400 interfaces/μm (Figure 2b), confirming the findings of other groups.[19,26] We observe a strong decrease of defects with increasing antimony content. Representative HRTEM micrographs are shown in Figure 2c−d, respectively. InAs$_{1-x}$Sb$_x$ nanowires with a Sb content of 16% show a reduced defect density and the hexagonal phase is completely suppressed. Nanowires with an antimony content greater than 35% are almost defect-free, with only a few twins per micrometer. Figure 2e summarizes the evolution of the structure as a function of the Sb content, by plotting the number of interfaces (ZB/WZ and stacking faults) as a function of the Sb content in the nanowires. For increasing antimony content, the number of interfaces is reduced steadily. At 11% Sb, the number of interfaces is reduced to approximately 300 interfaces per micron and wurtzite sections are shorter and less frequent. For an antimony content of 21%, there are only about 100 interfaces per micron, and for samples with a higher content, there are only a few interfaces per micron. For all InAs$_{1-x}$Sb$_x$ nanowires, we observe that the interface density is lower at the nanowire stem and increases toward the nanowire tip, implying slightly different conditions during growth. Our findings are in agreement with the results in ref 28 and 26, where the suppression of WZ stacking and a reduction of twin defects was reported for wires with an antimony content up to 15%. By further increasing the antimony incorporation, we were able to achieve almost complete suppression of defect formation. Compared to gold-catalyzed nanowires in ref 25, we observe that the threshold for defect-free nanowires is higher without a foreign catalyst. Figure 3a shows a high angular annular dark field (HAADF) scanning transmission microscope (STEM) micrograph of a wire with 21% antimony, showing a few twin defects along the wire. The antimony content along the nanowire is uniform for all samples, as shown by longitudinal EDX maps in Figure 3b−d.

To understand the growth of InAs$_{1-x}$Sb$_x$ nanowires in more detail, nanowire cross sections were fabricated by first embedding a nanowire forest in epoxy and cutting slices of 60 nm thickness with an ultramicrotome.[29,30] Figure 3e shows a HAADF STEM micrograph of a nanowire cross section, confirming the hexagonal nanowire morphology with {110} facets. A hexagonal core and a shell of approximately 15 nm thickness can be observed, suggesting radial overgrowth of the initial nanowire core. This radial overgrowth is further supported by a time series of the nanowire growth (more details available in Supporting Information). The interface shows some strain contrast due to the lattice mismatch of two materials with slightly different composition. Figure 3f shows a HRTEM micrograph of one of the nanowires corners. From the inverse Fourier transform image in the inset, we can see that there are no misfit dislocations at the interface. EDX maps of the cross section are shown for indium, arsenic, and antimony in Figure 3g−h. Overlaying the arsenic and the antimony map shows that the antimony content is homogeneous in the core, a bit lower in the shell, and there is antisegregation of antimony at the six corners of the hexagonal cross section. Our observations are in agreement with the

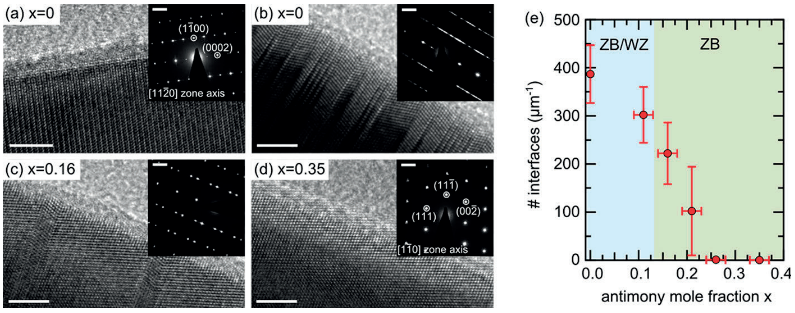

Figure 2. (a)−(d) High resolution TEM micrographs and diffraction patterns of different nanowires. The scale bar is 5 and 2 nm^{-1} respectively. (a) InAs nanowire stem where the crystal structure is pure WZ for several tens of nanometers. (b) Typical polytypic InAs nanowire crystal structure. (c) Nanowire with 16% antimony where the crystal structure is ZB with rotational twins. (d) Nanowire with 35% antimony. The nanowire is pure ZB with very few rotational twins. (e) Quantification of the number of interfaces as a function of the antimony content. The defect density dramatically decreases with increasing antimony content. Wurtzite segments are suppressed at an antimony content above 15% (green region).

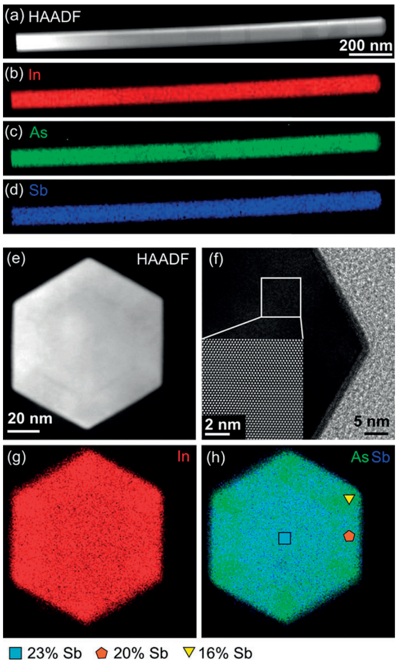

Figure 3. (a) HAADF STEM micrograph of a nanowire with 21% antimony. (b)−(d) EDX maps of indium, arsenic, and antimony showing a homogeneous composition along the wire. (e) HAADF STEM micrograph of a nanowire cross section showing a hexagonal nanowire core with a 15 nm thick shell. (f) High resolution image of a nanowire corner showing no dislocations at the shell interface. (g)−(h) EDX maps of the nanowire cross section. A homogeneous composition can be observed in the nanowire core. The shell has a slightly lower antimony content and shows antisegregation at the six corners.

results in ref 24, where a similar antisegregation of antimony was observed for $GaAs_{1-x}Sb_x$ nanowires. Quantification of the EDX map indicates the Sb content is 23% in the core, 20% in the shell, and 16% at the corners. Interestingly, it has been shown for gold-catalyzed nanowires that the antimony content in the core is lower compared to the radial overgrowth.[25] In this sense, catalyst-free growth may be a better approach for achieving a high, homogeneous antimony content compared to metal-assisted growth.

The impact of the crystal structure and composition on the properties of the nanowires is evaluated using field-effect transistor devices. All electrical transport measurements were performed at room temperature. Figure 4a shows the SEM micrograph of a nanowire device with four contacts. We studied as-grown InAs(Sb) nanowires as well as InAs(Sb) nanowires coated with a 10 nm shell of Al_2O_3. A high quality interface between the nanowire and the oxide was achieved by capping the nanowire with arsenic after growth and depositing 10 nm

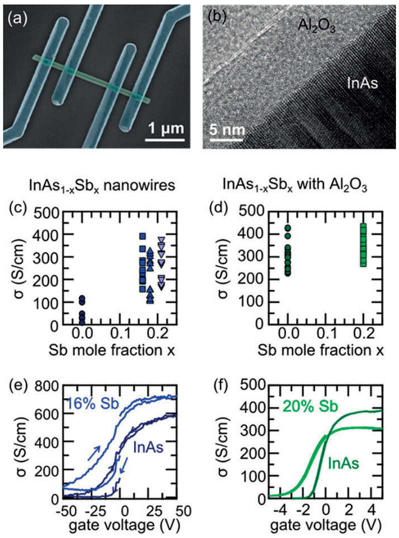

Figure 4. (a) False-colored SEM micrograph of a nanowire device. The nanowire (green) is contacted with four contacts (blue). (b) High resolution TEM micrograph of an InAs nanowire coated with 10 nm Al_2O_3. (c) Conductivity of $InAs_{1-x}Sb_x$ nanowires with different antimony content. (d) Conductivity of Al_2O_3 coated $InAs_{1-x}Sb_x$ nanowires with different antimony content. (e) Comparison of field-effect data for an InAs nanowire device and a device with 16% antimony using the substrate as back gate. (f) Comparison of field-effect data for Al_2O_3 coated nanowire devices using a top gate. The uncertainty in the conductivity measurements is about 10% due to uncertainty in the measurement of the device dimensions.

Al_2O_3 by atomic layer deposition.[31] Figure 4b is a TEM micrograph of an InAs−Al_2O_3 nanowire showing the crystalline nanowire core and the amorphous alumina shell. For these nanowires, a top gate was deposited between the two center contacts. The four-point configuration was used to measure the nanowire conductivity and the contact resistance. Ohmic contacts with a contact resistance less than $5 \times 10^{-7}\ \Omega\ \text{cm}^2$ were obtained without annealing, confirming high-quality contacts. We start by comparing the conductivity, σ, of four types of wires with an antimony content of 0%, 16%, 18%, and 21%. In general, the conductivity is found to be higher for antimony containing wires as shown in Figure 4c. This result is consistent with our expectations because (1) the conductivity of bulk InSb is higher compared to InAs[32] and (2) InAs shows a charge accumulation layer at the surface,[33,34] which makes scattering at surface defects a limiting factor for the conductivity. Values ranging from σ = 10−100 S/cm for InAs devices and σ = 100−400 S/cm for $InAs_{1-x}Sb_x$ devices have been measured. We observe a large variance in the conductivity values as well as fluctuation of the current over time. We attribute this to the surface accumulation layer and surface sensitivity of InAs nanowires, making it difficult to compare the results in a quantitative and absolute manner. In contrast, much more consistent values were achieved for wires coated with Al_2O_3. For these nanowires, conductivity values of 200−400 S/cm and 250−450 S/cm were obtained for InAs and $InAs_{0.8}Sb_{0.2}$ nanowires, respectively (see Figure 4d). The high conductivity of the alumina coated nanowires is a sign of a high quality oxide−nanowire interface and stands in contrast to previous results, where highly deteriorated electrical properties have been reported for oxide coated nanowires.[35] Particularly for InAs nanowires, we observe that the measured conductivity is significantly higher when the wires are coated with Al_2O_3. This result could be explained considering that Al_2O_3 often acts as a negative charge dielectric.[36] Negative fixed charges near the interface would suppress electron trapping at interface defects, resulting in a larger population of mobile carriers and therefore in a higher conductivity. Furthermore, the alumina will prevent water adsorption onto the nanowire, which has been shown to have a detrimental influence on electrical properties.[37]

Figure 4e,f show the gate-dependent measurements. For measurements of wires not coated by ALD-Al_2O_3, the two inner contacts were used as source and drain, and the highly doped silicon substrate was used as a back gate while nanowires coated with Al_2O_3 were gated by a local top gate. A table with all relevant device and measurement parameters can be found in the Supporting Information. Figure 4e shows typical field-effect measurements of an InAs nanowire and an InAsSb device with 16% antimony. Both devices show n-type hysteretic behavior, as commonly observed for InAs nanowires due to the presence of surface states.[38] The hysteresis was successfully reduced by applying a pulsed gate sweep.[39] The baseline current at zero gate voltage varied as a function of time and sweep history, which we attribute to the additional gating of surface contamination. Nanowires coated with Al_2O_3 showed a significantly reduced hysteresis, especially with the pulsed gate sweep, see Figure 4f. In this case, we also do not observe any major change in baseline current. This is consistent with a reduced electron trapping at the interface due to fixed negative charges in the alumina.

We move now to the quantitative analysis of the gate dependent measurements. Assuming diffusive transport in the linear regime of the standard transistor model, the field-effect mobility can be calculated by $\mu = g_m(L^2/C)/V_{ds}$. Here, g_m is the transconductance $g_m = (dI_{ds})/(dV_g)$, where V_g is the gate voltage, and C is the nanowire-gate capacitance. For bottom gated devices, the capacitance is typically approximated by $C = 2\pi\varepsilon_0\varepsilon_r L/\text{acosh}[(r + t_{ox})/r]$, where r is the nanowire diameter, t_{ox} is the thickness of the dielectric layer, and ε_r is the relative dielectric constant. Following ref 40, we use ε_r = 2.25 to account for the fact that the nanowire is not completely surrounded by the dielectric. Assuming bulk conductivity of electrons the carrier density at zero gate voltage, the electron density n can be estimated by $n = \sigma/e\mu$, where σ conductivity and e is the elementary charge of the electron. The transconductance of the data shown in Figure 4e would be consistent with a mobility of μ = 1540 $\text{cm}^2/(\text{V s})$ and μ = 2560 $\text{cm}^2/(\text{V s})$ and a charge density of $n = 5.6 \times 10^{17}$ cm^{-3} and $n = 7.3 \times 10^{17}$ cm^{-3} for the InAs and the InAsSb device, respectively. The trend of increased mobility with antimony content is in agreement with the results reported for gold-catalyzed nanowires.[11] The on−off ratios of the devices presented here are 58 and 9, respectively. We observe that the InAsSb nanowires cannot be turned off completely, which might be related to the larger diameter of the nanowires though future investigations are required to understand this behavior. One should also note that we observe a change in baseline current during the measurement, for example, the starting point and the end point of the gate sweep are not the same (more details in Supporting Information). Therefore, the mobility and the on−off ratio tend to be overestimated by the extracted values.

In order to extract the mobility in the case of Al_2O_3 coated nanowires, we estimate the capacitance of the top-gated devices by a parallel-plate capacitor, where the area is approximated as three nanowire facets, assuming shadowing of the bottom three nanowire facets during gate metal evaporation. A relative permittivity of ε_r = 8 was used for the amorphous ALD-Al_2O_3. The voltage across the gated nanowire length is obtained from the applied source-drain voltage and normalized using the ratio between the gated/nongated nanowire lengths (more details in Supporting Information). Mobility values consistent with μ = 1005 $\text{cm}^2/(\text{V s})$ and μ = 825 $\text{cm}^2/(\text{V s})$, charge densities of $n = 1.81 \times 10^{18}$ cm^{-3} and $n = 2.49 \times 10^{18}$ cm^{-3}, and on−off ratios of greater than 2755 and 29 were extracted from the gate sweeps respectively for InAs and InAsSb nanowires. However, it has been shown that in top-gated devices, the semiconductor capacitance has a significant contribution to the total capacitance.[41] To get a more realistic estimate of the mobility, the semiconductor capacitance C_s at the peak transconductance was calculated using a quasistatic model, which accounts for the electron degeneracy at the conduction band, the non-parabolicity effect of the Γ valley, and possible influence due to the interface traps.[42,43] In the calculation, the flat band voltage of the MOS structure was approximated to be the same as the threshold voltage in the I_{ds}/V_g curve. Using the total capacitance $1/C_{tot} = 1/C_{ox} + 1/C_s$, we estimate mobility values of 1400 $\text{cm}^2/(\text{V s})$ for InAs, which accounts for an error of 40% with the state-of-the-art formula. The uncertainty in the estimation of the gate capacitance along with hysteresis and unstable baseline-currents make it difficult to quantitatively assess mobility and carrier concentration from field-effect measurements. More sophisticated mobility measurements can be obtained by simulating the capacitance via finite element methods and directly fitting the transconductance[37] or also with Hall effect measurements,[44] Seebeck coefficient measurements,[45] terahertz spectroscopy,[46] and Raman spectroscopy. In the following, we present our estimations of the mobility and electron carrier concentration from Raman spectroscopy.

Figure 5 shows the Raman spectra of pristine InAs and InAsSb with Sb 35% nanowires. In the spectra, LO and TO phonons frequencies as well as the SO (surface optical modes) typically detected in nanowires[47,48] are indicated. In the case of InAs, TO and LO modes of zincblende phase are present, no modes related to wurtzite crystal phase are observed.[49] In the case of InAsSb, the position of the TO and LO modes are consistent with the composition and follow a two mode model of ternary alloys: Raman modes of InAs and InSb are present, the position and intensity weighted by the composition.[50,51]

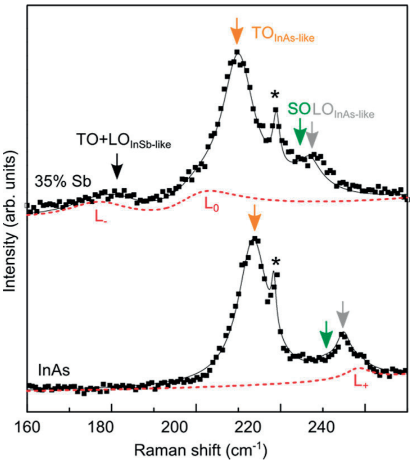

Figure 5. Raman spectra of InAs nanowires and of InAsSb nanowires with 35% antimony. The solid lines are the convolution of the ternary modes with a Lorentzian profile and the coupled modes' line shape obtained by fitting the model. The dashed lines show the coupled modes obtained by the fitting. The star indicates a plasma laser line.

The Raman spectra show additional spectral features in the LO region for the InAs and in the InAs-like TO mode region for InAsSb, which are not related to the composition, crystal phase, or shape of the nanowires. We attribute these additional peaks to the interaction of the carriers with the polar phonons. Longitudinal phonon−plasmon interaction is expected in polar semiconductor with free carriers.[52,53] Raman scattering by coupled plasmon−optical−phonon modes in n-type ternary III−V compounds results in three characteristic modes. In n-type InAsSb there is an intermediate mode (L_0) between the InAs-like TO and InSb-like LO phonon, in addition to lower frequency (L_-) and higher frequency (L_+) signatures.[52] The frequency position and the width of these modes are related to the plasmon (carrier) density and the lifetime (mobility). We fitted the whole spectra by modeling both the modes related to the composition and to the presence of free carriers. A Lorentzian profile was used for the TO and LO modes, whereas the line shape of the coupled modes included the effect of damping (mobility) as in ref 54. More details are given in the Supporting Information. We extract an electron concentration and mobility consistent with $n = 3.0 \times 10^{16}$ cm^{-3} and $\mu = 3900$ cm^2/(V s) for InAs and $n = 1.7 \times 10^{17}$ cm^{-3} and $\mu = 8300$ cm^2/(V s) for uncoated InAsSb nanowires. Overall, Raman spectroscopy gives higher mobility and lower carrier density values. The origin of this difference will be investigated in the future by contrasting with other measurements such as pump−probe THz spectroscopy.[55]

In conclusion, we have grown InAs$_{1-x}$Sb$_x$ nanowires with an antimony content up to 35% using a catalyst-free MBE growth process on GaAs substrates. The nanowires have a hexagonal cross section and show no tapering all along the wire. The crystal structure and chemical composition has been studied using HRTEM and EDX. We observed that the stacking fault density can be reduced to a few per micron by increasing the antimony content above 25%. These results confirm a universal trend of Sb to reduce stacking faults and polytypism in III−V nanowires, regardless of the synthesis method. We also studied for the first time the radial composition of the InAs$_{1-x}$Sb$_x$ nanowires using cross-sectional EDX analysis. A nanowire shell with slightly lower antimony content and antisegregation at the corners was observed, indicating that the nanowire diameter increases due to radial overgrowth. The electronic properties of InAs$_{1-x}$Sb$_x$ nanowires were studied using field-effect transistor measurements and Raman spectroscopy. We find that the incorporation of antimony increases the nanowire conductivity and mobility. We further use high-quality ALD grown Al_2O_3 as a gate dielectric for top gated nanowire devices and demonstrate better gate control and lower current drift without harming the nanowire properties. Raman spectroscopy shows that both the mobility and the charge density are increased for ternary antimonide nanowires. Our results shed light on the growth mechanism of ternary antimonide nanowires, and pave the pathway toward high-quality nanowire devices.

Experimental Methods. *Nanowire Growth.* The nanowires were grown in a DCA P600 MBE system on GaAs(111)B substrates by self-assembly and without the use of a foreign catalyst. The substrates were covered with a 4.5 nm silicon oxide layer, obtained by spin coating a diluted solution of hydrogen silsesquioxane (HSQ) (HSQ:MIBK 1:10) at 6000 rpm and annealing at 300 °C for 10 min. A similar substrate preparation was previously used for InAs and GaAs nanowire growth without a foreign catalyst.[19,56] The substrates were degassed at a manipulator temperature of 400 °C in ultrahigh vacuum conditions for 2 h prior to growth. Once in the growth chamber, they were annealed for 1 h at the growth temperature under constant arsenic and antimony flux. Nanowire growth was started by opening the indium shutter. After 60 min the growth was terminated by closing the indium and antimony supplies. The sample was cooled down under arsenic within 10 min. Standard fluxes are an indium beam equivalent pressure (BEP) of 1.4×10^{-7} Torr (corresponding to a 0.14 Å/s growth rate), and an arsenic BEP of 1.9×10^{-6} Torr. The antimony content in the nanowires was controlled by adjusting the antimony tank temperature, resulting in a BEP of 1.4−2.6 × 10^{-7} Torr. The cracker and conductance zone temperature was fixed at 800 °C for all samples. The crystal structure and composition of the nanowires was characterized by high resolution transmission electron microscopy (HRTEM) in a FEI Tecnai OSIRIS microscope operated at 200 kV. The antimony content of the nanowires was measured by EDX spectroscopy in the same microscope.

Device Fabrication. Single-nanowire field effect transistors (FET) were fabricated on highly p-doped silicon substrates with a 200 nm thermal oxide layer following a standard procedure.[57,58] For devices based on standard InAs$_{1-x}$Sb$_x$ nanowires the native oxide was removed by argon milling in order to achieve ohmic contacts. Chromium/gold (20 nm/100 nm) contacts were then deposited by sputtering in the same deposition chamber as the argon milling, thereby avoiding reoxidation of the surface. For devices based on Al_2O_3-coated $InAs_{1-x}Sb_x$ nanowires the nanowires were capped with arsenic in the MBE chamber after growth by cooling down the sample to room temperature and opening arsenic for 30 min. The protective arsenic layer was then evaporated in the ALD chamber before starting deposition of the oxide. This procedure allowed us to prevent the growth of native oxide on the nanowires and to obtain a high-quality interface between the InAs and the alumina. Titanium/gold (10 nm/100 nm) was deposited on the alumina as top gate using e-beam evaporation. For the contacts, the alumina was removed by ion beam etching before sputtering chromium/gold.

Raman Spectroscopy. Raman measurements were done using the 488 nm line of $Ar-Kr^+$ for excitation. The laser with power of 250 μW was focused on the nanowire with a microscope objective with numerical aperture NA = 0.75. The scattered light was collected by a TriVista spectrometer and detected by a CCD camera. The measurements were realized in backscattering geometry with the nanowires suspended over a trench, in order to enhance the response of the longitudinal optical phonon mode.[59]

■ ASSOCIATED CONTENT

Ⓢ Supporting Information

The Supporting Information is available free of charge on the ACS Publications website at DOI: 10.1021/acs.nanolett.5b04367.

> Additional information on the growth of InAsSb nanowires, electrical characterization, and Raman spectroscopy. (PDF)

■ AUTHOR INFORMATION

Corresponding Author

*E-mail: anna.fontcuberta-morral@epfl.ch.

Author Contributions

The manuscript was written through contributions of all authors. All authors have given approval to the final version of the manuscript.

Funding

SNF through NCCR-QSIT, projects nr 156081 and 143908 and Ambizione.

Notes

The authors declare no competing financial interest.

■ ACKNOWLEDGMENTS

We thank Duncan Alexander and Thomas La Grange for fruitful discussions, and Colette Vallotton for help with the ultramicrotome.

■ REFERENCES

(1) del Alamo, J. A. Nanometre-scale electronics with III-V compound semiconductors. *Nature* **2011**, *479*, 317.

(2) Li, Y.; Qian, F.; Xiang, J.; Lieber, C. M. Nanowire electronic and optoelectronic devices. *Mater. Today* **2006**, *9*, 18.

(3) Takei, K.; Takahashi, T.; Ho, J. C.; Ko, H.; Gillies, A. G.; Leu, P. W.; Fearing, R. S.; Javey, A. Nanowire active-matrix circuitry for low-voltage macroscale artificial skin. *Nat. Mater.* **2010**, *9*, 821.

(4) Dayeh, S. H.; Aplin, D. P. R.; Zhou, X.; Yu, P. K. L.; Yu, E. T.; Wang, D. High Electron Mobility InAs Nanowire Field-Effect Transistors. *Small* **2007**, *3*, 326.

(5) Lee, E. J. H.; Jiang, X.; Houzet, M.; Aguado, R.; Lieber, C. M.; De Franceschi, S. Spin-resolved Andreev levels and parity crossings in hybrid superconductor-semiconductor nanostructures. *Nat. Nanotechnol.* **2013**, *9*, 79.

(6) Hu, Y.; Kuemmeth, F.; Lieber, C. M.; Marcus, C. M. Hole spin relaxation in Ge-Se core-shell nanowire qubits. *Nat. Nanotechnol.* **2011**, *7*, 47.

(7) Shim, W.; Yao, J.; Lieber, C. M. Programmable Resistive-Switch Nanowire Transistor Logic Circuits. *Nano Lett.* **2014**, *14*, 5430.

(8) Mourik, V.; Zuo, K.; Frolov, S. M.; Plissard, S. R.; Bakkers, E. P. A. M.; Kouwenhoven, L. P. Signatures of Majorana Fermions in Hybrid Superconductor-Semiconductor Nanowire Devices. *Science* **2012**, *336*, 1003.

(9) Plissard, S. R.; van Weperen, I.; Car, D.; Verheijen, M. A.; Immink, G. W. G.; Kammhuber, J.; Cornelissen, L. J.; Szombati, D. B.; Geresdi, A.; Frolov, S. M.; Kouwenhoven, L. P.; Bakkers, E. P. A. M. Formation and electronic properties of InSb nanocrosses. *Nat. Nanotechnol.* **2013**, *8*, 859.

(10) Heiss, M.; Conesa-Boj, S.; Ren, J.; Tseng, H.-H.; Gali, A.; Rudolph, A.; Uccelli, E.; Peiro, F.; Morante, J. R.; Schuh, D.; Reiger, E.; Kaxiras, E.; Arbiol, J.; Fontcuberta i Morral, A. Direct correlation of crystal structure and optical properties in wurtzite/zinc-blende GaAs nanowire heterostructures. *Phys. Rev. B: Condens. Matter Mater. Phys.* **2011**, *83*, 045303.

(11) Thelander, C.; Caroff, P.; Plissard, S.; Dey, A. W.; Dick, K. A. Effects of Crystal Phase Mixing on the Electrical Properties of InAs Nanowires. *Nano Lett.* **2011**, *11*, 2424.

(12) Vainorius, N.; Lehmann, S.; Jacobsson, D.; Samuelson, L.; Dick, K. A.; Pistol, M.-E. Confinement in Thickness-Controlled GaAs Polytype Nanodots. *Nano Lett.* **2015**, *15*, 2652.

(13) Dick, K. A.; Thelander, C.; Samuelson, L.; Caroff, P. Crystal Phase Engineering in Single InAs Nanowires. *Nano Lett.* **2010**, *10*, 3494.

(14) Joyce, H.; Wong-Leung, J.; Gao, Q.; Tan, H. H.; Jagadish, C. Phase Perfection in Zincblende and Wurtzite III-V Nanowires Using Basic Growth Parameters. *Nano Lett.* **2010**, *10*, 908.

(15) Brotherton, S. D.; Lowther, J. E. Electron and Hole Capture at Au and Pt Centers in Silicon. *Phys. Rev. Lett.* **1980**, *44*, 606.

(16) Allen, J. E.; Hemesath, E. R.; Perea, D. E.; Lensch-Falk, J. L.; Yin, F.; Gass, M. H.; Wang, P.; Bleloch, A. L.; Palmer, R. E.; Lauhon, L. J.; Li, Z. Y. High-resolution detection of Au catalyst atoms in Si nanowires. *Nat. Nanotechnol.* **2008**, *3*, 168.

(17) Bar-Sadan, M.; Barthel, J.; Shtrikman, H.; Houben, L. Direct Imaging of Single Au Atoms Within GaAs Nanowires. *Nano Lett.* **2012**, *12*, 2352.

(18) Tambe, M. J.; Ren, S.; Gradecak, S. Effects of Gold Diffusion on n-Type Doping of GaAs Nanowires. *Nano Lett.* **2010**, *10*, 4584.

(19) Grap, Th.; Rieger, T.; Blömers, C.; Schäpers, T.; Grützmacher, D.; Lepsa, M. I. Self-catalyzed VLS grown InAs nanowires with twinning superlattices. *Nanotechnology* **2013**, *24*, 335601.

(20) Dimakis, E.; Lähnemann, J.; Jahn, U.; Breuer, S.; Hilse, M.; Geelhaar, L.; Riechert, H. Self-Assisted Nucleation and Vapor-Solid Growth of InAs Nanowires on Bare Si(111). *Cryst. Growth Des.* **2011**, *11*, 4001.

(21) Biermanns, A.; Dimakis, E.; Davydok, A.; Sasaki, T.; Geelhaar, L.; Takahasi, M.; Pietsch, U. Role of Liquid Indium in the Structural Purity of Wurtzite InAs Nanowires That Grow on Si(111). *Nano Lett.* **2014**, *14*, 6878.

(22) Dick, K. A.; Caroff, P.; Bolinsson, J.; Messing, M. E.; Johansson, J.; Deppert, K.; Wallenberg, L. R.; Samuelson, L. Control of III-V nanowire crystal structure by growth parameter tuning. Semiconductor Science and Technology. *Semicond. Sci. Technol.* **2010**, *25*, 024009.

(23) Yuan, X.; Caroff, P.; Wong-Leung, J.; Tan, H. H.; Jagadish, C. Controlling the morphology, composition and crystal structure in gold-seeded GaAs1-xSbx nanowires. *Nanoscale* **2015**, *7*, 4995.

(24) Conesa-Boj, S.; Kriegner, D.; Han, X.-L.; Plissard, S.; Wallart, X.; Stangl, J.; Fontcuberta i Morral, A.; Caroff, P. Gold-Free Ternary III-V Antimonide Nanowire Arrays on Silicon: Twin-Free down to the First Bilayer. *Nano Lett.* **2014**, *14*, 326.

(25) Xu, T.; Dick, K. A.; Plissard, S.; Nguyen, T. H.; Makoudi, Y.; Berthe, M.; Nys, J.-P.; Wallart, X.; Grandidier, B.; Caroff, P. Faceting, composition and crystal phase evolution in III-V antimonide nanowire heterostructures revealed by combining microscopy techniques. *Nanotechnology* **2012**, *23*, 095702.

(26) Sourribes, M. J. L.; Isakov, I.; Panfilova, M.; Liu, H.; Warburton, P. A. Mobility Enhancement by Sb-mediated Minimisation of Stacking Fault Density in InAs Nanowires Grown on Silicon. *Nano Lett.* **2014**, *14*, 1643.

(27) Zhuang, Q. D.; Anyebe, E. A.; Chen, R.; Liu, H.; Sanchez, A. M.; Rajpalke, M. K.; Veal, T. D.; Wang, Z. M.; Huang, Y. Z.; Sun, H. D. Sb-Induced Phase Control of InAsSb Nanowires Grown by Molecular Beam Epitaxy. *Nano Lett.* **2015**, *15*, 1109.

(28) Farrell, A. C.; Lee, W.-J.; Senanayake, P.; Haddad, M. A.; Prikhodko, S. V.; Huffaker, D. L. High-Quality InAsSb Nanowires Grown by Catalyst-Free Selective Area Metal-Organic Chemical Vapor Deposition. *Nano Lett.* **2015**, *15*, 6614.

(29) Watson, D. C.; Martinez, R. V.; Fontana, Y.; Russo-Averchi, E.; Heiss, M.; Fontcuberta i Morral, A.; Whitesides, G. M.; Loncar, M. Nanoskiving Core-Shell Nanowires: A New Fabrication Method for Nano-optics. *Nano Lett.* **2014**, *14*, 524.

(30) Zheng, C.; Wong-Leung, J.; Gao, Q.; Tan, H. H.; Jagadish, C.; Etheridge, J. Polarity-Driven 3-Fold Symmetry of GaAs/AlGaAs Core Multishell Nanowires. *Nano Lett.* **2013**, *13*, 3742.

(31) Ahn, J.; Kent, T.; Chagarov, E.; Tang, K.; Kummel, A. C.; McIntyre, P. C. Arsenic decapping and pre-atomic layer deposition trimethylaluminum passivation of Al2O3/InGaAs(100) interfaces. *Appl. Phys. Lett.* **2013**, *103*, 071602.

(32) Ioffe semiconductors database. http://www.ioffe.ru/SVA/NSM/Semicond/InAs/electric.html and http://www.ioffe.rssi.ru/SVA/NSM/Semicond/InSb/electric.html (accessed November 2015).

(33) Mead, C. A.; Spitzer, W. G. Fermi level position at semiconductor surfaces. *Phys. Rev. Lett.* **1963**, *10*, 471.

(34) Noguchi, M.; Hirakawa, K.; Ikoma, T. Intrinsic Electron Accumulation Layers on Reconstructed Clean InAs(100) Surfaces. *Phys. Rev. Lett.* **1991**, *66*, 2243.

(35) Storm, K.; Nylund, G.; Samuelson, L.; Micolich, A. P. Realizing Lateral Wrap-Gated Nanowire FETs: Controlling Gate Length with Chemistry Rather than Lithography. *Nano Lett.* **2012**, *12*, 1.

(36) Agostinelli, G.; Delabie, A.; Vitanov, P.; Alexieva, Z.; Dekkers, H. F. W.; De Wolf, S.; Beaucarne, G. Very low surface recombination velocities on p-type silicon wafers passivated with a dielectric with fixed negative charge. *Sol. Energy Mater. Sol. Cells* **2006**, *90*, 3438.

(37) Gül, Ö.; van Woerkom, D. J.; van Weperen, I.; Car, D.; Plissard, S. R.; Bakkers, E. P. A. M.; Kouwenhoven, L. P. Towards high mobility InSb nanowire devices. *Nanotechnology* **2015**, *26*, 215202.

(38) Dayeh, S. A.; Soci, C.; Yu, P. K. L.; Yu, E. T.; Wang, D. Influence of surface states on the extraction of transport parameters from InAs nanowire field effect transistors. *Appl. Phys. Lett.* **2007**, *90*, 162112.

(39) Mattmann, M.; Roman, C.; Helbling, T.; Bechstein, D.; Durrer, L.; Pohle, R.; Fleischer, M.; Hierold, C. Pulsed gate sweep strategies for hysteresis reduction in carbon nanotube transistors for low concentration NO2 gas detection. *Nanotechnology* **2010**, *21*, 185501.

(40) Wunnicke, O. Gate capacitance of back-gated nanowire field-effect transistors. *Appl. Phys. Lett.* **2006**, *89*, 083102.

(41) Heedt, S.; Otto, I.; Sladek, K.; Hardtdegen, H.; Schubert, J.; Demarina, N.; Luth, H.; Gruetzmacher, D.; Schapers, T. Resolving ambiguities in nanowire field-effect transistor charaterization. *Nanoscale* **2015**, *7*, 18188.

(42) Engel-Herbert, R.; Hwang, Y.; Stemmer, S. Quantification of trap densities at dielectric/III-V semiconductor interfaces. *Appl. Phys. Lett.* **2010**, *97*, 062905.

(43) Chen, H.-P.; Yuan, Y.; Yu, B.; Ahn, J.; McIntyre, P. C.; Asbeck, P. M.; Rodwell, M. J. W.; Taur, Y. Interface-State Modeling of Al2O3-InGaAs MOS From Depletion to Inversion. *IEEE Trans. Electron Devices* **2012**, *59*, 2383.

(44) Blömers, C.; Grap, T.; Lepsa, M. I.; Moers, J.; Trellenkamp, S.; Grützmacher, D.; Lüth, H.; SchäPers, T. Hall effect measurements on InAs nanowires. *Appl. Phys. Lett.* **2012**, *101*, 152106.

(45) Schmidt, V.; Mensch, Ph. F. J.; Karg, S. F.; Gotsmann, B.; Das Kanungo, P.; Schmid, H.; Riel, H. Using the Seebeck coefficient to determine charge carrier concetration, mobility, and relaxation time in InAs nanowires. *Appl. Phys. Lett.* **2014**, *104*, 012113.

(46) Joyce, H. J.; Docherty, C. J.; Gao, Q.; Tan, H. H.; Jagadish, C.; Lloyd-Hughes, J.; Herz, L. M.; Johnston, M. B. Electronic properties of GaAs, InAs and InP nanowires studied by terahertz spectroscopy. *Nanotechnology* **2013**, *24*, 214006.

(47) Adu, K. W.; Xiong, Q.; Gutierrez, H. R.; Chen, G.; Eklund, P. C. Raman scattering as a probe of phonon confinement and surface optical modes in semiconducting nanowires. *Appl. Phys. A: Mater. Sci. Process.* **2006**, *85*, 287.

(48) Spirkoska, D.; Abstreiter, G.; Fontcuberta i Morral, A. Size and environment dependence of surface phonon modes of gallium arsenice nanowires as measured by Raman spectroscopy. *Nanotechnology* **2008**, *19*, 435704.

(49) Hörmann, N. G.; Zardo, I.; Hertenberger, S.; Funk, S.; Bolte, S.; Döblinger, M.; Koblmüller, G.; Abstreiter, G. Effects of stacking variations on the lattice dynamics of InAs nanowires. *Phys. Rev. B: Condens. Matter Mater. Phys.* **2011**, *84*, 155301.

(50) Alarcón-Lladó, E.; Conesa-Boj, S.; Wallart, X.; Caroff, P.; Fontcuberta i Morral, A. Raman spectroscopy of self-catalyzed GaAs$_{1-x}$Sb$_x$ nanowires grown on silicon. *Nanotechnology* **2013**, *24*, 405707.

(51) Cherng, Y. T.; Ma, K. Y.; Stringfellow, G. B. Raman scattering in InAs$_{1-x}$Sb$_x$ grown by organometallic vapor phase epitaxy. *Appl. Phys. Lett.* **1988**, *53*, 886.

(52) Tell, B.; Martin, R. J. Raman Scattering by Coupled Optical-Phonon-Plasmon Modes in GaAs. *Phys. Rev.* **1968**, *167*, 381.

(53) Abstreiter, G.; Cardona, M.,: Pinczuk, A. Light scattering by free carrier excitations in semiconductors. In *Light Scattering in Solids IV*; Springer: Berlin/Heidelberg, 1984.

(54) Cuscó, R.; Alarcón-Lladó, E.; Artús, L.; Hurst, W. S.; Maslar, J. E. Raman scattering by LO-phonon−plasmon coupled modes in Ga$_{1-x}$In$_x$As$_y$Sb$_{1-y}$: Role of Landau damping. *Phys. Rev. B: Condens. Matter Mater. Phys.* **2010**, *81*, 195212.

(55) Joyce, H. J.; Docherty, C. J.; Gao, Q.; Tan, H. H.; Jagadish, C.; Lloyd-Hughes, J.; Herz, L. M.; Johnston, M. B. Electronic properties of GaAs, InAs and InP nanowires studied by teraherz spectroscopy. *Nanotechnology* **2013**, *24*, 214006.

(56) Matteini, F.; Tütüncüoglu, G.; Rüffer, D.; Alarcon-Llado, E.; Fontcuberta i Morral, A. Ga-assisted growth of GaAs nanowires on silicon, comparison of surface SiOx of different nature. *J. Cryst. Growth* **2014**, *404*, 246.

(57) Dufouleur, J.; Colombo, C.; Garma, T.; Ketterer, B.; Uccelli, E.; Nicotra, M.; Fontcuberta i Morral, A. P-Doping Mechanisms in Catalyst-Free Gallium Arsenide Nanowires. *Nano Lett.* **2010**, *10*, 1734.

(58) Blanc, P.; Heiss, M.; Colombo, C.; Mallorqui, A. D.; Safaei, T. S.; Krogstrup, P.; Nygard, J.; Fontcuberta i Morral, A. Electrical contacts to single nanowires: a scalable method allowing multiple devices on a chip. Application to a single nanowire radial p-i-n junction. *Int. J. Nanotechnol.* **2013**, *10*, 419.

(59) Amaduzzi, F.; Alarcon-Llado, E.; Hautmann, H.; Tanta, R.; Matteini, F.; Tütüncüoglu, G.; Vosch, T.; Nygard, J.; Jespersen, Th.; Uccelli, E.; Fontcuberta i Morral, A. Tuning the response of non-allowed Raman modes in GaAs nanowires. In review.

4.2 Understanding nanowire growth direction

Having complete control over the nanowire growth direction and their orientation with respect to the substrate is important for many applications. However, in standard samples we observe a significant density of tilted nanowires. In order to control or suppress their formation, it is necessary to understand the underlying mechanism which leads to the growth of tilted nanowires. To this end, we first measured the direction of the tilted nanowires, and then we studied the crystal structure of the nanowires. In order to understand the direction of the nanowires we considered several approaches: 1) Take atomic force microscopy (AFM) images and analyze the angle with respect to the substrate and a reference direction. While this approach would give the precise direction of a single nanowire, it is very challenging to do AFM on a nanowire forest. 2) Take SEM images and tilt the sample in order to get an image of the same nanowire from two different directions. This approach would also give the direction of a single nanowire, however it is not easy to stay at the exact position of a specific nanowire while tilting the sample significantly. (3) Take SEM images from two different directions and measure the projection angles of many different nanowires, and then plot the observed angles as histograms and compare with calculated projection angles for specific nanowire orientations. This approach is relatively fast and straight forward. The drawback is that several directions can show the same projection angles. Due to simplicity we chose the third approach, and then verified our assumptions using TEM studies.

For the calculation of projection angles we started with all low index crystalline orientations, i.e. <100>, <110>, <111>A, <112> and we only considered directions which point out of the substrate. We furthermore calculated the directions of all <111>B directions after a twin which are non-perpendicular to the $[\bar{1}\bar{1}\bar{1}]$ substrate normal (3D twin as explained in section 2.4), and found that they are oriented in (1,1,5) directions. For those 3D twinning directions we give their direction as a vector, using the crystalline orientation of the substrate as coordinate system. The expected projection angles can then be calculated using the same reference system as for the other low index crystalline orientations. It is important to keep in mind that the vector describing the orientation does not correspond to the crystalline direction of the nanowire: the nanowire is elongated in <111>B direction, even though it's orientation corresponds to a vector with higher indices.

Comparing the expected projection angles with the experimentally observed histograms we found that most projection angles of tilted InAs nanowires can be explained by 3D twinning. Our results are supported by TEM analysis, where twins non-perpendicular to the nanowire axis were observed. The results are presented in the publication below. In addition we also found a few angles which differ from the 3D twinning angles. Interestingly these nanowires also show different facets compared to vertical or 3D twinned nanowires (which both have hexagonal cross section). We found that their projection angles correspond to other low index crystalline orientations, mostly <11$\bar{2}$>, but also <100> and <110> directions. Nanowires in those unusual directions could also be observed in TEM.

Last but not least we also analyzed how the existence of tilted nanowires depends on the growth conditions. The most interesting result is that their formation is suppressed for high V/III ratios. This finding sheds light on the growth mechanism of the early stages of growth: for the 3D twinning mechanism the formation of non-horizontal facets is a requirement. This is unlikely during the VS growth mechanism, therefore suggesting that tilted nanowires started with an indium droplet, while at high V/III the droplet is significantly smaller or completely absent. Whether or not the droplet is consumed during later stages of growth remains unclear at this point. The full results are presented the publication below.

Reprinted with permission from H. Potts *et al.* Tilting catalyst-free InAs nanowires by 3D-twinning and unusual growth directions. *Crystal Growth & Design* **17**, 3596 (2017). © 2017 American Chemical Society.

CRYSTAL GROWTH & DESIGN

Communication

pubs.acs.org/crystal

Tilting Catalyst-Free InAs Nanowires by 3D-Twinning and Unusual Growth Directions

Heidi Potts,[†] Youri van Hees,[†,‡] Gözde Tütüncüoglu,[†] Martin Friedl,[†] Jean-Baptiste Leran,[†] and Anna Fontcuberta i Morral*[,†]

[†]Laboratoire des Matériaux Semiconducteurs, École Polytechnique Fédérale de Lausanne, 1015 Lausanne, Switzerland

[‡]Institute of Applied Physics, Eindhoven University of Technology, 5600 MB Eindhoven, The Netherlands

Supporting Information

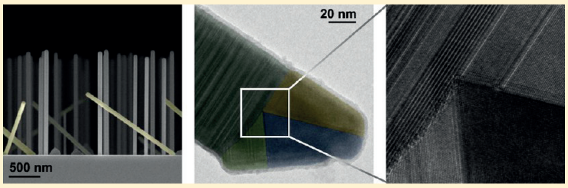

ABSTRACT: Controlling the growth direction of nanowires is of strategic importance both for applications where nanowire arrays are contacted in parallel and for the formation of more complex nanowire networks. We report on the existence of tilted InAs nanowires on (111)B GaAs. The tilted direction is predominantly the result of a three-dimensional twinning phenomenon at the initial stages of growth, so far only observed in VLS growth. We also find some nanowires growing in ⟨112⟩ and other directions. We further demonstrate how the tilting of nanowires can be engineered by modifying the growth conditions, and outline the procedures to achieve fully vertical or tilted nanowire ensembles. Conditions leading to a high density of tilted nanowires also provide a way to grow nanoscale crosses. This work opens the path toward achieving control over nanowire structures and related hierarchical structures.

INTRODUCTION

Semiconductor nanowires are promising candidates for future electronic, optoelectronic, and energy harvesting devices as well as a platform to investigate low-dimensional phenomena.[1−8] In certain applications such as light emitting diodes or solar cells, it is highly desirable that nanowires are contacted in parallel on as-grown substrates. In this case, a complete control of the nanowire growth direction is essential in order to avoid leakage or open-circuit pathways. For other applications such as Majorana Fermion quantum computing, the growth direction determines the g-factor and spin−orbit interaction. In addition, any quantum logic involving Majorana Fermions requires more than one branch, e.g., nanowire crosses are desired.[9−11]

In general, III−V nanowires grow preferentially in the ⟨111⟩B direction, resulting in mostly vertical nanowires when grown on (111)B substrates. Interest in nonconventional growth directions has increased significantly during the last years, and in the case of metal-catalyzed nanowires, a variety of different directions have been reported.[12] Recent examples include ⟨111⟩A oriented GaAs and GaSb nanowires,[13,14] and InP nanowires for which the direction can be switched between ⟨111⟩B and ⟨100⟩.[15] In addition, InAs nanowires in ⟨001⟩ direction and ⟨112⟩ direction have been demonstrated for gold-catalyzed MOVPE growth.[16] The change in growth direction has been attributed to a change of contact angle of the liquid droplet in the vapor−liquid−solid (VLS) mechanism, or by dynamics at the growth interface. Recently, unconventional growth directions have also been observed for self-catalyzed nanowires. A small fraction of GaAsSb nanowires was found to grow in ⟨112⟩ direction,[17] GaAs nanowires in the ⟨111⟩A direction have been engineered,[18] and InAs nanowires turning from ⟨111⟩B to ⟨11$\bar{2}$⟩ direction have been demonstrated.[19,20] However, tilted nanowires are not in all cases related to the growth in nonconventional crystalline directions. In some cases they can also explained by nucleation from parasitic growth (no crystalline relation with the substrate) or by multiple-order three-dimensional twinning.[21] 3D twinning is based on the formation of other {111} facets in additional to the (111)B growth front. A rotational twin around a nonvertical ⟨111⟩ direction then allows formation of a secondary seed crystal, for which the ⟨111⟩B directions are oriented differently compared to the original seed crystal. A multiple-order twinning process can therefore result in nanowires with a variety of quantized orientations, while the growth always proceeds by the formation of {111}B planes. 3D twinning was found in self-catalyzed GaAs nanowires on silicon,[21] as well as for gold-catalyzed InP nanowires.[22] In the case of GaAs nanowires, further work has explained how multiple order twinning depends on the substrate preparation,[23] and it has been shown that the wetting properties of the initial gallium droplets can be essential.[24] In the case of InAs nanowires grown without a foreign catalyst, tilted nanowires have been observed.[25,26] However, the exact orientation has never been determined. Understanding the underlying mechanism of the formation of tilted InAs nanowires is particularly interesting, since the growth mechanism of MBE grown InAs nanowires is still a matter of debate, and both VLS[26] and vapor−solid (VS) growth[27,28] have been reported under different conditions. The

Received: April 5, 2017
Revised: May 6, 2017
Published: May 9, 2017

DOI: 10.1021/acs.cgd.7b00487
Cryst. Growth Des. 2017, 17, 3596−3605

observation of multiple-order twinning would suggest that the growth is initiated with an indium droplet. The existence of tilted nanowires could therefore be an indicator of vapor−liquid−solid growth as opposed to vapor−solid growth.

In this work, we provide a quantitative analysis and crystallography of tilted InAs nanowires grown by MBE without a foreign catalyst. We find that tilted nanowires occur at quantized angles, and show that most of these angles match those which are theoretically expected from a 3D twinning process. In addition, InAs nanowires oriented in ⟨112⟩ and other low-index crystalline directions are demonstrated for the first time in the case of MBE growth without a foreign catalyst. By showing how the existence of tilted nanowires depends on the growth conditions we offer an approach to increase the number of tilted nanowires or suppress their formation completely—whichever is desired for a specific application.

■ RESULTS AND DISCUSSION

InAs nanowires are grown by molecular beam epitaxy (MBE) on GaAs(111)B substrates covered with 4.5 nm of HSQ oxide, as explained in ref 19. Figure 1a,b shows representative top view and cross-sectional scanning electron micrographs (SEM) of samples obtained under typical conditions (530 °C, V/III flux ratio of 13.5). We clearly observe not only nanowires growing perpendicular to the substrate but also some tilted nanowires. In order to determine the orientation of the nanowires we analyze their alignment with respect to main crystallographic directions of the substrate, both in top-view and cross-sectional SEM images. In Figure 1c we define the top view angle α as the angle between the nanowire projection onto the (111) plane and the $[\bar{2}11]$ direction (or the equivalent $[2\bar{1}\bar{1}]$ direction). For the cross-sectional analysis the samples were cleaved along the $(0\bar{1}1)$ plane. We define the cross-sectional angle β as the angle between the projection of the nanowire onto the $(0\bar{1}1)$ plane and the $[\bar{2}11]$ or $[2\bar{1}\bar{1}]$ direction as shown in Figure 1d. Top view and cross-sectional projection angles were measured on several hundred nanowires in samples obtained with a variety of growth conditions (V/III ratios of 4.3−25; growth temperatures of 490−550 °C). The resulting histograms are shown in Figure 1e,f for the top view and cross-sectional angles, respectively. For the top view projection angle, we observe that tilted nanowires occur predominantly at $\alpha \approx 19°$, 41°, and 79°. Cross-sectional angles show populations at $\beta \approx 35°$, 41°, and 70−80°. These measurements demonstrate that the tilted nanowires do not grow in random orientations and confirm the existence of a crystallographic relation with the substrate. The calculated projection angles which are marked in Figure 1e,f are explained in the following paragraph.

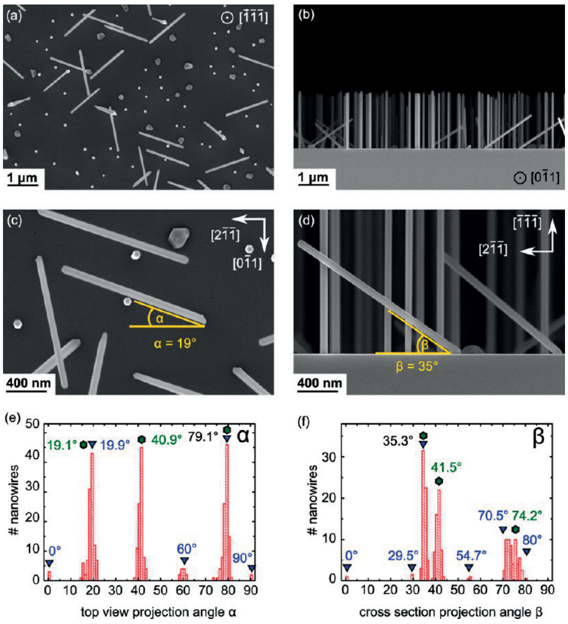

Figure 1. (a,b) Top view and cross-sectional SEM micrographs of a standard InAs nanowire sample. (c,d) Definition of the top view projection angle α and cross-sectional projection angle β. (e,f) Histograms of the occurrence of top view and cross-sectional projection angles. Green hexagons: 3D twinned wires. Blue triangles: ⟨100⟩, ⟨110⟩, ⟨112⟩, or ⟨111⟩A wires.

To analyze the orientation of the tilted nanowires, we calculate the projection angles of all low index crystalline directions (⟨100⟩, ⟨110⟩, ⟨111⟩A, ⟨112⟩), as well as the expected angles for nanowires after 3D twinning. The projection angles can be calculated by first calculating the projection of the wire onto a projection plane

$$\overrightarrow{\text{proj}} = \overrightarrow{\text{wire}} - \frac{\overrightarrow{\text{wire}}\cdot\overrightarrow{\text{plane}}}{|\overrightarrow{\text{plane}}|^2}\overrightarrow{\text{plane}} \tag{1}$$

where $\overrightarrow{\text{wire}}$ is the vector corresponding to the nanowire growth direction, and $\overrightarrow{\text{proj}}$ is the projection of the nanowire onto the projection plane which is defined by its normal vector $\overrightarrow{\text{plane}}$. Then the angle α with respect to the reference direction $\overrightarrow{\text{ref}}$ can be calculated by

$$\cos(\alpha) = \frac{\overrightarrow{\text{ref}}\cdot\overrightarrow{\text{proj}}}{|\overrightarrow{\text{ref}}||\overrightarrow{\text{proj}}|} \tag{2}$$

For the top view projection angle we choose $\overrightarrow{\text{plane}}$ as [111] and $\overrightarrow{\text{ref}}$ as $[\bar{2}11]$ or $[2\bar{1}\bar{1}]$, while for the cross-sectional angle we choose $\overrightarrow{\text{plane}}$ as $[0\bar{1}1]$. For the calculation of nanowire directions after multiple-order twinning we assume the formation of a seed crystal with a $(\bar{1}\bar{1}\bar{1})$ top facet since the substrate is a GaAs(111)B wafer. While growth then predominately occurs in the $[\bar{1}\bar{1}\bar{1}]$ direction with $\{1\bar{1}0\}$ facets leading to the hexagonal shape of nanowires, the seed crystal can also form additional facets in other ⟨111⟩ directions. Twinning can now also occur around those ⟨111⟩ directions and is referred to as 3D twinning. The crystalline directions of the 3D twinned crystal $\overrightarrow{x_{\text{rot}}}$ can therefore be calculated by

$$\overrightarrow{x_{\text{rot}}} = R\cdot\vec{x} \tag{3}$$

where $\vec{x}$ is the original direction and R is the rotation matrix around the direction $\vec{u} = (u_1, u_2, u_3)$ with $u_1^2 + u_2^2 + u_3^2 = 1$. For a twin, $\vec{u}$ is the normalized vector of one of the ⟨111⟩ directions, and is R is given by a 180° rotation; therefore

$$R = \begin{bmatrix} -1 + 2{u_1}^2 & 2u_1u_2 & 2u_1u_3 \\ 2u_1u_2 & -1 + 2{u_2}^2 & 2u_2u_3 \\ 2u_1u_3 & 2u_2u_3 & -1 + 2{u_3}^2 \end{bmatrix} \quad (4)$$

The coordinate system in our calculations corresponds to the orientation of the original seed crystal (and therefore the substrate). The rotated directions are obtained as a vector in this coordinate system and can as a consequence have higher indices. For clarity we denote the directions (and families of directions) before 3D twinning as $[x_1x_2x_3]$ (and $\langle x_1x_2x_3\rangle$), while the rotated directions are given as a vector (x_1, x_2, x_3). One should note that the directions of the rotated crystal are not in agreement with its crystalline orientations anymore.

Using this approach we calculate the orientations of the four $\langle 111\rangle$B directions after twinning around the other three $\langle 111\rangle$ directions. The resulting 12 first-order 3D twinned orientations are all found to be in equivalent (1, 1, 5) directions. Figure 2a shows a 3D model of nanowires growing in these new $\langle 111\rangle$B directions (only nanowires directed out of the substrate are shown). Since the original seed crystal can also be twinned with respect to the substrate (a twin around $[\bar{1}\bar{1}\bar{1}]$), we obtain six more directions. The two families of orientations are shown in dark and light green, respectively. We also present a top view projection and a cross-sectional projection of the model. The table shown in Figure 2b gives the expected directions and angles for new $\langle 111\rangle$B directions after twinning around the $[1\bar{1}1]$ direction. In addition to the projection angles α and β we also report γ, which corresponds to the angle between $[\bar{1}\bar{1}\bar{1}]$ and the new $\langle 111\rangle$B directions. We observe that one of the new directions is pointing into the substrate (denoted by †). The projection angles of the two out-of-plane directions α = 19.1°, 40.9°, and β = 35.3°, 41.5° are in good agreement with peaks observed in the histograms presented in Figure 1e,f. The other angles observed in the histograms can be explained by calculating the twinning around the other $\langle 111\rangle$B directions, or other low index crystalline orientations (a complete table of the expected projection angles is presented in the Supporting Information). The observation that the most pronounced peaks in the histogram correspond to angles which are expected after first order 3D twinning are a strong indication for the origin of tilted nanowires, but it is not enough as a proof since top view and cross-sectional projection angles are never measured on the same nanowire. Furthermore, as denoted in the histogram, several projection angles can result from both 3D twinned nanowires as well as other low index crystalline orientations (e.g., β = 35.3° is expected for $\langle 100\rangle$, $\langle 111\rangle$A, $\langle 112\rangle$, and 3D twinned nanowires). To gain more insight, we propose a way to calculate the real angle γ of the nanowire direction with respect to the surface normal ($[\bar{1}\bar{1}\bar{1}]$ direction), by matching top view angles α with cross-sectional angles β. This approach is based on the observation that all 3D twinned orientations exhibit the same real angle γ = 56.3°, while other low index orientations exhibit different angles. We can then use that for nanowires with the same angle γ; a small top view angle α corresponds a small cross-sectional angle β (and vice versa). Therefore, nanowires from top view images can be matched with nanowires from cross-sectional images. Figure 2c,d shows SEM micrographs of nanowires which are color-coded accordingly. From this figure we also derive an empirical relation between α and β as follows: In Figure 2c we define r to be the length of the projection of the nanowire onto the $(\bar{1}\bar{1}\bar{1})$ plane, and s as the component of r along the $[\bar{2}11]$ or $[2\bar{1}\bar{1}]$ direction. From this follows $s = r \cdot \cos\alpha$. In Figure 2d we see a projection of the nanowire onto the $(0\bar{1}1)$ plane, and define p as the component of this projection along the $[\bar{1}\bar{1}\bar{1}]$ direction, again finding s as the component along the $[\bar{2}11]$ or $[2\bar{1}\bar{1}]$ direction. Taking $\beta = \arctan\left(\frac{p}{s}\right)$ and combining it with $s = r \cdot \cos\alpha$ we find the empirical relation between β and α as

$$\beta = \arctan\left(\frac{p}{r\cdot\cos\alpha}\right) \quad (5)$$

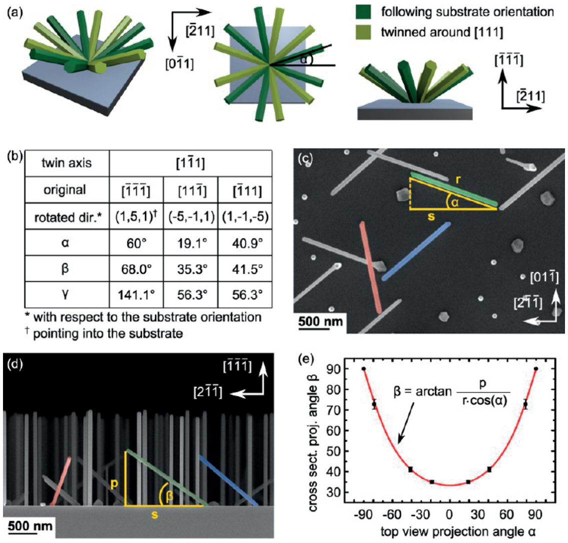

twin axis	$[1\bar{1}1]$		
original	$[\bar{1}\bar{1}\bar{1}]$	$[11\bar{1}]$	$[\bar{1}11]$
rotated dir.*	(1,5,1)†	(-5,-1,1)	(1,-1,-5)
α	60°	19.1°	40.9°
β	68.0°	35.3°	41.5°
γ	141.1°	56.3°	56.3°

* with respect to the substrate orientation
† pointing into the substrate

Figure 2. (a) 3D model of nanowire directions after first order 3D twinning. (b) Table summarizing the expected angles and directions of three new $\langle 111\rangle$B directions after twinning around the $[1\bar{1}1]$ direction. (c,d) Top view and cross-sectional SEM micrographs with wires in equivalent orientations color-coded, and projected lengths and angles annotated. (e) Plot of β as a function of α and a fit of their empirical relation.

From the histograms, we now match the three predominant peaks of top view angles α with cross-sectional angles β. Figure 2e shows a plot of the matched angles, including two theoretical points at β = 90° for α = ±90°. The data points are fitted with eq 5 giving $p/r = 0.66 \pm 0.01$. The accuracy of the fit indicates that the predominant projection angles result from a family of orientations which exhibit the same angle γ (and thereby validates our direct matching approach). At α = 0° we find $\gamma = 90° - \beta = 90° - \arctan(p\,/\,r) = 55.6° \pm 0.6°$, which is in agreement with the calculated angle of 56.3° for all first order twin directions. We have thus comprehensively shown that the predominant projection angles of tilted nanowires match those expected from first order 3D twinning.

We now turn to the analysis of the nanowire crystal structure of tilted nanowires by transmission electron microscopy (TEM). Our focus lies on the foot of the nanowires, where 3D twinning is expected to occur. For the analysis, wires from a sample showing a significant density of tilted nanowires were broken off of the substrate and transferred to TEM grids by sweeping the sample with a grid. Figure 3a shows cross-sectional and top view SEM micrographs of a sample before and after transferring the nanowires. From the cross-sectional

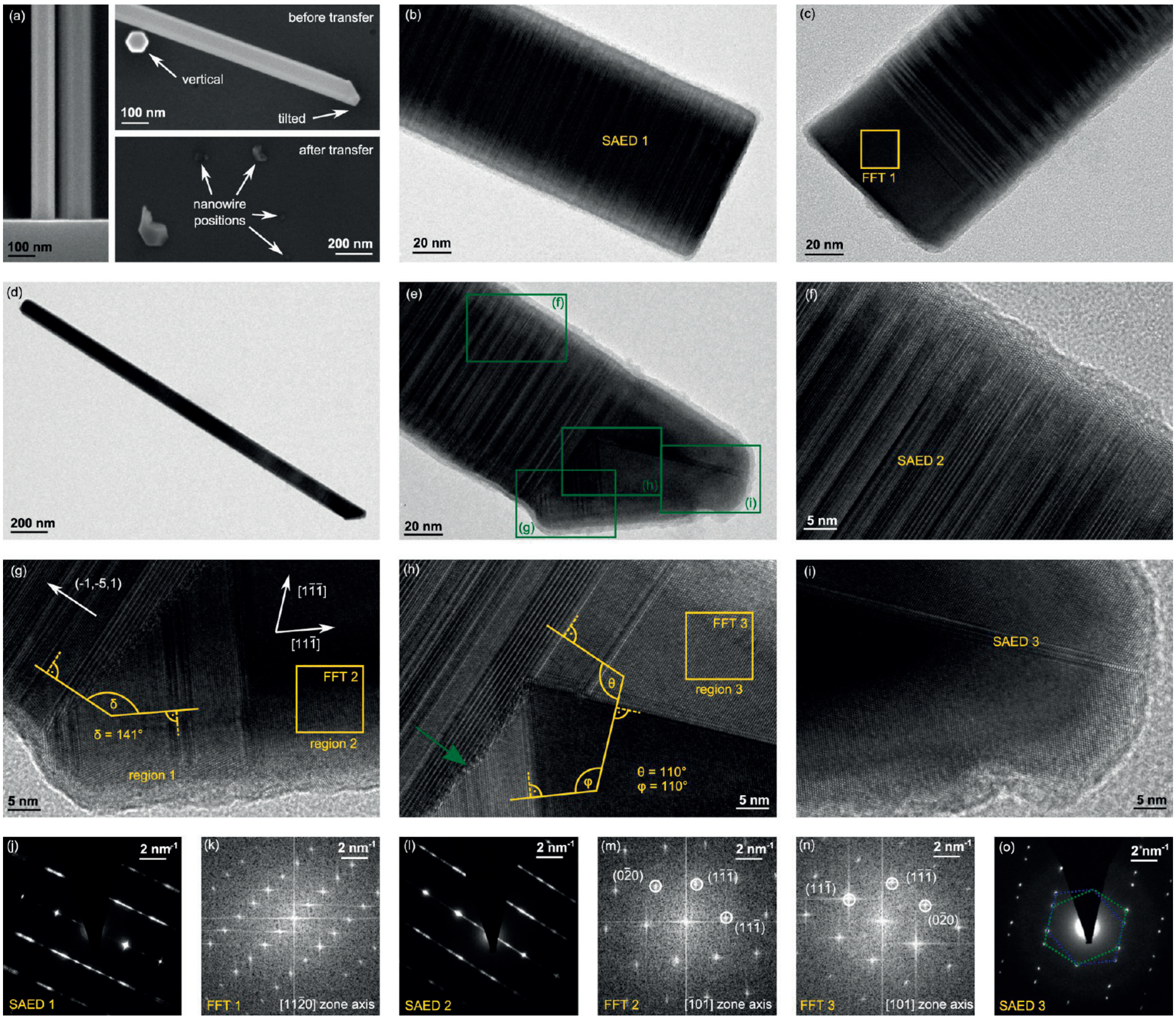

Figure 3. (a) Left: cross-sectional SEM micrograph of vertical nanowires. Right: top view SEM micrographs of a sample before and after transferring the nanowires to a TEM grid. (b,c) TEM micrographs of the foot of two vertical nanowires. (d) Overview TEM micrograph of a nanowire showing a similar foot as observed for the tilted nanowires by SEM. (e) Magnified image of the nanowire foot. (f–i) High-resolution TEM micrographs of the polytypic nanowire, the bottom left part of the foot, the center, and the bottom right part. (j–o) Selected area electron diffraction pattern and FFT images of the regions indicated.

image we observe that the foot of vertical nanowires is completely straight, while the top view image before nanowire transfer shows that the foot of tilted nanowires exhibits facets at a particular angle. After transferring the nanowires, the sample appears almost empty, with small crystallites remaining from the nanowires (indicated by arrows). This shows that most nanowires break off directly from the base, and the specific shape of the nanowire foot can therefore be used to distinguish tilted from vertical nanowires on the TEM grid. Figure 3b,c shows TEM micrographs of the foot of two different nanowires. We observe no change in morphology along the nanowire length. For the first sample, the crystal structure shows perpendicular stacking faults all along the nanowire. The polytypic crystal structure can also be observed in the selected area electron diffraction (SAED) pattern shown in Figure 3j. The second nanowire does not show any change in morphology either, and the crystal structure also shows stacking defects perpendicular to the growth direction. At the very beginning of the nanowire, a short Wurtzite (WZ) section can be observed, as shown by the fast Fourier transform (FFT) in Figure 3k. More information about the standard nanowire crystal structure of vertical nanowires can be found in the Supporting Information. Figure 3d shows a low-magnification TEM micrograph of a nanowire which exhibits a nanowire foot that looks similar to the ones observed in SEM images of tilted nanowires. A magnified TEM micrograph of the nanowire foot is presented in Figure 3e, with a change in crystal structure at the very beginning of the growth. Figure 3f–i shows high-resolution TEM micrographs of different locations of the nanowire foot (as indicated in (e)). In Figure 3f we observe the standard polytypic crystal structure with stacking defects perpendicular to the growth direction, which is also confirmed by the selected area diffraction pattern in Figure 3l. Figure 3g shows a high-resolution TEM micrograph of the left corner of the nanowire foot. We observe a zincblende (ZB) region with a few stacking defects on the left and then a pure zincblende region. An FFT image of the pure zincblende region is shown in Figure 3m and can be indexed, assuming that the image was taken in the $[\bar{1}0\bar{1}]$ zone axis. The angle between the $[11\bar{1}]$ direction of the pure zincblende region and the nanowire growth direction is found to be 141°. Figure 3h shows a high-resolution TEM micrograph of the center of the nanowire foot. The FFT of region 3 is shown in Figure 3n and can be indexed to show the crystal from the $[101]$ zone axis. The angles between region 2, region 3, and the nanowire growth direction are found to be 110°, which is in agreement with the angle expected between two $\langle 111 \rangle$ directions. Figure 3i shows the bottom right part of the nanowire foot. The corresponding selected area diffraction image in Figure 3o confirms the observation of the two zincblende regions with one rotational twin. In Figure 3h one can also observe that the interface between the bottom right part of the foot and the polytypic nanowire is perfectly crystalline, while the interface between the bottom left part and the polytypic nanowire (indicated with a green arrow) is defective, indicating that two different seed crystals merged here. Combining the information from the different micrographs and FFTs images, we suggest that growth started in region 2, followed by a twin around the $[1\bar{1}\bar{1}]$A direction to form region 3. Region 3 then started to exhibit a growth front in a new $\langle 111 \rangle$B direction, which then continued to grow as a nanowire. The growth front of the elongated nanowire corresponds to the $[11\bar{1}]$ direction in the coordinate system of region 3. Converting this direction to the original coordinate system of region 2 results in the vector $(-1, -5, 1)$, which indeed forms an angle of 141° with the $[11\bar{1}]$ direction of region 2. The bottom left part of the nanowire foot (region 1) then accumulated material until the gap was filled, explaining the defective interface with the final nanowire. We conclude that even though an unambiguous identification of the crystalline directions of a nanowire that has been removed from the substrate is not possible, a multiorder twinning process can explain the change in crystalline direction which is observed experimentally. More TEM images of other nanowire feet which show stacking defects nonperpendicular to the growth direction can be found in the Supporting Information.

We continue by exploring how the existence of tilted nanowires depends on the growth conditions. Figure 4a−e shows top view and cross-sectional SEM micrographs of samples that were grown under a V/III flux ratio of 4.3, 7.1, 13.5, 17.9, and 25, respectively. For this, the arsenic beam equivalent pressure (BEP) was changed as indicated in the figure, while all other growth conditions were kept constant. Figure 4a shows a high density of tilted nanowires for the lowest V/III ratio. A slightly lower density can be observed in Figure 4b. The sample in Figure 4c shows only very few tilted nanowires, and the two samples presented in Figure 4d,e show no tilted nanowires. To quantify our finding we counted the density of tilted nanowires and vertical nanowires. The percentage of tilted nanowires defined as p = tilted/(tilted + vertical) is presented in Figure 4f, showing a dramatic decrease of tilted nanowires with increasing V/III ratio. For each V/III ratio, several SEM micrographs with hundreds of nanowires were taken into account. The data represents the average and standard deviation of the nanowire density on different SEM images. The statistics also include a sample grown at a V/III ratio of 15, for which SEM micrographs will be presented as reference sample in Figure 6. One should note that with increasing V/III ratio also the optimal growth temperature slightly increases. For this study all samples were grown at a temperature of 530 °C and the analysis was done on the part of the wafer which showed the best nanowire homogeneity (i.e., the center for samples (a−c) and the edge for samples (d,e)). The change in nanowire morphology across the sample is related to a slight temperature gradient (~10 °C) due to the manipulator design in our MBE. The decrease in tilted nanowires reported here, however, is not related to the temperature; a higher growth temperature in fact favors the formation of tilted nanowires, as discussed in the Supporting Information. A strong dependence of the formation of tilted nanowires on the V/III ratio is in agreement with results observed in the literature, where nanowires are found to be all vertical for samples grown at high V/III ratio of 120, 200, or 320 (refs 28−30.), while some tilted nanowires are observed at a V/III ratio of 7−8 (ref 26.). One should note that the effective V/III ratio also depends on the growth temperature (due to re-evaporation from the substrate), explaining why no tilted nanowires are observed at a V/III ratio of 6.3 and a significantly lower growth temperature.[27] The V/III ratio dependence of the existence of tilted nanowires could be explained considering indium droplets as seed particles: A higher arsenic pressure leads to smaller indium seed droplets at the early stages of growth (or a complete absence of droplets), therefore avoiding the formation of additional {111} facets leading to a change of growth direction. This explanation implies that a catalyst droplet is present at the beginning of growth under low V/III ratio where tilted nanowires are observed, and absent (or significantly smaller) for nanowires grown at higher V/III ratios. Additionally, the existence of an elongated WZ section at the foot of nanowires grown at high V/III ratios (ref 25) may suppress 3D twinning, since the

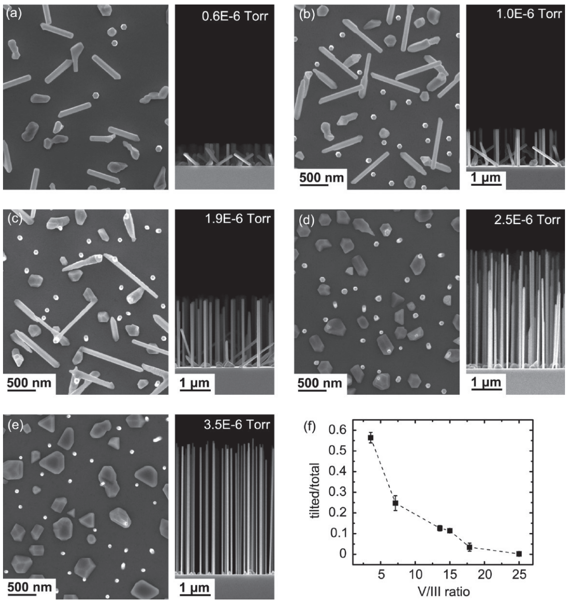

Figure 4. Arsenic dependence of the existence of tilted wires. (a−e) Top view and cross-sectional SEM micrographs of samples grown at a V/III ratio of 4.3, 7.1, 13.5, 17.9, and 25, respectively. (f) Percentage of tilted nanowires.

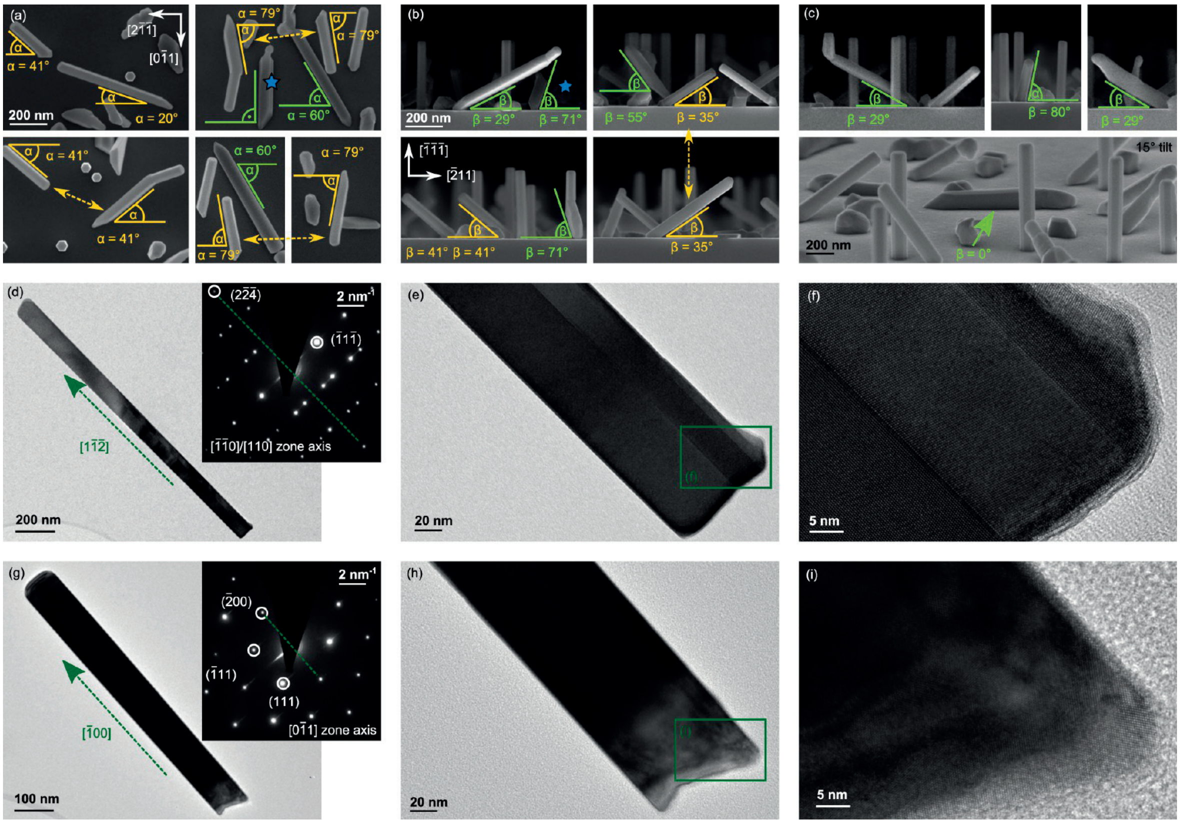

Figure 5. Detailed SEM and TEM analysis of a sample grown at a V/III ratio of 4.3. (a−c) Top view and cross-sectional SEM micrographs. Projection angles that can be explained by multiorder twinning are marked in yellow and other angles are marked in green. (d−f) TEM micrographs and SAED pattern of a nanowire growing in [1$\bar{1}\bar{2}$] direction. (g−i) TEM micrographs and SAED pattern of a nanowire growing in [$\bar{1}$00] direction.

formation of new ⟨111⟩B facets would be difficult in a hexagonal WZ seed crystal.

At very low V/III ratio we also observe projection angles that cannot be explained by multiple-order twinning. Figure 5 shows a more detailed SEM and TEM analysis of the sample presented in Figure 4a, which was grown at a V/III ratio of 4.3 (arsenic pressure of 6×10^{-7} Torr). Top-view SEM micrographs are presented in Figure 5a. We observe top-view projection angles of approximately 20°, 41°, 60°, 79°, and 90°. Projection angles of 60° and 90° (highlighted in green) cannot be explained by multiple-order twinning (see table with all projection angles of low-index crystalline orientations in Supporting Information). Orientations corresponding a projection angle of 60° and 90° could be in fact ⟨100⟩, ⟨110⟩, ⟨112⟩, and ⟨111⟩A growth directions. One should note that the calculation of projection angles also includes certain ⟨110⟩ and ⟨112⟩ directions which are found to be parallel to the substrate (crawling nanowires). Unfortunately, analyzing only top view angles is not conclusive, since many wire orientations show similar top view angles. In particular, the top view projection angles of ~20°, 41°, and 79° can result from both 3D twinned nanowires as well as ⟨112⟩ nanowires. In Figure 5a we highlighted a few nanowires that have the same projection angle but different morphologies/facets with arrows. This can be explained by different growth directions: while 3D twinned nanowires have a hexagonal shape with six {110} facets, ⟨112⟩ oriented nanowires are expected to have rectangular shape with two {110} and two {111} facets. Figure 5b,c shows cross-sectional SEM micrographs of the same sample. Here we observe projection angles of 0°, 29°, 35°, 41°, 55°, 71°, and 80°, where 0° corresponds to crawling wires as shown in the 15° tilted image. Comparing with the table of projection angles we find that (i) 35° and 41° can be explained by 3D twinning; (ii) 29°, 35°, 71°, and 80° would be consistent with ⟨112⟩ oriented nanowires; and (iii) 55° and 71° would agree with the projection of ⟨110⟩ oriented nanowires. The angles 29°, 55°, 71°, and 80° which are exclusive to ⟨110⟩ and ⟨112⟩ orientations are highlighted in green. Again, we also highlighted two nanowires with the same projection angle but clearly different faceting with an arrow. We also remark that a cross-sectional projection angle of 19° is not observed in any sample, indicating that ⟨$\bar{1}\bar{1}$1⟩A oriented nanowires are very rare or not present at all. This observation stands in contrast to the case of GaAs nanowires grown at very low V/III ratio, where a significant increase of A-polar wires was reported.[18] Figure 5d−i presents TEM micrographs of nanowires with unusual growth directions. Figure 5d shows a low resolution image and SAED pattern of the first nanowire. The SAED diffraction pattern shows zincblende stacking and two twin orientations which can be indexed assuming a [$\bar{1}\bar{1}$0] or [110] zone axis. By comparing the growth direction of the nanowire with the diffraction pattern, it can be observed that the nanowire axis corresponds

DOI: 10.1021/acs.cgd.7b00487
Cryst. Growth Des. 2017, 17, 3596−3605

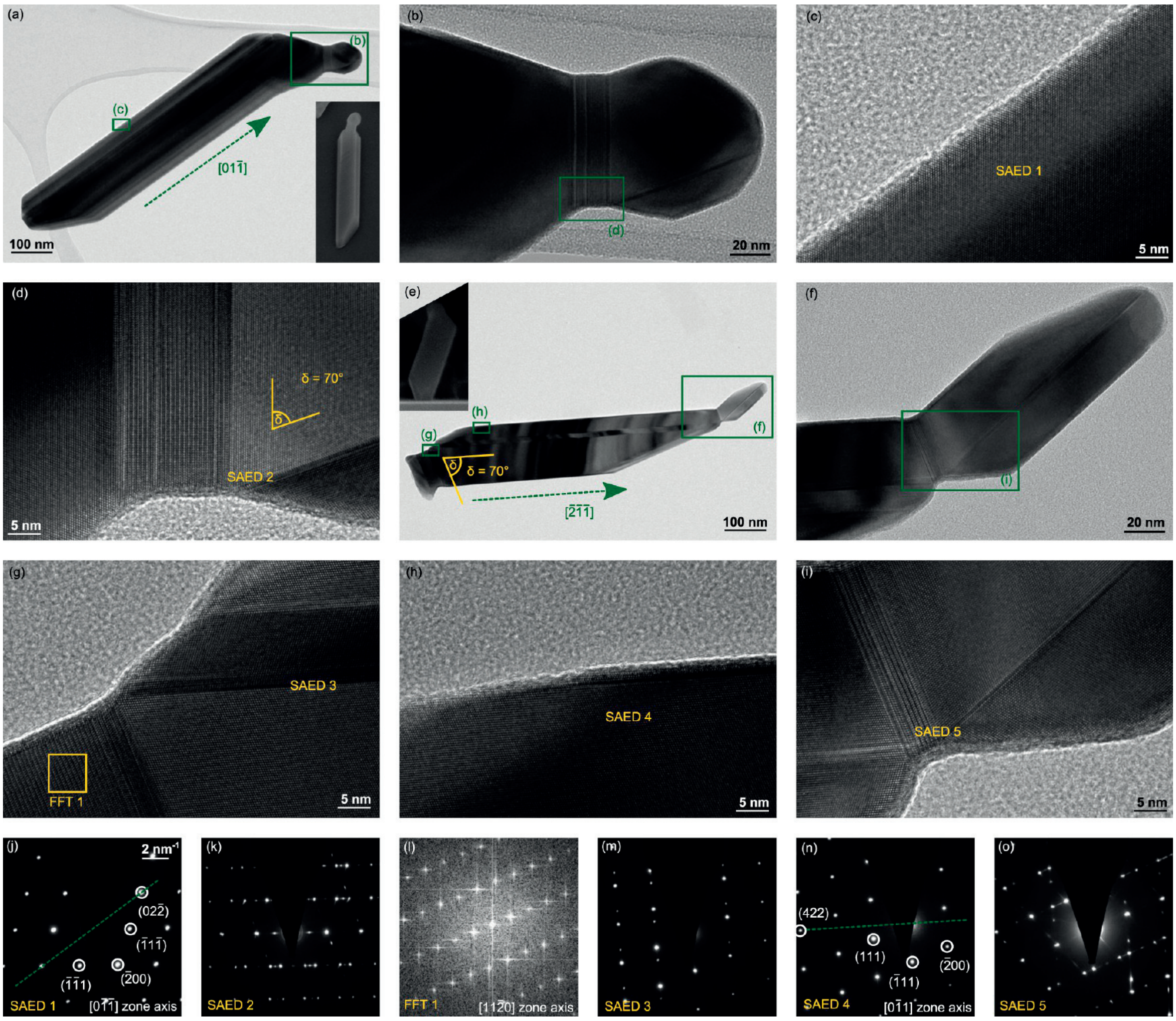

Figure 6. TEM analysis of nanowires with unusual morphology. (a–d) TEM micrographs of a nanostructure growing in [01$\bar{1}$] direction. Parts (j,k) present the corresponding diffraction images. (e–i) TEM micrographs of a nanostructure growing in the [$\bar{2}\bar{1}\bar{1}$] direction. The corresponding diffraction images are shown in (j–o).

to the [1$\bar{1}\bar{2}$] direction. Figure 5e,f shows a magnified image of the nanowire foot and a high-resolution TEM micrograph of the region indicated. The images show zincblende stacking with two rotation twins running along the nanowire (parallel to the growth axis). These longitudinal defects are characteristic for nanowires in the ⟨112⟩ direction.[16,31] TEM analysis of two more ⟨112⟩ oriented nanowires are presented in the Supporting Information. Figure 5g shows a low resolution TEM micrograph and SAED pattern of another nanowire. The diffraction pattern can be indexed assuming a [0$\bar{1}$1] zone axis and the nanowire growth direction therefore corresponds to the [$\bar{1}$00] direction. The expected rectangular shape of ⟨100⟩ nanowires explains why the nanowire appears very dark and no thinner region at the edges can be found. Figure 5h,i shows a magnified image and a high-resolution TEM micrograph of the foot of the nanowire, and confirms a defect-free zincblende crystal structure.

As seen from the SEM micrographs in Figure 5, nanowires in unusual orientations often show kinks and other changes in morphology. Figure 6 presents TEM micrographs of two nanowires showing an unusual morphology. Figure 6a shows a low magnification TEM micrograph of a nanowire resembling the morphology of the nanowire oriented in the [01$\bar{1}$] direction, which is marked with a star in the SEM image in Figure 5a. We observe a long defect-free part and then a change of direction and a small droplet. A magnified image of the tip region is shown in Figure 6b, showing a few defects at the interface. Figure 6c,d shows high-resolution TEM images of the defect-free nanowire and the defects at the tip. The SAED image of the defect-free region is presented in (j) and shows a pure ZB crystal structure which can be indexed assuming a [0$\bar{1}\bar{1}$] zone axis. We also present dashed lines corresponding to the direction of the nanowire both in the TEM micrograph and in the SAED image. From the SAED we observe that the nanowire direction is [01$\bar{1}$], which matches the direction observed in the SEM micrograph (it should be noted that this corresponds to a crawling nanowire). The defects near the tip can be identified as a few layers of WZ, and then the droplet

DOI: 10.1021/acs.cgd.7b00487
Cryst. Growth Des. 2017, 17, 3596–3605

itself shows a twin defect in a $\langle 111 \rangle$ direction at a 70° angle with respect to the WZ layers. The existence of the two polytypes and the rotational twin is confirmed by the SAED image shown in (k). Figure 6e shows a low magnification TEM micrograph of another nanowire, which resembles the small nanowire marked with a star in the background of the SEM image of Figure 5b. We observe a few defects at the foot of the nanowire and then an elongated section showing two defects parallel to the growth direction, and then a tip in a different direction. A magnified image of the tip region is presented in Figure 6f. Figure 6g–i shows high resolution TEM micrographs of the foot of the wire, the main part, and the transition to the tip. Figure 6g shows the foot of the nanowire and the beginning of the main part. We observe a few layers of WZ at the foot of the nanowire, which can also be seen in the FFT image in (l). The beginning of the main nanowire core shows ZB crystal structure with two twin defects, which can also be seen in the SAED image in (m). The main core of the nanowire is ZB as shown in (h) and the corresponding SAED shown in (n) can be indexed assuming a $[0\bar{1}1]$ zone axis. The dashed green line corresponds to the growth direction of the nanowire and can be found to be oriented in the $[\bar{2}11]$ direction. The transition to the tip (Figure 6i) shows again a few layers of WZ stacking and then a ZB region with a twin defect in the $\langle 111 \rangle$ direction at an angle of 70° with respect to the WZ layers. Figure 6o shows a SAED image of the whole tip region, showing diffraction spots from WZ stacking (very weak) as well as the ZB sections showing twins in two different directions. Summarizing the analysis in Figure 6, we find projection angles that can only be explained by $\langle 110 \rangle$ and $\langle 112 \rangle$ oriented nanowires, and TEM images support the existence of nanowires in those unconventional directions.

We have suggested the existence of the droplet at the beginning of growth as a possible explanation for formation of tilted nanowires. To study this hypothesis we investigate nanowire growth after the predeposition of indium droplets. For this, we first heat up and anneal a sample for 1 h at 480 °C under arsenic flux (as for standard samples). The arsenic valve is then closed and indium is deposited at the standard indium BEP of 1.4×10^{-7} Torr. Finally the sample is heated to the growth temperature of 530 °C and nanowires are grown for 1 h. As growth conditions we choose a relatively high V/III ratio of 15. Figure 7a shows a top view and cross-sectional SEM micrograph of a reference sample without indium predeposition, showing a very low density of tilted nanowires, as expected at high V/III ratio. Figure 7b shows a sample where indium was deposited for 3 min and then nanowire growth was started under identical growth conditions. A higher density of tilted nanowires can be observed, while the density of vertical nanowires dramatically decreases. The green arrow highlights a nanocross which was formed by merging of two tilted nanowires. Figure 7c shows a sample with a 10 min indium predeposition. Almost no vertical nanowires are found and only very few tilted nanowires. Instead the sample is covered with parasitic growth. In the inset, a top view SEM micrograph of a reference sample is presented, for which the process was stopped after the 10 min indium predeposition. We observe that the sample is covered with droplets, confirming that indium droplets can be formed under the conditions studied. Statistics on the percentage of tilted nanowires and the overall density are shown in Figure 7d. Our results show that predeposition of indium dramatically increases the occurrence of tilted nanowires, even under growth conditions for which normally only very few tilted nanowires are observed. This finding supports our hypothesis that the formation of tilted nanowires is related to the existence of an indium droplet at the beginning of growth. We can therefore conclude that under low V/III ratio nanowire growth starts with a droplet, while under high V/III ratio the droplet is significantly smaller or absent completely.

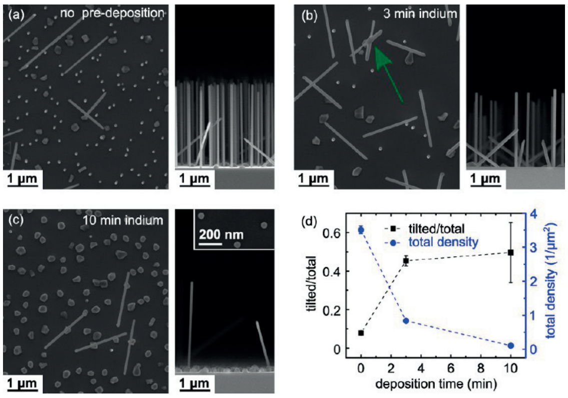

Figure 7. Nanowire samples grown at a V/III ratio of 15. (a) Top view and cross-sectional micrographs of a reference sample without indium deposition. (b,c) Samples with 3 and 10 min indium deposition, respectively. The inset in (c) shows a sample just after 10 min indium predeposition. (d) Statistics of the percentage of tilted nanowires and the nanowire density.

Finally, we also study the existence of tilted nanowires as a function of the growth temperature and the oxide thickness. All SEM micrographs and statistics can be found in Supporting Information. We find that increasing the growth temperature increases the ratio of tilted nanowires, which can be attributed to a change in effective V/III ratio, as mentioned above. With respect to the oxide thickness we find that a thicker oxide favors the formation of tilted nanowires. This result can be compared to the work by Matteini et al.,[24] where a thicker native silicon oxide was found to favor spilling of gallium droplets and therefore nucleation of tilted nanowires. Whether or not the explanation of the surface energy also applies in our case is subject to further investigation. Last but not least, we also note that incorporation of antimony suppresses the formation of tilted nanowires, as can be observed from the antimony series in ref 25. Considering that incorporation of antimony dramatically reduces the formation of rotational twins, this finding further supports the explanation of tilted nanowires due to 3D twinning.

■ CONCLUSION

In conclusion we presented a complete analysis of the existence of tilted InAs nanowires obtained without a foreign catalyst. Tilted nanowires are found to occur at specific angles, which can in most cases be explained by a 3D twinning process. At very low V/III ratio, also angles corresponding to $\langle 112 \rangle$ or other low-index orientations are found. TEM studies of both 3D twinned nanowires as well as nanowires growing in usual crystalline directions are presented. The formation of tilted nanowires depends on the growth conditions and on the substrate preparation. Most importantly we find that increasing the V/III ratio suppressed the formation of tilted nanowires almost completely. This result suggests that at low V/III ratios an indium droplet is present during the early stages of growth, allowing for the formation of different {111}B facets, while at high V/III ratio multiorder twinning is suppressed, possibly due to the absence of a catalyst droplet. Our results contribute to the understanding of the growth mechanism of InAs nanowires, and provide several pathways to achieve all vertical nanowires—which is an important requirement for the fabrication of devices where several nanowires are contacted in parallel as-grown on the substrate. Tuning the ratio of tilted nanowires also constitutes a pathway to make nanowire junctions and crosses, which are important building blocks for Majorana Fermion braiding.

■ ASSOCIATED CONTENT

Supporting Information

The Supporting Information is available free of charge on the ACS Publications website at DOI: 10.1021/acs.cgd.7b00487.

> Detailed explanation of 3D twinning, a complete table of projection angles, additional TEM analysis, and the study of growth temperature and oxide thickness (PDF)

■ AUTHOR INFORMATION

Corresponding Author

*E-mail: anna.fontcuberta-morral@epfl.ch.

ORCID

Anna Fontcuberta i Morral: 0000-0002-5070-2196

Author Contributions

H.P. and Y.v.H. grew the samples. Y.v.H. performed the quantitative analysis. H.P. performed the TEM analysis. H.P. and A.F.i.M designed the experiments. H.P., G.T., M.F., and J.-B.L. calibrated and maintained the MBE system. H.P. made the figures and artwork. H.P., Y.v.H., and A.F.i.M. wrote and edited the manuscript. All authors discussed the results and commented on the manuscript.

Notes

The authors declare no competing financial interest.

■ ACKNOWLEDGMENTS

The authors acknowledge the SNF for financial support via the project 200021_169908 and through the NCCR QSIT.

■ REFERENCES

(1) Mourik, V.; Zuo, K.; Frolov, S. M.; Plissard, S. R.; Bakkers, E. P. a M.; Kouwenhoven, L. P. Signatures of Majorana Fermions in Hybrid Superconductor-Semiconductor Nanowire Devices. *Science* **2012**, *336* (6084), 1003–1007.

(2) Das, A.; Ronen, Y.; Most, Y.; Oreg, Y.; Heiblum, M.; Shtrikman, H. Zero-Bias Peaks and Splitting in an Al–InAs Nanowire Topological Superconductor as a Signature of Majorana Fermions. *Nat. Phys.* **2012**, *8* (12), 887–895.

(3) Deng, M. T.; Yu, C. L.; Huang, G. Y.; Larsson, M.; Caroff, P.; Xu, H. Q. Anomalous Zero-Bias Conductance Peak in a Nb-InSb Nanowire-Nb Hybrid Device. *Nano Lett.* **2012**, *12* (12), 6414–6419.

(4) Brongersma, M. L.; Cui, Y.; Fan, S. Light Management for Photovoltaics Using High-Index Nanostructures. *Nat. Mater.* **2014**, *13* (5), 451–460.

(5) del Alamo, J. a. Nanometre-Scale Electronics with III–V Compound Semiconductors. *Nature* **2011**, *479* (7373), 317–323.

(6) Li, Y.; Qian, F.; Xiang, J.; Lieber, C. M. Nanowire Electronic and Optoelectronic Devices. *Mater. Today* **2006**, *9* (10), 18–27.

(7) Takei, K.; Takahashi, T.; Ho, J. C.; Ko, H.; Gillies, A. G.; Leu, P. W.; Fearing, R. S.; Javey, A. Nanowire Active-Matrix Circuitry for Low-Voltage Macroscale Artificial Skin. *Nat. Mater.* **2010**, *9* (10), 821–826.

(8) Dayeh, S. a.; Aplin, D. P. R.; Zhou, X.; Yu, P. K. L.; Yu, E. T.; Wang, D. High Electron Mobility InAs Nanowire Field-Effect Transistors. *Small* **2007**, *3* (2), 326–332.

(9) Plissard, S. R.; van Weperen, I.; Car, D.; Verheijen, M. a; Immink, G. W. G.; Kammhuber, J.; Cornelissen, L. J.; Szombati, D. B.; Geresdi, A.; Frolov, S. M.; Kouwenhoven, L. P.; Bakkers, E. P. a M. Formation and Electronic Properties of InSb Nanocrosses. *Nat. Nanotechnol.* **2013**, *8* (11), 859–864.

(10) Car, D.; Wang, J.; Verheijen, M. A.; Bakkers, E. P. A. M.; Plissard, S. R. Rationally Designed Single-Crystalline Nanowire Networks. *Adv. Mater.* **2014**, *26*, 4875–4879.

(11) Kang, J.-H.; Galicka, M.; Kacman, P.; Shtrikman, H. Wurtzite/Zinc-Blende "K"-Shape InAs Nanowires with Embedded Two-Dimensional Wurtzite Plates. *Nano Lett.* **2017**, *17* (1), 531–537.

(12) Fortuna, S. a; Li, X. Metal-Catalyzed Semiconductor Nanowires: A Review on the Control of Growth Directions. *Semicond. Sci. Technol.* **2010**, *25* (2), 24005.

(13) Yuan, X.; Caroff, P.; Wong-Leung, J.; Fu, L.; Tan, H. H. Tunable Polarity in a III-V Nanowire by Droplet Wetting and Surface Energy Engineering. *Adv. Mater.* **2015**, *27*, 6096–6103.

(14) Zamani, R. R.; Gorji Ghalamestani, S.; Niu, J.; Sköld, N.; Dick, K. A. Polarity and Growth Directions in Sn-Seeded GaSb Nanowires. *Nanoscale* **2017**, *9* (9), 3159–3168.

(15) Wang, J.; Plissard, S. R.; Verheijen, M. A.; Feiner, L. F.; Cavalli, A.; Bakkers, E. P. A. M. Reversible Switching of InP Nanowire Growth Direction by Catalyst Engineering. *Nano Lett.* **2013**, *13* (8), 3802–3806.

(16) Li, Z. A.; Möller, C.; Migunov, V.; Spasova, M.; Farle, M.; Lysov, A.; Gutsche, C.; Regolin, I.; Prost, W.; Tegude, F. J.; Ercius, P. Planar-Defect Characteristics and Cross-Sections of < 001>, < 111>, and < 112> InAs Nanowires. *J. Appl. Phys.* **2011**, *109* (11), 114320.

(17) Conesa-Boj, S.; Kriegner, D.; Han, X.-L.; Plissard, S.; Wallart, X.; Stangl, J.; Fontcuberta i Morral, A.; Caroff, P. Gold-Free Ternary III-V Antimonide Nanowire Arrays on Silicon: Twin-Free down to the First Bilayer. *Nano Lett.* **2014**, *14* (1), 326–332.

(18) Zamani, M. Growth and Characterization of high-quality GaAs nanowires; Master Thesis; Polytecnico di Milano, 2016.

(19) Potts, H.; Morgan, N. P.; Tütüncüoglu, G.; Friedl, M.; Morral, A. F. i. Tuning Growth Direction of Catalyst-Free InAs(Sb) Nanowires with Indium Droplets. *Nanotechnology* **2017**, *28* (5), 54001.

(20) Li, B.; Yan, X.; Zhang, X.; Ren, X. Self-Catalyzed Growth of InAs Nanowires on InP Substrate. *Nanoscale Res. Lett.* **2017**, *12* (1), 34.

(21) Uccelli, E.; Arbiol, J.; Magen, C.; Krogstrup, P.; Russo-averchi, E.; Heiss, M.; Mugny, G.; Nyg, J.; Morante, J. R.; Fontcuberta, A. Three-Dimensional Multiple-Order Twinning of Self-Catalyzed GaAs Nanowires on Si Substrates. *Nano Lett.* **2011**, *11*, 3827–3832.

(22) Fonseka, H. A.; Caroff, P.; Wong-Leung, J.; Ameruddin, A. S.; Tan, H. H.; Jagadish, C. Nanowires Grown on InP (100): Growth Directions, Facets, Crystal Structures, and Relative Yield Control. *ACS Nano* **2014**, *8* (7), 6945–6954.

(23) Matteini, F.; Tutuncuoglu, G.; Potts, H.; Jabeen, F.; Fontcuberta i Morral, A. Wetting of Ga on SiOx and Its Impact on GaAs Nanowire Growth. *Cryst. Growth Des.* **2015**, *15*, 3105.

(24) Matteini, F.; Tutuncuoglu, G.; Mikulik, D.; Vukajlovic-Plestina, J.; Potts, H.; Leran, J. B.; Carter, W. C.; Morral, A. F. Impact of the Ga Droplet Wetting, Morphology, and Pinholes on the Orientation of GaAs Nanowires. *Cryst. Growth Des.* **2016**, *16* (10), 5781–5786.

(25) Potts, H.; Friedl, M.; Amaduzzi, F.; Tang, K.; Tütüncüoglu, G.; Matteini, F.; Alarcon Lladó, E.; McIntyre, P. C.; Fontcuberta I Morral, A. From Twinning to Pure Zincblende Catalyst-Free InAs(Sb) Nanowires. *Nano Lett.* **2016**, *16* (1), 637–643.

(26) Grap, T.; Rieger, T.; Blömers, C.; SchäPers, T.; Grützmacher, D.; Lepsa, M. I. Self-Catalyzed VLS Grown InAs Nanowires with Twinning Superlattices. *Nanotechnology* **2013**, *24* (33), 335601.

(27) Hertenberger, S.; Rudolph, D.; Bolte, S.; Döblinger, M.; Bichler, M.; Spirkoska, D.; Finley, J. J.; Abstreiter, G.; Koblmüller, G. Absence of Vapor-Liquid-Solid Growth during Molecular Beam Epitaxy of Self-

Induced InAs Nanowires on Si. *Appl. Phys. Lett.* **2011**, *98* (12), 123114.

(28) Dimakis, E.; Lahnemann, J.; Jahn, U.; Hilse, M.; Geelhaar, L. Self-Assisted Nucleation and Vapor-Solid Growth of InAs Nanowires on Bare Si (111). *Cryst. Growth Des.* **2011**, *11*, 4001−4008.

(29) Kang, J.-H.; Ronen, Y.; Cohen, Y.; Convertino, D.; Rossi, A.; Coletti, C.; Heun, S.; Sorba, L.; Kacman, P.; Shtrikman, H. MBE Growth of Self-Assisted InAs Nanowires on Graphene. *Semicond. Sci. Technol.* **2016**, *31* (11), 115005.

(30) Madsen, M. H.; Aagesen, M.; Krogstrup, P.; Sørensen, C.; Nygård, J. Influence of the Oxide Layer for Growth of Self-Assisted InAs Nanowires on Si(111). *Nanoscale Res. Lett.* **2011**, *6* (1), 516.

(31) Oliveira, D. S.; Tizei, L. H. G.; Li, A.; Vasconcelos, T. L.; Senna, C. A.; Archanjo, B. S.; Ugarte, D.; Cotta, M. A. Interaction between Lamellar Twinning and Catalyst Dynamics in Spontaneous Core−shell InGaP Nanowires. *Nanoscale* **2015**, *7* (29), 12722−12727.

DOI: 10.1021/acs.cgd.7b00487
Cryst. Growth Des. 2017, 17, 3596−3605

4.3 Tuning nanowire growth direction

While some applications require all vertical nanowires, other applications e.g. quantum computation based on Majorana Fermions require the possibility to create nanowire networks, as discussed in section 2.4. Different approaches have been used to create nanowire junctions and networks, including growth from pyramids and groves which have {111} facets [Rieger16, Heedt16], and a change in direction during nanowire growth [Plissard13, Car14]. The first approach allows to create a high density of nanowire junctions, but it requires an additional substrate preparation step in order to produce the pyramids or groves. Changing direction during growth, on the contrary, does not require substrate processing. However the first results were based on manipulation of the gold catalyst participle, and therefore it is not clear to which extend this avenue works for self-catalyzed or even catalyst-free nanowires.

In this publication we studied the possibility to change growth direction of InAs nanowires grown without a foreign catalyst. In particular we found that indium droplets can be created by annealing of InAs nanowires under vacuum. The size of the droplets increases with time and the droplets, which are first created on the top facet of the nanowires, slide down onto the side facets once they exceed a certain size. The indium droplets can be used to initiate growth, and the growth continues in the direction of the droplet position. This results in nanowires that are vertical or L-shaped depending on the annealing time. The L-shaped nanostructures are interesting for the creation of nanowire networks. The vertical nanowires are also interesting, since they were grown following the VLS growth mechanism - at least for the first couple of nanometers. As discussed in 2.2, there is an extensive debate about the growth mechanism of InAs nanowires without a foreign catalyst. And it has also been reported that the presence of an indium droplet would favour the growth of defect-free crystals [Biermanns14]. Analyzing the vertical nanowires that were grown after droplet formation, we often find a thin section of defect-free zinc-blende within the otherwise polytypic crystal structure. This suggests that 1) the existence of a droplet is indeed related to a suppression of stacking defects, and 2) the droplet is readily consumed and the standard nanowire growth proceeds via the VS mechanism. Unfortunately, a direct observation of the growth mechanism and crystal structure would still require in-situ measurements. The full analysis is presented in the publication below. We furthermore also studied the droplet formation using $\mathrm{InAs}_{1-x}\mathrm{Sb}_x$ nanowires, and studied deposition of indium onto existing nanostructures. The latter could be used as an avenue to create heterostructures.

Reprinted with permission from H. Potts *et al.* Tuning growth direction of catalyst-free InAs(Sb) nanowires with indium droplets. *Nanotechnology* **28**, 054001 (2017). Ⓒ 2017 IOP Publishing.

IOP Publishing Nanotechnology
Nanotechnology 28 (2017) 054001 (9pp) doi:10.1088/1361-6528/28/5/054001

Tuning growth direction of catalyst-free InAs(Sb) nanowires with indium droplets

Heidi Potts, Nicholas P Morgan, Gözde Tütüncüoglu, Martin Friedl and Anna Fontcuberta i Morral[1]

Laboratoire des Matériaux Semiconducteurs, École Polytechnique Fédérale de Lausanne, 1015 Lausanne, Switzerland

E-mail: anna.fontcuberta-morral@epfl.ch

Received 2 October 2016, revised 16 November 2016
Accepted for publication 29 November 2016
Published 23 December 2016

Abstract

The need for indium droplets to initiate self-catalyzed growth of InAs nanowires has been highly debated in the last few years. Here, we report on the use of indium droplets to tune the growth direction of self-catalyzed InAs nanowires. The indium droplets are formed *in situ* on InAs(Sb) stems. Their position is modified to promote growth in the ⟨11–2⟩ or equivalent directions. We also show that indium droplets can be used for the fabrication of InSb insertions in InAsSb nanowires. Our results demonstrate that indium droplets can initiate growth of InAs nanostructures as well as provide added flexibility to nanowire growth, enabling the formation of kinks and heterostructures, and offer a new approach in the growth of defect-free crystals.

S Online supplementary data available from stacks.iop.org/NANO/28/054001/mmedia

Keywords: nanowire, InAs, catalyst-free growth, molecular beam epitaxy, growth direction

(Some figures may appear in colour only in the online journal)

Introduction

InAs and InSb nanowires offer an interesting platform for fundamental studies and electronic applications [1–8]. For high performance devices it is important to achieve high material purity, a defect-free crystal structure [9], and flexibility in terms of dimensions, morphology and growth direction [10, 11]. High purity nanowires can be obtained by molecular beam epitaxy (MBE) without a foreign catalyst, thereby avoiding the risk of impurity incorporation related to the catalyst particle [12, 13]. However, a challenge remains concerning the presence of stacking defects in self-catalyzed InAs nanowires [14, 15]. One pathway towards defect-free crystals is the growth of ternary nanowires, as recently demonstrated by the growth of $InAs_{1-x}Sb_x$ nanowires [16, 17]. Another approach to obtain defect-free nanowires would include a change of polarity [18] or growth direction [19], since the typical stacking defects observed in III–V nanowires are related to the formation of {111}B planes [20]. In the case of InP nanowires, different crystalline growth directions have been achieved by engineering the gold catalyst [21–25], or by spontaneous kinking in the case of self-catalyzed nanowires [26]. The resulting wires in ⟨100⟩ directions are defect-free [23]. Other directions, such as ⟨112⟩ exhibit twin planes non-perpendicular to the nanowire axis [20, 27]. The change in growth direction is not only relevant to suppress stacking defects, but also facilitates the integration with CMOS platforms where (100) wafers are typically used. Furthermore, *in situ* engineering of the droplet has opened many more perspectives, such as the growth of novel nanostructures, including nano-sheets [28–31] and nano-crosses [10, 32]. Branched nanostructures have received considerable attention as building blocks for braiding of Majorana Fermions [33]. In the case of self-catalyzed nanostructures droplet engineering is more difficult, and to the best of our knowledge, only one group has reported an *in situ* change of growth direction. In that work, branched GaAs nanowires were obtained by the accumulation of gallium on an InAs quantum dot on the nanowire side facet [34]. For InAs nanowires changing the growth direction by droplet engineering is particularly challenging, since there is still a debate as to whether InAs nanowires grow with or without an

---

[1] Author to whom any correspondence should be addressed.

indium droplet [14, 15, 35]. Catalyst-free growth of InAs nanowires along the ⟨100⟩ direction can be forced by using SiO_2 nanotube templates, although this strategy does not prevent the formation of stacking defects [36]. As far as we know, template and catalyst-free InAs nanowires have so far been limited to the ⟨111⟩B growth direction, and no *in situ* change of growth direction has been demonstrated yet.

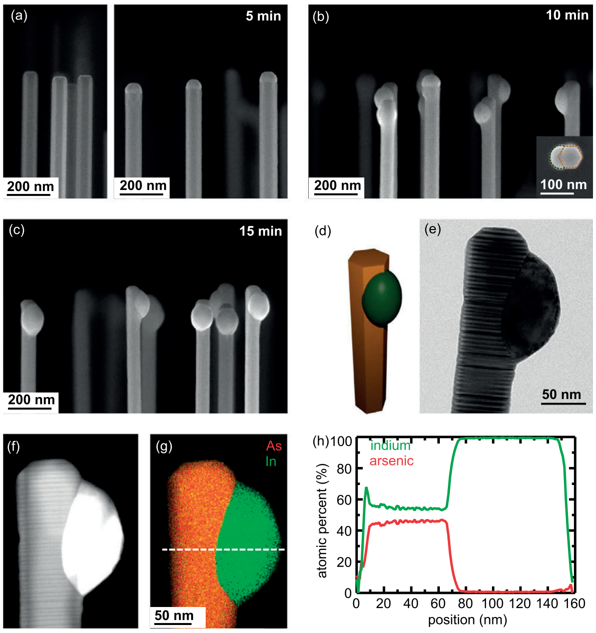

Figure 1. Droplet formation by annealing of InAs nanowires. (a) Cross sectional SEM micrographs of a standard InAs nanowire sample and after annealing for 5 min (b), (c) Nanowire samples which have been annealed for 10 min, and 15 min respectively. Droplets are formed on the top facet of the nanowires and then slide down onto two of the {1–10} facets when the droplets increase in size. Insert in (b) shows a top view SEM of a nanowire and droplet. (d) Schematic representation of the droplet position. (e) TEM micrograph of the tip of a nanowire with a droplet. (f), (g) STEM-HAADF image and EDX map of the same nanowire. (h) Elemental composition along the line indicated in (g), showing that the droplet is almost pure indium.

Results and Discussion

In this work, we demonstrate that indium droplets can initiate and modify the growth direction of self-catalyzed InAs nanowires, even though in the typical growth regime indium droplets might not be present. Indium droplets are obtained either by annealing nanowires in vacuum or by direct deposition on the nanowires. We investigate the behavior of both InAs and InAsSb nanowires, and demonstrate that the indium droplet size and position can be tuned by changing the annealing time. The indium droplets can then be used as seeds to continue nanowire growth, thereby enabling the growth of L-shaped InAs nanostructures (‘nano hockey sticks’) as well as axial changes in composition. The L-shaped structures are particularly interesting because they give access to self-catalyzed InAs nanostructures grown in ⟨11–2⟩ directions which adopt the crystal structure of the ⟨–1–1–1⟩ oriented host nanowire. In the case of pure InAs nanowires as a starting point, the resulting branches show stacking defects parallel to the growth direction. In the case of InAsSb nanowire host structures, branches with a very low defect density can be obtained.

We start by explaining the formation of indium droplets upon annealing of InAs nanowires. InAs nanowires are grown on GaAs(111)B substrates covered with 4.5 nm of HSQ oxide using a DCA P600 MBE system (more information about the nanowire growth can be found in [16]). After nanowire growth, all sources (In, As) are closed and the sample is kept at the growth temperature (530 °C) for a varying amount of time. We observe that arsenic evaporates at a higher rate compared to indium, as expected from the difference in vapor pressures. Since {111}B facets are thermally less stable than {110} facets, the evaporation occurs predominantly at the top facet of the nanowire, leading to the formation of an indium droplet on top of the wire. Representative scanning electron micrographs of the nanowires directly after growth and after being annealed for 5, 10 and 15 min are shown in figure 1. The indium droplets grow in size when increasing the annealing time, and slide down onto the side facets of the nanowire (figures 1(b), (c)) once they exceed a critical size. No significant change in diameter of the wires is observed as a function of the annealing time. This confirms that evaporation occurs mostly from the top facet and is negligible on the side facets, as opposed to what is observed in GaAs [37]. The droplets are located on the corner between two {1-10} facets and stay close to the tip of the nanowire as shown in the 3D schematic in figure 1(d). The pinning near the nanowire tip would be in agreement with the results on gold-catalyzed InSb nanosails [28], where it has been reported that a defect-free crystal structure allows for the droplet to slide down, while stacking defects cause pinning of the droplet. In our case the host InAs nanowire shows a high density of stacking defects, as shown in the high resolution transmission electron micrograph (TEM) in figure 1(e), therefore pinning the droplet near the nanowire tip. The indium droplet is found to be amorphous after cooldown. We further performed energy dispersive x-ray spectroscopy (EDX) in a scanning TEM to study the elemental composition of the droplet. Figures 1(f), (g) shows a high angular annular dark field image of a nanowire tip with a droplet, and an elemental map showing arsenic in red and indium in green. A linescan of the composition along the white dashed line is presented in figure 1(h). The indium content is slightly above 50% on the nanowire. This suggests that a small layer of indium may accumulate at the nanowire surface. The formation of an indium droplet upon annealing of the nanowires in vacuum is also a critical point when discussing the exact growth mechanism (vapor–liquid–solid or vapor–solid) of InAs nanowires: the presence of an indium droplet is not necessarily related to vapor–liquid–solid since it can also be formed if the arsenic cell is closed before sufficient cooling of the nanowires.

Since the formation of a droplet depends on the preferred evaporation of arsenic at the nanowire tip, the question arises,

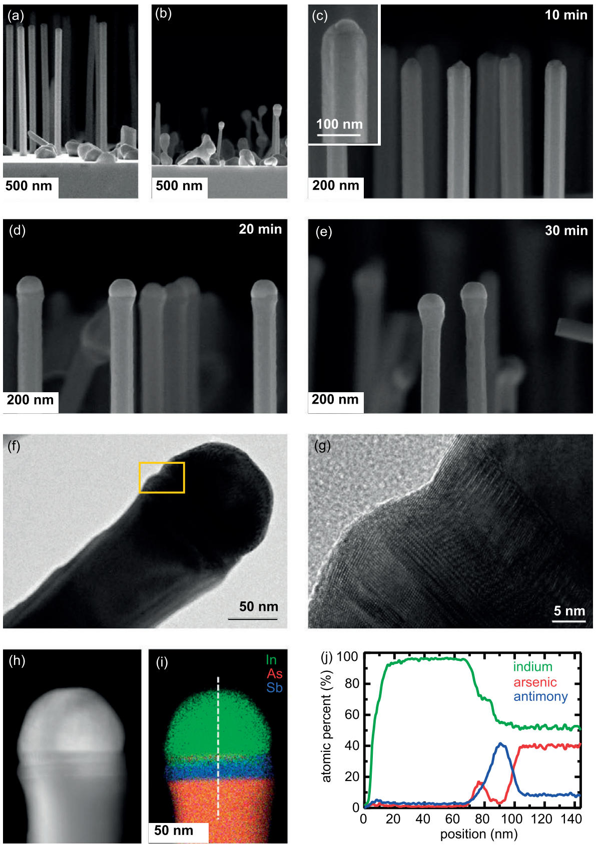

Figure 2. Droplet formation by annealing of InAsSb nanowires. (a) Standard InAsSb sample without annealing. (b) Nanowire sample which has been annealed for 10 min at 530 °C. (c)–(e) Nanowire samples which have been annealed at 500 °C for 10 min, 20 min, and 30 min respectively. (f), (g) TEM micrographs of a nanowire with a droplet, showing an interference pattern due to crystals with a different lattice constant. (h), (i) STEM-HAADF image and EDX map of the same nanowire. (j) Elemental composition along the line indicated in (i), showing an InSb section between the InAsSb wire and the indium droplet.

how does this effect change in ternary materials (with two group V elements)? We chose to study InAsSb nanowires with an antimony content of approximately 20%. The growth conditions and crystal structure analysis of InAsSb nanowires can be found in [16]. Figure 2(a) shows an SEM micrograph of an InAsSb nanowire sample before annealing. Similar to pure InAs nanowires, no droplet can be observed on the tip of standard InAsSb nanowires. Figure 2(b) shows an InAsSb sample which was annealed at 530 °C for 10 min, in conditions similar to those that were found to lead to droplet formation for pure InAs nanowires. We observe that InAsSb is more sensitive to temperature; the nanowires evaporate at a much higher rate and the nanowire forest almost disappears, leaving indium droplets and crystallites on the substrate. Lowering the evaporation temperature by 30 °C allows to form droplets on InAsSb nanowires. Figures 2(c)–(e) corresponds to SEM micrographs of samples annealed for 10, 20 and 30 min at 500 °C. The droplet size increases at the beginning, but then stays constant after a certain time. The droplets do not slide down and instead the evaporation takes place mostly from the side facets, resulting in thinner nanowires with tapering towards the droplet. It is as if the droplet formed at the tip protects the top facet from evaporating further. Figures 2(f), (g) shows high resolution TEM investigations after cooldown. A Moiré pattern between the nanowire and the droplet is observed, suggesting an overlap of materials with a different lattice constant. STEM and EDX analysis of the nanowire tip and droplet are illustrated in figures 2(h)–(j). This analysis reveals the formation of a thin section of InSb just below a predominantly indium droplet. An InSb section is present in all annealed InAsSb samples (more details in supporting information). Since an InSb section is not observed in any as-grown nanowire sample, we assume that it is formed during cooldown; at the annealing temperature, the droplet consists of indium and antimony. During cooldown, the solubility of antimony in the indium droplet decreases, leading to a crystallization of InSb. We note that our results are qualitatively similar to the case of self-catalyzed GaAsSb nanowires, where a thin GaSb section has been reported [38]. A back-of-the-envelope calculation was done to estimate the amount of antimony dissolved in the indium droplet before cooldown. Assuming that the number of antimony atoms corresponds to the InSb section of 19 ± 5 nm in height, we get an antimony concentration of 15 ± 4% in the indium droplet before cooldown. This value is comparable with self-catalyzed InSb nanowires grown by MOVPE, where an antimony concentration of up to 20% was measured in the droplet [39].

We turn now to the use of indium droplets as seed particles to drive InAs nanowire growth in new growth directions. After growing the InAs nanowires, we anneal them to form the indium droplets at the top or side facets of the nanowires, and then continue growth. For the second part of the growth we use typical InAs nanowire growth conditions in terms of substrate temperature and indium flux (530 °C and 1.4×10^{-7} Torr indium beam equivalent pressure (BEP)), while the arsenic BEP is lower and was varied between 2.5 and 7×10^{-7} Torr. Figures 3(a)–(c) show representative SEM micrographs of InAs samples annealed for 5 min, 10 min and 15 min which were then subjected to further InAs growth (1 h) at an arsenic BEP of 5×10^{-7} Torr. Figure 3(a) shows that after only 5 min annealing, growth mainly continues in the original $\langle -1-1-1 \rangle$ nanowire growth direction (the expected droplet position is marked with a dashed line). After 10 min annealing we observe the growth of L-shaped structures as shown in figure 3(b). Those structures are always perpendicular to the host nanowire, similar to the results by Suyatin *et al*, where kinked InAs nanowires were grown by a second gold deposition step and chemical beam epitaxy [40]. In figure 3(b) we also note that not all the wires form branches, as some wires also continue growing in the axial direction. We attribute this variation of shapes to the presence of indium droplets both at the nanowire tip and side facets after 10 min annealing. Growth after 15 min annealing results in 100% L-shaped nanostructures. This is in agreement with the 100% yield of droplet formation at the intersection of two nanowire side facets. It can therefore be concluded that the

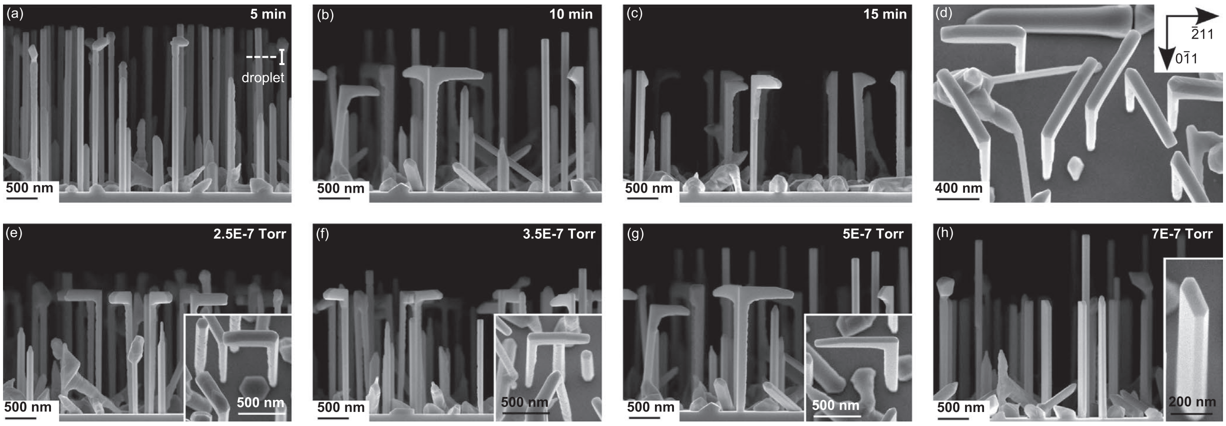

Figure 3. Growth of L-shaped InAs nanostructures. (a)–(c) Cross sectional SEM micrographs of InAs nanowire samples that have been annealed for 5 min, 10 min and 15 min respectively. The growth of the branch was performed under 5×10^{-7} Torr arsenic flux for 1 h. We observe that the growth direction after annealing is determined by the droplet position. (d) Top view image (15° tilted) of the sample which was annealed for 10 min, showing the crystalline direction of the branches. (e)–(h) Cross sectional SEM micrographs and top view images (15° tilted) of nanowire samples that have been annealed for 10 min and growth was re-initiated under an arsenic BEP of 2.5×10^{-7} Torr, 3.5×10^{-7} Torr, 5×10^{-7} Torr, and 7×10^{-7} Torr, respectively. We observe that growth in $\langle 11\text{–}2 \rangle$ direction is favored at low arsenic pressure, while flat nanostructures are observed at high arsenic pressure.

droplets act as seed particles to re-initiate growth following the vapor–liquid–solid (VLS) mechanism. At this point it is still unclear how long the droplet survives and whether or not the mechanism changes to vapor–solid (VS). Figure 3(d) shows a top view image (15° tilted) of the sample presented in (b). It can be observed that the growth direction of the L-shaped structures corresponds to one of the $\langle 11\text{–}2 \rangle$ directions, being in agreement with the positioning of the indium droplets at the corners between two $\{110\}$ facets. Interestingly the $\langle 11\text{–}2 \rangle$ direction is also the growth direction for which the growth of membranes and nanowires with elongated cross sections is possible in the case of GaAs in patterned silicon dioxide on GaAs(111)B [41, 42].

We will now discuss the role of the arsenic flux in the growth of $\langle 11\text{–}2 \rangle$ oriented nanostructures. In figures 3(e)–(h) we provide SEM micrographs of samples grown with an increasing value of arsenic BEP, after annealing the InAs stems for a duration of 10 min. The exact values of arsenic BEP are 2.5×10^{-7} Torr, 3.5×10^{-7} Torr, 5×10^{-7} Torr, and 7×10^{-7} Torr for samples (e)–(h), respectively (note that (b) and (g) are the same sample). We observe that increasing the arsenic flux significantly increases the growth both in the $\langle -1-1-1 \rangle$ direction for the linear nanowires and in the $\langle 11\text{–}2 \rangle$ direction for the L-shaped nanostructures (figures 3(e)–(g)). For very high arsenic flux growth in the $\langle 11\text{–}2 \rangle$ direction stops to be favorable, and nanowires with elongated cross sections are observed as shown in figure 3(h). Note that the threshold is lower than the arsenic BEP which is used for the growth of typical InAs nanowires (1.9×10^{-6} Torr). Time series reveal that the flat membranes form gradually; it is as if the droplets favor growth on the side facet they were initially sitting on (more information available in supporting information). The observed mechanism stands in contrast to gold catalyzed nanowires, for which flat nanowires were reported due to a downward movement of the catalyst particle [43].

In figure 4 we show how re-initiating growth with an indium droplet affects the crystal structure. Previously it has been suggested that the presence of liquid indium could favor the growth of defect-free Wurtzite [44], and it has been demonstrated that controlling the droplet is crucial for the growth of defect-free GaAs nanowires [45, 46]. We start by analyzing the crystal structure of the L-shaped nanostructures. An SEM micrograph of the sample is shown in figure 4(a). Figures 4(b), (c) show a low resolution TEM micrograph and the corresponding diffraction pattern of an InAs branch. High resolution TEM micrographs of different parts of the sample are shown in figures 4(d), (e). We observe that the crystal structure is polytypic, as is commonly observed for self-catalyzed InAs nanowires. Twins form perpendicular to the nanowire axis, as is also commonly observed for nanowires grown in the $\langle 111 \rangle$ direction [20]. Comparing a high-resolution TEM micrograph of the corner (figure 4(d)) with the end of the branch (figure 4(e)) we observe that the defects of the host nanowire propagate all along the horizontal part, being parallel to the growth direction. The $\langle 11\text{–}2 \rangle$ oriented part of the L-shaped structure therefore adopts the polytypic crystal structure from the host InAs nanowire. This observation stands in contrast to the work by Plissard *et al* [10], where the horizontal InSb nanowire has no epitaxial relation with the InP nanowire stem. We also study the crystal structure of the sample shown in figure 4(f), where the growth continues in axial direction. Figures 4(g), (h) show a low resolution TEM micrograph and the corresponding diffraction pattern. We observe that the general crystal structure is polytypic. However, in many wires we observe a thick pure zinc blende (ZB) section 800 nm below the tip of the nanowire, as shown in figures 4(i), (j). The location of the pure ZB region corresponds approximately to the expected position where the growth was re-initiated after the droplet formation. Since the existence of a pure ZB region in the middle of the

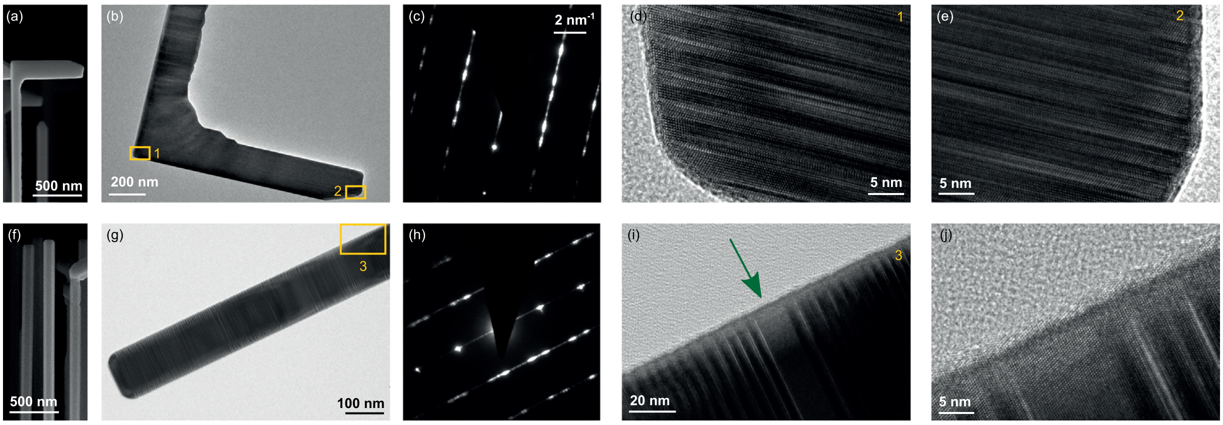

Figure 4. Crystal structure of InAs nanostructures grown with a droplet. (a) SEM micrograph of an L-shaped nanostructure. (b)–(e) TEM micrographs showing that the branch adopts the polytypic crystal structure of the InAs host nanowire. (f) SEM micrograph of an InAs nanowire sample where the upper part of the nanowire was grown after droplet formation (g)–(j) TEM micrographs showing the polytypic crystal structure with a pure ZB section of 10 nm.

polytypic InAs crystal structure is very unusual, we attribute it to the effect of the indium droplet and the VLS growth mechanism. After the pure ZB section the nanowire continues with the standard polytypic crystal structure, suggesting that the droplet is readily consumed and the growth proceeds droplet-free. Comparing our results to the findings of Biermanns *et al* [44], we agree that the existence of an indium droplet supports the suppression of twinning defects. One should note, however, that in our case the resulting crystal structure is ZB, while the original paper reported on wurtzite (WZ) stacking.

We go now a step further in the fabrication of hierarchical structures, and investigate the formation of droplets when annealing L-shaped nanostructures. Figure 5(a) shows a sample which has been annealed for 10 min at 530 °C. Different positions of the indium droplets can be observed. Figures 5(b)–(e) shows a sample where growth was re-initiated after the second droplet formation step. Different nanostructure shapes can be observed, including thicker L-shaped structures, longer branches, and nano-bridges. The nano-bridges are particularly interesting since the second 'leg', which is formed after the second annealing step, grows in $\langle 111 \rangle$A direction. A-polar growth is very untypical for self-catalyzed arsenide nanowires, and has only recently been observed in the case of InAs growing around Si/SiO_2 nanotubes [47]. Our results confirm that it is possible under certain conditions. A low resolution TEM micrograph of a nano-bridge is shown in figure 5(f). A high resolution TEM micrograph of the host nanowire is presented in figure 5(g), showing the standard polytypic crystal structure. In the high resolution TEM micrograph of the second 'leg' (figure 5(f)) we can observe a 20 nm thick pure ZB region. We attribute this pure phase section to the presence of a droplet when re-initiating growth. The rest of the second leg shows polytypism, similar to standard InAs nanowires. Please note that nano-bridges can also be formed when two L-shaped nanostructures merge during growth. However, in such a case the crystal structure of the horizontal part is not continuous (more details in supporting information). We conclude that the annealing and re-initiation process can be repeated multiple times in order to grow more sophisticated hierarchical structures. Further research is necessary to achieve control over the droplet position during consecutive annealing steps.

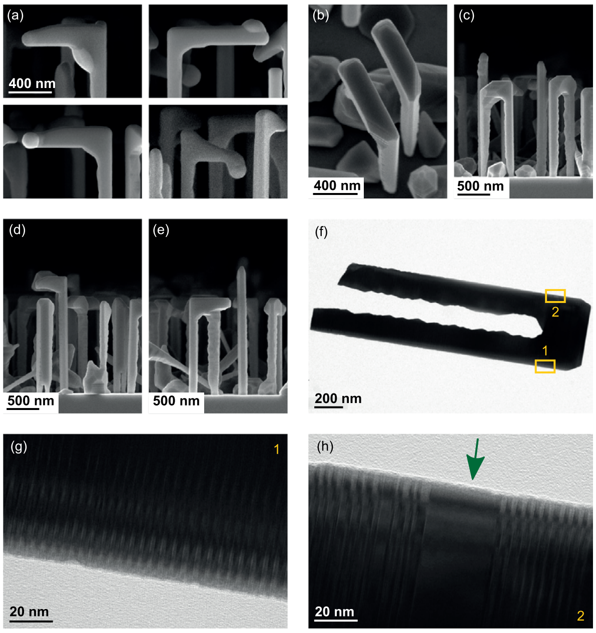

Figure 5. Droplet formation and growth re-initiation on L-shaped nanostructures. (a) Cross sectional SEM micrographs of a sample after annealing, showing different droplet positions on the L-shaped nanostructures. (b)–(e) Top view (15° tilt) and cross sectional SEM micrographs of a sample which was first annealed and then had growth continue to form a variety of different nanostructure shapes. (f)–(h) TEM micrographs of a nano-bridge. Both legs have a similar polytypic crystal structure. The upper leg, which was grown after the second droplet formation, shows a 20 nm pure ZB insertion.

Next we present re-initiation of InAs growth in the case of InAsSb nanowires after droplet formation. We have seen

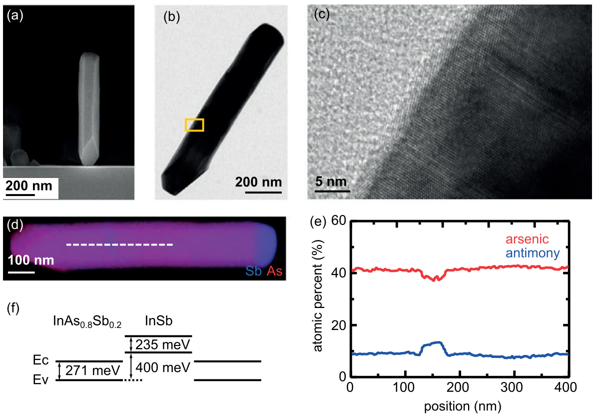

Figure 6. Growth of an InSb insertion in an InAsSb nanowire. (a) SEM micrograph of a nanowire sample which has an embedded InSb region. (b), (c) TEM micrographs showing the change in crystal structure due to the InSb section. (d), (e) EDX map and linescan confirmation of the existence of an InSb region. (f) Band alignment of the InSb section embedded in InAsSb at 4 K.

that in this case the droplet forms at the nanowire tip. When re-initiating growth after droplet formation all nanowires continue to grow vertically. Interestingly, no InSb section can be observed at the interface between InAsSb and InAs, suggesting that the InSb is formed during cooldown (more information is available in the supporting information). In order to grow InSb sections embedded in InAsSb samples we therefore investigate nanowire growth with a cooldown step after droplet formation. Figure 6(a) shows an SEM micrograph of a nanowire sample which was first annealed in order to form a droplet, then cooled down to form an InSb section and then overgrown with InAsSb. TEM micrographs of the sample are shown in figures 6(b), (c). We can observe a change in crystal structure within the otherwise defect-free InAsSb nanowire. The EDX map and linescan shown in figures 6(d), (e) confirm the existence of an InSb section of approximately 20 nm in length and 70 nm in diameter. The band alignment of an InSb section within $InAs_{0.8}Sb_{0.2}$ is shown in figure 6(f). The bandgap energy and band offset was calculated using the bowing parameters of [48]. We suggest that the InSb insertion can be used as a quantum dot memory for holes, or as an electron transport barrier after etching away the InAsSb radial overgrowth.

To add more flexibility to the choice of host structure, we also investigate the possibility to deposit indium on nanowires *in situ* after growth. This is achieved by opening the indium flux after growth while keeping arsenic closed. In order to avoid evaporation of the nanowires, the sample temperature is lowered to 480 °C (430 °C) for InAs (InAsSb) nanowires. Figure 7(a) shows an SEM micrograph of an InAs nanowire sample where indium has been deposited for 3 min. We observe the formation of indium droplets on the {110} facets of the nanowires. In this case the droplets are formed at the base of the nanowires, without wetting the HSQ oxide. Figures 7(b), (c) show SEM micrographs of an InAs sample where indium droplets were deposited and then growth was continued with the standard parameters for the growth of branches (3.5×10^{-7} Torr arsenic BEP). We will refer to this sample as InAs–In–InAs, according to the different steps during growth. We observe that the deposited indium acts as a seed particle to continue growth in ⟨11–2⟩ direction, similar to the samples presented above. Here, the horizontal part of the L-shaped structure is at the base of the nanowires, due to the location of the indium droplets. Figures 7(d)–(f) show SEM micrographs of the corresponding experiments on InAsSb nanowires as host structures. We observe that droplets also form at the base of the nanowires, resulting in L-shaped structures where the horizontal part is close to the substrate. Note that under the conditions presented here, not all nanowires have an indium droplet after indium deposition. Therefore there are also nanowires without the horizontal part after re-initiating growth. Figures 7(g)–(k) shows a crystal structure and composition analysis of the InAs–In–InAs sample. We find that the sample horizontal part of the nanostructure inherits the polytypic crystal structure of the host nanowire, similar to the results presented in figure 4. The STEM-EDX map shown in figure 7(i) confirms that the nanostructure is pure InAs. Figures 7(l)–(p) shows a crystal structure and composition analysis of the InAsSb–In–InAs sample. The diffraction pattern (figure 7(m)), which was acquired on the horizontal part, shows that the structure is pure ZB. The STEM-EDX analysis in figure 7(n) confirms that the host nanostructure is InAsSb, while the horizontal part is InAs. At the tip of the horizontal InAs part we note a few rotational twins, as shown in the high resolution TEM micrographs in figures 7(o), (p). The samples presented here show that depositing indium on a host structure allows to form heterostructures, where the horizontal part adopts the crystal structure of the host nanowire all along the branch. However, we need to note that the horizontal part of the structure can in some cases also exhibit defects which do not propagate from the host nanowire and suggest a change of the growth front (more information available in supporting information). We attribute this finding to the close proximity of the substrate.

Finally, we also study the electrical properties of the L-shaped nanostructures grown by the annealing method. Electrical contacts to the nanostructure were defined by e-beam lithography, followed by argon milling to remove the native oxide, and then sputtering of chromium/gold. A detailed description of the process can be found in [16]. Figure 8(a) shows an SEM micrograph of a device allowing 2-point electrical measurements of the 'main', 'branch' and 'corner' sections of the L-shaped structure. Figure 8(b) shows an AFM image of another such device with a linescan across the branch section of the device, showing it to have an approximately rectangular cross section. Figure 8(c) shows representative *I*–*V* curve behavior of such devices. The linearity indicates ohmic contact behavior. For the devices studied, the *I*–*V* characteristics were used to estimate the conductivity of the different parts of the nanostructure based on AFM height and SEM length/width measurements. The average conductivity of the branches was found to be $81 \pm 23\ \mathrm{S\ cm^{-1}}$ (for four devices), which is comparable to standard ⟨111⟩B self-catalyzed InAs nanowires [16].

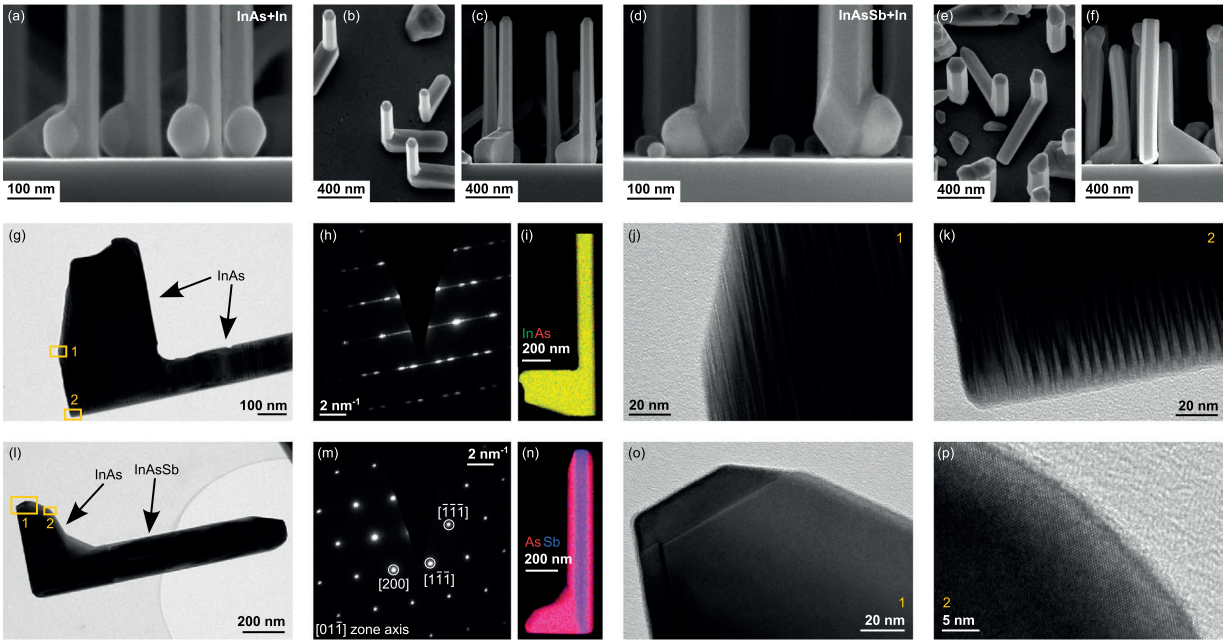

Figure 7. Deposition of indium droplets on InAs(Sb) nanowires to re-initiate growth. (a) InAs nanowires with indium deposition for 3 min (b), (c) Top view (15° tilt) and cross sectional SEM micrograph of an InAs-In-InAs sample. (d) InAsSb nanowires with indium deposition for 10 min. (e), (f) Top view (15° tilt) and cross sectional SEM micrograph of an InAsSb–In–InAs sample. (g) Low resolution TEM micrograph of an InAs–In–InAs nanostructure. (h) Diffraction pattern acquired on the horizontal part. (i) STEM-EDX map of the InAs–In–InAs nanostructure. (j), (k) High resolution TEM micrographs of the regions indicated by the yellow rectangles. (l)–(p) Similar analysis on an InAsSb–In–InAs nanostructure.

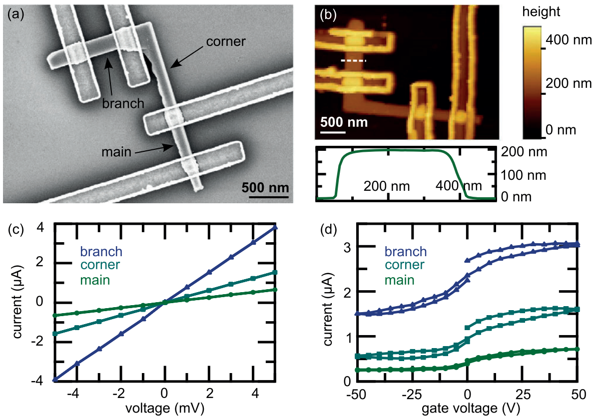

Figure 8. Electrical properties of L-shaped InAs nanostructures. (a) SEM micrograph of an electrical device. (b) AFM image and linescan of another electrical device, showing vertical profile of the branch section. (c) Representative *I*–*V* curve behavior of all three sections of a device as shown above. (d) Gate response of a typical device for a fixed source-drain voltage of 3 mV.

Figure 8(d) shows representative behavior of these devices when sweeping back-gate voltage for a fixed source-drain voltage of 3 mV. It was found that, in general, all parts of the device show n-type gate response, though the intensity of the response varied significantly. None of the devices could be turned off completely, probably due to charge screening of the gate by the relatively thick devices. Upon inspection of the devices after electrical testing, some of the devices appeared melted and amorphous. The results of the melted devices were not included in the conductivity calculation. At this point it is still unclear at which point during the measurements the melting occurred. More information on this phenomenon is given in the supporting information section.

Conclusions

In conclusion, we have demonstrated how to change the growth direction of self-catalyzed InAs nanostructures by *in situ* formation and manipulation of indium droplets. We have presented a detailed study on how to obtain indium droplets by annealing both for InAs and InAsSb nanowires. The indium droplets can then be used to initiate growth in different crystalline directions, resulting in linear or L-shaped nanostructures, depending on the position of the droplet. The conductivity of the branches was found to be roughly comparable to standard InAs nanowires, and all parts of the nanostructure show n-type gate response. Showing that indium droplets can be formed upon annealing further offers a new perspective when discussing whether or not a droplet is present during the growth of self-catalyzed InAs nanowires, and how the presence of liquid indium affects the crystal structure. In the case of InAsSb nanowires, our approach can be used to fabricate InSb sections within InAsSb wires, which are expected to act as quantum dot memories for holes. Furthermore, we demonstrate the flexibility of this technique by deposition of indium on InAs(Sb) after growth. Applying the indium deposition to different host nanostructures will allow for the growth of heterostructures or defect-free branches. Our results contribute to the understanding of the role of indium droplets in self-catalyzed InAs nanowire growth and offer a whole spectrum of new opportunities for indium-based nanostructures, including branched nanostructures, and the possibility to control defect formation. Demonstrating a change of growth direction for catalyst-free InAs nanowires also paves the route towards ⟨100⟩ oriented nanowires, which would facilitate the integration with CMOS technologies.

Acknowledgments

The authors acknowledge the SNF for financial support via the project 200021_169908 and through the NCCR QSIT. We would like to thank Jean-Baptiste Leran for help with MBE maintenance, Thomas La Grange, Duncan Alexander and Marco Cantoni from CIME for TEM support, and Philippe Caroff and Frank Glas for fruitful discussions.

References

[1] Mourik V, Zuo K, Frolov S M, Plissard S R, Bakkers E P A M and Kouwenhoven L P 2012 Signatures of majorana fermions in hybrid superconductor-semiconductor nanowire devices *Science* **25** 1003

[2] Brongersma M L, Cui Y and Fan S 2014 Light management for photovoltaics using high-index nanostructures *Nat. Mater.* **13** 451–60

[3] del Alamo J A 2011 Nanometre-scale electronics with III–V compound semiconductors *Nature* **479** 317

[4] Li Y, Qian F, Xiang J and Lieber C M 2006 Nanowire electronic and optoelectronic devices *Mater. Today* **9** 18

[5] Takei K, Takahashi T, Ho J C, Ko H, Gillies A G, Leu P W, Fearing R S and Javey A 2010 Nanowire active-matrix circuitry for low-voltage macroscale artificial skin *Nat. Mater.* **9** 821

[6] Dayeh S H, Aplin D P R, Zhou X, Yu P K L, Yu E T and Wang D 2007 High electron mobility InAs nanowire field-effect transistors *Small* **3** 326

[7] Deng M T, Yu C L, Huang G Y, Larsson M, Caroff P and Xu H Q 2012 Anomalous zero-bias conductance peak in a Nb–InSb nanowire-Nb hybrid device *Nano Lett.* **12** 6414

[8] Kang S L N, Fan D X, Wang L B, Huang Y Q, Caroff P and Xu H Q 2016 Coherent charge transport in ballistic InSb nanowire Josephson junctions *Sci. Rep.* **6** 24822

[9] Thelander C, Caroff P, Plissard S, Dey A W and Dick K A 2011 Effects of crystal phase mixing on the electrical properties of InAs nanowires *Nano Lett.* **11** 2424

[10] Plissard S R *et al* 2013 Formation and electronic properties of InSb nanocrosses *Nat. Nanotechnol.* **8** 859

[11] Dick K A, Deppert K, Larsson M W, Martensson T, Seifert W, Wallenberg L R and Samuelson L 2004 Synthesis of branched 'nanotrees' by controlled seeding of multiple branching events *Nat. Mater.* **3** 380

[12] Bar-Sadan M, Barthel J, Shtrikman H and Houben L 2012 Direct imaging of single Au atoms within GaAs nanowires *Nano Lett.* **12** 2352

[13] Koto M, Marshall A F, Goldthorpe I A and McIntyre P C 2010 Gold-catalyzed vapour–liquid–solid germanium-nanowire nucleation on porous silicon *Small* **6** 1032

[14] Grap T, Rieger T, Blömers C, Schäpers T, Grützmacher D and Lepsa M I 2013 Self-catalyzed VLS grown InAs nanowires with twinning superlattices *Nanotechnology* **24** 335601

[15] Dimakis E, Lähnemann J, Jahn U, Breuer S, Hilse M, Geelhaar L and Riechert H 2011 Self-assisted nucleation and vapor–solid growth of InAs nanowires on bare Si(111) *Cryst. Growth Des.* **11** 4001

[16] Potts H, Friedl M, Amaduzzi F, Tang K, Tütüncüoglu G, Matteini F, Alarcon Llado E, McIntyre P C and Fontcuberta i Morral A 2016 From twinning to pure zincblende catalyst-free InAs(Sb) nanowires *Nano Lett.* **16** 637

[17] Sourribes M J L, Isakov I, Panfilova M, Liu H and Warburton P A 2014 Mobility enhancement by Sb-mediated minimisation of stacking fault density in InAs nanowires grown on silicon *Nano Lett.* **14** 1643

[18] Wacaser B A, Deppert K, Karlsson L S, Samuelson L and Seifert W 2006 Growth and characterization of defect free GaAs nanowires *J. Cryst. Growth* **287** 504

[19] Yuan X, Caroff P, Wong-Leung J, Fu L, Tan H H and Jagadish C 2015 Tunable polarity in a III-V nanowire by droplet wetting and surface energy engineering *Adv. Mater.* **27** 6096

[20] Conesa-Boj S, Zardo I, Estrade S, Wei L, Alet P J, Roca I Cabarrocas P, Morante J R, Peir F, Fontcuberta i Morral A and Arbiol J 2010 Defect formation in Ga-catalyzed silicon nanowires *Cryst. Growth Des.* **10** 1534

[21] Krishnamachari U, Borgstrom M, Ohlsson B J, Panev N, Samuelson L, Seifert W, Larsson M W and Wallenberg L R 2004 Defect-free InP nanowires grown in [001] direction on InP(001) *Appl. Phys. Lett.* **85** 2077

[22] Fonseka H A, Caroff P, Wong-Leung J, Ameruddin A S, Tan H H and Jagadish C 2014 Nanowires grown on InP (100): growth directions, facets, crystal structures and relative yield control *ACS Nano* **8** 6945

[23] Wan J, Plissard S, Hocevar M, Vu T T T, Zehender T, Immink G G W, Verheijen M A, Haverkort J and Bakkers E P A M 2012 Position-controlled [100] InP nanowire arrays *Appl. Phys. Lett.* **100** 053107

[24] Wan J, Plissard S R, Verheijen M A, Feiner L-F, Cavalli A and Bakkers E P A M 2013 Reversible switching of InP nanowire growth direction by catalyst engineering *Nano Lett.* **13** 3802

[25] Mikkelsen A, Eriksson J, Lundgren E, Andersen J N, Weissenrieder J and Seifert W 2005 The influence of lysine on InP(001) surface ordering and nanowire growth *Nanotechnology* **16** 2354

[26] Yan X, Zhang X, Li J, Wu Y and Ren X 2015 Self-catalyzed growth of pure zinc blende ⟨110⟩ InP nanowires *Appl. Phys. Lett.* **107** 023101

[27] Li Z-A *et al* 2011 Planar-defect characteristics and cross-sections of ⟨001⟩, ⟨111⟩, and ⟨112⟩ InAs nanowires *J. Appl. Phys.* **109** 114320

[28] Kelrich A, Sorias O, Calahorra Y, Kauffmann Y, Gladstone R, Cohen S, Orenstein M and Ritter D 2016 InP nanoflag growth from a nanowire template by *in situ* catalyst manipulation *Nano Lett.* **16** 2837

[29] Pan D, Fan D X, Kang N, Zhi J H, Yu X Z, Xu H Q and Zhao J H 2016 Free-standing two-dimensional single-crystalline InSb nanosheets *Nano Lett.* **16** 834

[30] De La Mata M, Leturcq R, Plissard S R, Rolland C, Magén C, Arbiol J and Caroff P 2016 Twin-induced InSb nanosails: a convenient high mobility quantum system *Nano Lett.* **16** 825

[31] Aagesen M, Johnson E, Sorensen C B, Mariager S O, Feidenhans'l R, Spiecker E, Nygard J and Lindelof P E 2007 Molecular beam apitaxy growth of free-standing plane-parallel InAs nanoplates *Nat. Nanotechnol.* **2** 761

[32] Car D, Wang J, Verheijen M A, Bakkers E P A M and Plissard S R 2014 Rationally designed single-crystalline nanowire networks *Adv. Mater.* **26** 4875

[33] Alicea J, Oreg Y, Refael G, von Oppen F and Fisher M P A 2011 Non-Abelian statistics and topological quantum information processing in 1D wire networks *Nat. Phys.* **7** 412

[34] Yu Y *et al* 2013 Single InAs quantum dot grown at the junction of branched gold-free GaAs nanowire *Nano Lett.* **13** 1399

[35] Gomes U P, Ercolani D, Zannier V, David J, Gemmi M, Beltram F and Sorba L 2016 Nucleation and growth mechanism of self-catalyzed InAs nanowires on silicon *Nanotechnology* **27** 255601

[36] Borg M, Schmid H, Moselund K E, Signorello G, Gignac L, Bruley J, Breslin C, Das Kanungo P, Werner P and Riel H 2014 Vertical III–V nanowire device integration on Si(100) *Nano Lett.* **14** 1914

[37] Loitsch B *et al* 2015 Tunable quantum confinement in ultrathin, optically active semiconductor nanowires via reverse-reation growth *Adv. Mater.* **27** 2195

[38] Conesa-Boj S, Kriegner D, Han X-L, Plissard S, Wallart X, Stangl J, Fontcuberta i Morral A and Caroff P 2014 Gold-free ternary III–V antimonide nanowire arrays on silicon: twin-free down to the first bilayer *Nano Lett.* **14** 326

[39] Mandl B, Dick K A, Kriegner D, Keplinger M, Bauer G, Stangl J and Deppert K 2011 Crystal structure control in Au-free self-seeded InSb wire growth *Nanotechnology* **22** 145603

[40] Suyatin D B, Sun J, Fuhrer A, Wallin D, Fröberg L E, Karlsson L S, Maximov I, Wallenberg L R, Samuelson L and Xu H Q 2008 Electrical properties of self-assembled branched InAs nanowire junctions *Nano Lett.* **4** 1100

[41] Tutuncuoglu G, de la Mata M, Deiana D, Potts H, Matteini F, Arbiol J and Fontcuberta i Morral A 2015 Towards defect-free 1D GaAs/AlGaAs heterostructures based on GaAs nanomembranes *Nanoscale* **7** 19453

[42] Foster A P, Bradley J P, Gardner K, Krysa A B, Royall B, Skolnick S and Wilson L R 2015 Linearly polarized emission from an embedded quantum dot using nanowire morphology control *Nano Lett.* **15** 1559

[43] Paladugu M, Zou J, Guo Y-N, Auchterlonie G J, Joyce H J, Gao Q, Tan H H, Jagadish C and Kim Y 2007 Novel growth phenomena observed in axial InAs/GaAs nanowire heterostructures *Small* **3** 1873

[44] Biermanns A, Dimakis E, Davydok A, Sasaki T, Geelhaar L, Takahasi M and Pietsch U 2014 Role of liquid indium in the structural purity of wurtzite InAs nanowires that grow on Si(111) *Nano Lett.* **14** 6878

[45] Jacobsson D, Panciera F, Tersoff J, Reuter M C, Lehmann S, Hofmann S, Dick K A and Ross F M 2016 Interface dynamics and crystal phase switching in GaAs nanowires *Nature* **531** 317

[46] Balaghi L, Tauchnitz T, Hübner R, Bischoff L, Schneider H, Helm M and Dimakis E 2016 Droplet-confined alternate pulsed epitaxy of GaAs nanowires on Si substrates down to CMOS-compatible temperatures *Nano Lett.* **16** 4032

[47] Vukajlovic-Plestina J, Dubrovskii V, Tutuncuoglu G, Potts H, Ricca R, Meyer F, Matteini F, Leran J-B and Fontcuberta i Morral A 2016 Molecular beam epitaxy of InAs nanowires in SiO_2 nanotube templates: challenges and prospects for integration of III–Vs on Si *Nanotechnology* **27** 455601

[48] Wei S H and Zunger A 1995 InAsSb/InAs: A type-I or a type-II band alignment *Phys. Rev.* B **52** 12039

5 Conclusion & Outlook

In this thesis we investigated the growth and characterization of InAs(Sb) nanowires. We focused on their crystal structure, orientation with respect to the substrate, and the possibility to tune their direction during growth. Our results contribute to the understanding of the growth of InAs(Sb) nanowires and they provide a new pathway to the formation of nanowire networks.

In publication 1 we showed that polytypism can be suppressed by the incorporation of antimony, and pure zinc-blende nanowires are obtained for an antimony content above 25%. We also studied the homogeneity of the ternary alloy by fabricating nanowire cross sections, and observed slight segregation effects. In terms of electrical properties, we found by Raman spectroscopy that pure zinc-blende InAsSb nanowires have a higher electron mobility than polytypic InAs nanowires. The increase in mobility can be attributed to the pure crystal structure, but it may also be related to the fact that the mobility of InSb is much higher than for InAs. To gain more insights, temperature dependent Raman measurements and Terahertz spectroscopy are currently being performed by Francesca Amaduzzi (from EPFL) and Jessica Boland (from Oxford).

We further investigated the possibility to passivate the nanowire surface using ALD-grown alumina. By fabricating electrical devices we showed that conductivity measurements of passivated nanowires are more reproducible compared to unpassivated nanowires. We also demonstrated the possibility to make top-gated field-effect devices based on the alumina as gate dielectric. In future experiments we are planning to study the quality of the passivation layer in a more quantitative way. Terahertz spectroscopy on nanowires with different diameters allows to extract the surface recombination velocity and compare passivated with un-passivated nanowires. In order to gain more insights about the nature of traps, C/V-measurements are an interesting technique. The McIntyre group recently demonstrated C/V-measurements in solution, which allow to measure not only flat surface but also nanostructures. Dmitry Mikulik is currently adapting the process in order to extract information about the interface and border trap density from passivated InAs nanowires.

It future experiments it would also be interesting to gain more information about the location of charge carriers in nanowires. For this, TEM holography is an interesting technique. The carrier location can be extracted by studying nanowire devices with Schottky contacts, which allows to change the carrier density in the nanowires. These measurements are particularly interesting in views of the debate about a carrier accumulation at the surface of InAs(Sb) nanowires, and how it depends on the existence and the quality of a surface oxide or passivation layer.

In publication 2 we studied the existence of tilted nanowires on (111)B substrates. We found that the majority of the tilted nanowires can be explained by 3D twinning. The nanowires grow in <111>B direction, but their orientation with respect to the substrate is different due to a twin which is not perpendicular to the substrate normal. In addition, also nanowires growing in non-conventional crystalline directions were observed, e.g. <112> nanowires. We demonstrated how the ratio of tilted nanowires depends on the growth conditions and substrate preparation. The most important factor was found to be the V/III ratio, suppressing the formation of tilted nanowires completely for high V/III ratios. Also the oxide thickness has a significant impact. Our results allow to grow purely vertical nanowire samples or samples with a high density of tilted nanowires, whichever is desired for a specific application. Our results also provide some more insights regarding the growth mechanism of InAs nanowires, considering that the 3D twinning mechanism is expected to be related to the presence of a droplet. In future experiments it would be interesting to compare our results with the simulations by Matteini *et al* [Matteini16], which showed that in the case of self-catalyzed GaAs nanowires on silicon, the position and contact angle of the droplet determine the formation of tilted or vertical nanowires. The decisive factors in this case are the oxide thickness and surface energy.

In publication 3 we demonstrated a new approach to change the direction of InAs nanowires from <111> to <11$\bar{2}$> during growth, resulting in L-shaped nanostructures. Our approach is based on the formation of indium droplets by annealing of the nanowires in vacuum. We found that the droplets are initially located on the top facet ot the nanowires, and then slide down onto the side facets once they exceed a certain size. While our work demonstrates that indium droplets can be created and then used to initiate growth in new directions, it is still unclear why the droplets slide down onto the side facets. As presented in the article, this is not the case for other material systems either. For example we studied the annealing of $InAs_{0.8}Sb_{0.2}$ nanowires, and found that the droplets stay on the top facet of the nanowires. After a certain point the droplets stops to increase in size, and material evaporates from the side facets, resulting in thinner nanowires. Future studies by Lea Ghisalberti will focus on modeling the nanowires and droplets, in order to understand the role of the contact angle and the stability of the droplet. This will hopefully allow us to translate our approach to other material systems. In particular branched nanowires based on $InAs_{1-x}Sb_x$ are of interest, because they are expected to be defect-free.

Finally, we would like to highlight the possibility to make more sophisticated nanowire networks by merging of several L-shaped structures. In our current approach the probability to merge is very low, since the nanowires grow in random positions due to the spontaneous pinhole formation. By controlling the position of the host nanowires, the merging probability could be tremendously increased. Figure 5.1 shows a schematic of the proposed approach. Nanowires are grown in position-controlled openings which are fabricated by e-beam lithography and etching. A hexagonal pattern is chosen based on the six favoured <112> growth directions of the L-shaped structures. The nanowires are then annealed to form droplets, and re-initiation of growth leads to L-shaped structures. After a certain time, two or several nanostructures will merge. Depending on the annealing time, it is possible to choose conditions under which some nanowires continue to grow in <111> direction. Merging of those straight nanowires with L-shaped nanowires would then lead to h-structures, as shown in the schematic.

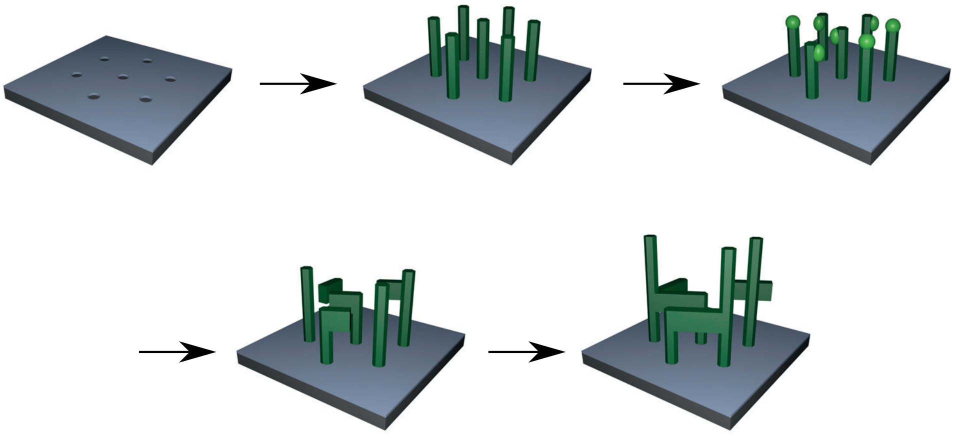

Figure 5.1 – Schematic of the growth of networks by merging of L-shaped nanostructures.

A Additional experimental results

A.1 In-situ TEM studies during nanowire annealing

In-situ experiments can offer valuable information about self-assembly processes as well as material changes due to temperature. Recently impressive insights have been obtained by monitoring nanowire growth using a growth chamber equipped with an in-situ TEM [Jacobsson16]. In our case we are interested in monitoring the decapping of arsenic capped nanowires, and in the indium droplet formation during annealing of InAs nanowires. For this, nanowires can be transferred to heatable TEM holders and then be imaged in a standard TEM.

During this thesis, annealing studies were performed using a Protochip Fusion TEM Heating and Electrical System [Protochips17] in the group of Rolf Erni at The Swiss Federal Laboratories for Materials Science and Technology (EMPA). For this, nanowires were transferred to a designated chip. In order not to break the membrane on the chip, nanowires are picked up with a corner of a cleanroom tissue and then transferred by carefully touching the chip with the tissue. The sample was then installed in a JEOL JEM2200fs microscope and the holder was connected to the Protochips temperature control unit. A temperature calibration file is provided for every chip, allowing to precisely control the temperature. The experiments were performed at EMPA with the help of Marta Rossell.

A.1.1 Decapping of arsenic capped nanowires

For the surface passivation of InAs nanowires using alumina, which was presented in publication 1, the nanowires were capped with a thick layer of arsenic in the growth chamber. This arsenic capping layer prevents the formation of a native oxide layer. Before the growth of alumina, the arsenic capping layer is removed by annealing under vacuum. In order to visualize the decapping procedure, we transferred arsenic capped nanowires to a chip, and then monitored the nanowires during annealing using STEM.

STEM bright field images of the annealing process are shown in Figure A.1. Figure (a) shows the

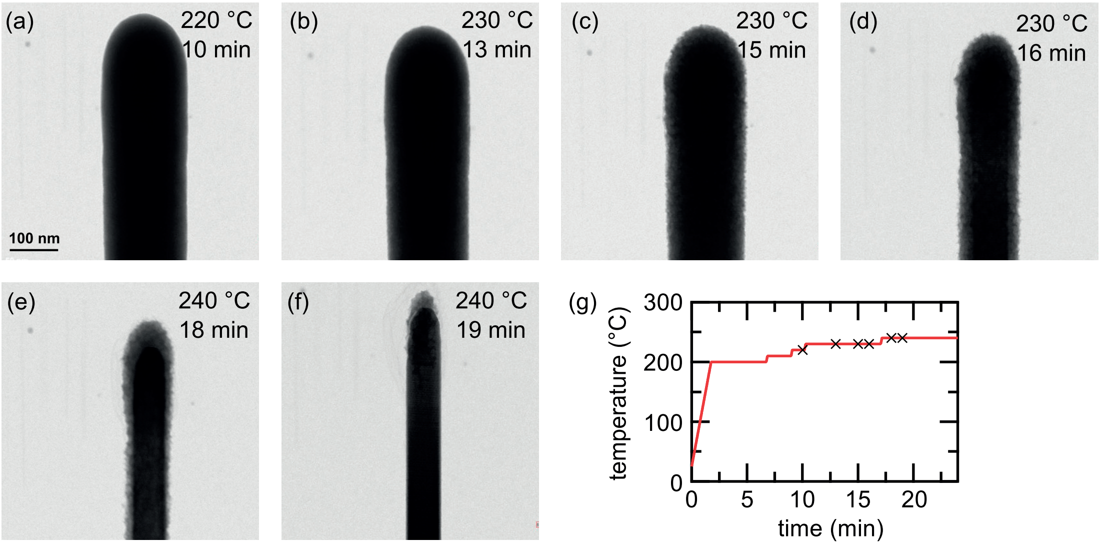

Figure A.1 – Decapping of arsenic capped nanowires. (a) Arsenic capped nanowire at 220°C. No change in the capping layer can be observed. (b)-(d) Time series of the same nanowire at 230°C, showing that the arsenic layer starts evaporating slowly. (e)-(f) Time series at 240°C. At this temperature the capping layer fully evaporates, while the InAs surface does not decompose. (g) Plot of the temperature ramping, indicating the times at which the images (a)-(f) were acquired.

tip of an InAs nanowire with a thick arsenic capping layer. The image was acquired at 220°C. Up to this temperature no change in morphology of the capping layer could be observed. At 230°C, the capping layer slowly starts to evaporate, as shown in Figure A.1(b)-(d). Increasing the temperature to 240°C increased the evaporation rate as shown in Figure A.1(e)-(f). We also observe that the InAs nanowire surface does not decompose at temperatures up to 240°C. A plot of the temperature ramping is shown in Figure A.1(g), indicating also the times at which images where acquired. Our results show that decapping of the nanowires is possible without harming the nanowire surface.

A.1.2 Annealing of InAs nanowires

In publication 3 we presented the formation of indium droplets when annealing nanowires in vacuum immediately after growth. The droplets were found to first form on the top facet of the nanowires and then slide down onto the side facets. To understand this behaviour we studied the annealing of InAs nanowires using the Protochips technology. In order to avoid any influence of the native oxide, we started with arsenic capped nanowires, and evaporated the capping layer in the TEM, as shown in the previous section. Figure A.2(a) shows a bright-field STEM image of the capped nanowire. The InAs nanowire after decapping is shown in Figure A.2(b). Surprisingly, a shadow of a shell can be observed. The origin of this shell is so far unclear, but it may be related to contamination of the chip. An influence of the electron beam can be excluded, since at the end of the experiment, a similar shell was also found on other nanowires which had not been imaged. At 250°C, the InAs slowly starts to evaporate from the tip of the nanowire, as can be seen when comparing the nanowire after 10 min (Figure (b)) and after 51 min (Figure (c)). At 300°C slightly faster evaporation can be observed, as shown in Figure A.2(d)-(e). At 350°C the nanowire rapidly disappears, as shown in Figure A.2(f)-h). It can be observed that the evaporation does not occur uniformly, which may be related to the presence of the shell. The nanowire is finally consumed completely by heating to 400-450°C. A plot of the temperature ramping is shown in Figure A.2(k).

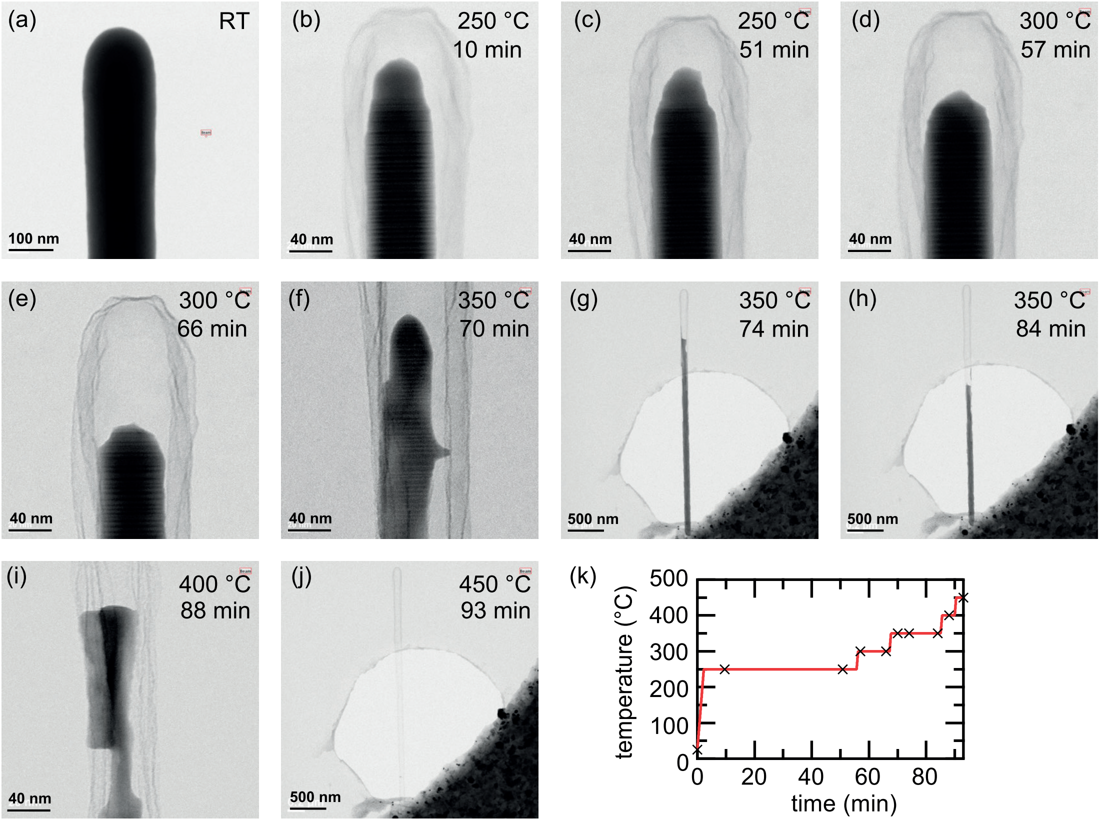

Figure A.2 – Annealing of InAs nanowires. (a)-(c) Sample at room temperature, showing the arsenic capping layer. (b) At 250°C the arsenic capping layer completely evaporated and the nanowire starts decomposing very slowly. (d)-(j) The nanowire rapidly evaporates when increasing the temperature above 350°C. The evaporation starts from the tip of the nanowire. (k) Plot of the temperature ramping, indicating the times at which the images (a)-(j) were acquired.

Our results are unexpected for two reasons:

1.) No droplet is observed during the annealing. The experiment is therefore not suited to study the dynamics of the droplet. The absence of an indium droplet is surprising, since the experiment is done in vacuum ($1 \cdot 10^{-7}$ Torr) and predominant evaporation of arsenic is expected due to the higher vapour pressure. On the other hand, the conditions of this experiment are not identical to the annealing in the MBE chamber immediately after growth.

The formation of a droplet could be suppressed by the presence of the observed shell, or due to the fact that the nanowires are lying on the carbon film, allowing the indium to diffuse away.

2.) The InAs nanowire starts to evaporate at 250°C. This temperature is significantly lower than expected. In the case of alumina passivation by ALD, the arsenic capping layer is evaporated at 300°C, leaving the InAs nanowire unaffected, as shown in publication 1. We therefore suspect that the temperature calibration of the chips may not be very accurate.

A.1.3 Annealing of InAsSb nanowires

We also investigated annealing of $InAs_{0.8}Sb_{0.2}$ nanowires. For this experiment we used standard nanowires without any capping layer, meaning that they are covered with a thin layer of native oxide. Figure A.3(a) shows two nanowires at the beginning of the experiment at room temperature. At 400°C the nanowires start to decompose slowly, as shown in Figure A.3(b)-(c). Interestingly the evaporation is not limited to the tip of the nanowire, but it can be observed in different locations along the nanowire. Also the triangular shape of the voids is different compared to the case of InAs nanowires. At 500°C the nanowires evaporate completely, as shown in Figure A.3(d). We note that the evaporation temperature here is higher compared to the experiment with InAs nanowires. This is unexpected since InSb is known to be less stable than InAs. At this point we do not know whether this observation is related to the different nanowire surface (native oxide versus prestine surface after arsenic decapping) or whether it is an artifact, possibly due to a mistake in the temperature calibration of the Protochips. We would like to thank Marta Rossell for carrying out this experiment and providing the images.

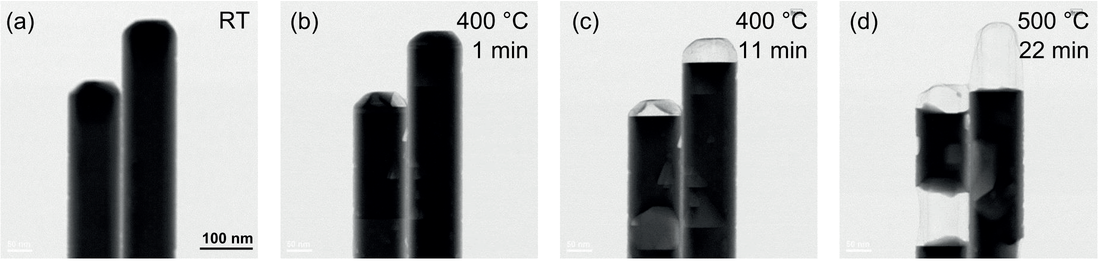

Figure A.3 – Annealing of $InAs_{0.8}Sb_{0.2}$ nanowires. (a) Sample at room temperature. (b)-(c) at 400°C the nanowires slowly decompose, starting from different locations along the nanowire. (d) At 500°C the nanowires readily evaporate.

In conclusion, we have studied annealing of different nanowires by in-situ TEM. In particular we monitored the decapping procedure of an arsenic passivated nanowire sample, and we studied the decomposition of InAs and InAsSb nanowires. In these experiments we were not able to reproduce the droplet formation reported in publication 3, probably due to a difference of the exact conditions and nanowire environment. Nevertheless, in-situ TEM studies are found to be a powerful tool and can provide interesting information about temperature dependent processes.

A.2 Thinning of InAs nanowires

Nanowires are interesting structures due to their one-dimensional morphology. Reducing the size of a structure leads to the formation of sub-bands. Quantization effects can be observed if the sub-band spacing is large compared to the thermal energy. The sub-band spacing scales with the inverse of the dimensions and the inverse of the effective mass. For InAs the effective mass of the electron is $0.023m_e$ [Ioffe17]. Due to the small effective mass, quantization effects are expected already for relatively large dimensions. The exciton Bohr radius of $a \approx 34$ nm is often cited as a length scale [Norris05, Ford09].

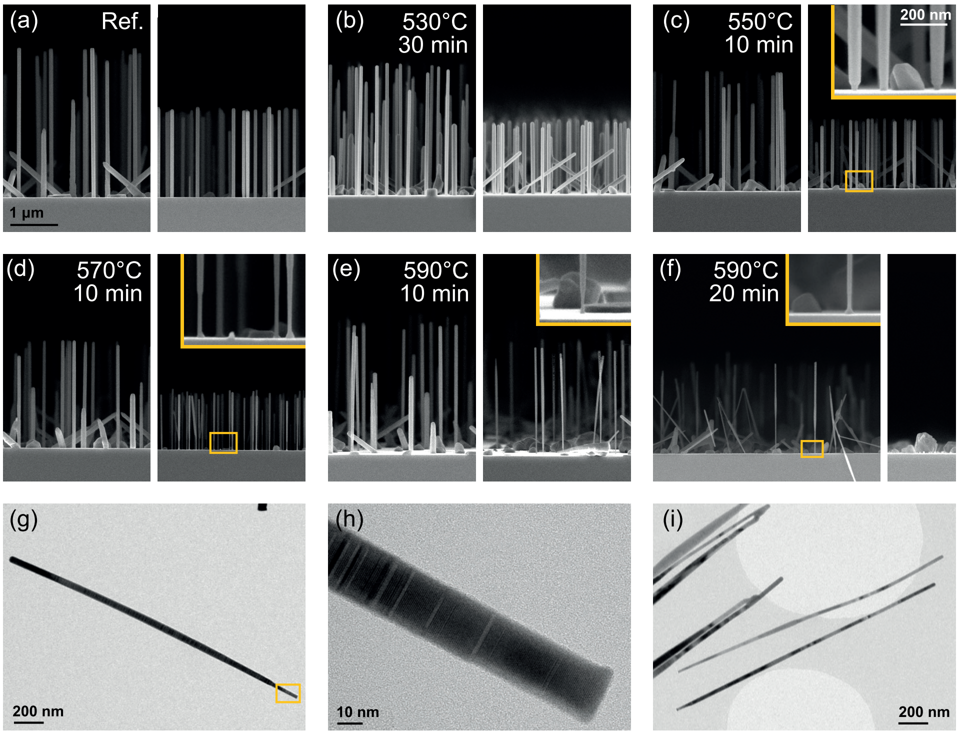

Figure A.4 – Thinning of standard InAs nanowires. (a) Cross sectional SEM micrographs of a reference sample (center and edge). (b)-(f) Samples which were annealed under $1.9\cdot10^{-6}$ Torr arsenic flux. (b) 530°C for 30 min, (c)-(e) 550°C, 570°C and 590°C for 10 min, (f) 590°C for 20min. (g)-(h) TEM micrographs of the sample presented in (e). (i) TEM micrograph of the sample presented in (f).

By bottom-up growth it is challenging to achieve nanowires with a diameter below 50 nm. Therefore it can be desired to thin the nanowires after growth, in order to achieve dimensions for which quantization effects can be observed. Thinning can be achieved by congruent evaporation, i.e. by choosing conditions under which group III and group V atoms evaporate at the same rate. The congruent evaporation temperature T_c defines the temperature below which congruent evaporation is obtained. Above T_c, arsenic preferentially evaporates from the surface, leaving behind droplets of the group III material, as observed in publication 3. The conditions for congruent evaporation depend on the surface orientation and the pressure. It has been demonstrated that the congruent evaporation temperature of GaAs can be modified by the presence of an external arsenic flux [Zhou10].

Figure A.4(a)-(f) shows cross sectional SEM micrographs of nanowire samples which have been annealed under different conditions. The image on the left of each subfigure was taken at the center of the sample, while the image on the right corresponds to the edge of the sample. Due to the design of the manipulator in our MBE system, a small temperature gradient (< 10°C) is present across the sample, leading to a change in nanowire morphology for very temperature sensitive samples. Figure (a) shows a reference sample, which was cooled down immediately after growth. The other samples were annealed at different temperatures under constant arsenic flux of $1.9{\cdot}10^{-6}$ Torr. Figure (b) shows a sample which was annealed at 530°C for 30 min. No significant change in nanowire morphology can be observed. The samples presented in (c)-(e) were annealed for 10 min at 550°C, 570°C, and 590°C respectively. We observe that the nanowires get thinner with increasing temperature. The biggest change happens at the foot of the nanowires at the sample edge, as shown in the inserts. Figure (f) shows a sample which was annealed at 590°C for 20 min, resulting in very thin nanowires in the center and complete evaporation of the nanowires at the edge. The nanowire density in the center is significantly lower compared to the other samples, suggesting that some nanowires evaporated completely or broke off due to the predominant thinning at the foot. We also observe that the diameter changes along the wires, often showing a thicker part in the center. Figure (g)-(h) shows TEM micrographs of the sample presented in (e), where the nanowire foot can be as thin as 20 nm but the rest of the nanowire is significantly thicker. Figure (i) shows a TEM micrograph of the nanowire from the sample presented in (f).

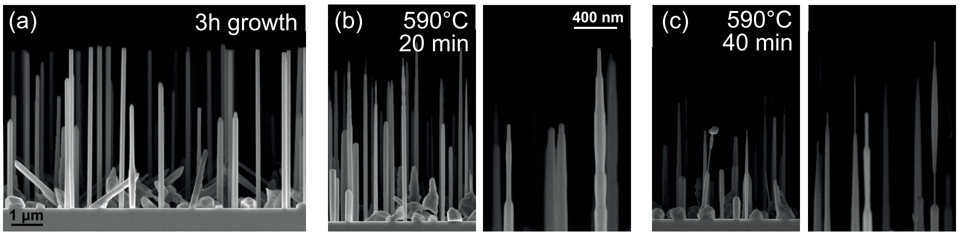

Figure A.5 – Thinning of long InAs nanowires. (a) Cross sectional SEM micrographs of a reference sample which was grown for 3 h (center and edge). (b)-(c) Samples which were annealed under $1.9{\cdot}10^{-6}$ Torr arsenic flux at 590°C for 20 min and 40 min respectively.

In order to make electrical devices, the nanowires should ideally be at least 2 μm in length. During annealing the material not only evaporates from the side facets but also from the top facet, leading to shorter nanowires. We therefore investigated annealing of nanowire samples that were grown for 3 h, resulting in a nanowire length of approximately 5 μm as shown in the reference sample in Figure A.5(a). Figure (b)-(c) show samples after annealing under $1.9{\cdot}10^{-6}$ Torr arsenic flux at 590°C for 20 min and 40 min respectively. The images on the right of each subfigure show a magnified version of the nanowire tips. We observe a very non-uniform nanowire morphology with significant changes in diameter along the nanowires. We conclude that more investigations are needed in order to achieve long and thin nanowires.

One should note that for annealing experiments the nanowire density also plays a role by locally changing the pressure. Due to our substrate preparation process, slight variations in the nanowire density cannot be avoided, making a quantitative comparison between different samples difficult. Better control would be achieved by using position-controlled growth.

A.3 InAsSb nanowires - additional information

In publication 1 we presented the growth and properties of $InAs_{1-x}Sb_x$ nanowires. We found that the stacking defect density is dramatically reduced by the incorporation of antimony, allowing to grow nanowires with a defect density on the order of $1/\mu m$ for an antimony content above 25%. Here we would like to add that the defect density usually changes along the nanowire. While this effect is almost irrelevant for short nanowires (as presented in the article), it is clearly visible in longer nanowires. Figure A.6(a) shows a low magnification TEM micrograph of a nanowire with 28% antimony. Apart from a few defects at the beginning of growth, only four defects can be observed in the rest of the nanowire. In the low magnification image the defects can be recognized as changes in contrast and are high-lighted with green arrows.

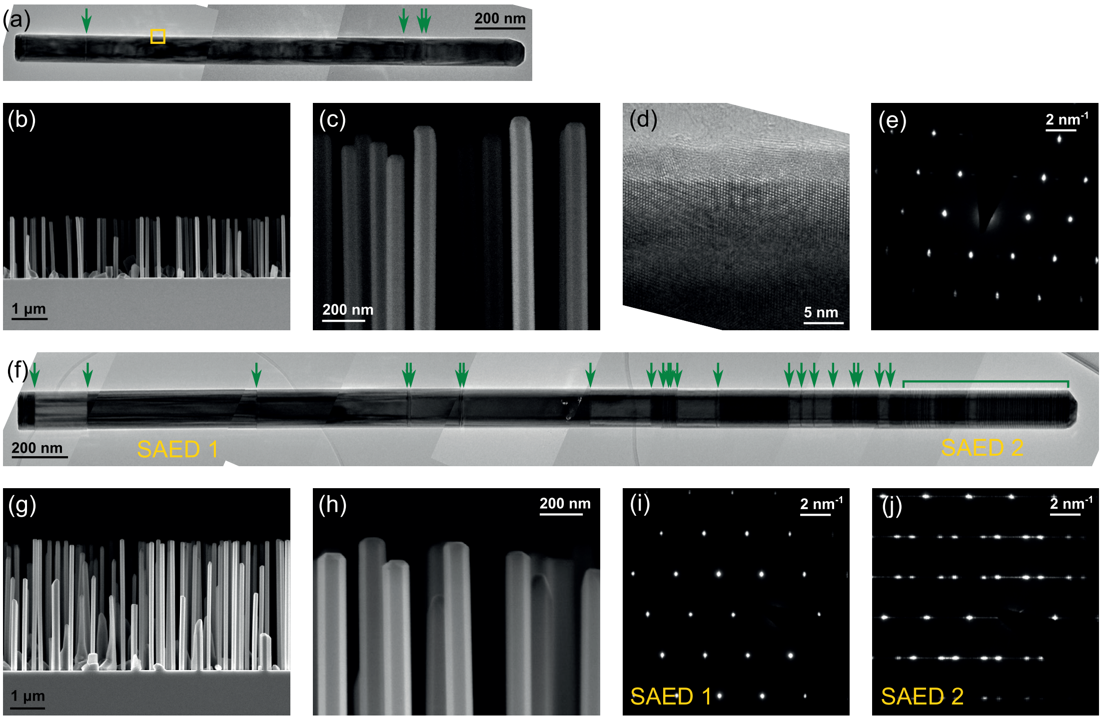

Figure A.6 – Crystal structure evolution of long InAsSb nanowires. (a) Low magnification TEM micrograph of an $InAs_{0.72}Sb_{0.28}$ nanowire which was grown for 1 h. (b)-(c) Cross-sectional SEM images of the corresponding nanowire forest. (d)-(e) High resolution TEM micrograph and SAED pattern. (f) Low magnification TEM micrograph of a nanowire which was grown for 3 h under similar conditions. (g)-(h) SEM images of the corresponding nanowire sample. (i)-(j) SAED images of the foot of the nanowire and the tip of the nanowire.

Figure A.6(b)-(c) show cross-sectional SEM micrographs of the corresponding nanowire forest. A high resolution TEM micrograph and a SAED pattern is presented in Figure (d)-(e), showing a pure zinc-blende crystal structure.

Figure A.6(f) shows a low magnification TEM micrograph of a nanowire that was grown for 3 h instead of 1 h using similar parameters. The resulting nanowires are significantly longer and have slightly larger diameters, as can be seen from the cross-sectional SEM images in (g)-(h). In terms of crystal structure, we observe that the first two micrometers show a very low defect density, similar to what has been observed in the short nanowire presented above. Towards the tip of the nanowire the defect density increases. At the very end of the nanowire the crystal structure shows a high density of stacking defects, almost comparable to pure InAs nanowires. Two representative SAED images are shown in (i)-(j). A similar behaviour has been found in many long InAsSb nanowires, suggesting that the growth conditions change along the nanowire. One possible explanation is that the incorporation of antimony is higher at the early stages of growth due to re-evaporation from the substrate. Unfortunately EDX analysis at different locations along the nanowire does not show a clear decrease in antimony content towards the nanowire tip. However the EDX analysis is also sensitive to the shell which is formed due to radial overgrowth (refer to cross sectional analysis in publication 1), therefore making it difficult to analyze the composition of the nanowire core.

A.4 InAs/GaSb core/shell nanowires

InAs/GaSb shows a broken band alignment, with the conduction band of InAs being lower than the valence band of GaSb. Figure A.7(a) shows the band alignment of a AlSb/InAs/GaSb/AlSb quantum well structure. The AlSb layers serve as barriers. Thin quantum wells show discrete energy levels, as schematically depicted by E_1 and H_1. Hybridization of can occur if the energy levels overlap, leading to the opening of a band gap. The band gap is called an inverted band gap due to the fact that the hole-like band is higher than the electron-like band as shown in Figure (b). Interest in InAs/GaSb heterostructures has arisen due to the work by Liu *et al*, predicting that an InAs/GaSb quantum well heterostructure could show quantum spin hall effect behaviour [Liu08]. At the edge of an InAs/GaSb heterostructure the band gap closes, leading to conducting edge states. Since the prediction in 2008, several groups have investigated InAs/GaSb quantum well structures and edge conduction has been reported [Knez11, Spanton14, Du15, Qu15, Mueller15].

Considering the unique properties of InAs/GaSb quantum well heterostructures, the question arises whether InAs/GaSb nanowire heterostructures could also show interesting properties. For nanowires we distinguish radial and axial heterostructures. Figure A.7(c) shows a schematic of a radial core-shell heterostructure on the top and an axial heterostructure on the bottom. InAs/GaSb core-shell nanowires have been studied theoretically, and an inverted bandgap has been found for certain core and shell dimensions [Kishore12, Luo16, Vinas17]. While the exact numbers are slightly different, all articles show that it is important to have extremely thin

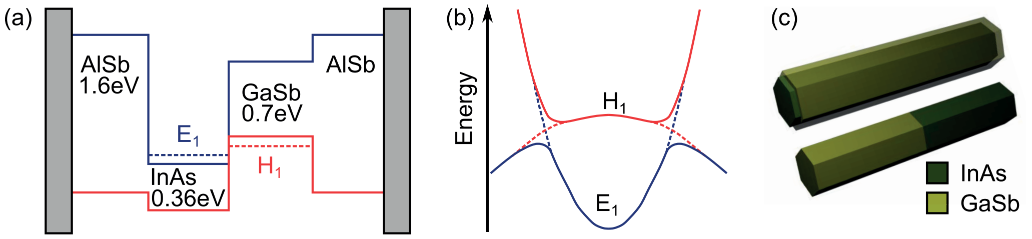

Figure A.7 – InAs/GaSb heterostructures. (a) Band alignment of an AlSb/InAs/GaSb/AlSb quantum well heterostructure (adapted from Ref. [Liu08]). (b) Opening of a hybridization gap. (c) Schematic of a core-shell (top) and an axial (bottom) nanowire heterostructure.

nanowires with diameters on the order of 20 nm. The opening and closing of the hybridization gap in dependence on the dimension would be interesting to observe. However the most interesting feature would be the edge modes that may arise at the interface between of the heterostructure with vacuum at the bottom and top facet of the nanowires, but unfortunately none of the theoretical works have studied the edge modes at the ends of a core/shell nanowire.

Heterostructures with a broken band alignment are not only interesting due to the possible opening of a hybridization gap, but they have also been studied as a material platform for a tunnel field effect transistor (TFET) [Ionescu11]. With this goal in mind, several groups have investigated InAs/GaSb nanowire heterostructures [Borg10, Ganjipour11, Dey13a, Dey13b]. Also basic physical phenomena like electron-hole interaction during transport have been studied using InAs/GaSb nanowires [Ganjipour15].

In the following pages we present our preliminary results on the growth of InAs(Sb)/GaSb core-shell nanowire heterostructures using MBE. The first attempt is shown in Figure A.8. Figure (a)-(b) show a top view (15° tilt) and a cross sectional SEM micrograph. Big crystallites can be observed on the nanowire surface. The LMSC Christmas card of 2014 is shown in (c). Figure (d) shows a TEM micrograph and SAED image, showing additional diffraction spots due to the crystallites. A STEM-EDX analysis is presented in Figure (e)-(h). From the elemental maps we can observe that the crystallites consist of antimony. We assume that the crystallites were formed during cooldown of the nanowires, where the antimony flux was left open in order to avoid evaporation of antimony from the shell.

In the following experiments were terminated by closing the gallium and antimony fluxes simultaneously, resulting in the absence of antimony crystallites, as shown in Figure A.9. Figure (a)-(c) shows SEM micrographs of an InAs/GaSb sample. First the InAs core was grown for 1 h using standard conditions. Then the the temperature was lowered to 500°C and the GaSb shell was grown for 10 min using a Ga BEP of 2.6E-7 Torr (corresponding to a layer growth rate of 1.1 Å/s) and a Sb BEP of 3.9 E-6Torr. The growth was stopped by closing both sources and the sample temperature was ramped down rapidly. Figure (a) shows a top view (15° tilt) and a cross-sectional micrograph of the nanowires at the center of the sample. Magnified images of the tip and the foot of the nanowires are shown in Figure (b). We observe a nice uniform shell at the tip of the nanowires and lots of faceting at the lower part of the nanowires. Towards the

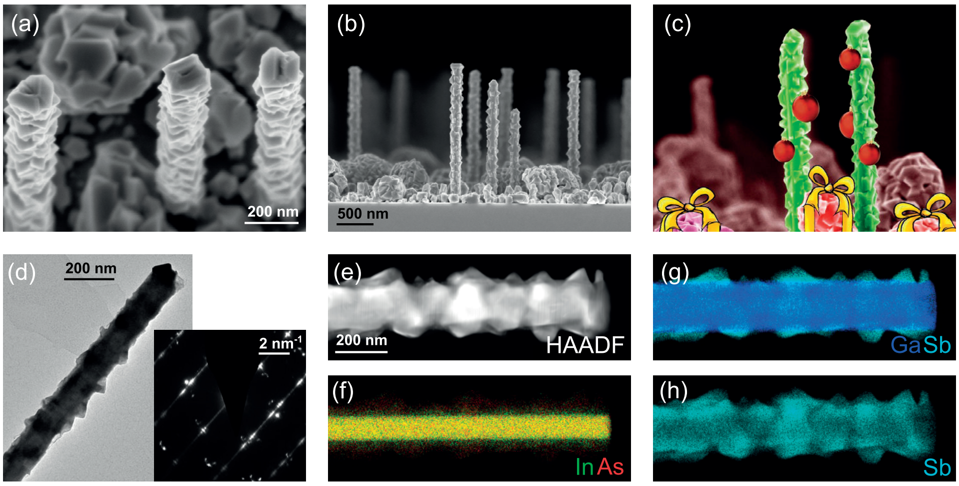

Figure A.8 – InAs/GaSb nanowires: first attempt. (a)-(b) Top view (15° tilt) and cross sectional SEM micrographs. (c) 2014 LMSC Christmas card. (d) TEM micrograph and SAED image. (e)-(h) STEM-HAADF image and EDX elemental maps.

edge of the sample, where, due to the design of our manipulator, the temperature is slightly higher, the shell is slightly nicer. However, the nanowires are significantly shorter. Figure (d) shows a STEM-HAADF image and EDX elemental maps of a nanowire from the same sample. We observe that the InAs core is uniform along the whole nanowire, while the GaSb shell is responsible for the faceting. From the contrast in the HAADF image one can see that the whole nanowire shows a high density of stacking faults. Figure A.9(e) shows SEM micrographs of InAsSb/GaSb nanowires, the core having an antimony content of approximately 20% according to the growth conditions and stacking defect density. For this sample, the GaSb shell is uniform all along the nanowire length, even though the shell growth conditions were the same as for the InAs/GaSb sample presented before. Comparing the results from the two samples, one can consider the following explanations: 1) GaSb preferentially grows with zinc-blende crystal structure. On polytypic InAs it therefore does not grow uniformly. This explanation would be in agreement with the findings from MOCVD grown nanowires, where the GaSb shell growth was suppressed on WZ InAs segments [Namazi15]. However, it is then surprising that the shell at the tip of the InAs/GaSb is nicely uniform, even though the tip is also polytypic. 2) The faceting could be a result of shadowing, and a uniform shell is observed for shorter nanowires. To test this hypothesis we grew long InAsSb/GaSb nanowires. Figure A.9(f)-(g) show SEM micrographs of a sample for which the InAsSb core was grown for 3 h. We observe that most nanowires show a uniform GaSb shell all along the nanowire. The nanowires here have a similar density and are significantly longer than the nanowires presented in (a), thereby excluding shadowing as the only cause for the faceting. 3) As a third option one can consider the lattice mismatch as the cause for faceting. The lattice constants are $a_{InAs} = 6.06\,\text{Å}$ for InAs, $a_{GaSb} = 6.10\,\text{Å}$ for GaSb, and $a_{InSb} = 6.48\,\text{Å}$ for InSb [Ioffe17]. Considering Vegard's law (and

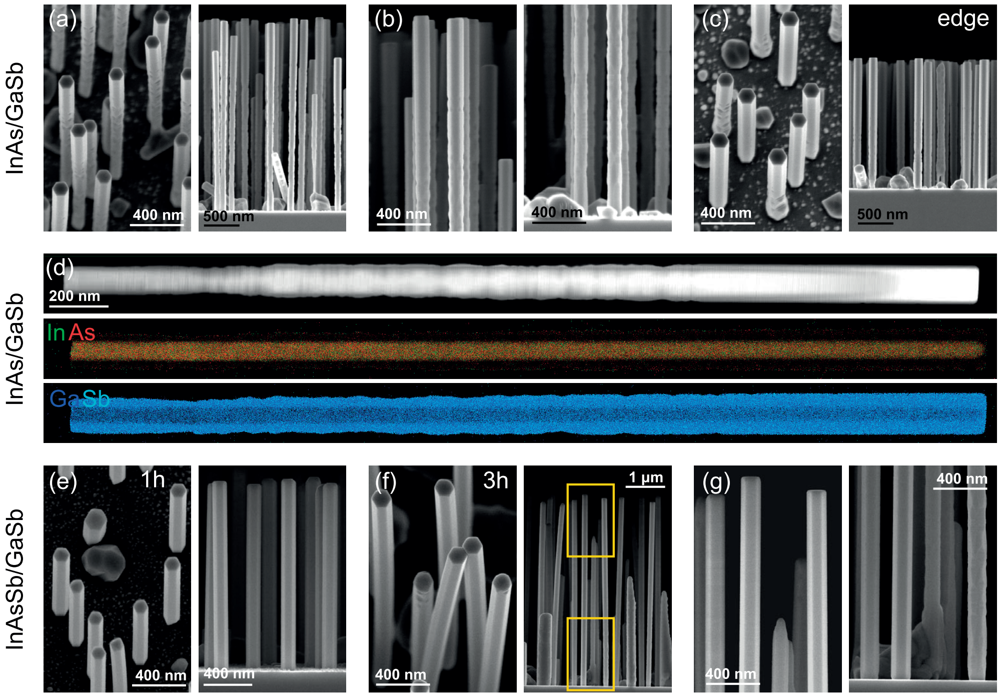

Figure A.9 – InAs/GaSb and InAsSb/GaSb nanowires. (a) Top view (15° tilt) and cross sectional SEM micrograph of an InAs/GaSb sample. (b) Magnified images showing a homogeneous GaSb shell at the tip and irregular faceting at the stem. (c) Images at the sample edge, which corresponds to a slightly higher temperature. (d) STEM HAADF image and EDX maps of a nanowire from the same sample, showing that the faceting can be attributed to the GaSb shell. (e) SEM images from a $InAs_{0.8}Sb_{0.2}$ sample grown for 1 h. (f)-(g) SEM analysis from a InAsSb/GaSb sample grown for 3 h under similar conditions.

no bowing) the lattice constant of $InAs_{0.8}Sb_{0.2}$ can be estimated to be

$$a_{InAs0.8Sb0.2} = 0.2\cdot a_{InSb} + 0.8\cdot a_{InAs} = 6.14\text{Å} \tag{A.1}$$

The lattice mismatch of GaSb-on-InAs can therefore be calculated to be -0.62%, while the lattice mismatch of GaSb-on-$InAs_{0.8}Sb_{0.2}$ would be 0.76%. From this rough estimation the lattice mismatch does not seem to be the root cause either.

In order to further investigate the possibility of growing uniform InAs/GaSb core-shell nanowire samples we also studied the effect of the shell growth temperature, the shell V/III ratio and the nanowire spacing (by changing the SiO_2 thickness).

Figure A.10 (a)-(c) show SEM micrographs of InAs/GaSb samples for which the GaSb shell was grown at different temperatures, while all other growth parameters were kept constant. The approximate shell temperatures of the samples are 460°C, 530°C and 560°C for (a)-(c) respectively. These sample can be compared to the reference sample which was grown at 500°C and is shown in (e). We observe from figure (a) that lowering the shell growth temperature

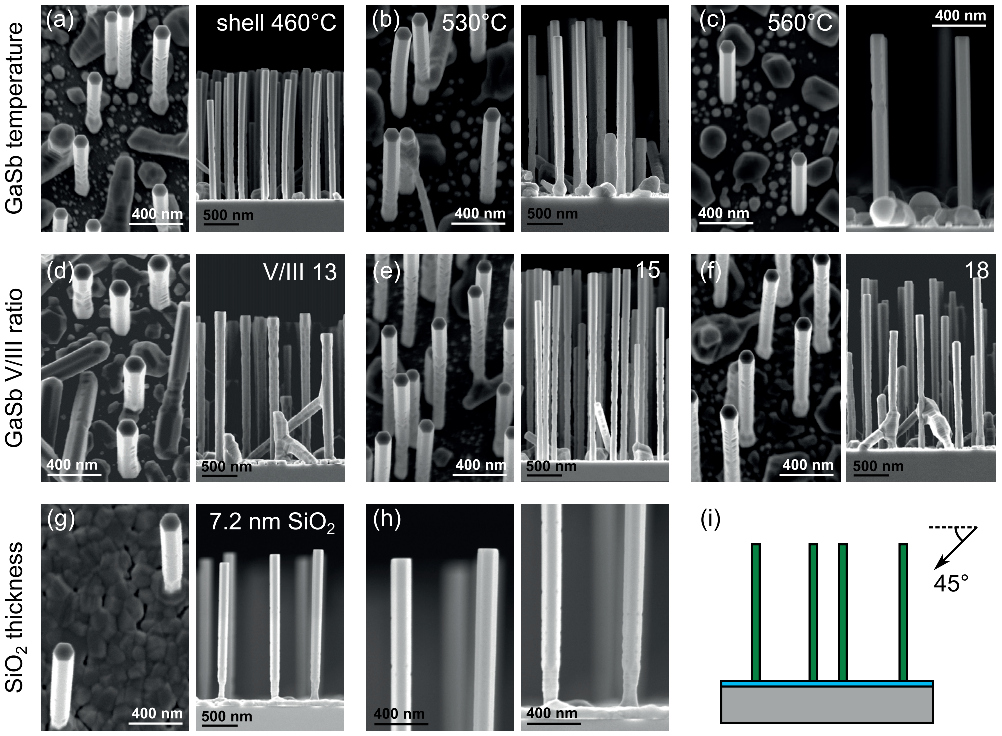

Figure A.10 – Growth conditions of InAs/GaSb nanowires. (a)-(c) Top view (15° tilt) and cross sectional SEM micrographs of a shell growth temperature series. The GaSb shell was grown at 460°C, 530°C and 560°C with a V/III ratio of 15. (d)-(f) SEM analysis of a V/III ratio series. The GaSb shell was grown at 500°C and a Sb/Ga ratio of 13, 15 and 18. The sample presented in (e) is also part of the shell temperature series. (g)-(h) SEM images of a sample grown using a7.2 nm thick SiO_2 instead of 4.5 nm. (i) Schematic of the angle of incoming fluxes in our MBE.

from 500°C to 460°C does not have a positive effect on the shell uniformity. Increasing the temperature to 530°C results in slightly nicer facets, as shown in figure (b). A further increase of temperature to 560° allows to grow a quite uniform shell, as shown in figure (c). However, one should note that also the nanowire density is significantly lower and droplets can be observed on the substrate, suggesting that some of the InAs nanowires evaporated during the shell growth. The shell homogeneity can therefore also be related to the absence of shadowing. Our findings can be compared to the results by Rieger *et al*, who also found a dependence of the GaSb uniformity on the shell growth temperature [Rieger15]. In the article the report on an ideal shell temperature of approximately 360°C, and show that both lower and higher temperatures lead to faceting.

We further studied the influence of the GaSb V/III ratio. So far, all samples were grown at a V/III ratio of 15, as shown in the reference sample in figure A.10(e). To change the V/III ratio we changed the gallium cell temperature, resulting in a V/III ratio of 13 for the sample presented in (d), and a V/III ratio of 18 for the sample presented in (f). Comparing with the reference sample, we observe that a lower V/III ratio to 13 significantly reduces the shell homogeneity, while increasing the V/III ratio to 18 shows little effect. Again, this study can not be analyzed independently from the other growth parameters, since the effective V/III ratio always depends on the growth temperature due to re-evaporation. Due to the higher vapour pressure, it is predominantly the group V material which re-evaporated from the surface, therefore leading to a lower effective V/III ratio at higher growth temperatures.

Finally we also studied substrates with different oxide thickness. Figure A.10(g)-(h) show SEM micrographs of a sample with an oxide thickness of 7.2 nm, which is higher than the standard oxide thickness of 4.5 nm. We observe a significantly lower nanowire density, as expected due to the absence of spontaneous pinhole formation. In terms of the GaSb shell, a higher uniformity can be observed. However, faceting is not completely absent as shown in the magnified images in figure (h). In our MBE system, the incoming fluxes arrive at an angle of 450°, as shown in figure (i). Therefore one would expect shadowing to occur as soon as the nanowire length is equal or higher than the spacing of the nanowires. However, shadowing would only occur during a fraction of the time, due to the sample rotation which is set to 7 rpm in all our experiments. Faceting as observed in figure (h) can therefore not only be a result of shadowing, similar to what was concluded from the growth of long InAsSb/GaSb nanowires in Figure A.9(f)-(g).

In conclusion, we have studied the growth conditions for InAs(Sb)/GaSb nanowires. We have found that the GaSb shell shows faceting when grown around an InAs core nanowire, while in the case of InAsSb core nanowires a homogeneous shell can be obtained. The faceting depends on the exact growth conditions, but so far we have not been able to suppress it completely. Position-controlled growth of nanowires would be helpful in order to be able to exclude shadowing effects and study the effect of different growth parameters independently. Finally, we would like to note that also the position of the gallium and antimony cell may influence the results. In our MBE chamber the two cells are almost on opposite sides of the chamber, therefore creating the need for adatom diffusion in order to create a homogeneous layer.

In order to visualize the core-shell heterostructures we fabricated nanowire cross sections. Figure A.11 shows cross sections of two different InAs/GaSb samples. The first sample was grown with a 30 min waiting time between the core and shell and the shell. During this time, the antimony shutter and valve were open, while waiting for the gallium and antimony cells to heat up to operational temperature. TEM micrographs are shown in figure (a)-(b). The SAED image in figure (c) confirms the alignment in a [111] zone axis. A STEM-HAADF image and EDX maps are shown in figure (d)-(h). As discussed previously, only very little contrast is observed in the HAADF image, since the mass of InAs and GaSb is approximately equal. In the elemental maps in figure (e)-(h) indium, arsenic, gallium and antimony can be clearly distinguished. Interestingly we find that the InAs core of the nanowire is round, rather than hexagonal. This indicates some alloying during the shell growth, and may be related to the waiting step under antimony flux. To analyze our hypothesis, we grew the following samples by changing from InAs growth to GaSb growth immediately without any waiting step. Cross sections of a representative sample are shown in figure A.11 (i)-(l). For this sample, the InAs

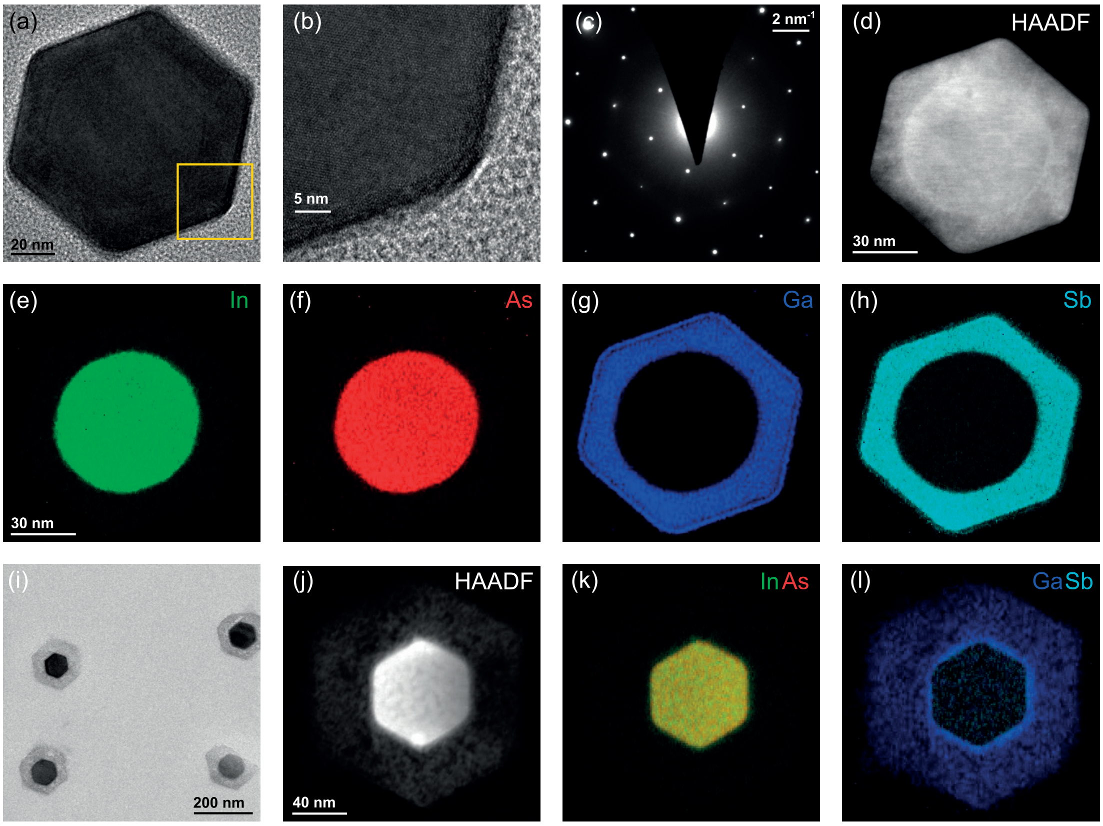

Figure A.11 – InAs/GaSb nanowire cross-sections. (a)-(h) Cross sections of a sample with a 30 min waiting step between the core and the shell growth. (a)-(b) TEM micrographs. (c) SAED image confirming a [111] zone axis. (d) STEM-HAADF image showing a round nanowire core and a hexagonal shell. (e)-(h) EDX elemental maps, confirming a round InAs core and a hexagonal GaSb shell. (i)-(l) Cross sections of a sample for which the shell growth was performed immediately after the core growth. (i) TEM micrograph. (j) STEM-HAADF image showing a hexagonal nanowire core and traces of a hexagonal shell. (k)-(l) EDX elemental maps, showing an InAs core and a Ga shell. There are only traces of Sb left in the shell very close to the nanowire core.

core is found to be hexagonal as expected. One should note, that a different epoxy was used to embed the nanowires for the second cross sections. Using the EPO-TEK OG142-87 UV curable epoxy, it was often difficult to detach the nanowires from the substrate, and most of the substrates broke. Changing to EPON [Epon17], allowed to solve this problem. However in the case of nanowires with a GaSb shell, we found that the epoxy attacks the GaSb. This results in an amorphous shell with a very low antimony content rather than a crystalline GaSb shell, as shown in Figure A.11(i)-(l). So far, no solution has been found to overcome this problem, in particular after protecting the surface with a 10 nm layer of ALD grown TiO_2 layer it was impossible to detach the epoxy from the substrate.

Last but not least we also performed some initial experiments to study the electrical properties of InAs/GaSb core-shell nanowires. We started by contacting the InAs core. Nanowire devices were fabricated following the standard procedure. Before metalization of the contacts, the sample was dipped in the etchant solution in order to remove the GaSb shell, ideally without attacking the InAs core. The etching only takes place in the contact regions, while the rest of the nanowire is covered with the ebeam resist. As an etchant we investigated a KNa-tartrate solution, which has been reported to selectively etch GaSb in a GaSb/GaAs stack [Kim13]. Figure A.12(a) shows an SEM micrograph of a nanowire device after etching for 5 s and stripping the ebeam resist afterwards. The ratio of chemicals was chosen to be ($KNaC_4H_4O_6 \cdot 4H_2O$):H_2O(deionized):HCl(30%):H_2O_2(30%)=0.5 g:250 mL:4 mL:10 mL where the H_2O_2 was added just before the etching. This solution is strongly diluted compared to the work by Kim *et al* [Kim13], because their solution was found to be too strong, and removed the nanowires completely. We observe that the nanowire is etched in the contact openings, however the etching is not selective and seems to attack the InAs core as well. In addition, there is some under-etching as shown in the insert of Figure (a), meaning that the etchant solution can propagate along the interface between the ebeam resist and the substrate. For a first test, we continued using the samples and proceeded with the metalization of the contacts using Cr/Au 20nm/100nm. An SEM micrograph of a finished device is shown in Figure A.12(b). The devices were then tested by I/V measurements and back-gated field-effect measurements. All devices showed ohmic behaviour as shown in Figure A.12(c). Assuming a shell thickness of 15 nm a conductivity of 308±5 S/cm was calculated from 8 devices. The average conductivity therefore is slightly higher compared to standard InAs nanowire, possibly due to a passivation effect of the GaSb shell at the surface. A representative field-effect measurement at a source-drain voltage of 2 mV is shown in Figure A.12(d). We observe an n-type behaviour, confirming that the transport happens in the InAs core. However the gate response is very low compared to measurements on standard InAs nanowires.

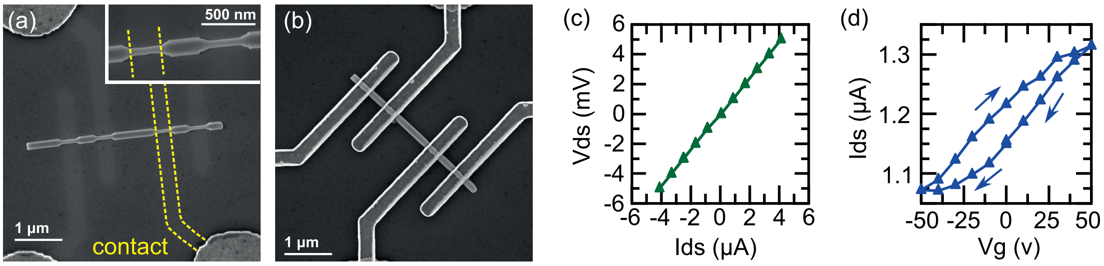

Figure A.12 – InAs/GaSb electrical devices. (a) SEM micrographs of a nanowire where the GaSb has been etched in the contact openings and then the ebeam resist was stripped. (b) SEM micrograph of an InAs/GaSb nanowire device. (c) Current/voltage measurement of the InAs core. (d) Back-gated field-effect measurement.

These preliminary experiments show that it is possible to contact the InAs core of InAs/GaSb core-shell nanowires. Future experiments include finding a selective etch (testing for example NaOH [Rocci16] or ammonia solution NH_{aq} [Fahed16]), studying why the gate response of InAs/GaSb nanowires is significantly lower compared to standard InAs nanowires, and establishing a contacting procedure for the GaSb shell.

B Supporting information of articles

In this section we include the supplementary information for each of the published articles presented in Chapter 4.

Supporting Information: From twinning to pure zinc-blende catalyst-free InAs(Sb) nanowires

Heidi Potts,[†] Martin Friedl,[†] Francesca Amaduzzi,[†] Kechao Tang,[‡] Gözde Tütüncüoglu,[†] Federico Matteini,[†] Esther Alarcon Llado,[†] Paul C. McIntyre,[‡] and Anna Fontcuberta i Morral[*,†]

†*Laboratoire des Materiaux Semiconducteurs, Ecole Polytechnique Federale de Lausanne, 1015 Lausanne*

‡*Department of Materials Science and Engineering, Stanford University, Stanford, California 94305, United States*

E-mail: anna.fontcuberta-morral@epfl.ch

Growth conditions of $\mathrm{InAs}_{1-x}\mathrm{Sb}_x$ nanowires

The nanowires were grown on substrates covered with a thin layer of silicon oxide obtained by spin-coating and annealing hydrogen silsesquioxane (HSQ). We first optimized the thickness of the oxide layer and found that an oxide thickness of 4.5 nm gives a reasonable density of wires and a narrow distribution in diameter and length. The similar morphology of all nanowires, meaning that growth starts almost at the same time, and the absence of a droplet on the nanowire tip are in agreement with the vapor-solid (VS) mechanism proposed by Dimakis *et al*[1] and Hertenberger *et al.*[2] The growth temperature was then optimized for $\mathrm{InAs}_{1-x}\mathrm{Sb}_x$ nanowires with an antimony content of approximately 18 %. Figure 1(a)-

(d) show SEM micrographs of samples grown for one hour at different temperatures while keeping all other growth parameters constant. The dimensions of the samples were studied quantitatively in Figure 1(e). We observe that the ideal growth temperature is around 515-520 °C to get high aspect-ratio nanowires, which is similar to the growth temperature range of InAs nanowires.

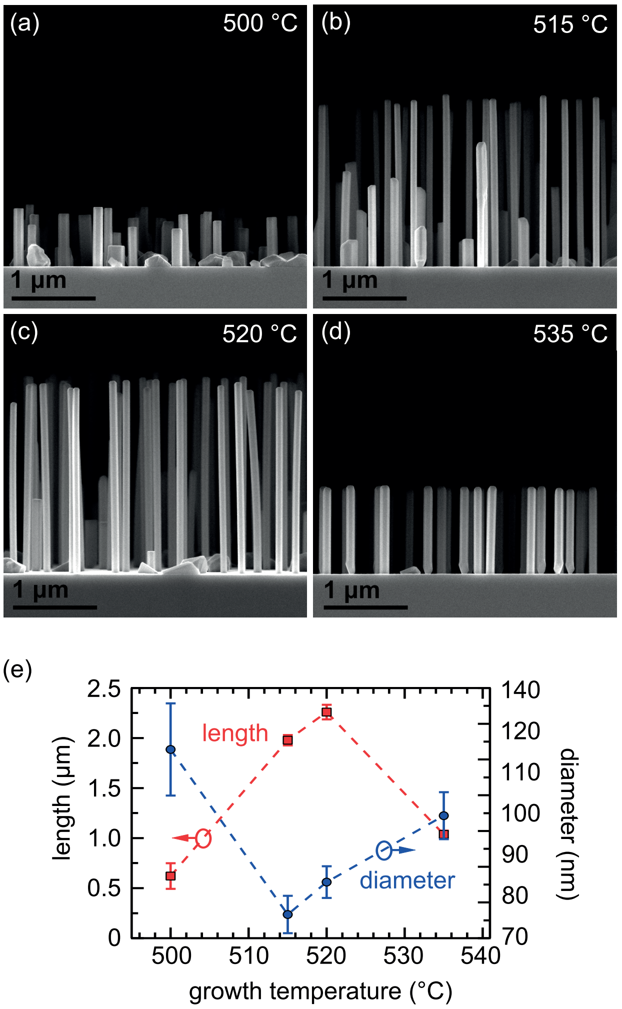

Figure 1: (a)-(d) Cross-sectional SEM micrographs of $InAs_{1-x}Sb_x$ nanowire samples grown for 1 hour at 500 °C, 515 °C, 520 °C and 535 °C respectively. (e) Quantification of the nanowire length and diameter in dependence of the growth temperature.

InAs nanowires show a strong dependence of the morphology on the arsenic pressure. Figure 2(a)-(d) show SEM micrographs of samples grown for 1 hour at different arsenic pressures while keeping all other growth parameters constant. Increasing the arsenic flux increases the nanowire length and decreases the diameter as shown in Figure 2(e). Increasing the antimony flux on the other hand has an opposite effect on the nanowire morphology as discussed in the main article.

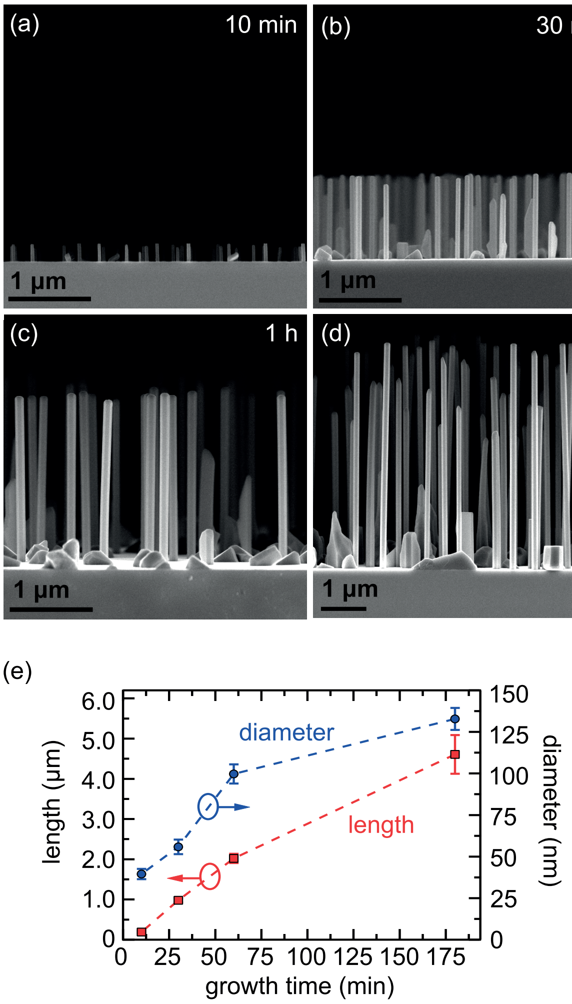

Figure 2: (a)-(d) Cross-sectional SEM micrographs of InAs nanowire samples grown for 1 hour at an arsenic pressure of 1E-6 Torr, 1.9E-6 Torr, 2.5E-6 Torr and 3.5E-6 Torr respectively. (e) Quantification of the nanowire length and diameter in dependence of the growth temperature.

InAs$_{1-x}$Sb$_x$ nanowire cross-sections show a non-uniform antimony content and we observe a core-shell like structure as discussed in the main article. Time series were performed to study the origin of this finding. SEM micrographs are shown in Figure 3(a)-(d) for samples with an antimony content of approximately 18 %. With time the nanowire length increases but also the diameter increases as shown in Figure 3(e). We conclude that the increase in diameter and the non-uniform antimony content can be explained by radial overgrowth. No tapering is observed even for long growth times, indicating that nuclei formed on the nanowire facets are highly unstable and grow laterally on the surface until the monolayer is completed.

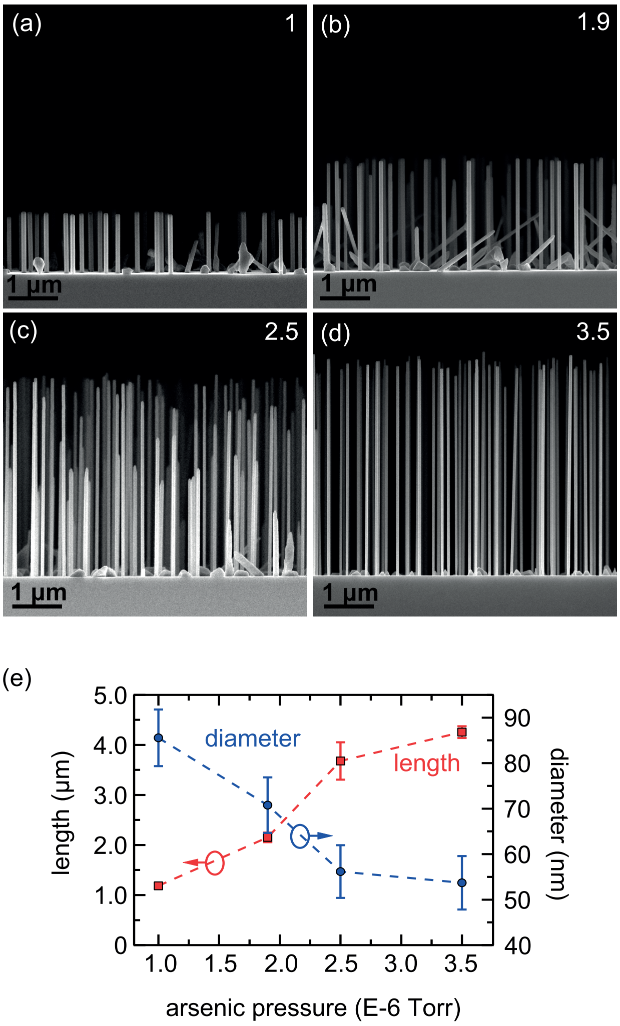

Figure 3: (a)-(d) Cross-sectional SEM micrographs of $InAs_{1-x}Sb_x$ nanowire samples grown for 10 min, 30 min, 1 hour and 3 hours respectively. (e) Quantification of the nanowire length and diameter in dependence of the growth temperature.

Electrical measurements

General remarks

All electrical measurements presented in the paper were performed at room temperature and atmospheric pressure but we also studied samples in vacuum and observed that the hysteresis was present even after leaving the samples vacuum (4E-6 mbar) for over 24 hours, indicating that it is not (or not only) related to surface adsorption. In the main article we report on the conductivity in order to compare InAs and InAsSb devices independent of the nanowire/device dimensions. For further information on the transistor behaviour we are presenting current measurements in Figure 4(a)-(b) for a representative InAs and InAsSb devices respectively (for simplicity only the forward sweep is shown). This representation allows us to clearly distinguish InAs and InAsSb devices, InAs devices show n-type transistor characteristics, while InAsSb devices show much smaller gate control and cannot be turned off with the back gate. For the alumina covered nanowires the top gate does not cover the full nanowire and we therefore get a significant contribution from the ungated nanowire on both sides of the top gate. Figure 4(c) shows a schematic of the device dimensions. For transconductance data extraction we treat the ungated nanowire section as series resistance. We first measured the nanowire resistance at zero gate voltage $R_{total}(@V_g = 0)$ and then calculate the ungated series resistance by $R_{series} = R_{total}(@V_g = 0) \cdot (1 - L_{gate}/L_{total})$. At the point of maximum transconductance we calculated the voltage drop across this ungated portion of the nanowire as $V_{series} = I(@g_{m,max}) \cdot R_{series}$. This then gave us the corrected voltage drop across only the gated portion of the nanowire $V_{ds,eff} = V_{ds} - V_{series}$. Using $V_{ds,eff}$ as source drain voltage we then calculated the mobility by the standard peak transconductance. We also investigate the transfer characteristics of alumina coated wires by applying a back gate voltage to devices with and without a top gate. None of the devices show hysteresis, confirming that the alumina coating successfully prevents hysteresis. Devices without a top gate show rather weak gate control as shown for an InAs device in Figure 4(d) blue curve, which can be explained by the overall thicker gate dielectric. In contrast to that, top-gated devices show a very strong change in conductivity when sweeping the back gate while leaving the top gate floating as shown in Figure 4(d) green curve. This finding can be explained by coupling of the back gate and the top gate, therefore enhancing the overall gating effect. Concerning the device morphology we found that some nanowires change shape during electrical measurements. Figure 4(e) and (f) show nanowire devices before after electrical measurements, showing that the original hexagonal morphology (Figure 4(e)) can change and become round (Figure 4(f)). Surprisingly these nanowires are still conductive. To avoid artifacts all devices were imaged after the measurement and only nanowires which preserve their hexagonal shape are included for data analysis.

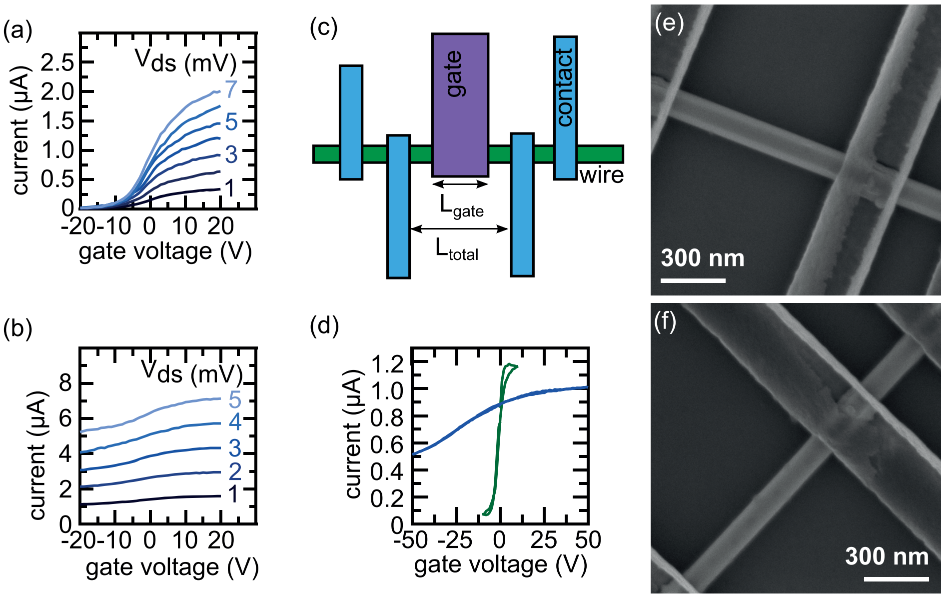

Figure 4: (a) IV curve for an InAs device. (b) IV curve for an InAsSb device with 20% antimony. (c) Device morphology of our top gated devices. (d) Back-gated measurements with alumina coated nanowires. Blue: InAs device without a top gate. Green: InAsSb device with a top gate, where the top gate was left floating during the back-gate sweep. (e)-(f) Nanowire device showing the original hexagonal shape of the wire and a wire with shows a round morphology after electrical measurements.

Pulsed gate voltage technique

When sweeping the gate voltage, strong hysteresis was observed for all wires. In order to reduce the hysteresis we performed measurements with a pulsed gate voltage as proposed by Mattmann et al.[3] Figure 5(a) shows the applied gate voltage sweep (red) and the resulting current measurement (blue) over time. For simplicity, a gate voltage step of 10 V was used for this graph (instead of 1V for the actual measurements). The data of interest is highlighted by dots. After every measurement the gate voltage was first reversed and then ten measurements at zero gate voltage were done. Figure 5(b) shows a gate sweep for an InAs nanowire with (solid line) and without (dotted line) pulsing the gate voltage. We observe that the hysteresis is significantly reduced but not completely suppressed. Our biggest concern is the change in baseline current which results in a difference in conductivity before and after the gate sweep. This change is more pronounced for pulsed measurements since the overall measurement time is much longer. The extraction of mobility and on-off ratio from the gate sweep will therefore overestimate the actual result. In Figure 5(c) the same comparison is done for an alumina coated InAs nanowire. Here the hysteresis is negligible when using the pulsed gate sweep and no change in baseline current is observed. Interestingly the sign of the hysteresis is opposite compared to bare InAs nanowires: for alumina coated wires a lower current is measurement positive sweep direction, while in bare InAs nanowires the current in positive sweep direction is larger. This confirms that trapped charges in the oxide which are responsible for hysteresis are of opposite sign in the SiO_2 substrate and the Al_2O_3 coating.[4]

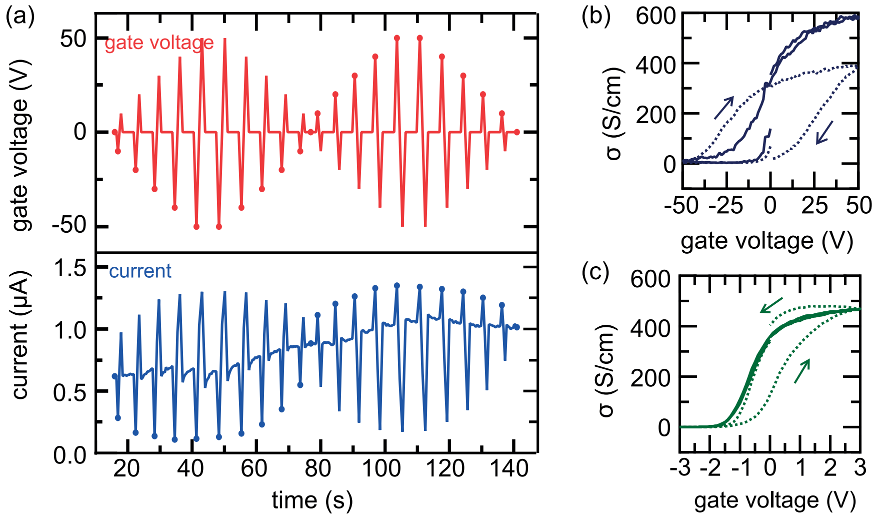

Figure 5: (a) Pulsed measurement data. The applied gate voltage is shown in red and the measured current is shown in blue. (b)-(c) Comparison of non-pulsed (dashed line) and pulsed (solid line) measurement on the same the device for non-coated and alumina coated InAs nanowires respectively.

Additional measurement data

The following table gives additional information on the devices presented in the main text:

	InAs	InAsSb	InAs-Al_2O_3	InAsSb-Al_2O_3
Device length (nm)	939	940	1125	1093
Gated length (nm)	939	940	498	508
Nanowire diameter (nm)	89	117	101	145
V_{ds} ($V_{ds,eff}$) (mV)	2	2	2 (1.4)	2 (1.4)
Peak transcond. (A/V)	1.9E-8	3.5E-8	3.07E-7	3.46E-7
Subtreshold swing (V/dec)	3.4	8.3	0.45	2.24

Raman spectroscopy

We have considered the standard dielectric theory in the formalism of Hon and Faust as theoretical model of the LOPCM lineshapes.[5] The differential Raman cross section from the coupled phonon-plasmon modes of a doped two mode ternary alloy $A_xB_{1-x}C$ has the form:[6]

$$\begin{aligned}\frac{\partial^2\sigma}{\partial\omega\partial\Omega} \propto (n_\omega+1)\mathrm{Im}\Bigg\{ \frac{-1}{\epsilon(\omega,x)}\Bigg[& \frac{1}{4\pi} + 2\frac{A_1}{\epsilon_{\infty,1}}\chi_1(\omega,x) + 2\frac{A_2}{\epsilon_{\infty,2}}\chi_2(\omega,x) \\ & - 4\pi\left(\frac{A_1}{\epsilon_{\infty,1}} - \frac{A_2}{\epsilon_{\infty,2}}\right)^2 \chi_1(\omega,x)\chi_2(\omega,x) \\ - \left(1 + \frac{4\pi}{\epsilon_\infty(x)}\chi_e(\omega)\right)\epsilon_\infty(x) & \left[\left(\frac{A_1}{\epsilon_{\infty,1}}\right)^2 \chi_1(\omega,x) + \left(\frac{A_2}{\epsilon_{\infty,2}}\right)^2 \chi_2(\omega,x)\right]\Bigg]\Bigg\} \qquad (1)\end{aligned}$$

where n_ω the Bose-Einstein distribution, $\epsilon(\omega,x) = \epsilon_\infty(x) + 4\pi(\chi_1(\omega,x) + \chi_2(\omega,x) + \chi_e(\omega))$ is the dielectric function of the alloy with $\epsilon_\infty(x) = x\epsilon_{\infty,1} + (1-x)\epsilon_{\infty,2}$ the average high-frequency dielectric function, the i-sublattice contribution to the susceptibility $\chi_i(\omega,x) = x_i \frac{\epsilon_{\infty,i}}{4\pi}\frac{(\omega^0_{LO,i})^2-(\omega^0_{TO,i})^2}{((\omega_{TO,i})^2-\omega^2-i\omega\Gamma_i)}$ with Γ_i the phenomenological damping constant, and $\omega^0_{TO,i}$ and $\omega^0_{LO,i}$ are the frequencies of TO and LO modes of the pure end-member compounds, whereas the $\omega_{TO,i}$ is the TO phonon frequency of the alloy i-sublattice and χ_e the electronic susceptibility contribution, n_ω the Bose-Einstein distribution, and $A_i = C^0_i \frac{\omega^2_{TO,i}}{(\omega^0_{LO,i})^2-(\omega^0_{TO,i})^2}$ with C^0_i being the Faust-Henry coefficient for the pure member compound.

We calculate the electronic susceptibility using the Hydrodynamical model [7] :

$$\chi_e = -\frac{\epsilon_\infty}{4\pi}\frac{\omega_p^2}{\omega^2 - <v^2> q + i\omega\Gamma_e} \qquad (2)$$

where ω_p is the plasma frequency ($\omega_p^2 = \frac{4\pi}{\epsilon_\infty}\frac{Ne^2}{m^*}$), Γ_e is the damping constant related to the lifetime of the plasmon, $<v^2>$ the electron mean square velocity and q the wavevector. Considering the low band gap energy of $\mathrm{InAs}_{1-x}\mathrm{Sb}_x$, we expect that the non-parabolicity of the conduction band is not negligible. For this reason, we use the Kane two band model to calculate the electronic dispersion: [7]

$$E(k) = \frac{E_G}{2}\left[\sqrt{1 + \frac{4}{E_G}\frac{\hbar^2k^2}{m^*}} - 1\right] \qquad (3)$$

In the following table we summarize the input parameters for the LOPCM line-shape model discussed above:

Symbol	Description	Value	Ref.
$\omega^0_{LO,InAs}$	LO, InAs	235 cm^{-1}	*
$\omega^0_{TO,InAs}$	TO, InAs	214 cm^{-1}	*
$\omega^0_{LO,InSb}$	LO, InSb	191 cm^{-1}	[8]
$\omega^0_{TO,InSb}$	TO, InSb	180 cm^{-1}	[8]
$\omega_{TO,InAs}$	TO, InAs-like	211 cm^{-1}	*
$\omega_{TO,InSb}$	TO, InSb-like	180 cm^{-1}	[8]
Γ_{InAs}	InAs phonon damping constant	4 cm^{-1}	[9]
Γ_{InSb}	InSb phonon damping constant	12 cm^{-1}	[9]
C^0_{InAs}	InAs Faust-Henry coefficient	-0.61	[9]
C^0_{InSb}	InSb Faust-Henry coefficient	-0.36	[9]
$m^*(x)$	electron effective mass	$(0.023 - 0.039x + 0.03x^2)\mathrm{m}_0$	[10]
$\epsilon_{\infty,InAs}$	InAs high-frequency dielectric constant	12.2	[9]
$\epsilon_{\infty,InSb}$	InSb high-frequency dielectric constant	15.7	[9]
$E_G(x)$	Bandgap energy	$0.41 - 3.4 \cdot 10^{-4}\mathrm{T}^2/(210+\mathrm{T}) - 0.876$ $+0.70x^2 + 3.4 \cdot 10^{-4}\mathrm{T}x(1-x)$ eV	[11]

* present work

Figure 6 shows a comparison of the Raman spectra obtained from alumina coated and uncoated InAs and InAsSb nanowires. Both for InAs and InAsSb wires we observe a downshift of the surface optical modes. This shift is expected, since the position of the SO mode depends on the wire diameter and on the dielectric constant of the medium surrounding the wire. For InAsSb nanowires, the spectra do not show any other differences, resulting in the same extracted electron concentration and mobility. For InAs nanowires we observe that the high frequency coupled mode L_+ disappears for alumina coated nanowires (the peak is not visible outside the reported range either). One should note that the free carrier density determines not only the position of the coupled modes but also their character. For an increasing carrier concentration, the high frequency mode changes from a phonon-like behaviour to a mixed character between phonon and plasmon, resulting in a broader peak. The increased width of the high frequency mode, along with a possible overlap with the second order peak of silicon at 300 cm^{-1}, would make it difficult to resolve the L_+ peak. The absence of the peak therefore suggests an increased carriers density, but it is not possible to estimate a value for it.

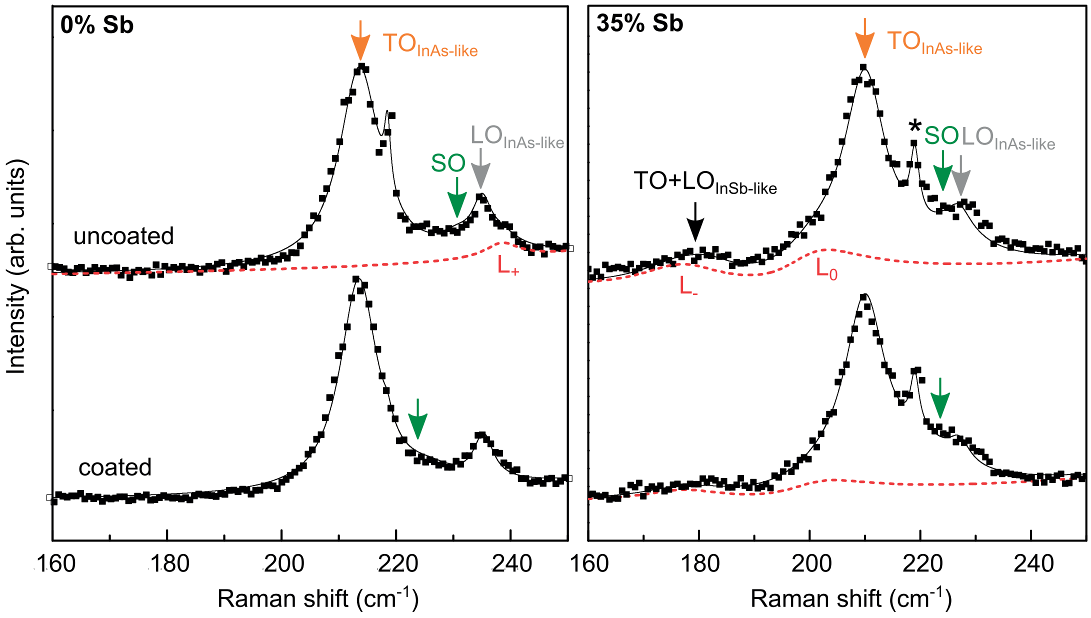

Figure 6: Raman spectra of InAs nanowires and of InAsSb nanowires with x=0.35 coated with alumina and uncoated. The solid lines is the convolution of the ternary modes with a Lorentzian profile and the coupled modes lineshape obtained by fitting the model.

References

(1) Dimakis, E.; Laehnemann, J.; Jahn, U.; Breuer, S.; Hilse, M.; Geelhaar, L.; Riechert, H. *Crystal Growth & Design* **2011**, *11*, 4001–4008.

(2) Hertenberger, S.; Rudolph, D.; Bolte, S.; Doeblinger, M.; Bichler, M.; Spirkoska, D.; Finley, J. J.; Abstreiter, G.; Koblmueller, G. *Applied Physics Letters* **2011**, *98*, –.

(3) Mattmann, M.; Roman, C.; Helbling, T.; Bechstein, D.; Durrer, L.; Pohle, R.; Fleischer, M.; Hierold, C. *Nanotechnology* **2010**, *21*, 185501.

(4) Mallorqui, A.; Alarcon-Llado, E.; Mundet, I.; Kiani, A.; Demaurex, B.; De Wolf, S.; Menzel, A.; Zacharias, M.; Fontcuberta i Morral, A. *Nano Research* **2015**, *8*, 673–681.

(5) Hon, D. T.; Faust, W. L.; Spitzer, W. G.; Williams, P. F. *Phys. Rev. Lett.* **1970**, *25*, 1184–1187.

(6) Cuscó, R.; Artús, L.; Hernández, S.; Ibáñez, J.; Hopkinson, M. *Phys. Rev. B* **2001**, *65*, 035210.

(7) Nowak, U.; Richter, W.; Sachs, G. *physica status solidi (b)* **1981**, *108*, 131–143.

(8) Li, Y. B.; Dosanjh, S. S.; Ferguson, I. T.; Norman, A. G.; de Oliveira, A. G.; Stradling, R. A.; Zallen, R. *Semiconductor Science and Technology* **1992**, *7*, 567.

(9) Cuscó, R.; Alarcón-Lladó, E.; Artús, L.; Hurst, W. S.; Maslar, J. E. *Phys. Rev. B* **2010**, *81*, 195212.

(10) ioffe semiconductors database. `http://www.ioffe.ru/SVA/NSM/Semicond/InAsSb/basic.html`.

(11) Rogalski, A. *New Ternary Alloy Systems for Infrared Detectors*; SPIE press monographs; SPIE Optical Engineering Press, 1994.

Supporting Information: Tilting catalyst-free InAs nanowires by 3D twinning and unusual growth directions

Heidi Potts,[†] Youri van Hees,[†,‡] Gözde Tütüncüoglu,[†] Martin Friedl,[†]
Jean-Baptiste Leran,[†] and Anna Fontcuberta i Morral[*,†]

†*Laboratoire des Materiaux Semiconducteurs, Ecole Polytechnique Federale de Lausanne, 1015 Lausanne*

‡*Institute of Applied Physics, Eindhoven University of Technology, 5600 MB Eindhoven, The Netherlands*

E-mail: anna.fontcuberta-morral@epfl.ch

With this document we provide supporting information about the origin of tilted self-catalyzed InAs nanowires. Multiple-order 3D twinning is explained with a cube model and a complete table with projection angles of all low index crystalline orientations is given. We also show more TEM analysis of nanowires starting with an unusual crystal structure, and give some information how the crystal structure depends on the growth conditions, composition, and nanowire length. In the end we also present the existence of tilted nanowires in dependence on the growth temperature and HSQ silicon oxide thickness.

3D twinning and projection angles

In the main article we explained how multiple-order 3D twinning can lead to <111> directions in unusual orientations. Figure 1(a) shows a cube model[1] oriented with the $[\bar{1}\bar{1}\bar{1}]$, direction pointing up, as expected for a seed crystal on a GaAs(111)B substrate. The <111>B directions are highlighted in red. Conventionally nanowire growth now occurs vertical on the substrate following the [$\bar{1}\bar{1}\bar{1}$], direction. However in a seed crystal also other <111> facets could form. After a twin around a non-vertical <111> direction the cube exhibits facets in other orientations. In Figure 1 we show a twin around the [$\bar{1}11$] direction. In the rotated cube, the facet which was originally in [$11\bar{1}$] direction is now pointing in (-1,-5,1) direction with respect to the original coordinate system. A nanowire growing in this new <111>B direction would then show a top view projection angle of α=79.1° and a cross sectional projection angle of β=74.2°. The real angle γ with respect to [$\bar{1}\bar{1}\bar{1}$] is 56.3°. Please note that in this case the twin occurs around a direction which is pointing into the substrate. This may not be favorable, but it can be possible for the case of relatively large seed crystals. Otherwise also twins around <111>A directions (which are pointing in opposite direction out of the substrate) would lead to the same rotated crystals. Figure 1(b)-(c) show SEM micrographs of nanowire samples with a high density of tilted nanowires. Statistic about the occurrence of specific projection angles were already discussed in the main article. Here we show two additional images in order to point out that tilted nanowires can have very smooth facets similar to vertical nanowires, but often they exhibit rough facets as shown in (c). Further analysis is needed to study the origin of the change of facet morphology.

In order to identify tilted nanowires in SEM micrographs a detailed calculation of projection angles is necessary. As explained in the main article we define the top view projection α as the angle between the nanowire projection onto the (111) plane and the [$\bar{2}11$] or the [$2\bar{1}\bar{1}$] direction, and the cross sectional projection angle β as the angle between the projection onto the (0-11) plane and the [$\bar{2}11$] or the [$2\bar{1}\bar{1}$] direction. The real angle γ is defined as the angle between the nanowire direction and the vertical growth direction [$\bar{1}\bar{1}\bar{1}$]. In table 1 we give all projection angles and real angles for low index crystalline orientations, as well as the angles for <111>B directions after 3D twinning. As discussed in the main article, we observe that certain projection angles can be explained by several nanowire orientations,

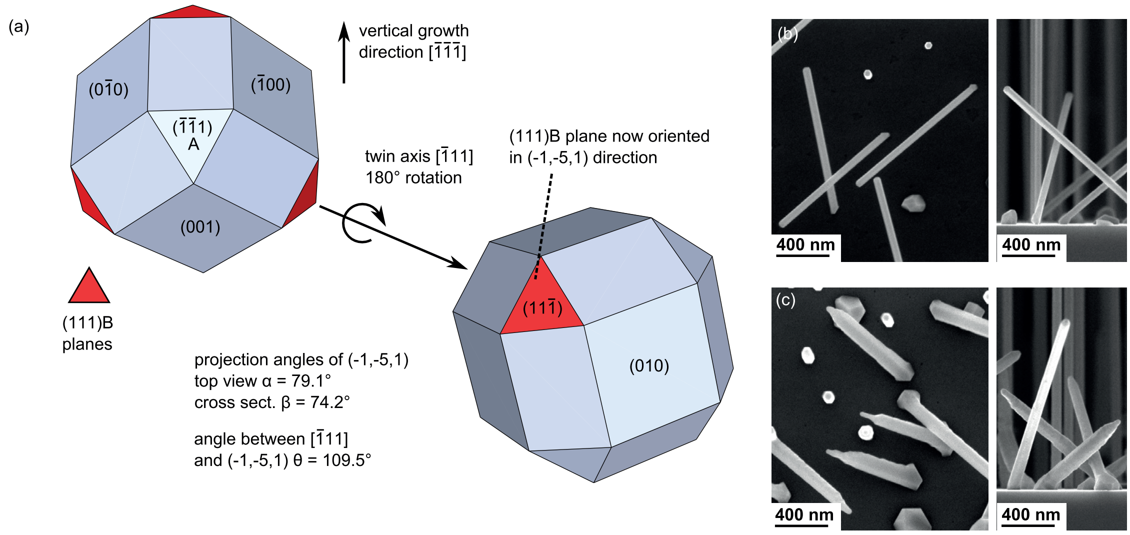

Figure 1: (a) Cube model of a 3D twin. (b)-(c) Top-view and cross-sectional SEM micrographs showing samples with tilted nanowires. The facets of the nanowires can be flat or rough.

e.g. a top-view projection angle of α=79.1° can be observed for <112> oriented nanowires as well as for nanowires after a first order 3D twin. But there are also projection angles which are unique for 3D twinned nanowires or other unconventional growth directions, for example a cross-sectional projection angle of β=41.5° is unique for 3D twinned nanowires, while β=54.7° indicates <110> and β=80.0° indicates <112>.

Table 1: Projection angles of all low-index crystalline orientations and 3D twinned directions. For simplicity, only the projection angles of nanowires above the substrate plane are given. 3D twinned* denotes orientations which are twinned around <111>before 3D twinning (odd number of 180° rotations).

direction	top view proj. α	cross sectional proj. β	real angle γ
<100>	0°, 60°	35.3°	54.7°
<110>	0°, 30°, 60°, 90°	0°, 54.7°, 70.5°, NA	35.3°, 90°,
<112>	0°, 19.9°, 40.9°, 60°, 79.1°	0°, 29.5°, 35.3°, 70.5°, 80°	19.5°, 61.9°, 90°
<111>A	0°, 60°	35.3°, 19.5°	70.5°
3D twinned	19.1°, 40.9°, 79.1°	35.3°, 41.5°, 74.2°	56.3°
3D twinned*	10.9°, 49.1°, 70.9°	35.3°, 41.5°, 74.2°	56.3°

TEM analysis

3D twinning can be observed as a change of growth direction at the foot of tilted nanowires. Twinning defects which are perpendicular to the growth front can be used as an indication of the growth direction. Here we show a few more nanowires which exhibit twin planes non-perpendicular to the final growth direction. Figure 2(a) shows a low resolution TEM micrograph of a nanowire with a particular shape at the foot, as commonly observed for tilted nanowires. Figure 2(b) shows a magnified image of the nanowire foot. In the high resolution TEM micrographs in Figure 2(c)-(d) we observe a change in twin orientation. Fast Fourier transform (FFT) images of three parts of the foot are presented in (e)-(g). In (e) we observe a pure zinc-blende region which can be indexed assuming a $[\bar{1}10]$ zone axis. Figure (f) shows predominantly wurtzite stacking with stacking defects perpendicular to the nanowire elongation. Figure (g) shows a FFT image at the bottom of the nanowire, showing twins at an 110° angle with respect to the nanowire elongation. The new nanowire direction can explained by assuming a 180° rotation of the original $[11\bar{1}]$B direction around $[1\bar{1}\bar{1}]$. The final nanowire elongation points then in (-1,-5,1) direction with respect to the original substrate coordinate system. In Figure 2(d) we observe that the interface between

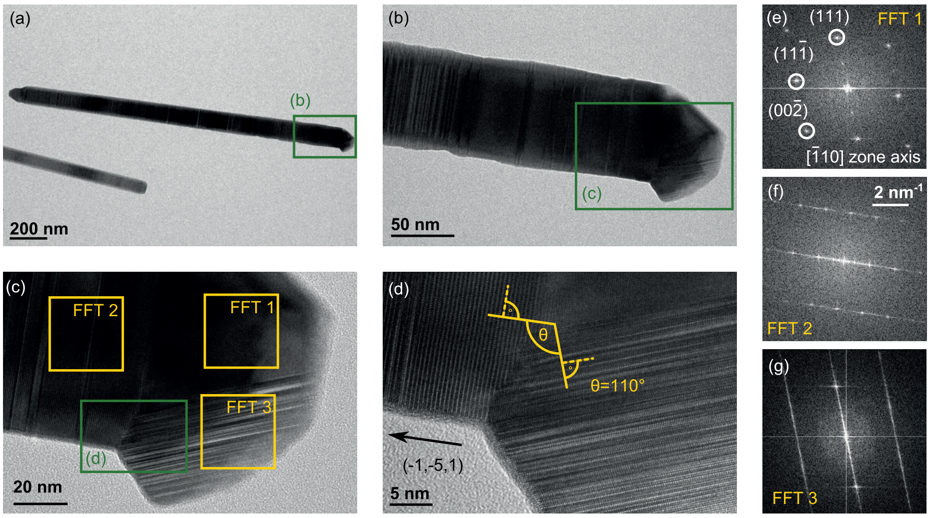

Figure 2: TEM micrographs and FFT images of a nanowire showing a change of growth direction at the nanowire foot.

the twinned region at the bottom and the nanowire elongation is rough, suggesting that two crystals of different orientation have merged here.

We find that twins which are non-perpendicular to the nanowire elongation can sometimes exist if the nanowire foot has a uniform morphology. TEM Micrographs of three different nanowires are shown in Figure 3. All three nanowires show twin planes at an 110° angle with respect to the nanowire elongation. While the first two nanowires only exhibits one additional orientation, the third nanowire shows a more complicated behaviour.

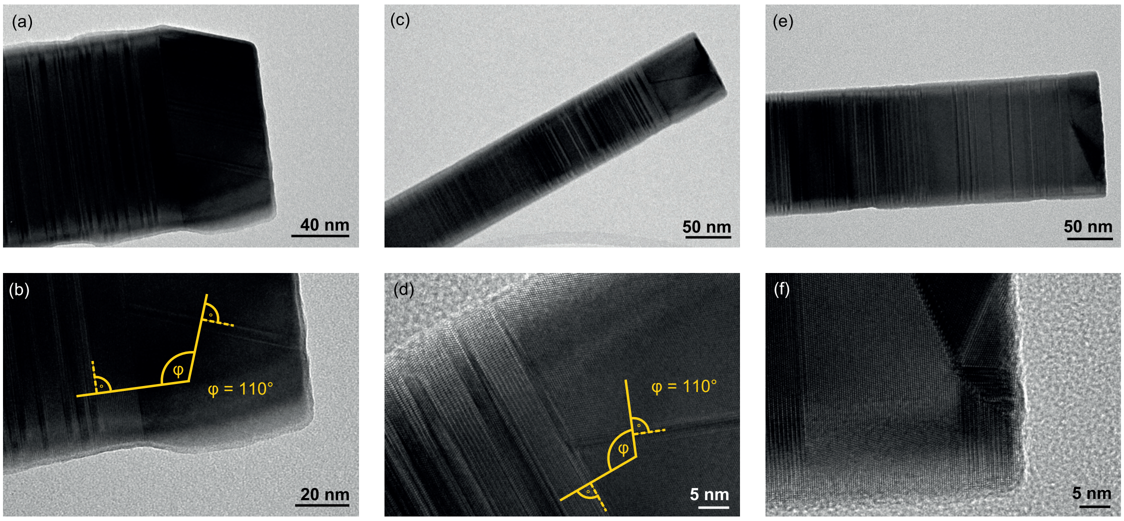

Figure 3: TEM micrographs of three different nanowires showing a change of growth direction at the nanowire foot. Overview micrographs are presented in the top row and high resolution micrographs in the bottom row.

As shown in the main article, we also observe nanowires growing in other low index crystalline orientations. The most common direction is $<112>$. Figure 4 shows TEM micrographs of two other nanowires which were found to grow along a $<1\bar{1}\bar{2}>$ direction. Figure 4(a)-(c) show a nanowire which is zincblende with only one rotational twin parallel to the growth direction. Comparing the nanowire axis with the indexed SAED pattern, confirms that the nanowire growth direction was $<1\bar{1}\bar{2}>$. Please note that the zone axis cannot be defined due to the existence of the two twin orientations. Figure 4(d)-(f) show a nanowire which is zincblende with two different twin orientations and a thin wurtzite section in between. The existence of both ZB and WZ stacking can also be observed in the diffraction pattern. At the tip of the wire a droplet in a different crystalline orientation can be observed. Between the main nanowire and the droplet a rotational twin is found. The angle corresponds to the $<1\bar{1}\bar{1}>$ direction, which forms an angle of 20° with the $<1\bar{1}\bar{2}>$ growth direction.

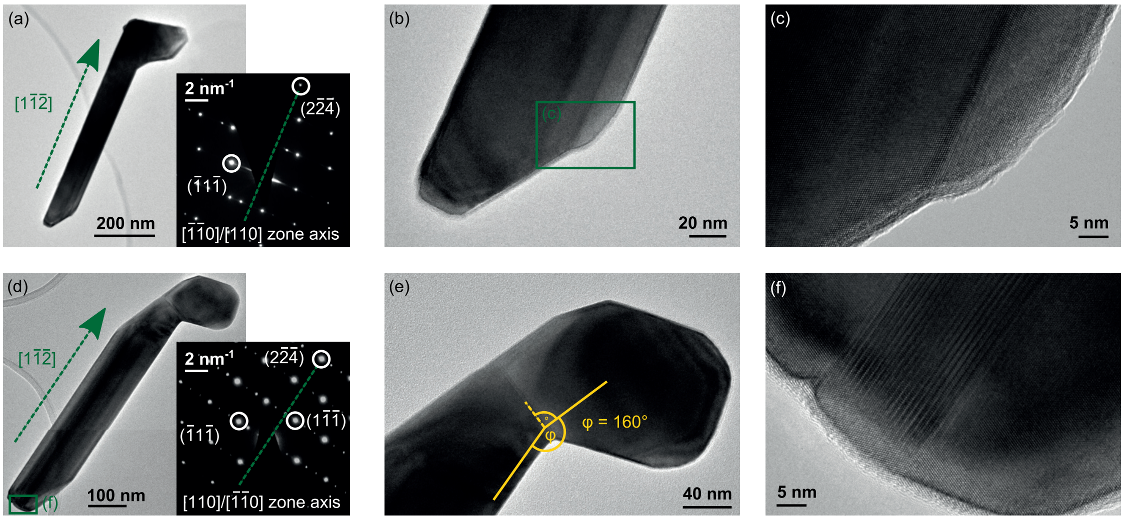

Figure 4: TEM micrographs of two nanowires growing in $<1\bar{1}\bar{2}>$ direction. (a)-(c) Nanowire which is mostly zincblende, with one rotational twin near the right facet. (d)-(f) Nanowire which is mostly zincblende with a thin wurtzite section in the center of the nanowire, running all along it's length.

In the main article we discussed how the existence of tilted nanowires may be related to the crystal structure at the nanowire foot. In Figures 4(a)-(c) we show cross-sectional SEM micrographs of nanowires grown at low V/III ratio, high V/III ratio and InAsSb nanowires with 35% antimony. Tilted nanowires are only observed in the first sample. Figures 4(d)-(f) show high resolution TEM micrographs and selected area electron diffraction (SAED) images of the respective nanowires. For the nanowires grown under low V/III ratio we observe that the crystal structure is mostly zinc-blende with rotational twins (Figure (d)). At higher arsenic pressure long wurtzite sections can be observed, in particular at the beginning of growth (Figure (e)). Incorporation of antimony strongly suppresses the formation of twins, [2] resulting in a pure zinc-blende crystal structure as shown in Figure (f). As discussed in the main text, incorporation of antimony ensures all vertical nanowires by suppressing twin formation completely. At high arsenic pressure no tilted nanowires are observed, which can be attributed to an initiation of growth without a droplet, also favouring the formation of wurtzite.

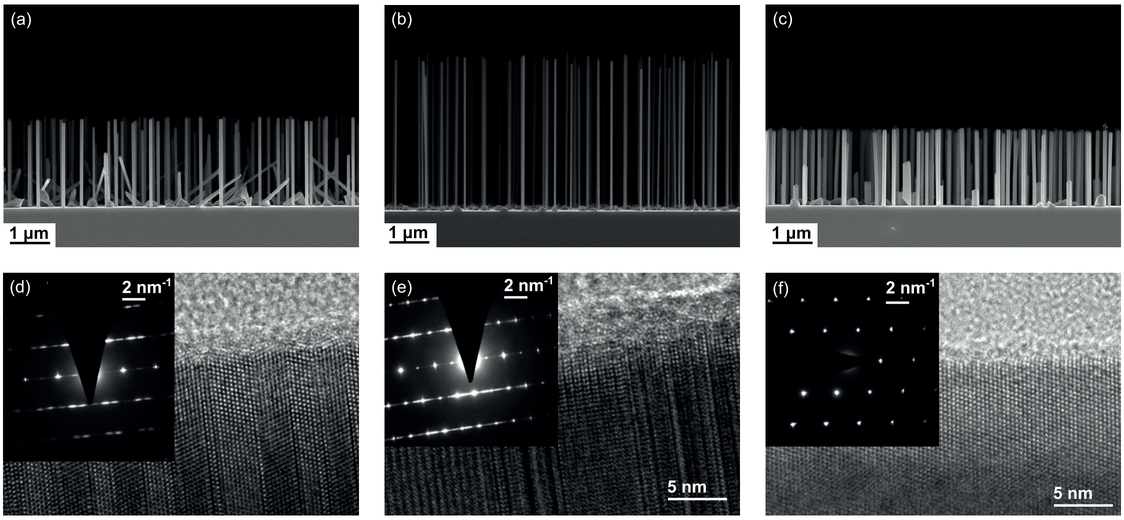

Figure 5: Cross-sectional SEM micrographs and high resolution TEM micrographs of different nanowire samples. (a) Nanowires grown at low V/III ratio. (b) Nanowires grown at high V/III ratio. $\mathrm{InAs}_{1-x}\mathrm{Sb}_x$ nanowires with 35% antimony.

The crystal structure of nanowires usually changes slightly along the nanowire elongation. Figure 5(a)-(c) show low resolution TEM micrographs of a nanowire grown at very high V/III ratio. High resolution micrographs and SAED images are presented in Figure 5(d)-(f). We observe a pure wurtzite section at the foot of the nanowire and then a change towards zinc-blende stacking with rotational twins toward the tip. The observations are supported by the SAED images. The long pure wurtzite section shown here is particular for nanowires grown under very high V/III ratio, while the trend of more wurtzite at the early stages of growth can be observed in all nanowires. We assume this is related to the very thin nanowire diameter at the beginning of growth, which then increases due to radial overgrowth.

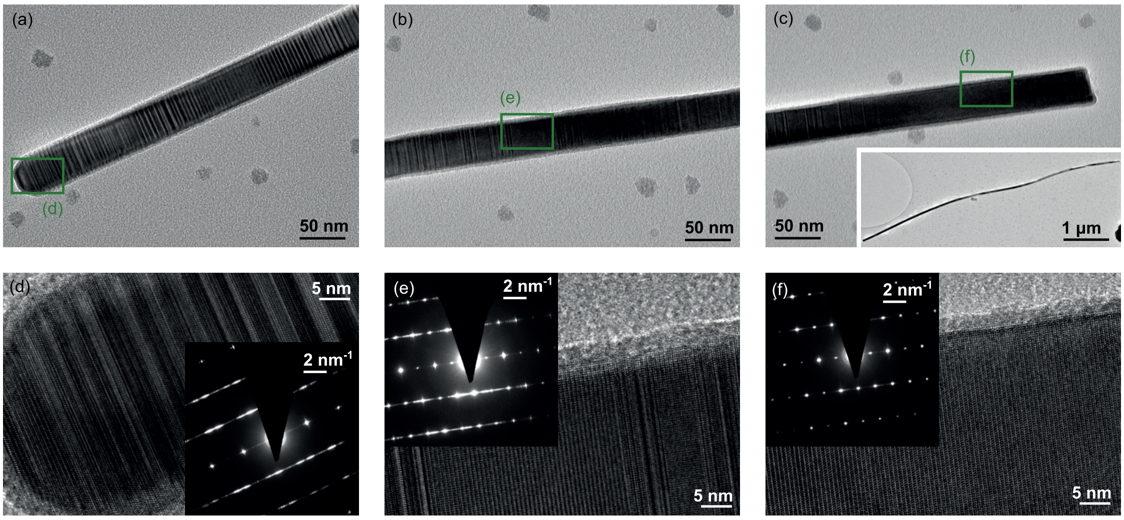

Figure 6: TEM micrographs of a nanowire grown at high V/III ratio. (a)-(c) Low magnification images. (d)-(f) High resolution TEM images and SAED images of the region indicated above.

Dependence on growth conditions

In the main article we demonstrated how the existence of tilted nanowires depends on the V/III ratio as well as indium pre-deposition. Here we present how the occurrence of tilted nanowires depends on the temperature dependence. Figure 6(a)-(f) show SEM micrographs of samples grown at 490°, 510°C, 520°C, 530°C, 540°C and 550°C, respectively. In the top row of each sub-figure we present a top view and a 15° tilted image of the wafer center and in the bottom row we present top view and tilted image at the wafer edge. We observe that for uniform nanowire growth a temperature of 530°C is ideal, as mentioned before. At lower temperature we observe a higher density of nanowires at the wafer edge, where the local temperature is expected to be slightly higher due to the design of the manipulator (Figures (a)-(c)). At temperatures above 530°C, the growth precursors re-evaporate, leading to a much lower nanowire density (Figures (e)-(f)). The edge of the 550°C sample (not shown) is completely empty. In terms of tilted nanowires we observe that a higher temperature favours the formation of tilted nanowires. A quantitative analysis is presented in Figure 6(g).

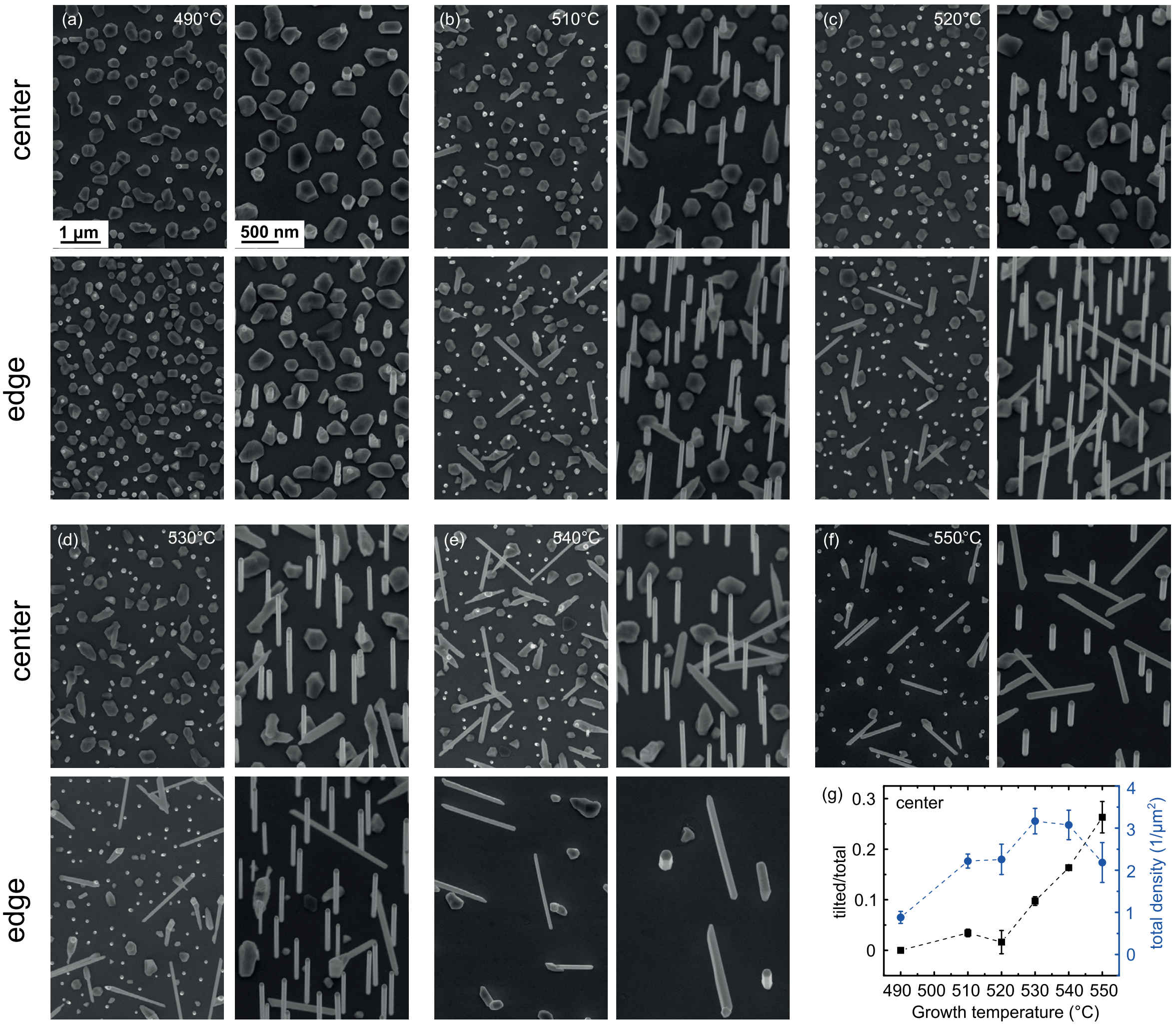

Figure 7: (a)-(f) Top view and 15° tilted SEM micrographs of samples grown at 490°, 510°C, 520°C, 530°C, 540°C and 550°C. The wafer center (edge) is shown in the top (bottom) row for each sample. The scale bar is identical for all top view images and for all tilted images, respectively. (g) Quantitative analysis of tilted nanowires and the nanowire density.

For all samples presented in the main article and the sections above, the SiO$_x$ thickness on the GaAs(111)B wafer was kept constant at 4.5 nm. Here we varied oxide thickness while keeping all other parameters constant. Figure 7(a)-(e) show SEM micrographs of samples with 2.2 nm, 2.8 nm, 4.5 nm, 6 nm and 8 nm, respectively. We observe that the ideal oxide thickness is approximately 4.5 nm. At very low oxide thickness (Figure (a)) only parasitic growth is observed. At slightly higher oxide thickness (Figure (b)) only vertical nanowires are observed, however their morphology is very non-homogeneous. At high oxide thickness a much lower nanowire density is observed (Figures (d)-(e)). This can be explained considering that the formation of pinholes becomes difficult, therefore suppressing nanowire nucleation. The density of tilted nanowires shows an increase with increasing oxide thickness as shown in Figure 7(f), however for high oxide thicknesses a quantitative analysis becomes difficult due to the low nanowire density. Our results are in agreement with a report on InAs nanowires grown on silicon where a significant increase of tilted InAs nanowires was observed for increasing oxide thickness,[3] and a comparable trend has also been shown in the case of self-catalyzed GaAs nanowires.[4]

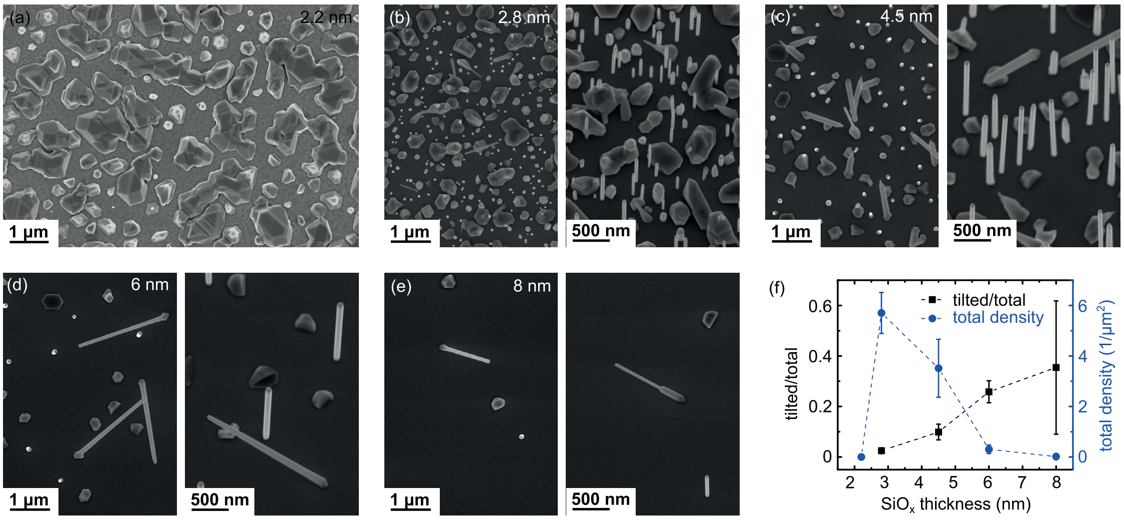

Figure 8: (a)-(e) Top view and 15° tilted SEM micrographs of samples with 2.2 nm, 2.8 nm, 4.5 nm, 6 nm and 8 nm oxide thickness. (f) Quantitative analysis of tilted nanowires and the nanowire density.

References

(1) The Silcion Cube. `http://www.thingiverse.com/thing:4375`.

(2) Potts, H.; Friedl, M.; Amaduzzi, F.; Tang, K.; Tutuncuoglu, G.; Matteini, F.; Alarcon Llado, E.; McIntyre, P. C.; Fontcuberta i Morral, A. *Nano Letters* **2016**, *16*, 637.

(3) Madsen, M. H.; Aagesen, M.; Krogstrup, P.; Sørensen, C.; Nygård, J. *Nanoscale research letters* **2011**, *6*, 516.

(4) Matteini, F.; Tutuncuoglu, G.; Potts, H.; Jabeen, F.; Fontcuberta i Morral, A. *Crystal Growth and Design* **2015**, *15*, 3105.

Supporting Information: Tuning growth direction of catalyst-free InAs(Sb) nanowires with indium droplets

Heidi Potts, Nicholas P. Morgan, Gözde Tütüncüoglu, Martin Friedl, and Anna Fontcuberta i Morral*

Laboratoire des Materiaux Semiconducteurs, Ecole Polytechnique Federale de Lausanne, 1015 Lausanne

E-mail: anna.fontcuberta-morral@epfl.ch

Annealing of InAsSb nanowires

In the main text we discussed the droplet formation upon annealing of InAsSb nanowires, and showed how the nanowire and droplet morphology changes with annealing time. We also presented a TEM and STEM-HAADF analysis of a nanowire after annealing for 20 min at 500°C, showing that an InSb section can be observed after cooldown. Here we give additional information on how the InSb section depends on the annealing time. Figure 1(a)-(d) shows an SEM micrograph, a TEM micrograph, a STEM-HAADF image and an EDX map of an InAsSb nanowire sample which has been annealed for 10 min at 500 °C. A thin InSb section can already be clearly observed in the EDX map presented in (d). Figure 1(e)-(h) show the corresponding images for an InAsSb nanowire sample which has been annealed for 30 min at 500°C. We observe a thicker InSb section compared to the 10 min sample. However, compared to the 20 min sample presented in the main text, the InSb section thickness did not significantly increase in length. This is consistent with the observation that material stops to evaporate from the top facet and starts to evaporate from the side facets when increasing the annealing time, leading to cone shaped nanowires.

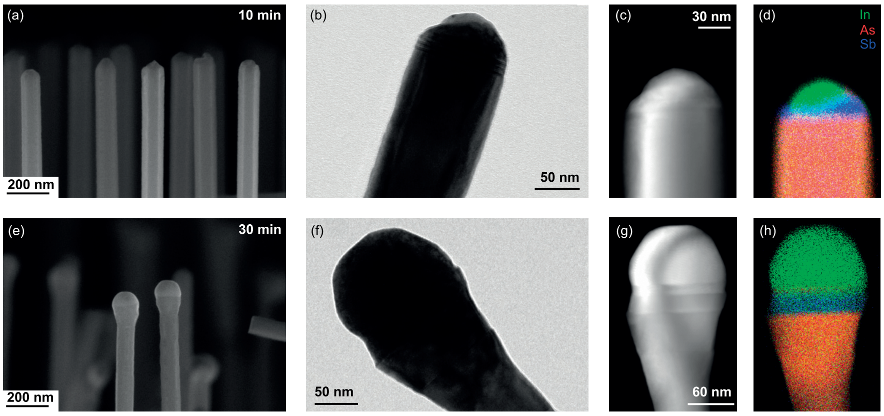

Figure 1: Droplet formation by annealing of InAsSb nanowires. (a)-(d) Cross sectional SEM micrograph, TEM micrograph, STEM-HAADF image, and EDX map of a nanowire sample which has been annealed at 500°C for 10 min. (e)-(h) Similar analysis for a nanowire sample which has been annealed at 500°C for 30 min.

Re-initiating growth on InAsSb nanowires

In the case of annealed InAsSb nanowires the droplets stay on the tip of the nanowires, as discussed above. Therefore, we expect growth to continue in the vertical direction when re-initiating InAs growth after droplet formation on the nanowires. Figure 2(a) shows a representative SEM micrograph of an InAsSb sample which was first annealed to form indium droplets, and then InAs growth was re-initiated. Interestingly, the nanowires are formed by flat {1-10} facets and do not show the tapering which is observed after droplet formation and cooldown. Figure 2(b) shows a low resolution TEM micrograph of the transition from InAsSb to InAs and indicates the regions which are presented in the high resolution TEM micrographs (Figure 2(c)-(e)). In Figure 2(c) we observe that the initial InAsSb nanowire is pure ZB. The InAs part shown in Figure 2(d) is polytypic, as commonly observed for self-catalyzed InAs nanowires. Figure 2(e) shows that the crystal structure changes abruptly at the transition from InAsSb to InAs. We also observe that there is no Moiré pattern at the transition. Figure 2(f)-(h) show a STEM EDX map of the transition and two linescans. In the axial linescan in Figure 2(g) we observe that the compositional transition is relatively sharp and there is no InSb section at the transition. This finding suggests that the InSb section is formed during cooldown of the sample after droplet formation. The radial linescan presented in Figure 2(h) shows that there is some radial overgrowth, explaining why there are flat {1-10} facets.

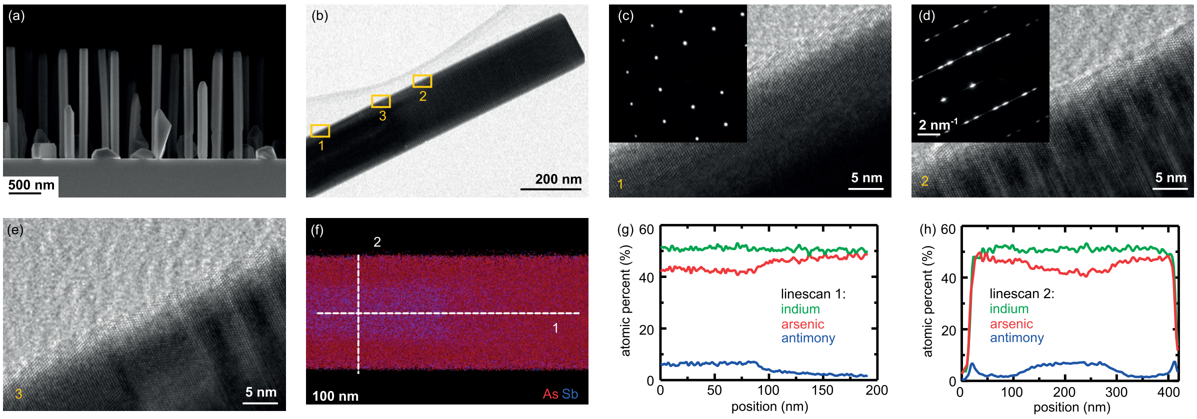

Figure 2: Re-initiating growth with an indium droplet on InAsSb nanowires. (a) Cross sectional SEM micrograph of the sample. (b) Low resolution TEM micrograph of a wire, indicating the parts which are presented with higher resolution. (c) Defect-free crystal structure of the InAsSb stem. (d) Polytypic crystal structure of the InAs tip. (e) Interface between InAsSb and InAs, showing an abrupt transition. (f) STEM-EDX analysis of the transition, indicating the linescans which are presented in (g)-(h).

Time series of the nano-membrane formation

When re-initiating growth after droplet formation on InAs nanowires, we observe nano-membranes if the arsenic pressure is above a certain threshold (refer to the discussion of Figure 3(h) in the main text). We further analyze the formation of these membranes by doing a time series, which is presented in Figure 3. Figure 3(a) shows a sample with indium droplets which were formed by annealing at 530°C for 10 min. Figure 3(b) shows a sample which was first annealed to form and droplets and then growth was re-initiated at 7x10-7

Torr arsenic BEP for 10 min. We observe that the droplets are consumed and the nanowire side facets below the 'droplet' start accumulating material. Figure 3(c) shows a sample where the growth was continued for 20 min. The material continues to accumulate on the side facets below the 'droplet'. After 30 min the flat nano-membrane is complete, as shown in Figure 3(d). This mechanism stands in contrast to the finding of Paladugu et al,[1] where flat membranes are formed when the gold droplets moves down along the nanowire.

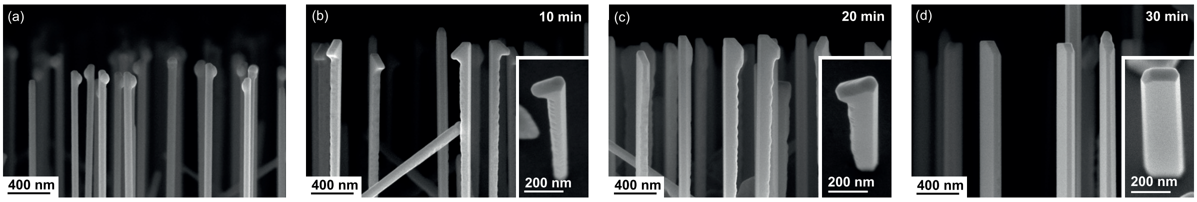

Figure 3: Time series of nano-membrane formation. (a) Cross sectional SEM micrograph of an InAs sample with droplets which were formed by annealing for 10 min. (b)-(d) Cross sectional SEM micrographs and top view images (with 15° tilt) of samples which were grown at 7x10-7 Torr arsenic BEP for 10 min, 20 min and 30 min respectively.

Growth re-initiation on branched nanostructures

We presented in the main article that annealing L-shaped nanostructures leads to the formation of indium droplets and various positions on the original structure, resulting in a variety of structures when re-initiating growth. Here we present the TEM analysis of another nano-bridge and explain how to determine that the bridges are formed from a single host nanowire, as opposed to by merging of two branches. Figure 4(a) shows a low resolution TEM micrograph of a nano-bridge. By the shape of the structure we can assume that the host structure was L-shaped, and the second leg (the top part in the image) was initiated by a droplet on the horizontal part. A magnified image of the beginning of the second leg is shown in Figure 4(b) and a diffraction pattern of the same region is shown in Figure 4(c). High resolution TEM images both of the original host nanowire and the beginning of the second leg are shown in Figure 4(d)-(e). We observe that the crystal structure is polytypic and it is continuous along the whole nanostructure. This nano-bridge shows that growth can be initiated at different locations on the host nanostructure. Further research is needed in order to control the positioning of the droplets, and therefore allow to grow more sophisticated hierarchical structures. Figure 4(f)-(i) present the TEM analysis of a nano-bridge which was formed by the merging of two branches. Figure 4(g) shows a magnified image of the center region between the two legs. We can clearly identify the interface between the two original structures, therefore supporting our assumption that this nano-bridge was formed by two L-shaped nanostructures. Figure 4(h)-(i) are high resolution TEM micrographs of the two legs, and show that the crystal structure is polytypic.

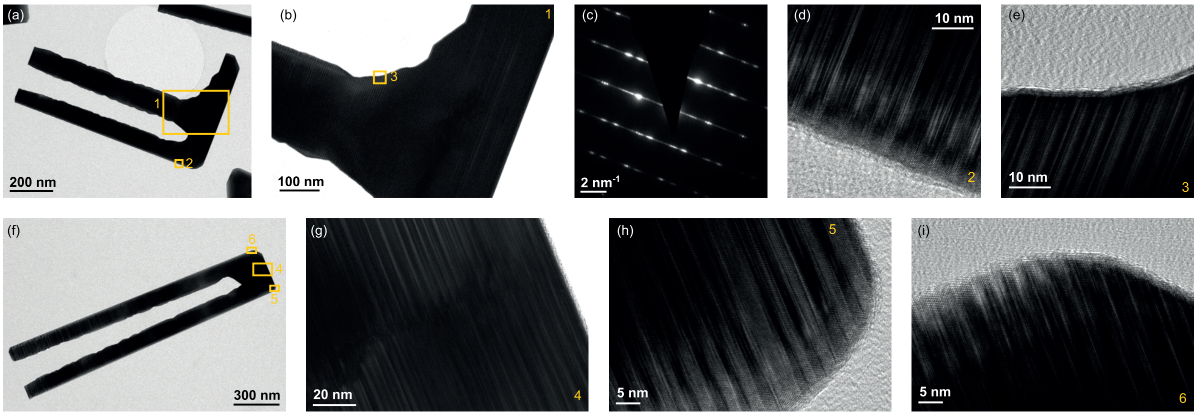

Figure 4: Growth re-initiation onL-shaped nanostructures and merging of branches. (a)-(e) TEM micrographs and diffraction pattern of a nano-bridge formed by re-initiating growth after annealing a sample with L-shaped nanostructures. (f)-(i) TEM micrographs of a nano-bridge formed by merging of two branches.

Re-initiating growth with deposited indium droplets

Indium droplets as a seed particle to initiate growth offer a variety of opportunities. In the main articles we presented that indium can be deposited on InAs or InAsSb nanowires and used a seed particles to form L-shaped nanostructures which adopt the crystal structure of the host nanowires all along the branch. However, we have found that in some cases, branches can show a change in crystal structure along their growth direction. Figure 5(a) shows an SEM micrograph of an InAs nanowire sample with deposited indium droplets and the resulting L-shaped structures sticks after re-initiating growth. Figure 5(b) shows a TEM micrograph and diffraction pattern of the horizontal part of an L-shaped structure. We observe that the branch at first adopts the crystal structure of the host nanowire, and then starts to exhibit stacking defects which are at an angle of 110° with respect to the substrate plane. This direction corresponds to the <-111> direction, assuming that the branch grows along <-211> direction. Figure 5(d) shows a STEM-EDX map of the structure, confirming that it is pure InAs. A high resolution TEM micrograph of the nanostructure (Figure 5(e)) shows that there are both stacking defects perpendicular to the <-1-1-1> and to the <-111> direction. Figure 5(f)-(j) shows a similar analysis of an L-shaped structure where indium was deposited on InAsSb nanowires and then growth of InAs was re-initiated. Here we observe that the host nanowire is defect-free, as expected for InAsSb nanowires with 20% antimony. The horizontal InAs part again shows stacking defects perpendicular to the <-111> direction. We also observe from the STEM-EDX map presented in Figure 5(i) that the InAs overgrowth is only on one side of the host nanowire. This can be attributed to a local change of conditions, for example by shadowing, and explains that the host nanowire is bent due to strain. Comparing the TEM analysis presented here to the TEM analysis presented in Figure 7 in the main article we observe that re-initiating growth with deposited indium can in some cases lead to branches which adopt the host crystal structure all along their length, and in other cases the branch starts to exhibit defects. The reason for one behaviour or the other can at the moment not be understood completely. However, we believe that the formation of defects perpendicular to the <-111> direction occurs as soon as the growth proceeds with a {-111} facet. The formation of such facets might be favoured in proximity of the substrate, which is why such defects are never observed in branches where the indium droplet was near the nanowire tip. The formation of defects perpendicular to the <-111> direction can also be observed during the radial overgrowth of InAsSb nanowires. SEM and TEM micrographs of an InAsSb nanowire sample with 35% antimony are shown in Figure 5(k)-(o). Figure 5(k) shows a cross sectional SEM micrograph of the sample, showing the formation of facets at the nanowire stem. From time series we know that there is significant radial overgrowth in InAsSb samples.[2] In the TEM micrographs presented in Figure 5(l)-(m) we observe stacking defects which are at a 110° angle with respect to the axial growth direction. The Fourier transform images presented in Figure 5(n)-(o) confirm the defect free nature of the host structure and the existence of stacking faults near the edge.

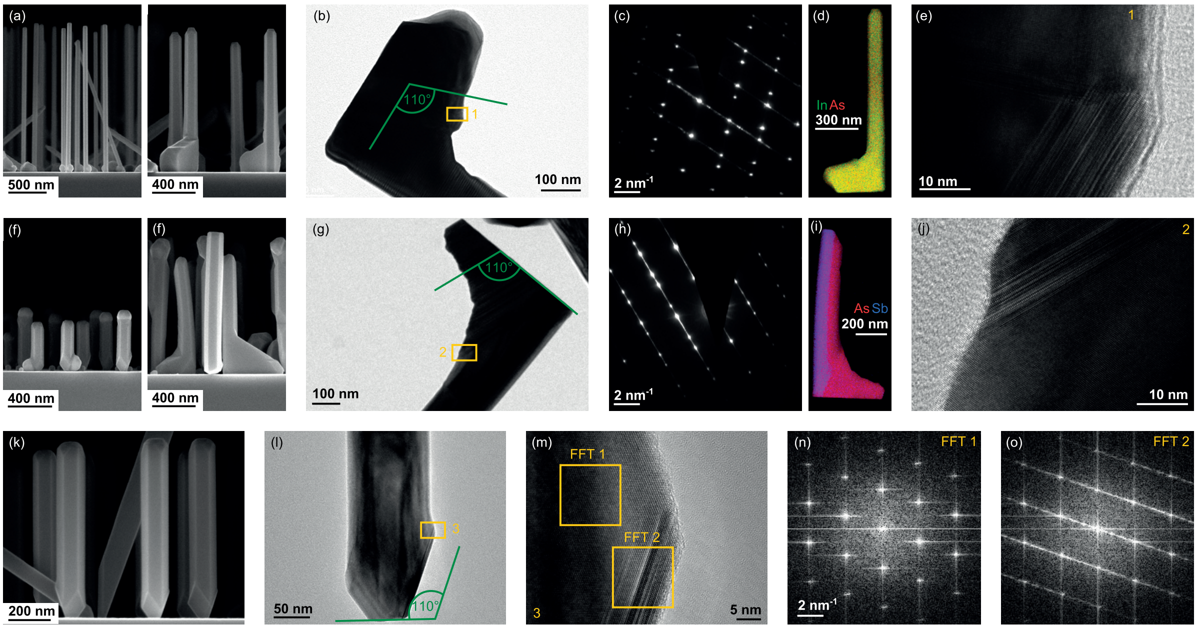

Figure 5: TEM analysis of L-shaped nanostructures which were formed by depositing indium on InAs and InAsSb nanowires. (a) Cross sectional SEM micrographs of InAs nanowires with deposited indium droplets and L-shaped nanostructures after re-initiating growth. (b)-(c) TEM micrograph and diffraction pattern of a branch. (d) STEM-EDX map of the structure. (e) High resolution TEM micrograph showing stacking defects. (f)-(j) Similar analysis for indium droplets on InAsSb nanowires. (k) Cross sectional SEM micrograph of an InAsSb nanowire sample with 35% antimony. (l)-(o) TEM micrographs and Fourier transform images of the stem of a nanowire showing stacking defects.

Droplet formation using axial heterostructures

Another possibility to create indium droplets, is to start with a host nanowire, then overgrow it with InAs, and then anneal the sample to evaporate the arsenic in the InAs part. The resulting indium droplets can then be used to re-initiate growth of InAs. In Figure 6 we present the formation of droplets and the resulting L-shaped structures for InAsSb host nanowires which were overgrown with InAs. Figure 6(a) shows cross sectional SEM micrographs of a sample which was overgrown with InAs for 20 min and then annealed at 530 °C for 10 min. We chose standard InAs nanowire growth conditions for the InAs overgrowth in order to have mostly axial growth and also a bit of radial overgrowth in order to protect the host InAsSb nanowires. We observe the formation of droplets and some additional faceting of the nanowire. The faceting can be attributed to the lattice mismatch between InAsSb and InAs. The top part of the nanowires, however, does not show faceting, suggesting that the indium droplets are on the pure InAs part. Figure 6(b) shows SEM micrographs of a sample which was overgrown for 15 min and then annealed for 10 min. We observe faceting all along the nanowires and a different shape of droplets, suggesting that the indium droplets might be located on the InAsSb/InAs core-shell part of the host structure. Figure 6(c)-(d) show a top view (15° tilt) and cross sectional SEM micrographs of an L-shaped structure, where the droplets were formed with similar conditions as the sample presented in (b) and then InAs growth was re-initiated. We observe two types of branches: (1) horizontal branches and (2) branches which grow slightly downwards. Figure 6(e)-(g) show TEM micrographs of a downward growing branch. We observe that the stem of the host nanowire is defect-free, but the top part of the host nanowire and the branch show polytypism perpendicular to the axial growth direction. This suggests that the droplet was still located on InAs when re-initiating growth. The STEM-HAADF image and EDX map confirm that the top part of the sample is pure InAs, while the lower part of the host nanowire is InAsSb/InAs core-shell. We conclude that overgrowth with InAs and consecutive annealing to form indium droplets is a powerful tool to form heterostructures, but extreme control of the length of the axial InAs section and annealing time is needed in order to make sure that the droplets are located on the host/InAs core-shell part of the host nanowire.

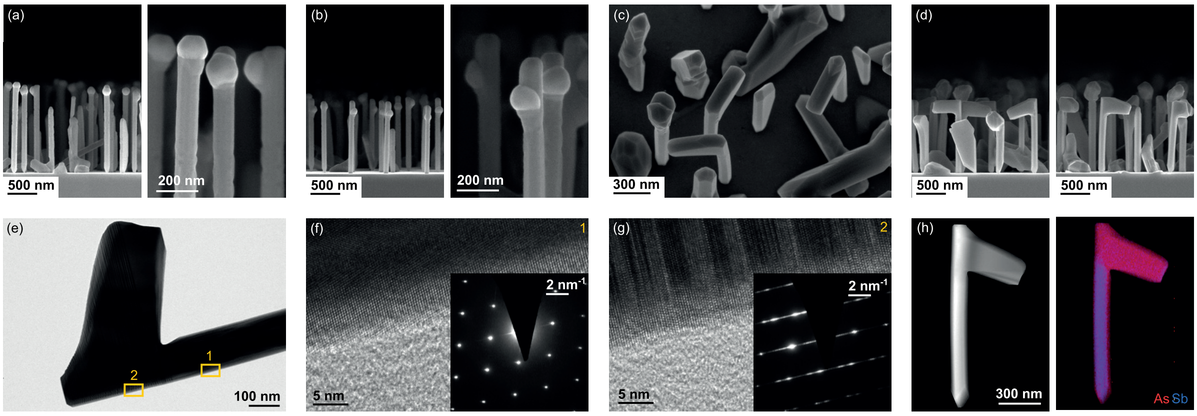

Figure 6: Droplet formation and re-initiation of growth on InAsSb/InAs nanowires. (a)-(b) Cross sectional SEM micrograph of a InAsSb sample with was overgrown with InAs and then annealed for 10 min. The InAs growth time was for 20 min and 15 min for (a) and (b), respectively. (c)-(d) Top view (15° tilt) and cross sectional SEM micrographs an L-shaped nanostructure based on an InAsSb+InAs(15min)+annealing(10min) sample. (e)-(g) TEM micrographs of a branched nanowire showing a defect-free stem and a defective branch. (h) STEM-HAADF image and EDX map.

Electrical Characterization

In the main article we presented the electrical characterization of a few L-shaped nanostructures and found that the conductivity is roughly comparable to standard InAs nanowires and they show n-type behaviour. In order to compare with standard nanowires we also fabricated devices based on linear wires from a sample after annealing and growth re-initiation, as well as standard InAs nanowires with comparable thickness. Representative SEM micrographs of the as-grown nanostructures are shown in Figure 7(a)-(b). However, after electrical measurements we found that many devices had melted and appeared amorphous. Interestingly, they still conduct, making it difficult to determine at which point during the testing the change happened, and therefore making a quantitative comparison impossible. In the main article we therefore only presented data of devices which remained crystalline during testing. Here we give the complete analysis for additional information. Figure 7(c) shows an SEM micrograph of a device where the main part was melted while the branch remained crystalline. Figure 7(d)-(e) shows SEM micrographs of standard nanowires being crystalline and melted. The table in Figure 7(f) presents the complete analysis of all devices measured. For each device type we report the conductivity and the On/Off ratio for melted and crystalline devices. We also present a total average, for which all devices were taken into account, including devices that blew up during the last test and therefore their morphology could not be determined after testing.

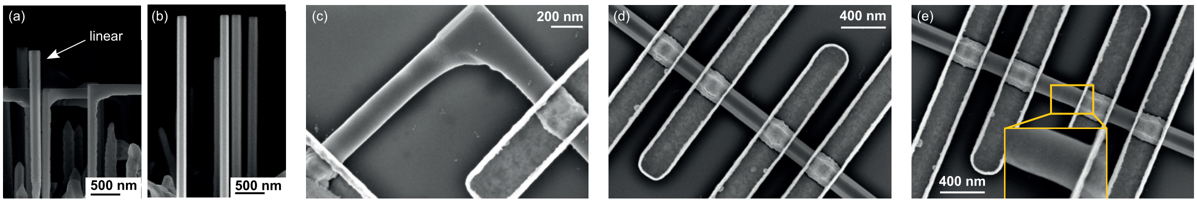

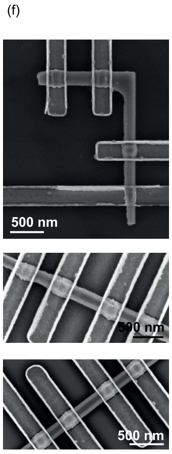

Type		#	σ_avg (S/cm)	min	max	#	On/Off_avg	min	max
Hockey branch	total	5	75.6 ± 22.9	49.7	105.7	18	4.5 ± 4.6	1.8	18.0
	melted	0	N/A	N/A	N/A	2	14.0 ± 5.6	10.0	18.0
	crystalline	4	80.5 ± 23.3	49.7	105.7	11	2.5 ± 0.6	1.8	3.6
Hockey main	total	4	47.8 ± 19.0	19.8	62.4	17	1.8 ± 0.9	0.9	3.6
	melted	4	47.8 ± 19.0	19.8	62.4	11	1.8 ± 0.9	0.9	3.1
	crystalline	0	N/A	N/A	N/A	0	N/A	N/A	N/A
Hockey linear	total	2	107.5 ± 93.3	41.5	173.4	2	1.3 ± 0.4	1.0	1.5
	melted	1	173.4	N/A	N/A	1	1.0	N/A	N/A
	crystalline	1	41.5	N/A	N/A	1	1.5	N/A	N/A
Standard wires	total	8	158.3 ± 76.9	59.0	282.0	15	1.5 ± 0.5	1.0	2.6
	melted	7	172.5 ± 70.9	98.6	282.0	13	1.4 ± 0.5	1.0	2.5
	crystalline	1	59.0	N/A	N/A	2	2.2 ± 0.6	1.8	2.6

Figure 7: Electrical devices. (a)-(b) Cross sectional SEM micrographs of a sample showing branched nanowires and linear nanowires (hockey linear), and of a standard nanowire sample. (c) SEM micrograph of a device after electrical measurements. The main nanowire melted while the branch remained crystalline. (d)-(e) SEM micrographs of standard nanowires, showing a crystalline and a melted device after testing. (f) Table summarizing the conductivity and On/Off ratio for different device types. The standard deviation corresponds to the variation between the measured devices.

References

(1) Paladugu, M.; Zou, J.; Guo, Y.-N.; Auchterlonie, G.; Joyce, H.; Gao, Q.; Hoe Tan, H.; Jagadish, C.; Kim, Y. *Small* **2007**, *11*, 1873.

(2) Potts, H.; Friedl, M.; Amaduzzi, F.; Tang, K.; Tutuncuoglu, G.; Matteini, F.; Alarcon Llado, E.; McIntyre, P. C.; Fontcuberta i Morral, A. *Nano Letters* **2016**, *16*, 637.

Bibliography

[Ahn13] J. Ahn, T. Kent, E. Chagarov, K. Tang, A. C. Kummel, and P. C. McIntyre. Arsenic decapping and pre-atomic layer deposition trimethylaluminum passivation of Al2O3/InGaAs(100) interfaces. *Applied Physics Letters* **103**, 071602 (2013).

[Akopian10] N. Akopian, G. Patriarche, L. Liu, J.-C. Harmand, and V. Zwiller. Crystal phase quantum dots. *Nano Letters* **10**, 1198 (2010).

[Alarcon-Llado13] E. Alarcon-Llado, S. Conesa-Boj, X. Wallart, P. Caroff, and A. Fontcuberta i Morral. Raman spectroscopy of self-catalyzed GaAs(1-x)Sb(x) nanowires grown on silicon. *Nanotechnology* **24**, 405707 (2013).

[Alicea11] J. Alicea, Y. Oreg, G. Refael, F. V. Oppen, and M. P. A. Fisher. information processing in 1D wire networks. *Nature Physics* **7**, 412 (2011).

[Allen08] J. E. Allen, E. R. Hemesath, D. E. Perea, J. L. Lensch-Falk, Z. Y. Li, F. Yin, M. H. Gass, P. Wang, A. L. Bleloch, R. E. Palmer, and L. J. Lauhon. High-resolution detection of Au catalyst atoms in Si nanowires. *Nature nanotechnology* **3**, 168 (2008).

[Amaduzzi16] F. Amaduzzi, E. Alarc, and H. Hautmann. Tuning the response of non-allowed Raman modes in GaAs nanowires. *Journal of Physics* **49**, 095103 (2016).

[Bar-Sadan12] M. Bar-Sadan, J. Barthel, H. Shtrikman, and L. Houben. Direct imaging of single Au atoms within GaAs nanowires. *Nano letters* **12**, 2352 (2012).

[Beenakker13] C. Beenakker. Search for Majorana Fermions in Superconductors. *Annual Review of Condensed Matter Physics* **4**, 113 (2013).

[Bermudez-Urena17] E. Bermudez-Urena, G. Tutuncuoglu, J. Cuerda, C. L. C. Smith, J. Bravo-Abad, S. I. Bozhevolnyi, A. Fontcuberta i Morral, F. J. García-Vidal, and R. Quidant. Plasmonic waveguide-integrated nanowire laser. *Nano Letters* **17**, 747 (2017).

[Biermanns14] A. Biermanns, E. Dimakis, A. Davydok, T. Sasaki, L. Geelhaar, M. Takahasi, and U. Pietsch. Role of liquid indium in the structural purity of wurtzite InAs nanowires that grow on Si(111). *Nano letters* **14**, 6878 (2014).

[Björk02] M. T. Björk, B. J. Ohlsson, T. Sass, A. I. Persson, C. Thelander, M. H. Magnusson, K. Deppert, L. R. Wallenberg, and L. Samuelson. One-dimensional heterostructures in semiconductor nanowhiskers. *Applied Physics Letters* **80**, 1058 (2002).

[Blanc13] P. Blanc, M. Heiss, C. Colombo, A. D. Mallorquì, T. S. Safaei, P. Krogstrup, J. Nygard, and A. F. I. Morral. Electrical contacts to single nanowires: a scalable method allowing multiple devices on a chip. Application to a single nanowire radial p-i-n junction. *International Journal of Nanotechnology* **10**, 419 (2013).

[Borg10] B. M. Borg, K. A. Dick, B. Ganjipour, M. E. Pistol, L. E. Wernersson, and C. Thelander. InAs/GaSb heterostructure nanowires for tunnel field-effect transistors. *Nano Letters* **10**, 4080 (2010).

[Borgström07] M. T. Borgström, G. Immink, B. Ketelaars, R. Algra, and E. P. a. M. Bakkers. Synergetic nanowire growth. *Nature nanotechnology* **2**, 541 (2007).

[Brotherton80] S. Brotherton and J. Lowther. Electron and hole capture at Au and Pt centers in silicon. *Physical Review Letters* **44**, 1 (1980).

[Bryllert06] T. Bryllert, L. E. Wernersson, L. E. Fröberg, and L. Samuelson. Vertical high-mobility wrap-gated InAs nanowire transistor. *IEEE Electron Device Letters* **27**, 323 (2006).

[Burgess16] T. Burgess, D. Saxena, S. Mokkapati, Z. Li, C. R. Hall, J. A. Davis, Y. Wang, L. M. Smith, L. Fu, P. Caroff, H. H. Tan, and C. Jagadish. Doping-enhanced radiative efficiency enables lasing in unpassivated GaAs nanowires. *Nature Communications* **7**, 11927 (2016).

[Car14] D. Car, J. Wang, M. A. Verheijen, E. P. A. M. Bakkers, and S. R. Plissard. Rationally Designed Single-Crystalline Nanowire Networks. *Advanced Materials* **26**, 4875 (2014).

[Castleton13] C. W. M. Castleton, A. Höglund, M. Göthelid, M. C. Qian, and S. Mirbt. Hydrogen on III-V (110) surfaces: Charge accumulation and STM signatures. *Phys. Rev. B* **88**, 045319 (2013).

[Cherng88] Y. T. Cherng, K. Y. Ma, and G. B. Stringfellow. Raman scattering in InAs(1-x)Sb(x) grown by organometallic vapor phase epitaxy. *Applied Physics Letters* **53**, 886 (1988).

[Colombo08] C. Colombo, D. Spirkoska, M. Frimmer, G. Abstreiter, and a. Fontcuberta i Morral. Ga-assisted catalyst-free growth mechanism of GaAs nanowires by molecular beam epitaxy. *Physical Review B* **77**, 155326 (2008).

[Conesa-Boj14] S. Conesa-Boj, D. Kriegner, X.-L. Han, S. Plissard, X. Wallart, J. Stangl, A. Fontcuberta i Morral, and P. Caroff. Gold-free ternary III-V antimonide nanowire arrays on silicon: twin-free down to the first bilayer. *Nano letters* **14**, 326 (2014).

[Das12] A. Das, Y. Ronen, Y. Most, Y. Oreg, M. Heiblum, and H. Shtrikman. Zero-bias peaks and splitting in an Al–InAs nanowire topological superconductor as a signature of Majorana fermions. *Nature Physics* **8**, 887 (2012).

[Dayeh07] S. A. Dayeh, D. P. R. Aplin, X. Zhou, P. K. L. Yu, E. T. Yu, and D. Wang. High electron mobility InAs nanowire field-effect transistors. *Small* **3**, 326 (2007).

[Dayeh10] S. A. Dayeh. Electron transport in indium arsenide nanowires. *Semiconductor Science and Technology* **25**, 024004 (2010).

[Dey13a] A. W. Dey, B. M. Borg, B. Ganjipour, M. Ek, K. A. Dick, E. Lind, C. Thelander, and L. E. Wernersson. High-current GaSb/InAs(Sb) nanowire tunnel field-effect transistors. *IEEE Electron Device Letters* **34**, 211 (2013).

[Dey13b] A. W. Dey, J. Svensson, M. Ek, E. Lind, C. Thelander, and L. E. Wernersson. Combining axial and radial nanowire heterostructures: Radial Esaki diodes and tunnel field-effect transistors. *Nano Letters* **13**, 5919 (2013).

[Dick10a] K. A. Dick, P. Caroff, J. Bolinsson, M. E. Messing, J. Johansson, K. Deppert, L. R. Wallenberg, and L. Samuelson. Control of III–V nanowire crystal structure by growth parameter tuning. *Semiconductor Science and Technology* **25**, 024009 (2010).

[Dick10b] K. A. Dick, C. Thelander, L. Samuelson, and P. Caroff. Crystal phase engineering in single InAs nanowires. *Nano Letters* **10**, 3494 (2010).

[Dimakis11] E. Dimakis, L. Jonas, U. Jahn, M. Hilse, and L. Geelhaar. Self-assisted nucleation and vapor-solid growth of InAs nanowires on bare Si(111). *Crystal Growth and Design* **11**, 4001 (2011).

[Du15] L. Du, I. Knez, G. Sullivan, and R.-R. Du. Robust helical edge transport in gated InAs/GaSb bilayers. *Phys. Rev. Lett.* **114**, 096802 (2015).

[Epon17] Epon. Epoxy embedding medium kit (accessed July 26, 2017).

[Fahed16] M. Fahed, L. Desplanque, D. Troadec, G. Patriarche, and X. Wallart. Selective area heteroepitaxy of GaSb on GaAs(001) for in-plane InAs nanowire achievement. *Nanotechnology* **27**, 505301 (2016).

[Farrell15] A. C. Farrell, W.-J. Lee, P. Senanayake, M. a. Haddad, S. V. Prikhodko, and D. L. Huffaker. High-quality InAsSb nanowires grown by catalyst-free selective-area metal–organic chemical vapor deposition. *Nano Letters* **15**, 6614 (2015).

[Ford09] A. C. Ford, J. C. Ho, Y.-l. Chueh, Y.-C. Tseng, and V. Gaines. Diameter-Dependent Electron Mobility of 2009. *Nano letters* **9**, 2 (2009).

[Ganjipour11] B. Ganjipour, A. W. Dey, B. M. Borg, M. Ek, M.-E. Pistol, K. A. Dick, L.-E. Wernersson, and C. Thelander. High current density esaki tunnel diodes based on GaSb-InAsSb. *Nano letters* **11**, 4222 (2011).

[Ganjipour15] B. Ganjipour, M. Leijnse, L. Samuelson, H. Q. Xu, and C. Thelander. Transport studies of electron-hole and spin-orbit interaction in GaSb/InAsSb core-shell nanowire quantum dots. *Physical Review B* **91**, 1 (2015).

[Glas07] F. Glas, J.-C. Harmand, and G. Patriarche. Why does wurtzite form in nanowires of III-V zinc blende semiconductors? *Physical Review Letters* **99**, 146101 (2007).

[Glas14] F. Glas. *Wide Band Gap Semiconductor Nanowires 1*, chapter 2 Stress relaxation in nanowires with heterostructures, pages 25–57, (John Wiley and Sons, Inc., 2014).

[Goldberger06] J. Goldberger, A. I. Hochbaum, R. Fan, and P. Yang. Silicon vertically integrated nanowire field effect transistors. *Nano Lett* **6**, 973 (2006).

[Grap13] T. Grap, T. Rieger, C. Blömers, T. Schäpers, D. Grützmacher, and M. I. Lepsa. Self-catalyzed VLS grown InAs nanowires with twinning superlattices. *Nanotechnology* **24**, 335601 (2013).

[Grundmann16] M. Grundmann. *The Physics of Semiconductors: An Introduction Including Nanophysics and Applications*, (Springer International Publishing, 2016).

[Gül15] Ö. Gül, D. J. V. Woerkom, I. V. Weperen, D. Car, S. R. Plissard, E. P. a. M. Bakkers, and L. P. Kouwenhoven. Towards high mobility InSb nanowire devices. *Nanotechnology* **26**, 215202 (2015).

[Guo13] Y.-N. Guo, T. Burgess, Q. Gao, H. H. Tan, C. Jagadish, and J. Zou. Polarity-driven nonuniform composition in InGaAs nanowires. *Nano Letters* **13**, 5085 (2013).

[Gupta13] N. Gupta, Y. Song, G. W. Holloway, U. Sinha, C. M. Haapamaki, R. R. Lapierre, and J. Baugh. Temperature-dependent electron mobility in InAs nanowires. *Nanotechnology* **24**, 225202 (2013).

[Halpern12] E. Halpern, G. Elias, A. V. Kretinin, H. Shtrikman, and Y. Rosenwaks. Direct measurement of surface states density and energy distribution in individual InAs nanowires. *Applied Physics Letters* **100** (2012).

[Heedt16] S. Heedt, D. Vakulov, T. Rieger, D. Rosenbach, S. Trellenkamp, D. Gruetzmacher, M. I. Lepsa, and T. Schapers. Electronic properties of complex self-assembled InAs nanowire networks. *Advanced Electronic Materials* **2**, 1 (2016).

[Heiss11] M. Heiss, S. Conesa-Boj, J. Ren, H.-H. Tseng, A. Gali, A. Rudolph, E. Uccelli, F. Peiró, J. R. Morante, D. Schuh, E. Reiger, E. Kaxiras, J. Arbiol, and A. Fontcuberta i Morral. Direct correlation of crystal structure and optical properties in wurtzite/zinc-blende GaAs nanowire heterostructures. *Physical Review B* **83**, 045303 (2011).

[Heiss13] M. Heiss, Y. Fontana, a. Gustafsson, G. Wüst, C. Magen, D. D. O'Regan, J. W. Luo, B. Ketterer, S. Conesa-Boj, a. V. Kuhlmann, J. Houel, E. Russo-Averchi, J. R. Morante, M. Cantoni, N. Marzari, J. Arbiol, a. Zunger, R. J. Warburton, and a. Fontcuberta i Morral. Self-assembled quantum dots in a nanowire system for quantum photonics. *Nature materials* **12**, 439 (2013).

[Heiss14] M. Heiss, E. Russo-Averchi, A. Dalmau-Mallorquí, G. Tütüncüoğlu, F. Matteini, D. Rüffer, S. Conesa-Boj, O. Demichel, E. Alarcon-Lladó, and A. Fontcuberta i Morral. III-V nanowire arrays: growth and light interaction. *Nanotechnology* **25**, 014015 (2014).

[Hjort14] M. Hjort, S. Lehmann, J. Knutsson, A. A. Zakharov, Y. A. Du, S. Sakong, R. Timm, G. Nylund, E. Lundgren, P. Kratzer, K. A. Dick, and A. Mikkelsen. Electronic and structural differences between wurtzite and zinc blende InAs nanowire surfaces: Experiment and theory. *ACS Nano* **8**, 12346 (2014).

[Holt96] D. Holt, C. Hardingham, L. Lazzarini, L. Nasi, C. Zanotti-Fregonara, G. Salviati, and M. Mazzer. Properties and structure of antiphase boundaries in GaAs/Ge solar cells. *Materials Science and Engineering: B* **42**, 204 (1996).

[Hörmann11] N. G. Hörmann, I. Zardo, S. Hertenberger, S. Funk, S. Bolte, M. Döblinger, G. Koblmüller, and G. Abstreiter. Effects of stacking variations on the lattice dynamics of InAs nanowires. *Physical Review B* **84**, 155301 (2011).

[IBM17] IBM. Quantum experience (accessed July 26, 2017).

[Ioffe17] P.-T. I. Ioffe. Electronic archive - new semiconductor materials (accessed July 26, 2017).

[Ionescu11] A. M. Ionescu and H. Riel. Tunnel field-effect transistors as energy-efficient electronic switches. *Nature* **479**, 329 (2011).

[Jacobsson16] D. Jacobsson, F. Panciera, J. Tersoff, M. C. Reuter, S. Lehmann, S. Hofmann, K. A. Dick, and F. M. Ross. Interface dynamics and crystal phase switching in GaAs nanowires. *Nature* **531**, 317 (2016).

[Joyce10] H. J. Joyce, J. Wong-Leung, Q. Gao, H. H. Tan, and C. Jagadish. Phase perfection in zinc blende and wurtzite III-V nanowires using basic growth parameters. *Nano Letters* **10**, 908 (2010).

[Joyce16] H. J. Joyce, J. L. Boland, C. L. Davies, S. Baig, and M. B. Johnston. Electrical properties of semiconductor nanowires: Insights gained from terahertz conductivity spectroscopy. *Semiconductor Science and Technology* **31**, 1 (2016).

[Ketterer11] B. Ketterer, M. Heiss, M. J. Livrozet, A. Rudolph, E. Reiger, and A. Fontcuberta i Morral. Determination of the band gap and the split-off band in wurtzite GaAs using Raman and photoluminescence excitation spectroscopy. *Phys. Rev. B* **83**, 125307 (2011).

[Ketterer12] B. Ketterer, E. Uccelli, and A. Fontcuberta i Morral. Mobility and carrier density in p-type GaAs nanowires measured by transmission Raman spectroscopy. *Nanoscale* **4**, 1789 (2012).

[Kim13] J. M. Kim, P. S. Dutta, E. Brown, J. M. Borrego, and P. Greiff. Wet chemical etching process for wafer scale isolation and interconnection of GaSb based device layers grown on GaAs substrates. *Journal of Vacuum Science & Technology B* **31**, 6 (2013).

[Kishore12] V. V. R. Kishore, B. Partoens, and F. M. Peeters. Electronic structure of InAs/GaSb core-shell nanowires. *Physical Review B* **86**, 165439 (2012).

[Knez11] I. Knez, R.-R. Du, and G. Sullivan. Evidence for helical edge modes in inverted InAs/GaSb quantum wells. *Physical Review Letters* **107**, 136603 (2011).

[Krishnamachari04] U. Krishnamachari, M. Borgstrom, B. J. Ohlsson, N. Panev, L. Samuelson, W. Seifert, M. W. Larsson, and L. R. Wallenberg. Defect-free inp nanowires grown in [001] direction on InP (001). *Applied Physics Letters* **85**, 2077 (2004).

[Krogstrup10] P. Krogstrup, R. Popovitz-Biro, E. Johnson, M. H. Madsen, J. Nygård, and H. Shtrikman. Structural phase control in self-catalyzed growth of GaAs nanowires on silicon(111). *Nano letters* **10**, 4475 (2010).

[Krogstrup13a] P. Krogstrup, H. I. Jørgensen, M. Heiss, O. Demichel, J. V. Holm, M. Aagesen, J. Nygard, and A. Fontcuberta i Morral. Single-nanowire solar cells beyond the Shockley–Queisser limit. *Nature Photonics* **7**, 306 (2013).

[Krogstrup13b] P. Krogstrup, H. I. Jørgensen, E. Johnson, M. H. Madsen, C. B. Sørensen, A. F. I. Morral, M. Aagesen, J. Nygård, and F. Glas. Advances in the theory of III–V nanowire growth dynamics. *Journal of Physics D: Applied Physics* **46**, 313001 (2013).

[Kunert08] B. Kunert, I. Németh, S. Reinhard, K. Volz, and W. Stolz. Si (001) surface preparation for the antiphase domain free heteroepitaxial growth of GaP on Si substrate. *Thin Solid Films* **517**, 140 (2008).

[Liu08] C. Liu, T. Hughes, X.-L. Qi, K. Wang, and S.-C. Zhang. Quantum Spin Hall Effect in Inverted Type-II Semiconductors. *Physical Review Letters* **100**, 236601 (2008).

[Lowe03] M. J. Lowe, T. D. Veal, C. F. McConville, G. R. Bell, S. Tsukamoto, and N. Koguchi. Passivation and reconstruction-dependent electron accumulation at sulphur treated InAs(001) surfaces. *Surface Science* **523**, 179 (2003).

[Luo16] N. Luo, G.-Y. Huang, G. Liao, L.-H. Ye, and H. Q. Xu. Band-inverted gaps in InAs/GaSb and GaSb/InAs core-shell nanowires. *Scientific Reports* **6**, 38698 (2016).

[Matteini14] F. Matteini, G. Tütüncüo, D. Rüffer, and E. Alarcón-lladó. Ga-assisted growth of GaAs nanowires on silicon, comparison of surface SiOx of different nature. *Journal of Crystal Growth* **404**, 246 (2014).

[Matteini15] F. Matteini, G. Tutuncuoglu, H. Potts, F. Jabeen, and A. Fontcuberta i Morral. Wetting of Ga on SiOx and its impact on GaAs nanowire growth. *Crystal Growth and Design* **15**, 3105 (2015).

[Matteini16] F. Matteini, G. Tutuncuoglu, D. Mikulik, J. Vukajlovic-Plestina, H. Potts, J. B. Leran, W. C. Carter, and A. F. Morral. Impact of the ga droplet wetting, morphology, and pinholes on the orientation of GaAs nanowires. *Crystal Growth and Design* **16**, 5781 (2016).

[Mayer13] B. Mayer, D. Rudolph, J. Schnell, S. Morkötter, J. Winnerl, J. Treu, K. Müller, G. Bracher, G. Abstreiter, G. Koblmüller, and J. J. Finley. Lasing from individual GaAs-AlGaAs core-shell nanowires up to room temperature. *Nature Communications* **4**, 2931 (2013).

[Mead63] C. A. Mead and W. G. Spitzer. Fermi level position at semiconductor surfaces. *Phys. Rev. Lett.* **10**, 471 (1963).

[MIT17] MIT. Technology review - 10 breakthrough technologies in 2017 (February 2017) (accessed July 26, 2017).

[Mooradian66] A. Mooradian and G. B. Wright. Observation of the interaction of plasmons with longitudinal optical phonons in GaAs. *Physical Review Letters* **16**, 999 (1966).

[Mourik12] V. Mourik, K. Zuo, S. M. Frolov, S. R. Plissard, E. P. a. M. Bakkers, and L. P. Kouwenhoven. Signatures of Majorana fermions in hybrid superconductor-semiconductor nanowire devices. *Science* **336**, 1003 (2012).

[Mueller15] S. Mueller, A. N. Pal, M. Karalic, T. Tschirky, C. Charpentier, W. Wegscheider, K. Ensslin, and T. Ihn. Nonlocal transport via edge states in InAs/GaSb coupled quantum wells. *Physical Review B* **92**, 081303 (2015).

[Namazi15] L. Namazi, M. Nilsson, S. Lehmann, C. Thelander, and K. A. Dick. Selective GaSb radial growth on crystal phase engineered InAs nanowires. *Nanoscale* **7**, 10472 (2015).

[Nilsson16] M. Nilsson, L. Namazi, S. Lehmann, M. Leijnse, K. A. Dick, and C. Thelander. Single-electron transport in InAs nanowire quantum dots formed by crystal phase engineering. *Phys. Rev. B* **93**, 195422 (2016).

[Norris05] D. J. Norris. *Semicondcutor and Metal Nanocrystals - Synthesis and Electronic and Optical Properties*, chapter I - 2 Electronic Structure in Semiconductor Nanocrystals, page 66, (CRC Press, 2005).

[Olsson96] L. O. Olsson, C. B. M. Andersson, M. C. Håkansson, J. Kanski, L. Ilver, and U. O. Karlsson. Charge accumulation at InAs surfaces. *Phys. Rev. Lett.* **76**, 3626 (1996).

[Plissard13] S. R. Plissard, I. van Weperen, D. Car, M. A. Verheijen, G. W. G. Immink, J. Kammhuber, L. J. Cornelissen, D. B. Szombati, A. Geresdi, S. M. Frolov, L. P. Kouwenhoven, and E. P. A. M. Bakkers. Formation and electronic properties of InSb nanocrosses. *Nature nanotechnology* **8**, 859 (2013).

[Popkin17] G. Popkin. Science latest news - scientists are close to building a quantum computer that can beat a conventional one (December 2016) (accessed July 26, 2017).

[Protochips17] Protochips. Fusion TEM heating and electrical system (accessed July 26, 2017).

[Qu15] F. Qu, A. J. Beukman, S. Nadj-Perge, M. Wimmer, B.-M. Nguyen, W. Yi, J. Thorp, M. Sokolich, A. a. Kiselev, M. J. Manfra, C. M. Marcus, and L. P. Kouwenhoven. Electric and magnetic tuning between the trivial and topological phases in InAs/GaSb double quantum wells. *Physical Review Letters* **115**, 036803 (2015).

[Raman17] C. V. Raman. The molecular scattering of light - nobel lecture (1930) (accessed July 26, 2017).

[Rieger15] T. Rieger, D. Grutzmacher, and M. I. Lepsa. Misfit dislocation free InAs/GaSb core–shell nanowires grown by molecular beam epitaxy. *Nanoscale* **7**, 356 (2015).

[Rieger16] T. Rieger, D. Rosenbach, D. Vakulov, S. Heedt, T. Schäpers, D. Grützmacher, and M. I. Lepsa. Crystal phase transformation in self-assembled InAs nanowire junctions on patterned Si substrates. *Nano letters* **16**, 1933 (2016).

[Rocci16] M. Rocci, F. Rossella, U. P. Gomes, V. Zannier, F. Rossi, D. Ercolani, L. Sorba, F. Beltram, and S. Roddaro. Tunable Esaki Effect in Catalyst-Free InAs/GaSb Core-Shell Nanowires. *Nano Letters* **16**, 7950 (2016).

[Saxena13] D. Saxena, S. Mokkapati, P. Parkinson, N. Jiang, Q. Gao, H. H. Tan, and C. Jagadish. Optically pumped room-temperature GaAs nanowire lasers. *Nature Photonics* **7**, 963 (2013).

[Scheffler09] M. Scheffler, S. Nadj-Perge, L. P. Kouwenhoven, M. T. Borgstroom, and E. P. a. M. Bakkers. Diameter-dependent conductance of InAs nanowires. *Journal of Applied Physics* **106**, 124303 (2009).

[Sourribes14] M. J. L. Sourribes, I. Isakov, M. Panfilova, H. Liu, and P. a. Warburton. Mobility enhancement by Sb-mediated minimisation of stacking fault density in InAs nanowires grown on silicon. *Nano letters* **14**, 1643 (2014).

[Spanton14] E. M. Spanton, K. C. Nowack, L. Du, G. Sullivan, R.-R. Du, and K. A. Moler. Images of edge current in InAs/GaSb quantum wells. *Physical Review Letters* **113**, 026804 (2014).

[Spirkoska08] D. Spirkoska, G. Abstreiter, and A. Fontcuberta i Morral. Size and environment dependence of surface phonon modes of gallium arsenide nanowires as measured by Raman spectroscopy. *Nanotechnology* **19**, 435704 (2008).

[Tambe10] M. J. Tambe, S. Ren, and S. Gradecak. Effects of gold diffusion on n-type doping of GaAs nanowires. *Nano letters* **10**, 4584 (2010).

[Tang15] K. Tang, R. Winter, L. Zhang, R. Droopad, M. Eizenberg, and P. C. McIntyre. Border trap reduction in Al2O3/InGaAs gate stacks. *Applied Physics Letters* **107**, 0 (2015).

[Tell68] B. Tell and R. J. Martin. Raman scattering by coupled optical-phonon-plasmon modes in GaAs. *Physical Review* **167**, 381 (1968).

[Thelander03] C. Thelander, T. Mårtensson, M. T. Björk, B. J. Ohlsson, M. W. Larsson, L. R. Wallenberg, and L. Samuelson. Single-electron transistors in heterostructure nanowires. *Applied Physics Letters* **83**, 2052 (2003).

[Thelander11] C. Thelander, P. Caroff, S. Plissard, A. W. Dey, and K. A. Dick. Effects of crystal phase mixing on the electrical properties of InAs nanowires. *Nano letters* **11**, 2424 (2011).

[Thelander12] C. Thelander, P. Caroff, S. Plissard, and K. A. Dick. Electrical properties of InAs(1-x)Sb(x) and InSb nanowires grown by molecular beam epitaxy. *Applied Physics Letters* **100**, 232105 (2012).

[Timm11] R. Timm, M. Hjort, A. Fian, C. Thelander, E. Lind, J. N. Andersen, L.-E. Wernersson, and A. Mikkelsen. Interface composition of atomic layer deposited HfO2 and Al2O3 thin films on InAs studied by X-ray photoemission spectroscopy. *Microelectronic Engineering* **88**, 1091 (2011).

[Tomioka12] K. Tomioka, M. Yoshimura, and T. Fukui. A III-V nanowire channel on silicon for high-performance vertical transistors. *Nature* **488**, 189 (2012).

[Tsan17] D. Tsan. The silicon cube (October 2010) (accessed July 26, 2017).

[Tsao93] J. Y. Tsao. *Materials Fundamentals of Molecular Beam Epitaxy*, (Academic Press, 1993).

[Tutuncuoglu15] G. Tutuncuoglu, M. de la Mata, D. Deiana, H. Potts, F. Matteini, J. Arbiol, and A. Fontcuberta i Morral. Towards defect-free 1-D GaAs/AlGaAs heterostructures based on GaAs nanomembranes. *Nanoscale* **7**, 19453 (2015).

[Uccelli11] E. Uccelli, J. Arbiol, C. Magen, P. Krogstrup, E. Russo-averchi, M. Heiss, G. Mugny, J. Nyg, J. R. Morante, and A. Fontcuberta. Three-dimensional multiple-order twinning of self-catalyzed GaAs. *Nano letters* **11**, 3827 (2011).

[Vinas17] F. Vinas, H. Q. Xu, and M. Leijnse. Extracting band structure characteristics of GaSb/InAs core-shell nanowires from thermoelectric properties. *Phys. Rev. B* **95**, 115420 (2017).

[Vukajlovic-Plestina17] J. Vukajlovic-Plestina, W. Kim, V. G. Dubrovski, G. Tütüncüoğlu, M. Lagier, H. Potts, M. Friedl, and A. Fontcuberta i Morral. Engineering the size distributions of ordered GaAs nanowires on silicon. *Nano Letters* **17**, 4101 (2017).

[Wagner64] R. S. Wagner and W. C. Ellis. Vapor-liquid-solid mechanism of single crystal growth. *Applied Physics Letters* **4**, 89 (1964).

[Webb15] J. L. Webb, J. V. Knutsson, M. Hjort, S. Gorji Ghalamestani, K. A. Dick, R. Timm, and A. Mikkelsen. Electrical and surface properties of InAs/InSb nanowires cleaned by atomic hydrogen. *Nano Letters* pages 4865–4875 (2015).

[Weber10] J. R. Weber, A. Janotti, and C. G. V. de Walle. Intrinsic and extrinsic causes of electron accumulation layers on InAs surfaces. *Applied Physics Letters* **97**, 192106 (2010).

[Wei95] S. H. Wei and A. Zunger. InAsSb/InAs: A type-I or a type-II band alignment. *Physical Review B* **52**, 12039 (1995).

[Wildöer97] J. W. G. Wildöer, C. J. P. M. Harmans, and H. van Kempen. Observation of landau levels at the InAs(110) surface by scanning tunneling spectroscopy. *Phys. Rev. B* **55**, R16013 (1997).

[Wunnicke06] O. Wunnicke. Gate capacitance of back-gated nanowire field-effect transistors. *Applied Physics Letters* **89**, 083102 (2006).

[Yazawa92] M. Yazawa, M. Koguchi, A. Muto, M. Ozawa, and K. Hiruma. Effect of one monolayer of surface gold atoms on the epitaxial growth of InAs nanowhiskers. *Applied Physics Letters* **61**, 2051 (1992).

[Zadeh16] I. E. Zadeh, A. W. Elshaari, K. D. Jöns, A. Fognini, D. Dalacu, P. J. Poole, M. E. Reimer, and V. Zwiller. Deterministic integration of single photon sources in silicon based photonic circuits. *Nano Letters* **16**, 2289 (2016).

[Zhou10] Z. Y. Zhou, C. X. Zheng, W. X. Tang, D. E. Jesson, J. Tersoff, Z. Y. Zhou, and C. X. Zheng. Congruent evaporation temperature of GaAs(001) controlled by As flux. *Applied Physics Letters* page 121912 (2010).

HEIDI POTTS

Rue de la Paix 9
1020 Renens
Switzerland
+41 79 388 77 02

pottsheidi@gmail.com
skype: heidi.potts
www.linkedin.com/in/heidi-potts

STRENGTHS

- Materials scientist specialized in semiconducting nanostructures and microfabrication
- Expert for operation and maintenance of a molecular beam epitaxy (MBE) cluster tool
- Excellent language and communication skills, project management

HIGHER EDUCATION

present **Ecole Polytechnique Fédérale de Lausanne EPFL (CH)**
PhD in Materials Science and Engineering (expected October 2017)

2013 **University of Basel (CH)**
Master of Science in Nanoscience, grade 5.9 (highest: 6)
2012-2013 Master Thesis at University of Toronto UofT (CA)

2011 **University of Basel (CH)**
Bachelor of Science in Nanoscience, grade 5.7 (highest: 6)

2007 **Abitur (D)** grade 1.0 (highest: 1)

CORE EXPERIENCE

present **Laboratory of Semiconductor Materials (EPFL):**
Doctoral thesis: Growth and Characterization of InAs(Sb) Nanowires

- Management of three research projects involving six Master students
- Operation and maintenance of a ultra-high vacuum (UHV) molecular beam epitaxy (MBE) cluster tool (>2Mio CHF)
- Purchase, installation and programming of a new antimony cell (120 kCHF)
- Collaborations with Stanford (McIntyre group) and Oxford (Johnston group)
- teaching assistant

2012-2013 **Advanced Photovoltaics Photonics and Devices Group (UofT):**
Master thesis: Passivation of Silicon for High-Efficiency Photovoltaics

- Planning, installation, and operation of an oxidation chamber using ozone
- Surface passivation and characterization

2012 **Poggio Lab for Nano-mechanics, Magnetism and MRI (University of Basel):**
Master project: Dissipation Measurements of Annealed Nano Cantilevers

- Planning (SolidWorks), installation, and operation of an annealing chamber for nano-mechanical cantilevers

LANGUAGES

German (native), English (C2), French (B2), Spanish (B1)

ADDITIONAL EXPERIENCE

present	**QSIT Network:** Organization of a 3-day conference for 40 PhD students (budget 17 kCHF)
2015	**Materials Research Society:** Conference assistant at the MRS Spring Meeting 2015
2011– 2012	**Department of Mathematics (University of Basel):** Teaching assistant for calculus and linear algebra (20%)
2008	**Fraunhofer IWM and EMI, Freiburg:** Internship (6 months) ▪ Simulation of nano-indentation (Fortran) ▪ Hardware communication for a pico-satellite using an FPGA (C)

TECHNICAL SKILLS

Growth and characterization of materials:

Molecular beam epitaxy (MBE), scanning and transmission electron microscopy (SEM and TEM), energy dispersive x-ray spectroscopy (EDX), electrical measurements at room temperature and 4K, spectroscopic ellipsometry, angle-resolved photoelectron spectroscopy (XPS), recombination measurements

Nanofabrication (ISO 5 cleanroom):

Photo and ebeam lithography, evaporation, sputtering, atomic layer deposition (ALD), plasma enhanced chemical vapor deposition (PECVD), wet and dry etching

Computer & IT:

Matlab, Igor, Origin, Latex, Adobe Illustrator, MS Office (working knowledge)
Python, LabView, Blender (basic knowledge)
Machine Learning (course on Coursera by Stanford University)

HONOURS & AWARDS

2016	Best poster nominee at the MRS Fall Meeting, Boston
2014	Best poster award at the Nanowire Growth Workshop, Eindhoven
2013	Best Master thesis in Nanoscience, University of Basel
2012	Nanoscience Argovia travel grant for Master Thesis, University of Basel
2005 – 2006	Invent a Chip and Pro7 Wissenspreis

EXTRACURRICULAR ACTIVITIES

2010 – 2012	**IAESTE Switzerland: Active member** Contact person for international trainees in Basel, organization of group events
2008 – 2012	**University of Basel: member of the nanoscience students association** Treasurer, organization of events, creation of information material
2007	**Verein Staufen-Paraguay: Volunteer in Paraguay (6 months)** Teacher for English, mathematics and German

PERSONAL INFORMATION & INTERESTS

29 years old, German and Canadian citizen (B permit in Switzerland), drivers licence
Traveling, alpine sports, sailing, playing accordion (active member in an orchestra for 8 years)

PUBLICATIONS

W. Kim, V. Dubrovski, J. Vukajlovic-Plestina, G. Tutuncuoglu, L. Francaviglia, L. Guniat, **H. Potts**, M. Friedl, J.-B. Leran, A. Fontcuberta i Morral. Bi-stability of contact angle and its role in achieving quantum-thin self-assisted GaAs nanowires (submitted)

J. Vukajlovic-Plestina, W. Kim, V. G. Dubrovski, G. Tutuncuoglu, M. Lagier, **H. Potts**, M. Friedl, and A. Fontcuberta i Morral. Engineering the size distributions of ordered GaAs nanowires on silicon. *Nano Letters* **17**, 4101 (2017)

H. Potts, Y. van Hees, G. Tutuncuoglu, M. Friedl, J.-B. Leran, A. Fontcuberta i Morral. Tilting catalyst-free InAs nanowires by 3D-twinning and unusual growth directions. *Crystal Growth & Design* **17**, 3596 (2017)

J. Vukajlovic-Plestina, V. Derek, L. Francaviglia, F. Amaduzzi, **H. Potts**, M. Ivanda, and A. Fontcuberta i Morral. Nanoporous silicon tubes: the role of geometry in nanostructure formation and application to light emitting diodes. *Journal of Physics D: Applied Physics* **50**, 265101 (2017)

H. Potts, N. P.Morgan, G. Tutuncuoglu, M. Friedl, and A. Fontcuberta i Morral. Tuning growth direction of catalyst-free InAs(Sb) nanowires with indium droplets. *Nanotechnology* **28**, 054001 (2017)

F. Matteini, G. Tutuncuoglu, D.Mikulik, J. Vukajlovic-Plestina, **H. Potts**, J.-B. Leran,W. Carter, and A. Fontcuberta i Morral. Impact of the Ga droplet wetting, morphology, and pinholes on the orientation of GaAs nanowires. *Crystal Growth & Design* **16**, 5781 (2016)

J. Vukajlovic-Plestina, V. Dubrovskii, G. Tutuncuoglu, **H. Potts**, R. Ricca, F. Meyer, F. Matteini, J.-B. Leran, and A. Fontcuberta i Morral. Molecular beam epitaxy of InAs nanowires in SiO2 nanotube templates: challenges and prospects for integration of III-Vs on Si. *Nanotechnology* **27**, 455601 (2016)

M. Glaser, A. Kitzler, A. Johannes, S. Prucnal, **H. Potts**, S. Conesa-Boj, L. Filipovic, H. Kosina,W. Skorupa, E. Bertagnolli, C. Ronning, A. Fontcuberta i Morral, and A. Lugstein. Synthesis, morphological, and electro-optical characterizations of metal/semiconductor nanowire heterostructures. *Nano Letters* **16**, 3507 (2016)

H. Potts, M. Friedl, F. Amaduzzi, K. Tang, G. Tutuncuoglu, F. Matteini, P. C. McIntyre, and A. Fontcuberta i Morral. From twinning to pure zincblende catalyst-free InAs(Sb) nanowires. *Nano Letters* **16**, 637 (2016)

A. D. Alvarez, T. Xu, G. Tutuncuoglu, T. Demonchaux, J. P. Nys,M. Berthe, F.Matteini, **H. Potts**, D. Troadec, G. Patriarche, J.-F. Lampin, C. Coinon, A. Fontcuberta i Morral, R.E. Dunin-Borkowski, Ph. Ebert, and B. Grandidier. Nonstoichiometric low-temperature grown GaAs nanowires. *Nano Letters* **15**, 6440 (2015)

G. Tutuncuoglu, M. de la Mata, D. Deiana, **H. Potts**, F. Matteini, J. Arbiol, and A. Fontcuberta i Morral. Towards defect-free 1-D GaAs/AlGaAs heterostructures based on GaAs nanomembranes. *Nanoscale* **7**, 19454 (2015)

F. Matteini, G. Tutuncuoglu, **H. Potts**, F. Jabeen, and A. Fontcuberta i Morral. Wetting of Ga on SiOx and its impact on GaAs nanowire growth. *Crystal Growth & Design* **15**, 3105 (2015)

E. Wiesenmayer, H. Luetkens, G. Pascua, R. Khasanov, A. Amato, **H. Potts**, B. Banusch, H. Klauss and D. Johrendt. Microscopic coexistence of superconduductivity and magnetism in $Ba_{1-x}K_xFe_2As_2$. *Physical Review Letters* **107**, 233201 (2011)

CONFERENCES

2017	**Nanowire Week, Lund (SE)** Self-catalyzed InAs nanowires in many different directions (talk)
2017	**German-Swiss Conference on Crystal Growth, Freiburg (D)** Controlling the growth direction of self-catalyzed InAs nanowires (talk)
2017	**QSIT general meeting, Arosa (CH)** Bottom-up engineered nanostructures for quantum applications (poster)
2016	**MRS Fall Meeting, Boston (USA)** Defect-free InAsSb and branching of InAs nanostructures (poster)
2016	**19th International Conference on Molecular Beam Epitaxy, Montpellier (F)** InAsSb nanostructures for transport experiments (talk)
2016	**Swiss Nano Convention, Basel (CH)** Growth and Characterization of InAsSb nanostructures (poster)
2016	**EMN meeting on Nanowires, Amsterdam (NLD)** Catalyst-free growth of III-V nanowires and heterostructures (talk, invited)
2016	**QSIT general meeting, Arosa (CH)** Growth and characterization of InAsSb and ZnAs nanostructures (poster)
2015	**Nanowire Growth Workshop, Barcelona (ES)** Growth and characterization of twin-free InAsSb nanowires (poster)
2015	**Quantum Systems and Technology, Ascona (CH)** Defect-free InAsSb nanowires and core-shell heterostructures (poster)
2015	**Swiss Nano Convention, Neuchatel (CH)** III-V nanostructures and their properties (poster)
2015	**DGKK Arbeitskreistreffen Epitaxie von III-V Halbleitern (D)** Twin-free InAsSb nanowires: Growth and characterization (talk)
2015	**MRS Spring Meeting, San Francisco (USA)** MBE growth of defect-free InAsSb nanowires (poster)
2015	**18th European Molecular Beam Epitaxy workshop, Canazei (IT)** Defect-free InAsSb nanowires for InAs/GaSb heterostructures (poster)
2015	**QSIT general meeting, Arosa (CH)** Towards defect-free InAs(Sb)/GaSb core-shell nanowire heterostructures (talk)
2014	**Nanowire Growth Workshop, Eindhoven (NLD)** Self-assisted InAs nanowires for InAs/GaSb heterostructures (poster)
2014	**QSIT junior meeting, Passugg (CH)** Towards defect-free InAs Nanowires for Novel III-V Heterostructures (talk)
2014	**QSIT general meeting, Arosa (CH)** Quantum systems in III-V core-shell nanowires (poster)